Diamond Nanostructured Devices

For Chemical Sensing Applications

Rezal Khairi bin Ahmad

This thesis is submitted for the degree of Doctor of Philosophy

Department of Electronic and Electrical Engineering

University College London

University of London

2011

Declaration

The work in this thesis is the result of research activities carried out with the Diamond Electronics Group at the London Centre for Nanotechnology, University College London. I declare it to be my own work unless referenced to the contrary in the text

Acknowledgement

This thesis is dedicated to God Almighty, with my utmost sincere gratitude for providing me the opportunity, strength, patience, perseverance, compassion, love and importantly guidance. This is for You.

My deepest gratitude goes to Yayasan Khazanah and Khazanah Nasional Berhad for selecting me to be part of the 'chosen few' in Malaysia and crucially, financing this PhD study. Specifically, I must thank Suhayati Dzali and Noorlida Jihen for personally looking out for me in your designated respective capacities and more. Honourable mention to Tan Sri Azman Mokhtar, Tan Sri Ahmad Tajuddin, Azman Hussein and Dr. Ikmal for those interview sessions.

I would like a big thank-you to my research supervisor, Prof. Richard B. Jackman for agreeing to accept me as his PhD student. His intellectual inputs, support, high-level enthusiasm, friendship and trust are priceless. Our lively debate on the existence of God will be a salient fond memory of mine. Other activities such as curry lunches, quick-pint (QP) sessions, Diamond Conference 2009 in Athens and that one Christmas dinner in 2007 sit right up as one many highlights of this journey. Gratitude to Dr Haitao Ye for that invaluable and unforgettable trip to Oxford for my first experimental work. My heartfelt appreciation to Dr Niall Tumilty, Dr Mose Bevilacqua, Aysha Chaudhary, Robert Edgington and Joseph Welch the UCL Diamond Group, for many cerebral, controversial, provocative, heart-warming conversations and moments. Not forgetting Benjamin Kupfer, Aiman Zainal and Farahana Azmin for their kind contributions in aspects of this work. Special thanks to Carolina Parada for her assistance in making 2010 a very productive year. And to Steve Hudziak for accommodating the needs of the experimental work notably with the AFM.

Prof John S. Foord and his then apprentice, Montree Sawangphruk are thanked for access to the Chemistry Research Lab in Oxford University and

importantly, their assistance in the electrochemistry work on my lovely diamond transistors.

To my crew here in London, Husni Abdul Wahab, Azura Abas, Fazlina Nordin, Budi Aslinie Sabri, Tye Gee Jun, Hazrina Hadi, Hazreen Majid, Hikmah Mohd Nor, Haszelini Hassan and Malaysian Post Graduate Council members, high-fives to you guys. Malaysia does not feel too far away with you around, especially at our 'makan-makan' gatherings and, on weekends of indulgence and road-trips.

And to my gym buddies Igor, Ingrid, Hang and the rest, thanks for the therapeutic nonsensical conversations (Igor, you would know this!) and weighty supports, pun intended.

My sincere gratitude is extended to a great friend of mine, Sivadass Tiruchelvam for the long-distance moral support and encouragement. A special mention to the Unit Kenchang gang, notably Hariana and Francis, your friendships are beyond measure.

To my dearest Dura, the most beautiful thank you for your lovely presence in my life. 2010 was truly memorable and thesis writing more bearable with you around. Stay amazing just the way you are.

With critical importance, it is with gratitude and appreciation I extend a very deep and special gratitude to my late father Dr Ahmad Dato' Abdullah, my mother Rahmah Yahya, my 'other' late father Ungku Mohd Khalid Ungku Ibrahim, my 'other' mother Zainab Yahya, my brothers Danial and Shahrin, my sisters Maya and Alisa, my beloved nieces and nephews Mari, Gabe, Aiman, Amir, Ayra and Aaron, and my other 'sisters' the late Ungku Suhainah and Ungku Salwa, and Ungku Zubaidah. It has been an honour to have had received unconditional support, encouragement, words of wisdom and love from each one of you.

Abstract

Research in the area of CVD single crystal diamond plates of which only recently has been made commercially available saw significant advancements during the last decade. In parallel to that, detonation nanodiamond (DND) particles also now widely made accessible for requisition are provoking a lot of scientific investigations. The remarkable properties of diamond including its extreme hardness, low coefficient of friction, chemical inertness, biocompatibility, high thermal conductivity, optical transparency and semiconducting properties make it attractive for a number of applications, among which electronic and micro electrical-mechanical systems devices for chemical and biological applications are few of the key areas. A detailed knowledge of diamond devices at the prototypical stage is therefore critical.

The work carried out encapsulated in this thesis describes the employment of the nanometer-scale diamond structures for the design, fabrication and testing of electronic devices and micro electrical-mechanical system (MEMS) structures for chemical sensing applications. Two major approaches are used to achieve engineering novelty. The first type being devices based on single crystal diamond substrates, which include state of the art δ-doped single crystal diamond Ion Sensitive Field Effect Transistor with an intrinsic layer capping the delta-doped layer for pH sensing and the fabrication and characterization of a triangular-face single crystal diamond MEMS. A comprehensive set of characterisations was systematically performed on the delta ISFET devices. Cyclic Voltammetry has been used to determine the devices' potential window determining the limits of the applied potential for the Current-Voltage measurements. In solutions of different pH levels, an improved sensitivity of 55mV/pH compared to cap-less design in a previous study is taken as the salient figure of merit. Electrochemical Impedance Spectroscopy sheds some light on device performance in terms of flatband voltages and conduction pathways through circuit modelling. Improved ISFET characteristics such as lower flat-band voltage at 3.74V, simpler conduction paths and drain current saturation onsets show the chosen design is correct

and advances delta-doped diamond ISFET research and development work. For the single crystal diamond cantilever, the theoretical modelling supports the triangular-face design to be a better option, generating 3x greater deflections in relation to the conventional rectangular-face design, when operated as a static mode sensor. Based on experimental characterisation methods such as Raman and Energy Dispersive Spectroscopy, the focused-ion beam only milling technique inflicts minimum damage to the beam structure.

In the second approach, a novel hybrid device idea was conceived and implemented using off-the-shelf silicon ISFETs and cantilevers with a coat of nanodiamond particles on the 'active area' surfaces of the respective devices. These nanodiamond-coated silicon devices exhibit high sensitivity for tracing threat signatures such as explosive precursors and analogues with the former in both liquid and vapour medium, and the latter in the vapour phase. The nanodiamond-gated ISFET shows a voltage response of a commendable maximum voltage shift of ~90 mV throughout 0 to 0.1M concentration range of NO_2^- and ClO_3^- solutions. In the vapour phase detecting 2,4-DNT, a sensitivity of ~20mV/0.4ppm is observed. The nanodiamond-coated silicon cantilever demonstrates a performance advantage of 7.4 Hz/ppb to 1.7 Hz/ppb in a previous study. Fourier Transform Infra-red spectroscopy was carried out on the nanodiamond surfaces hosted by potassium bromide (KBr) discs to ascertain the vapour chemisorption. With the fabrication technique simplified, commercialisation of these proof-of-concept devices should be less time consuming thus enabling quicker deployment of diamond-based surface sensing technology.

Table of Contents

Chapter 1

Introduction

1.1 Introduction

Diamonds have been treasured as gemstones particularly for adornment, a use that dates back into antiquity. The dispersion of white light into spectral colours is the primary gemmological characteristic of gem diamonds. The popularity of diamonds has risen since the 19th century because of increased supply, improved cutting and polishing techniques, growth in the world economy, and innovative and successful advertising campaigns. In the 20th century, experts in gemmology have developed methods of grading diamonds and other gemstones based on the characteristics most important to their value as a gem. Four characteristics, known informally as the four Cs, are now commonly used as the basic descriptors of diamonds: these are carat, cut, colour, and clarity.

Due to the outstanding mechanical, chemical and electronics properties, diamonds have generated a lot scientific activities with research outputs confirming the possibility of commercially available diamond-based devices of superior performances compared to those of other semiconductor materials. The high-pressure high temperature synthesis technology developed in 1950s paved way for the diamond production. However, it was only with advent of the Chemical Vapour Deposition (CVD) technology in the 1960s [1-3] diamond as a semiconductor material became a possibility. Progress made in the form of the production of electronic grade material and the incorporation of impurities or dopants during growth further cemented the viability of diamond-based devices. Dopant candidates for diamond are boron, nitrogen, phosphorous, and lithium amongst others. Practical doping could only be achieved using boron with ionisation energy of 0.37eV above the valence band edge, rendering diamond p-type. Available n-type dopants carry much larger ionisation energies with nitrogen and phosphorous at 1.7eV and 0.6eV respectively below the conduction band edge. This means, room temperature operation for diamond bipolar devices is not possible at the current state of technology. The commercial availability of detonation nanodiamonds (DND) opened the doors to scientific exploration where chemically inert and

biocompatible nanometre-sized particles are required, and inception of simpler device concepts employing a coat of DNDs.

Chapter 2 reviews the field of diamond technology, reporting on structure, growth, properties and applications. An account of the chemical vapour deposition methods for growing diamond is included in this presentation. Also covered here are doping techniques with respective p and n-type dopants. Synthesis of nanodiamond particles and corresponding properties are also reviewed. Chapter 3 takes a retrospective view on relevant diamond-based electronic and micro electrical-mechanical systems devices. This is followed by Chapter 4, which explains the experimental methods and techniques used in this thesis.

In Chapter 5, ion-sensitive field effect transistors (ISFETs) have been fabricated based upon intrinsic-capped boron δ-doped single crystal diamond substrates. Device characterisation was made using cyclic voltammetry, current-voltage measurements and electrochemical impedance spectroscopy. ISFET output and transfer characteristics, Nernstian pH sensitivities, and flatband voltages have been recorded. The devices are also subjected to electrochemical impedance spectroscopy characterisation to further elucidate the observed results.

Chapter 6 presents a hybrid concept to designing a diamond-based ISFET. A coat of detonation nanodiamond particles has been applied onto the active or sensing area of an off-the-shelf silicon ISFET. Basic potentiometry concept is used to describe the observed changes in the output voltage in response to target particles both in the liquid and vapour phases.

In Chapter 7, focused-ion beam (FIB) is used to mill triangular face cantilever structures made from HPHT Ib-type single crystal diamond. Using beam theory, the deflectivity of the cantilever is modelled against that of the traditional rectangular face. Raman and Energy Dispersive Spectroscopy are applied to characterise the freestanding structure in terms of lattice damage and contamination induced by the FIB-only milling technique.

Chapter 8 describes the duplication of the concept realised in Chapter 6 onto silicon cantilever array. Using the AFM cantilever as a micro-indenter, the nanodiamond coated silicon cantilevers are mechanically characterised producing the spring constant (k). Results from the dynamic mode characterisation allow nanodiamond coverage to be determined and correspondingly, nanodiamond-loaded quiescent deflected state are then calculated using beam theory. As a proof of sensor concept, the cantilever arrays are exposed to an explosive analogue 2,4-dinitrotoluene in the dynamic mode and changes in resonance frequency are taken as a measure of sensing events. Trends observed are duly discussed therein.

Lastly, Chapter 9 summarises the thesis and puts forward concluding remarks based on the work achieved at UCL, as well as laying in general direction for future work. The significance and impact of the results obtained here on the potential use of diamond for chemical and biological application are also discussed.

1.2 References

[1] W.G. Eversole, U.S. Patent, 030, 188, April 17, 1962
[2] J.C. Angus et al. J. Appl. Phys. 39:2915 (1968)
[3] B.V. Deryagin and D.V Fedoseev, Rus. Chem. Rev. 39 39:783 (1970)

Chapter 2

Structure and synthesis of diamond

2.1 Introduction to Carbon

Carbon is a group IV element, symbolically denoted as C and carries an atomic number of 6. It has 4 electrons in its outer shell, in the configuration $1s^2\ 2s^2\ 2p^2$. The 1st or K shell can accommodate 2 electrons of opposite spin, therefore for carbon the first shell is full. This shell is at the lowest possible energy and completely stable. The 2nd or L shell, consisting of 2 sub-shells namely 2s and 2p orbitals contains the remaining 4 electrons with equal distribution. The 2 electrons in the $2s^2$ take on opposite spins whilst possessing the same energy and the last 2 electrons in the $2p^2$ are in parallel or separate sub-orbitals. Figure 2.1(a) below represents the aforementioned distribution of electrons in a carbon atom at their ground state. When carbon bonds are formed, orbital hybridization occurs allowing the 4 electrons in the L shell to take up places in separate orbitals. One of the $2s^2$ orbital electrons gets promoted up to a vacant 2p orbital, forming hybrid set of orbitals appropriately designated sp^3 having one s orbital and 3 p orbitals [1].

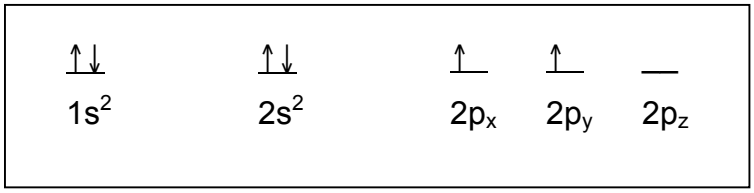

Figure 2.1: Distribution of electrons at available energy levels for carbon at its ground state

The four sp^3 hybrid orbitals will arrange themselves in three dimensional space to get as far apart as possible (to minimize repulsion). The geometry that achieves this is tetrahedral geometry, where any bond angle is 109.5^o. The stable electronic configuration for the 2nd shell is 8 and as a result, each one of the 4 sp^3 valence electrons covalently bonds with 1 valence electron of other carbon atoms making each carbon attached to 4 carbon atoms thus forming a tetrahedral carbon interconnected structure called the diamond lattice which is the atomic structure for diamond, a carbon allotrope. Each

bond is a sigma (σ) bond and the hybridization energy amounts to 230kJ mol^{-1} [2].

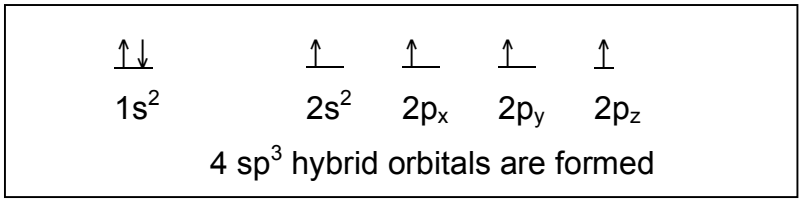

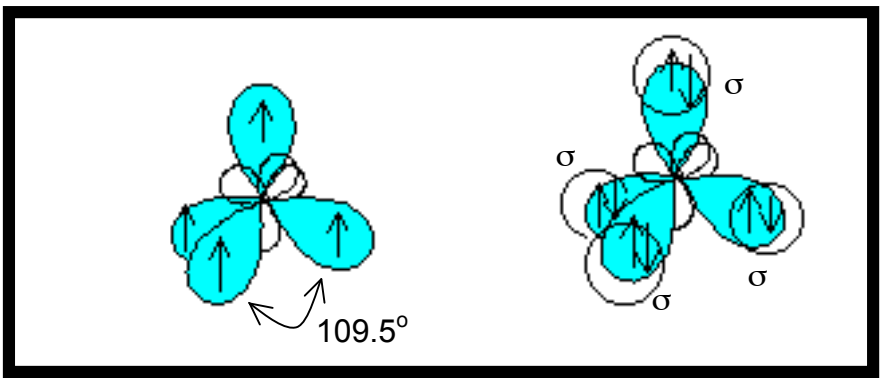

Figure 2.2: sp^3 hybridization and formation of sigma (σ) bonds [1]

Other carbon allotropes such as graphite, graphene and carbon nanotubes are examples of sp^2 hybridization. The sp^2 hybrid orbitals are generated when 3 of the 4 electrons in the 2s and 2p orbitals combine and achieve a planar trigonal geometry where the bond angle between the hybrid orbitals is 120°. The lone 2p electron remains unchanged and is perpendicular to this plane. Therefore a single carbon atom sigma (σ) bonds with 3 other forming carbon '2-D' sheets called graphene and the rolled-up version in the shape of tubular structure, carbon nanotubes. Sheets of graphene stack up to create graphite with the unhybridized 2p electrons establishing pi (π) bonds, weakly binding the carbon layers together by Van der Waals forces. This allows the planes to slide over each other and the reason behind the low shear modulus of graphite [2].

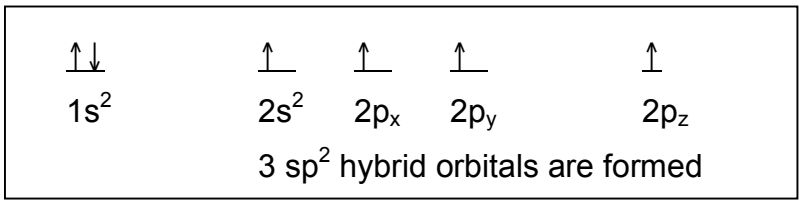

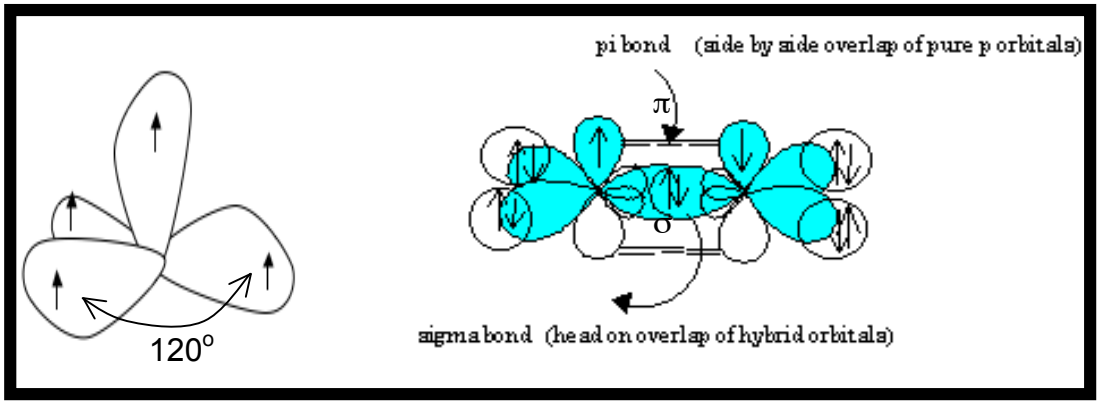

Figure 2.3: sp^2 hybridization and formation of sigma (σ) and pi (π) bonds [1]

The abovementioned allotropes are shown in figure 2.4. Each allotropic form exhibits different physical, chemical and effectively electrical properties.

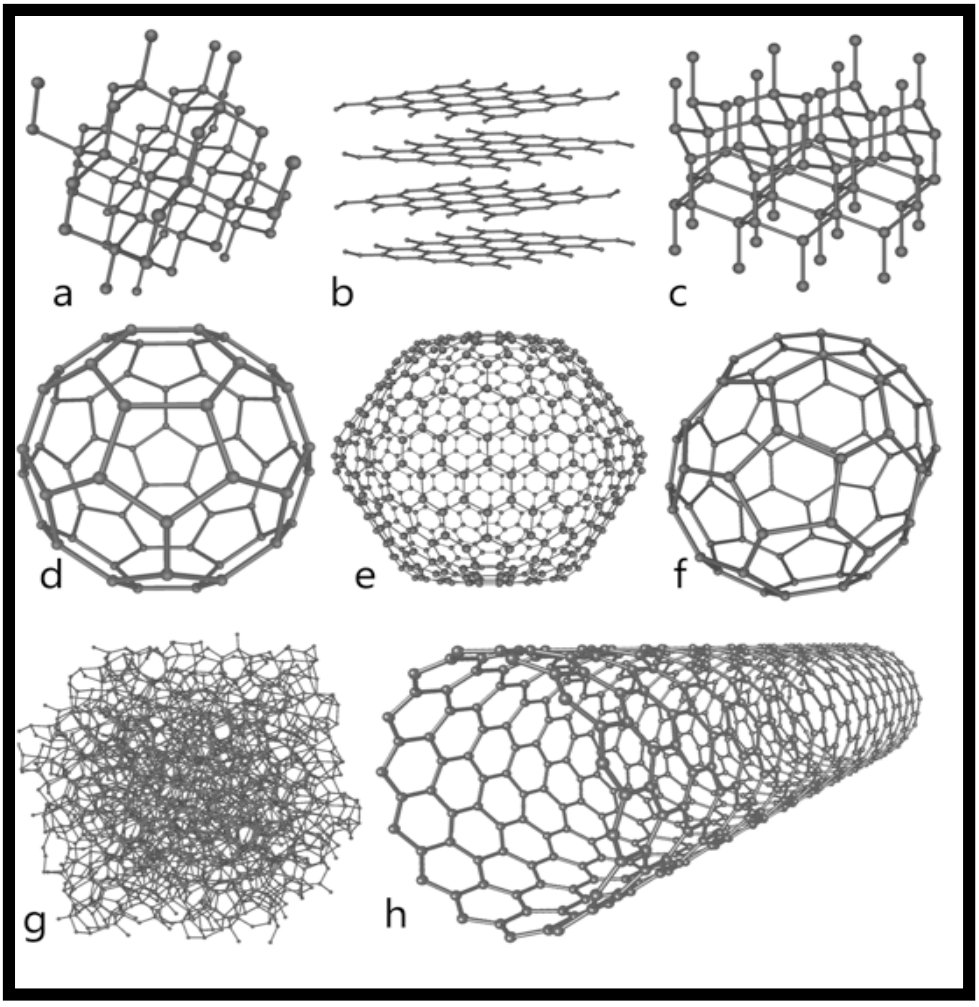

Figure 2.4: (a) diamond, (b) graphite (c) lonsdaleite, (d)-(f) buckyballs, (g) amorphous carbon (h) carbon nanotube [3]

2.2 Diamond

Diamonds are classified broadly under the categories of natural Diamond, synthetic industrial diamond and thin film diamonds on the basis of their process of origination. The word “diamond” is derived from a Greek word “adamas” which stands for “invincible". Due to its atomic structure, diamond is the hardest natural matter [4].

2.2.1 Properties of Diamond

Diamond exhibits extreme mechanical and outstanding electronic properties. The excellent properties exhibited by diamond such as high values of mobility with wide band-gap, high thermal conductivity and breakdown field strength serves as a primary motivation to use diamond as platform material for the realisation of electronic devices. The mechanical properties put diamond in good stead for micro electrical-mechanical systems applications.

Property	Value
Relative hardness	10 Mohs
Knoop hardness	8000
Abrasive hardness	140,000
Modulus of elasticity	700-1200 GPa
Young’s Modulus	1000 GPa
Poisson’s ratio	0.1-0.29
Volume compressibility	18×10^{-10} m^2 N^{-1}
Compressive yield strength	8680-16530 MPa
Density (300K)	3515.25 kg m^{-3}
Atomic concentration (300K)	1.763×10^{23} cm^{-3}
Bulk modulus	442.3 GPa
Thermal expansion	1.05×10^{-6} K^{-1}
Sound propagation velocity	18.2 km s^{-1}
Thermal conductivity (300K)	2000 W m^{-1} K^{-1}

Table 2.1: Mechanical properties of diamond [4]

Property	Value
Dielectric constant (300K)	5.5-5.7
Dielectric strength	1000 kV mm^{-1}
Band-gap type	Indirect
Electronic band-gap	5.48 eV
Electron mobility	1800 cm^2 V^{-1} s^{-1}
Hole mobility	1200 cm^2 V^{-1} s^{-1}
Relative permittivity	5.57
Intrinsic resistivity	10^{16} Ω-cm
Saturation electron velocity	2.7 x 10^7 cm s^{-1}

Table 2.2: Electronic properties of diamond [5]

2.2.2 Natural Diamond

Natural Diamonds, as the name indicates, are diamonds, which originate in nature. Natural Diamonds are further classified into four categories depending on the type and amount of impurities in them. They are:

Types	Description
Ia	Nitrogen being the dominant impurity with concentrations up to 5000ppm and is present as aggregates or clustered together within the carbon lattice. Its appearance takes on the pale yellow or brown colour. 98% of diamonds belong to this category.
Ib	Refers to diamond in which the nitrogen is present as single substitutional atoms and are uniformly distributed throughout the carbon lattice. This type of diamonds can appear deep yellow, orange, brown or greenish depending on the concentration and distribution of nitrogen atoms. They account for 0.1% of diamonds.
IIa	These diamonds are considered the “purest of the pure” with no or miniscule amount of impurities present. They are colorless unless for lattice defects which would render them appearing yellow, brown,

	pink or red. About 1-2% of diamonds are of this type
IIb	With no nitrogen present, this type contains boron as an impurity. They appear blue, grey and sometimes near-colorless. There make up about 0.1% of the available diamonds.

Table 2.3 Classification of natural diamond [6]

2.3 Synthetic diamond

2.3.1 Crystallinity

Diamond can be one single, continuous crystal or it can be made up of many smaller crystals (polycrystal). Large, clear and transparent single-crystal diamond is typically used in gemstones. Polycrystalline diamond consists of numerous small grains and it is unsuitable for gems and is used for industrial applications such as mining and cutting tools as well as in recent years, pioneering research work to create electronic devices. The average (grain) size of the crystal defines the polycrystalline diamond. Grain sizes range from nanometers to hundreds of micrometers usually referred to as nanocrystalline and microcrystalline diamond, respectively [7].

Diamonds in the form discrete nano-sized grains are tersely called nano-diamonds and typically kept suspended in solutions. Some of these nano-diamond particles agglomerate to form microsized clusters while some are individually dispersed. An in-depth description covering the synthesis and processing of nanodiamonds will be adequately presented later in this chapter.

2.3.2 High Pressure – High Temperature Synthesis

Diamonds can be synthetically grown using the High Pressure – High Temperature (HPHT) method. Under very high pressure and temperature conditions, diamond is thermodynamically stable and thus be formed, typically

from a solid graphite source [2]. The first HPHT diamond synthesis was reported in 1955 achieved by General Electric (US), AESA (Sweden) and Institute of High-Pressure Physics (then USSR) [8]. In essence, the HPHT synthesis duplicates the natural process in a manufacturing unit. Although thermodynamically feasible at relatively low pressure and temperature, the graphite-diamond transformation faces a considerable kinetic barrier since the rate of transformation apparently decreases with increasing pressure. This kinetic consideration supersedes the favorable thermodynamic conditions and it was found experimentally that very high pressure and temperature (>130 kb and ~3300 K) were necessary in order for the direct graphite-diamond transformation to proceed at any observable rate [8][9]. These conditions are very difficult and costly to achieve. Fortunately, it is possible to bypass this kinetic barrier by the solvent-catalyst reaction as illustrated in Figure 2.5. Shown in the figure 2.6 are the conditions for HPHT diamond growth.

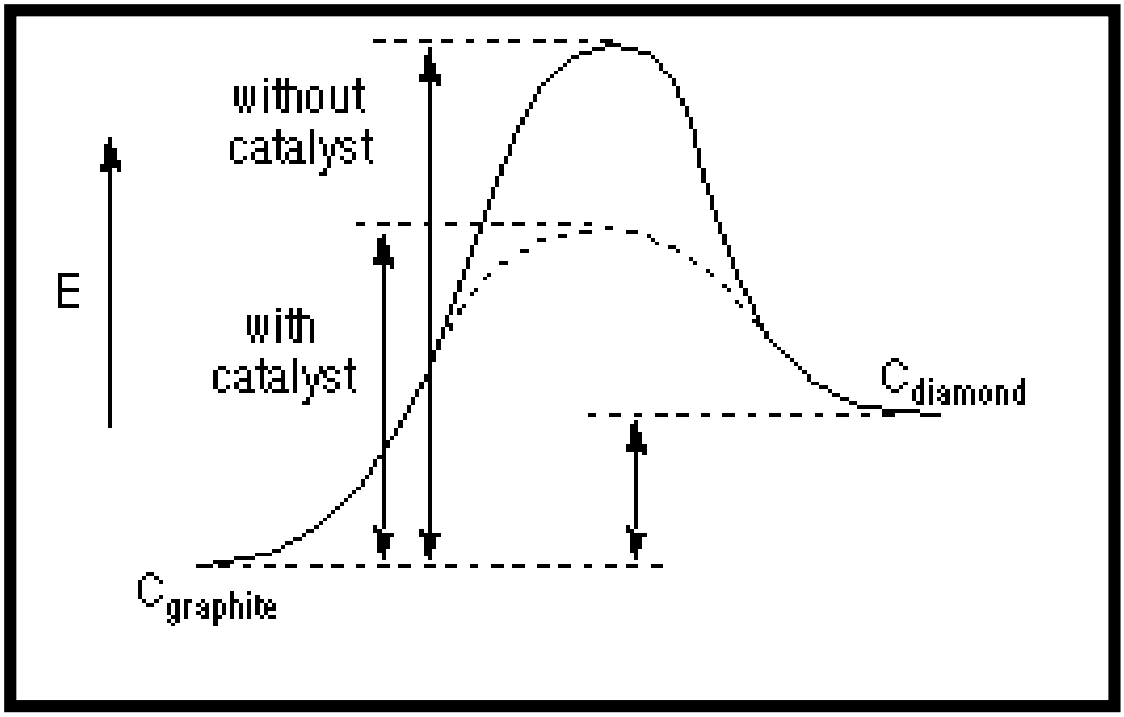

Figure 2.5: Diamond catalyst energy diagram [10]

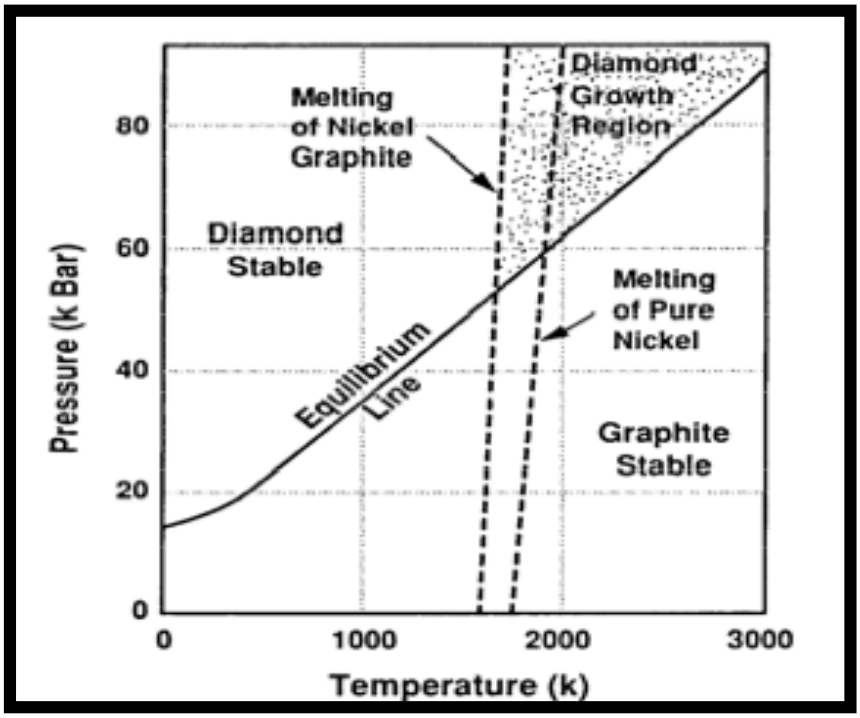

Figure 2.6: Pressure-temperature diagram of diamond-graphite and melting lines of nickel and nickel-graphite eutectic [10]

Formation of diamond at standard thermodynamic equilibrium occurs at pressures greater than 100,000 atmospheres and temperatures of 1000°C or more.

The solvent-catalyst process, developed by General Electric and others establishes a reaction path with lower activation energy than that of the direct transformation. This permits a faster transformation under more benign conditions. Basically, molten metal catalysts are used to dissolve carbon and accelerate its conversion into diamond thus reducing these required temperatures and pressures. As a result, solvent-catalyst synthesis is readily accomplished and is now a viable and successful industrial process. Not all carbon materials are suitable for the solvent-catalyst transformation. For instance, while graphitized pitch cokes form diamond readily, no transformation is observed with turbostratic carbon [11]. The solvent-catalysts are the transition metals such as iron, cobalt, chromium, nickel, platinum, and palladium. These metal-solvents dissolve carbon extensively, break the bonds between groups of carbon atoms and between individual atoms, and transport the carbon to the growing diamond surface [2].

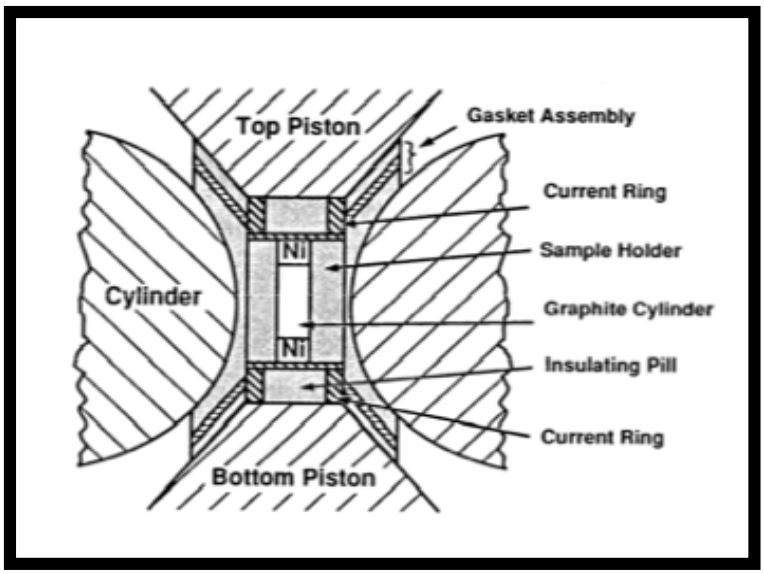

Figure 2.7: High Pressure High Temperature cell for the production of diamond [8]

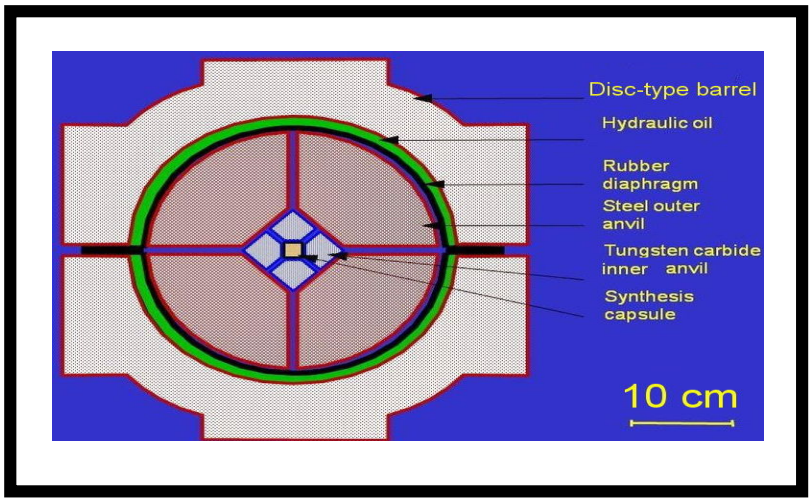

Figure 2.8: Schematic of a BARS system, a modern HPHT synthesis [12]

2.3.3 Chemical Vapour Deposition

Chemical vapor deposition is a technique used to grow diamond from a carbonaceous gas source. However, growing diamond from the vapour phase critically requires dynamic non-equilibrium system predominantly favouring sp^3 carbon bonds. The CVD growth essentially involves substrate preparation, feeding varying amounts of gases into a chamber and energizing them. It is critical to choose the correct crystallographic orientation for the substrate because it is duplicated in the epitaxial layer formed. The gas mixture always

includes a carbon source, typically methane, and hydrogen at a typical ratio of ~1:99 [13]. The basic reaction in the CVD of diamond involves the decomposition of a hydrocarbon such as methane [2]:

$$CH_4\ (g) \rightarrow C\ (\text{diamond}) + 2H_2\ (g)$$

Hydrogen is thought to selectively etch away non-diamond carbon whilst stabilizing the sp^3 structure and preventing it from collapsing into the sp^2 form thus promoting diamond growth. The gases are ionized into chemically active radicals in the growth chamber commonly using microwave power (microwave plasma enhanced CVD - MPECVD), a hot filament (hot filament CVD – HFCVD) and a welding torch (combustion flame CVD) [2].

The common essential growth procedures amongst the aforementioned technologies:

(i) formation of highly reactive radicals and reactant species

(ii) delivery of growth species to the growth surface

(iii) regulating the correct temperature at the growth surface

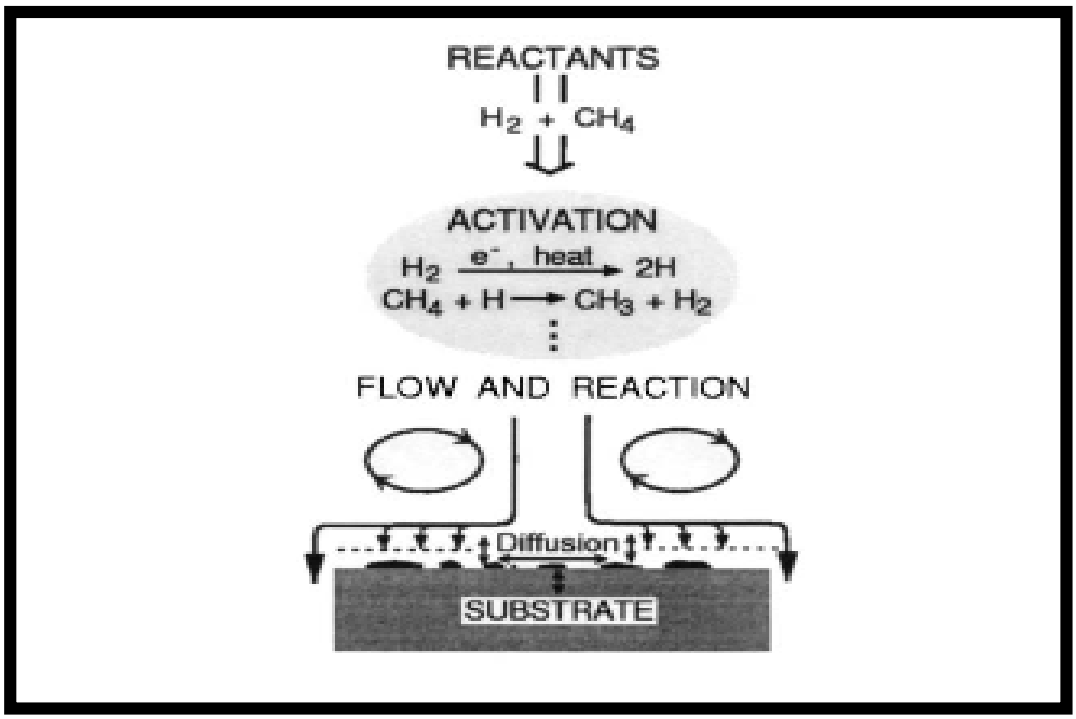

Figure 2.9: The diamond CVD process shown schematically [14]

2.3.3.1 Microwave Plasma Enhanced CVD (MEPCVD)

A glow-discharge (non-isothermal) plasma is generated in a gas by a high-frequency electric field such as microwave at relatively low pressure. In such a plasma, the following events occur. In the high-frequency electric field**,** the gases are ionized into electrons and ions. The electrons, with their very small mass, are quickly accelerated to high energy levels corresponding to 5000 K or higher. The heavier ions with their greater inertia cannot respond to the rapid changes in field direction, As a result, their temperature and that of the plasma remain low, as opposed to the electron temperature (hence the name non-isothermal plasma). The high-energy electrons collide with the gas molecules with resulting dissociation and generation of reactive chemical species and the initiation of the chemical reaction. The most common frequencies in diamond deposition are the microwave (MW) frequency at 2.45 GHz. Typical microwave deposition conditions are:

(i) Incident Power: 600W
(ii) Substrate Temperature: 800 - 1000°C
(iii) Gas mixture H_2/CH_4: 50/l to 200/l
(iv) Pressure: 10 to 5000 Pa
(v) Total gas flow: 20 - 200 sccm/min
(vi) Typical growth rate: 1-5μm/hr

A typical microwave plasma for diamond deposition has an electron density of approximately 10^{20} electrons/m^3, and sufficient energy to dissociate hydrogen. A microwave-deposition reactor is shown schematically in Fig. 2.10. [16][22] The substrate (typically a silicon wafer) is positioned at the lower end of the plasma. Gases are introduced at the top of the reactor, flow around and react at the substrate, and the gaseous by-products are removed into the exhaust. The substrate must be heated to 800 - 1000°C for diamond to form. This can be done by the interaction with the plasma and microwave power but this is difficult to regulate and, more commonly, the substrate is heated directly by radiant or resistance heaters which provide more accurate temperature

control. However, this tubular set-up allows severe contamination of the deposited films due to plasma etching of the silica tube. An improved design takes shape by coupling the rectangular waveguide to a cylindrically symmetric resonant cavity as shown in figure 2.10b. A plasma ball without interacting with the inner silica wall reduces contamination, allows independent substrate heating and uniform large areas deposition (diameters > 100mm) [2].

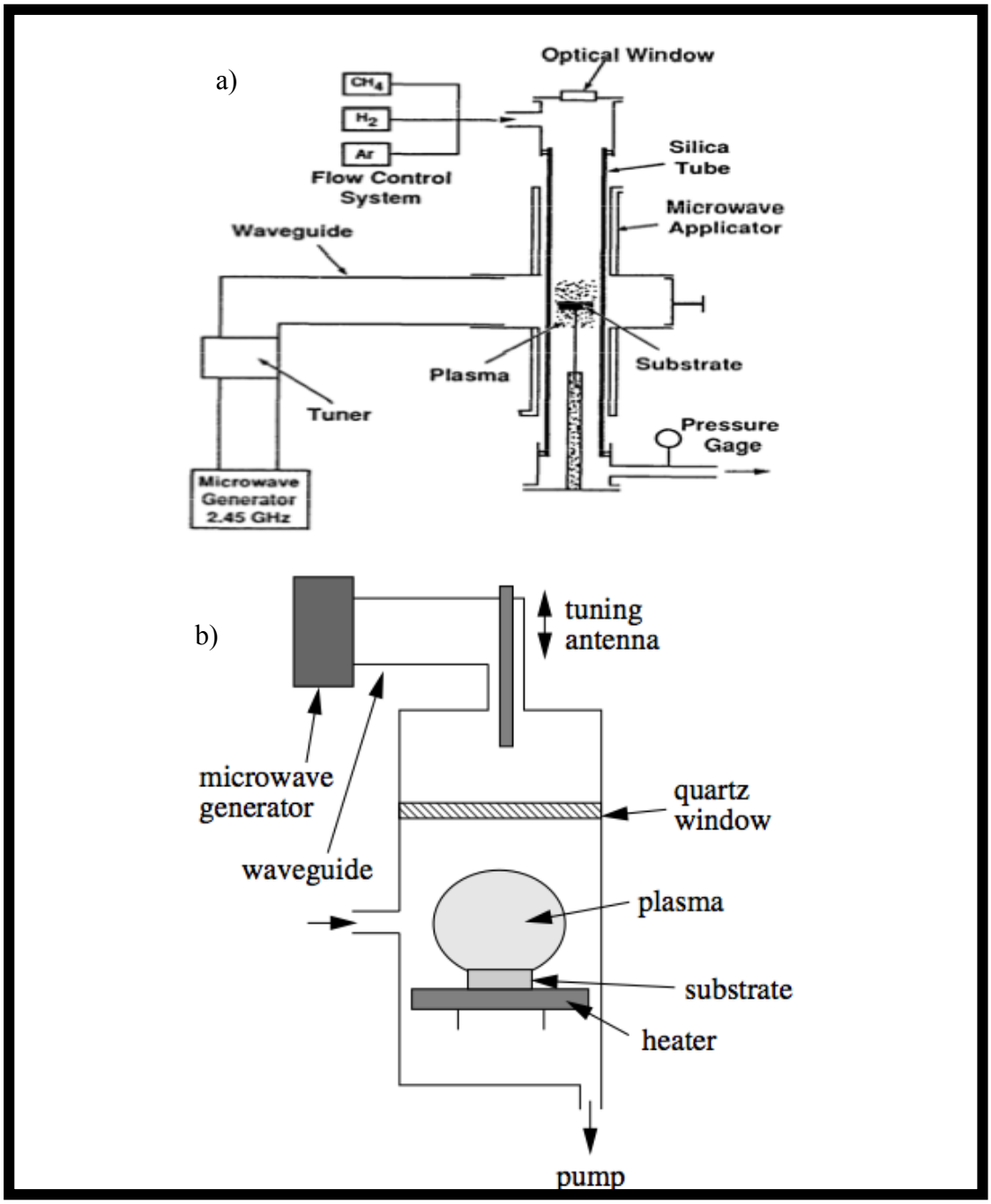

Figure 2.10: Schematic of a microwave-plasma deposition apparatus [15-16] (b) [17]

2.3.3.2 Hot filament CVD (HFCVD)

A plasma can also be generated by high temperature which, in the case of diamond deposition, is obtained by a resistively heated wire or tube made of tungsten or tantalum.[18-20] A schematic of the equipment is shown in Fig. 2.11.

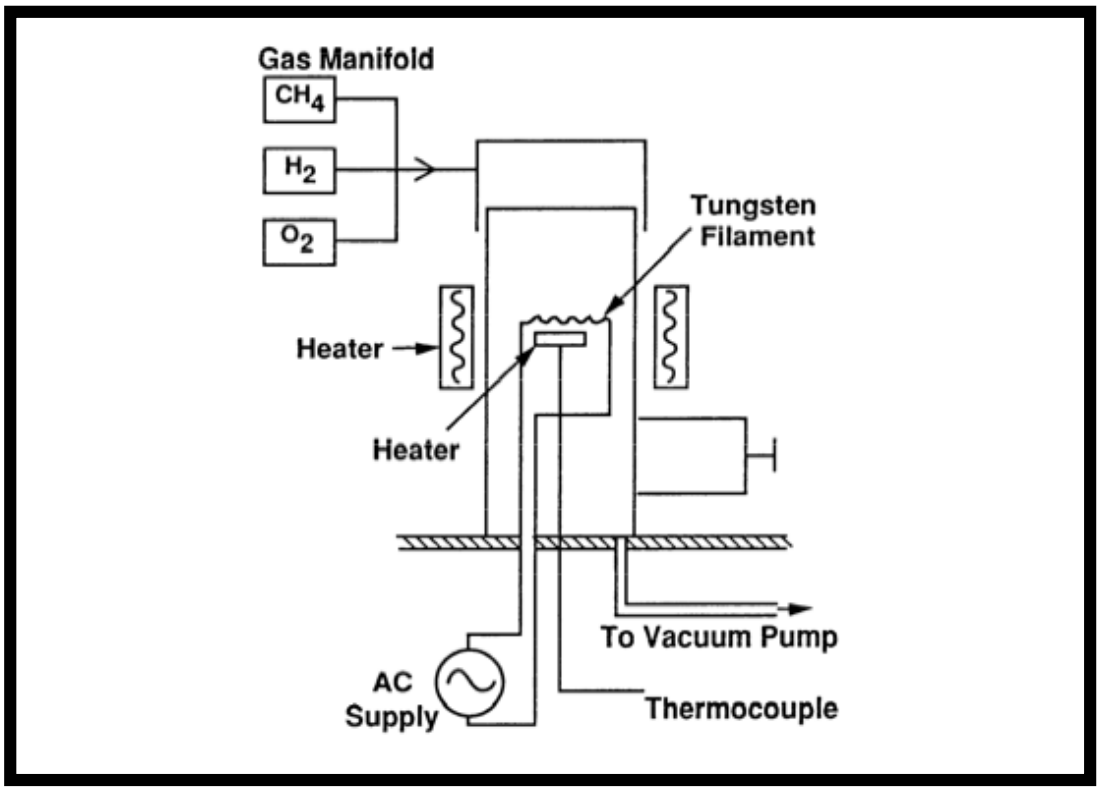

Figure 2.11: Schematic of a hot-filament CVD apparatus [19-20]

The metal temperature is maintained at 2000°C or slightly higher. Atomic hydrogen is formed and the carbon species become activated in the vicinity of the hot metal. The deposition rate and the composition and morphology of the deposit are functions of the temperature and the distance between the hot metal and the substrate. This distance is usually 1 cm or less. Much beyond that, most of the atomic hydrogen recombines and no diamond is formed. The substrate temperature should be kept between 800 and 1000°C and cooling may be necessary. Gas composition and other deposition parameters are similar to those used in a microwave-plasma system. Deposition rate is low, reported as 0.5 to 1μm/h. A disadvantage of the hot- filament process is the short life of the metallic heater, which tends to carburize, distort, and embrittle

rapidly. In this respect, tantalum performs better than tungsten with an estimated life of 600 hrs (vs. 100 hrs for tungsten) [20]. The heated metal may also evaporate and contaminate the diamond film. Furthermore, it is not advisable to add oxygen or an oxygen compound at these temperatures, as tungsten (or most other refractory metals) would oxidize rapidly. However, the equipment is relatively inexpensive and experiments are readily carried out. Other heating-element materials such as graphite or rhenium are being investigated [21].

Method	Process	Rate	Control	Product
Glow-discharge plasma	Microwave	Low (0.1-1μm/hr)	Good	Coating
Thermal	Hot-filament	Low (0.1-10μm/hr)	Good	Coating
Arc plasma	DC arc RF arc	High (50-1000μm/hr)	Poor	Coating
Combustion	Torch	High	Poor	Coating Powder

Table 2.4: Comparison of CVD diamond growth methods [22]

2.3.4 Nanodiamond synthesis

A technologically important class of nanodiamond materials is ultra-dispersed diamond (UDD). UDD synthesis is performed by the detonation of solid explosives in an inert atmosphere. The product obtained in detonation synthesis, called detonation soot, contains the diamond phase, which is separated by chemical treatment based on moderate temperature oxidation of the impurities by nitric acid under pressure [23]. Therefore, the final morphology of the particles is influenced by the treatment conditions [24]. The major methods for diamond synthesis using explosives produces materials that are very different, and it is necessary to be aware of this difference when making a choice of the material for particular applications. There are three major methods that had been commercialized [25].

The first is the transformation of carbon precursors (e.g., graphite, coal, and carbon black) to diamond in a capsule compressed by a shockwave (~ 140 GPa) generated outside the capsule (the 'Du Pont method'). To prevent diamond regraphitization, a mixture of graphite (6 to 10%) with metallic powder (Cu, Al, Ni) is used. The diamond yield is about 60 mass percent of the carbon phase or about 5% of the initial mixed material loaded into a capsule [24]. The synthesized nanodiamond had a bimodal size distribution; the first maximum was within the 1 to 4 nm size range and the second was within the 10 to 150 nm range. The product of the synthesis always contained the londsdalite phase due to the martensitic type of transformation graphite-rhombohedral graphite-londsdalite-diamond. However, there are several modifications of this method [25].

The second method of ND production is based on the detonation of a mixture of carbon-containing material with explosives. In this case diamond formation takes place both within the carbon-containing particles as well by condensation of carbon atoms contained in the explosives. The explosion can be done in air or in an inert atmosphere relative to the product of synthesis. In the latter case, a diamond cubic phase not more than 20 nm in size is formed. When the formation is in an atmosphere of air, the samples always contain londsdalite and the particle size is smaller — about 8 nm. The diamond yield constitutes up to 17% of the mass of the initial carbon material or about 3.4% of the mass of the explosives. The characteristic feature of the diamond obtained by these two methods based on the shock wave compression of the initial graphite phase is formation of polycrystalline material with particle sizes comparable to the particle sizes of the precursor carbon material. The particles consist of nanocrystalline diamond grains. After purification the particles produced by detonation are classified by fractions (from 1 to 60 μm) for use in polishing applications [25].

In the third method of using explosion energy for diamond production, diamond clusters are formed from carbon atoms contained within explosive molecules themselves, so only the explosive material is used as a precursor

material (Figure 2.12). A wide variety of explosive materials can be used, including products for military applications (so that UDD synthesis is a good way of utilizing of the stock pile materials). A typical explosive is a mixture of TNT (2-Methyl-1,3,5-trinitrobenzene) and hexogen (1,3,5-Trinitroperhydro-1,3,5-triazine) in proportion of 60/40, composed of C, N, O, and H with a negative oxygen balance (i.e., with the oxygen content lower than the stoichiometric value), so that 'excess' carbon is present in the system. A negative oxygen balance in the system is an important condition for UDD formation. The explosion takes place in a nonoxidizing medium (Figure 2.12) of either gas (N_2, CO_2, Ar, or other medium — that can be under pressure) or water (ice) — 'dry' or 'wet' synthesis, correspondingly, that plays the role of a coolant. To prevent the UDD formed in the detonation wave from transforming into graphite at the high temperature generated by the detonation, the cooling rate of the reaction products should be no less than 3000 K/min [25]. The initial shock from a detonator compresses the high-explosive material, heating it and causing chemical decomposition that releases enormous amounts of energy in a fraction of a microsecond (Figure 2.12).

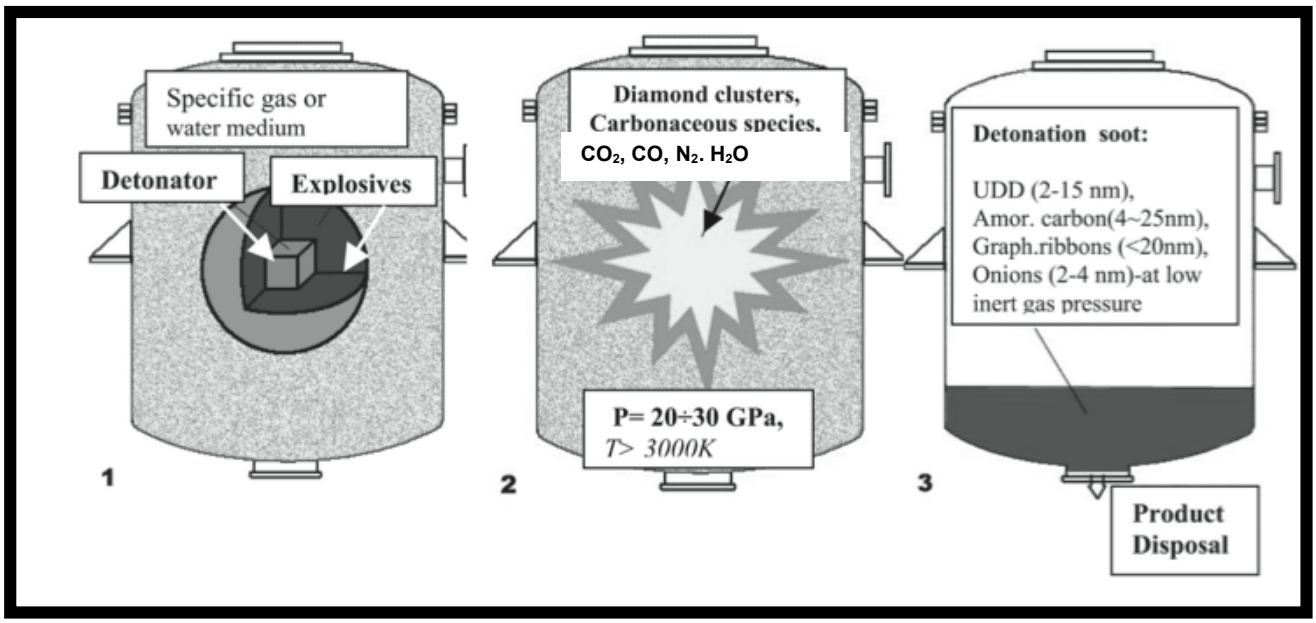

Figure 2.12: Schematic illustration of the steps in the controlled detonation synthesis of nanodiamond from carbon- containing explosives (pictures of the detonation process courtesy of PlasmaChem GmbH, Mainz/Germany)

As the detonation wave propagates through the material it generates high temperatures (3000 to 4000K) and high pressures (20 to 30 GPa) that correspond to conditions of thermodynamic stability for diamond. During detonation, the free carbon coagulates into small clusters, which grow larger by diffusion [26-28]. The product of detonation synthesis, called detonation soot or diamond blend, contains 40 to 80 wt.% of the diamond phase depending on the detonation conditions. The carbon yield is 4 to 10% of the explosive weight for the most effective of the three industrial methods of diamond production using explosives.

In summary, there are two major technical requirements for UDD synthesis using explosives. First, the composition of the explosives must provide the thermodynamic conditions for diamond formation, and second the composition of the gas atmosphere must provide the necessary quenching rate (by appropriate thermal capacity) to prevent diamond oxidation. The diamond yield depends to a large extent on the explosive mixture (Figure 2.13) [27]. The shape of the explosive also influences the yield; the ideal shape is spherical, but for convenience a cylindrical shape is used regularly. The relationship between the mass of the explosives and the mass of the surrounding media influences also yield (e.g., 5 kg of explosive requires ~11 m^3 of detonation volume with gas media at ambient pressure to provide the necessary quenching rate) [25].

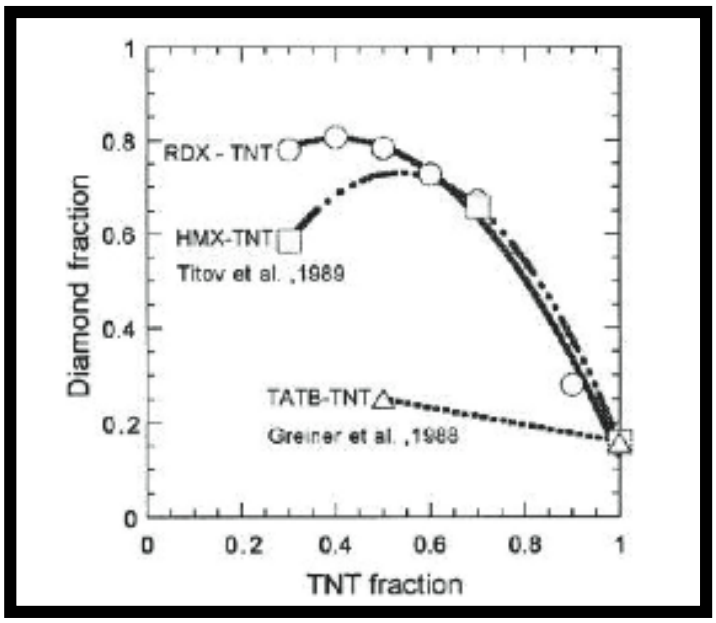

Figure 2.13: Diamond weight fraction recovered from soot as a function of the composition of the explosive mixture. The abbreviation for explosives is as follow: TNT — 2-methyl-1,3,5-trinitrobenzene; HMX — octahydro-1,3,5,7-tetranitro-1,3,5,7-tetrazocine; TATB — 2,4,6-trinitro-1,3,5-benzenetriamine; RDX — hexahydro-1,3,5-trinitro-1,3,5-triazine [27]

2.3.4.1 Purification

The diamond blend in addition to UDD contains graphite-like structures (35 to 45 wt.%), and incombustible impurities (metals and their oxides — 1 to 5wt.%) [23] as shown in Figure 2.14. Using X-ray diffraction and small angle X-ray scattering, it was shown that an UDD cluster in *detonation soot* has a complex structure consisting of a diamond core of about 4.3 nm in size and a shell made up of sp^2 coordinated carbon atoms [29]. The shell structure and thickness vary with the cooling kinetics of the detonation products (dry vs. wet synthesis) and conditions of chemical purification of the UDD clusters from the detonation soot [29]. According to the X-ray diffraction spectra and the results of electron microscopy, UDD of the highest degree of purification contain no intermediate amorphous phase, graphite, or londsdalite [30,31].

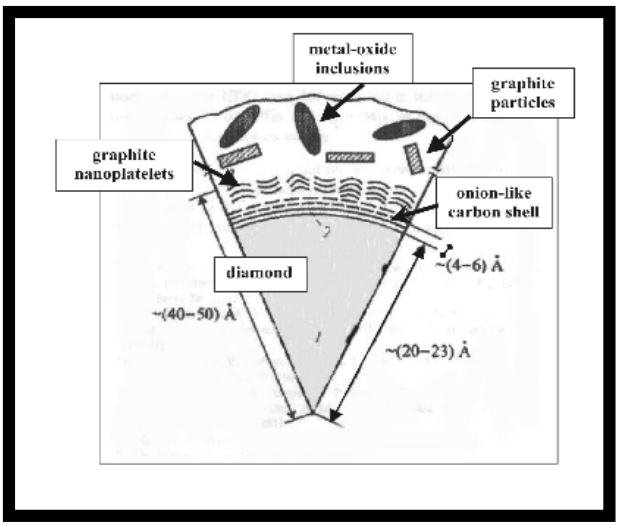

Figure 2.14: Model structures of detonation-produced carbon. Depending on purification conditions, different layers of the UDD shell can be 'stripped-off' [29]

UDD purification is performed by mechanical and chemical methods (Figure 2.15). After mechanical removal of process admixtures, the diamond-carbonic powder is subjected to thermal wet oxidation with nitric acid under pressure to separate the diamond phase [23]. The method of acid purification at elevated temperatures is the most efficient purification method at the present time because it comprehensively influences all admixtures: metals are dissolved and non-diamond carbon is oxidized simultaneously. The diamond should be flushed with water after separation from the acidic media. After a typical purification step, powders of UDD can be considered as a composite consisting of different forms of carbon (80 to 89%), nitrogen (2 to 3%), hydrogen (0.5 to 1.5%), oxygen (up to 10%), and an incombustible residue (0.5 to 8%) [23]. The carbon consists of a mix of diamond (90 to 97%) and non-diamond carbon (3 to 10%).

In detonation synthesis of nanodiamonds, the impurity content is higher when compared with other artificial diamonds (i.e., HPHT diamonds contain no less than 96% carbon). Therefore, the effect of impurities is more pronounced for UDD compared with other diamonds [23]. Impurities in UDD, in principle, can be divided into the following groups: [23] (1) water-soluble ionized species (free electrolytes); (2) chemically bonded to diamond surfaces and prone to

hydrolysis and ionization (salt forms of functional surface groups); (3) water insoluble; and (4) incorporated into the diamond lattice and encapsulated. The impurities of the first and second groups are formed in the chemical purification of UDD by acid stage [23]. The major water-soluble admixtures (first group) are removed by washing the UDD with water. The surface functional groups (second group) can be efficiently removed by ion-exchange resins that involve demineralization of surface groups. The water insoluble impurities represent both individual micro-particles of metals, oxides, carbides, salts, and metal oxides that do not dissociate. For their removal, UDD particles are treated with acids. By using different methods of UDD purification, one can remove 40 to 95% of the impurities of these three groups. It is practically not possible to remove the impurities of the fourth group by chemical methods. The UDD of the highest purity available at 'Diamond Center', Inc. contains 98.5% of diamond [24].

Commercial products of purification have the following grades: a water suspension of diamond and powder obtained from suspensions by drying and grinding of UDD are a gray powder containing up to 99.5 wt.% of a pure diamond (without counting adsorbed gases) [23]. To remove non-carbon impurities, the chemically purified product is subjected in some cases to additional purification using ion-exchange and membrane technologies. In general, the UDD production consists of detonation synthesis, chemical purification and acid washing of UDD, product conditioning, and modifying of diamond [24].

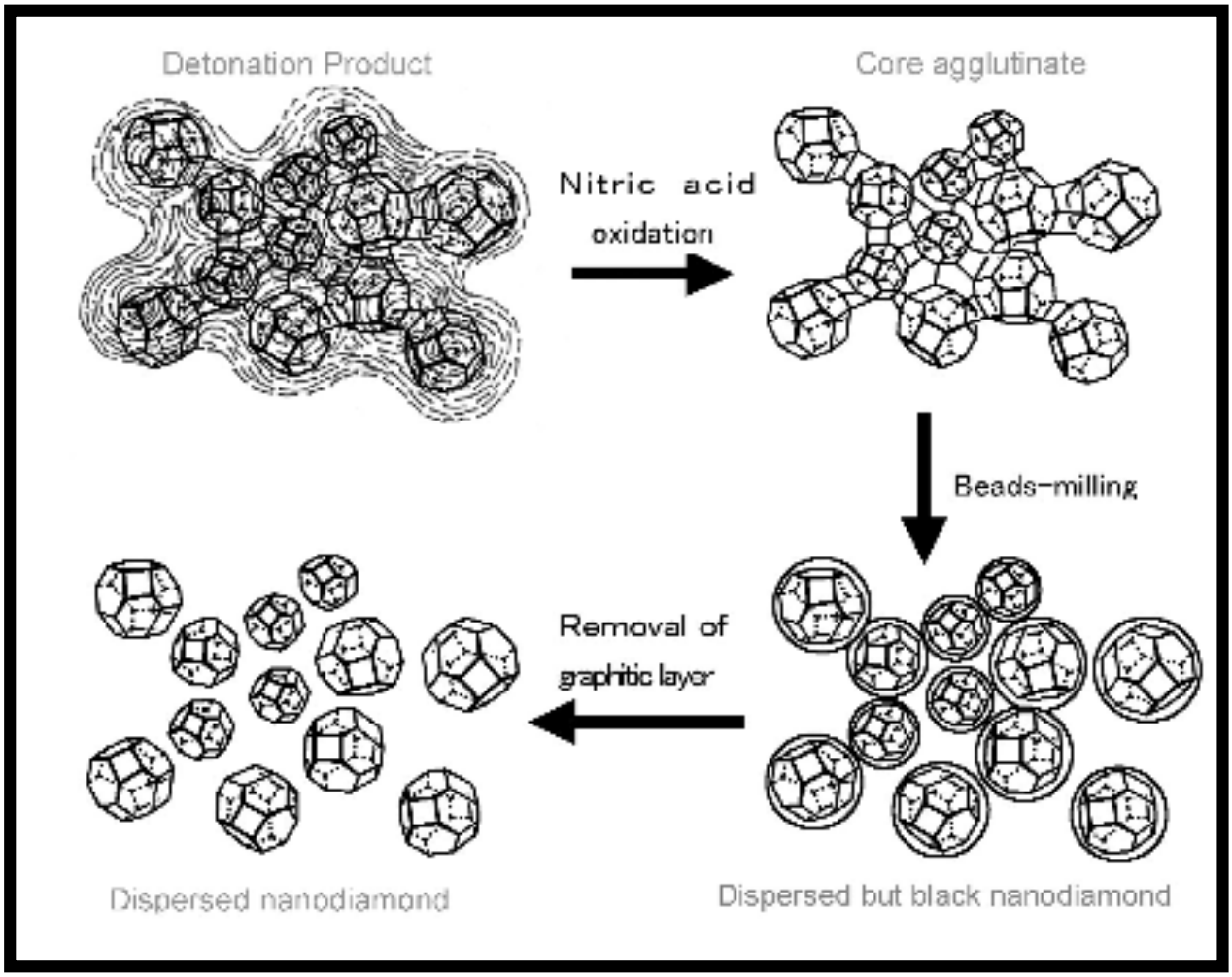

Figure 2.15: Illustrations of complex transformation occurring on a core agglutinate during the purification process of detonation synthesis of nanodiamond. Core agglutinate (upper right) may contain graphitic fragments in the grain boundary region, kept intact during nitric acid oxidation. However, it is thought that beads-milling process produces graphitic carbons by converting some of the carbon atoms on the surface of primary particles into graphitic patches as the primary particles are exposed to the impact of beads. Fragmented hatch (in upper left drawing) means soot, truncated octahedra means particles, and circles (lower right) mean partial graphitic layers [32].

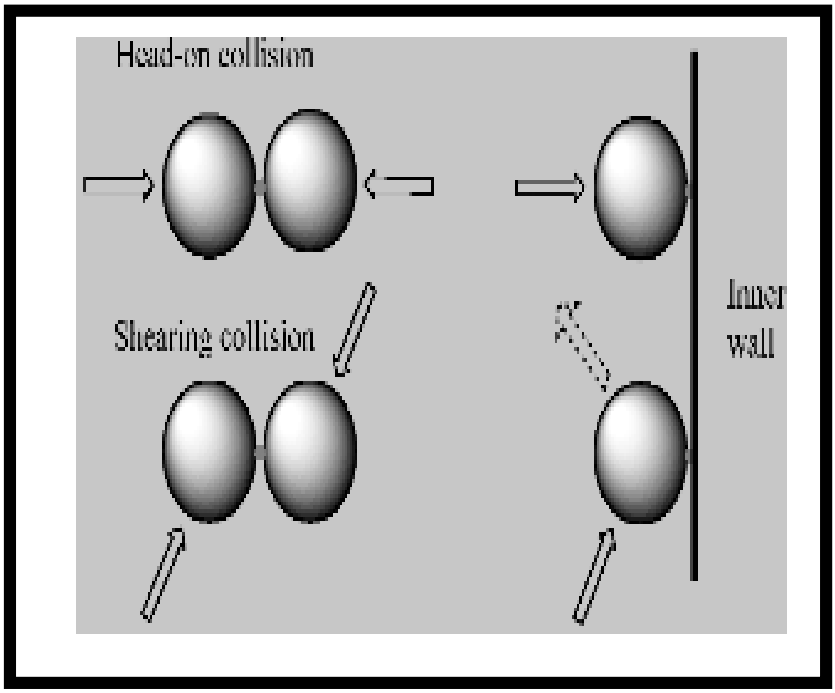

Figure 2.16: Mechanism of beads-milling. In the case of crushing crude product of DN (secondary aggregates or core agglutinates, gray spots), heavy and hard zirconia beads (sphere) is packed to fill much of the mill space and rotated at high speed. The impact of colliding beads upon the pinched substrate particles should be enormous. As the milling proceeds to release more and more primary diamond particles, more and more primary diamond particles are directly exposed to the impact of collision. The diamond-zirconia collisions lead to (1) scraping of beads material which contaminates diamond product, and (2) conversion of surface diamond atoms into graphitic patches as the major consequences [32]

A recent breakthrough by Osawa *et al* led to the isolation of primary particles having the expected size of 4–5 nm by wet-milling with zirconia micro-beads. (Figure 2.15 and 2.16) Thus, long-waited primary particles of detonation nanodiamond (DN) finally became available in kg quantities in the form of colloidal sol, gel, and readily re-dispersible flakes. These primary particles are tersely called mono-dispersed single nanodiamond (*mdsn*-D) [32].

Item	Description
Physical const.	Not yet determined due to lack of standard sample
Elemenatry analysis	Impossible due to high hygroscopicity
Hydration	In aqueous gel, nonfreezing layer of water surrounds the surface with a thickness of about 1 nm.
Shape	Irregular and spherical polyhedra probably relating defective truncated octahedra
Diameter, nm	4.5 ± 0.5 (coherent scattering region) 4.6 ± 0.8 (DLS)
Self-organization	High. Upon removal of water from aqueous colloid, gelation starts at about 8 wt %. At concentrations above 20 %, self-organized to shapes like ribbon-like films, fine rod-like flakes and whiskers. Freeze drying often leads to fine needles or extremely long whiskers longer than 1 cm.
Color	Flakes are colored brown to black, while colloidal solution looks deep black in concentrations higher than 1 %, but deep to pale brown at concentrations lower than 0.2 %. Colors are considered to arise from partial graphitic patches on the surface.
Fluorescence	650 nm, weak but intensifies upon bombarding with nitrogen ions
IR, cm^{-1}	3430(vs, ν_{OH}), 2925(sh, ν_{CH}), 1708(s, $\nu_{C=O}$), 1631(s, δ_{OH}), 1500–1000 (br) with peaks at 1363 and 1228
^{13}C MAS NMR, ppm	34–35 (diamond, sp^3C), 111 (graphitic, sp^2C), intensity ratio 8.8 :1
Aggregation	Very strong upon thorough drying to give solids difficult to redisperse. Colloid solutions and gels are stable and do not produce precipitates after long standing.
Stable region of aq. colloid	pH 3~6, ζ-potential +40~+50, maximum ζ-potential of +53 mV occurs at pH 4.88
Good media for colloidal solution	Water, DMSO, EtOH, ethylene glycol, 1-methyl-2-pyrrolidinone, 2-methoxyethanol
Biocompatibility	Cell toxicity none, genetic toxicity under examination

Table 2.5: Properties of mono-dispersed single nanodiamond (*mdsn*-D) particles [32].

2.4 Diamond Doping

Extrinsic semiconducting materials are usually employed for electronic purposes. To generate such a material other atoms, which generate additional electron energy levels within the band gap, are inserted into the crystal structure. This process is called doping.

If the dopant atoms containing extra electrons generate energy levels near the conduction band, they act as donors. These electrons can then be thermally excited into the conduction band to carry an electric current (n-type conduction). Typical atoms that can act as donors for diamond when substituting substrate atoms on lattice sites are the group V atoms in the periodic table: nitrogen, phosphorus, and arsenic. If on the other hand, dopant atoms generate energy levels (but, in this case, devoid of electrons) near the valence band, they act as acceptors. Electrons can then be excited from the valence band into these levels, leaving behind positive holes which can act as carriers for the generation of an electric current (p-type conduction). Typical acceptor atoms are from group III such as boron and aluminum [33].

Diamond cannot be heated to temperatures at which vacancies and interstitial atoms form by thermal excitation and consequently making any diffusion process relying on these defects as carriers not possible. It is thus difficult for dopant incorporation by in-diffusion. Should interstitial diffusion take place, there will be no available vacant lattice sites for occupancy therefore preventing it become electrically active. This leaves only 2 possible methods for diamond doping, during growth and ion implantation [32].

2.4.1 Doping during Growth

2.4.1.1 P-type diamond

P-type extrinsic, semiconducting diamonds, doped with boron acceptors, are found in nature and are known as type IIb diamonds. Owing to the availability of these diamonds, the boron acceptor has been well studied. It is situated at E_A = 0.37eV above the valence band. This is still quite a large energy, which means that at room temperature only about two out of every thousand acceptors are ionized to create holes in the valence band. It has been argued that the magnitude of this activation energy makes diamond electronic devices not feasible. However, there are transistor types for which this factor is of no consequence. Notwithstanding the large value for E_A, p-type

diamonds can conduct well at room temperature, and transistor action has been demonstrated in them [33].

Incorporation of boron into diamond has been demonstrated during HPHT as well as PACVD growth. Under HPHT conditions, the solvent catalyst often contains materials that getter the nitrogen in order to stop its incorporation and to prevent these atoms from compensating the boron. In general, these boron-doped diamonds tend to be overdoped. This can result in a change of the conduction mechanism, from hole conduction in the valence band to conduction by carriers that tunnel from one acceptor state to the next (called hopping conduction). The latter conduction degrades device performance and, if possible, should be avoided. Doping during PACVD growth is accomplished by introducing diborane (B_2H_6), boric acid or boron oxides. The quality of boron-doped diamond layers grown by PACVD has improved steadily over the last ten years, and single crystalline layers grown homoepitaxially on diamond with hole mobilities in excess of 1000 $cm^2V^{-1}s^{-1}$ can now be produced. The activation energy required for hole excitation into the valence band has been demonstrated to be concentration dependent, down to a few meV at boron concentrations >$1x10^{20}cm^{-3}$ [33].

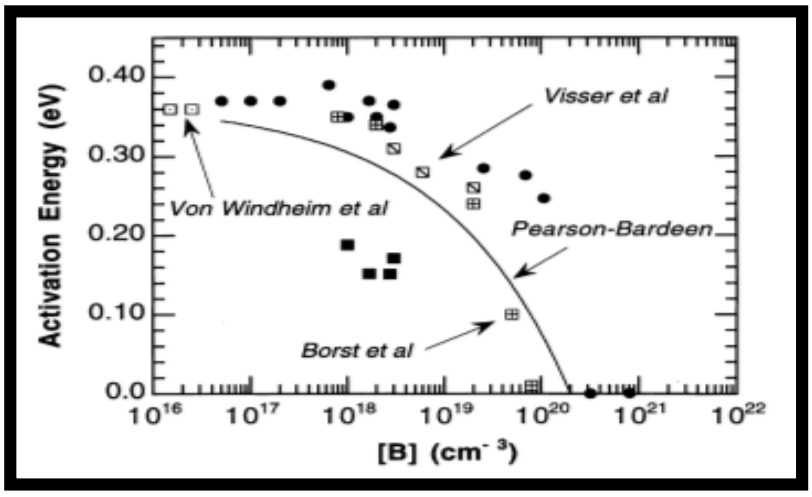

Figure 2.17: Conductivity activation energies at 300K as a function of boron content. At about [B] > 3 x 10^{18} cm^{-3} the activation energy starts to decrease and finally vanish for [B] > 2 x 10^{20} cm^{-3}. The theoretical dependence accprding to the model of Pearson and Bardeen (solid curve) [34] is for comparison [35].

2.4.1.2 N-type diamond

N-type diamonds, which can conduct at room temperature, have not been found in nature, and many attempts have been made to create them in the laboratory. Good-quality n-type diamond still poses a problem. It has not yet been possible to grow such diamonds by HPHT methods [33], although a limited amount of doping with phosphorus atoms can be observed optically [36]. Using phosphine (PH_3), many attempts have been made to incorporate phosphorus atoms during PACVD growth. Unequivocal proof of phosphorus-donor activation has been demonstrated for homoepitaxial diamond (111) layers [37]. The quality of these layers is still poor and the activation energy for electron excitation into the conduction band lies at $E > 0.5$eV which is still uncomfortably high [33]. Nitrogen, a deep donor, has an energy level of 1.7 eV below the conduction band [38]. Sulphur has most recently been reported to act as a donor ($E_A = 0.37$ eV) in CVD diamond [39].

2.4.2 Ion Implantation

Ion-implantation is a technique widely used to dope common semiconductors. In this method atoms are forced into the crystal, regardless of solubility or diffusivity considerations; hence it is one of the attractive methods for the introduction of the desired impurities into any crystal, including diamond [40]. Unfortunately, ion-implantation is always accompanied by the creation of many defects in the material. These have to be removed by proper annealing. For the case of diamond, the annealing of defects is more complex than in other group IV semiconductors due to the metastability of the sp^3 (diamond) bonding with respect to the sp^2 (graphitic) bonding. Broken sp^3 bonds and other implantation-related defects or graphitic clusters can give rise to electrical effects which may be mistaken for real chemical doping due to the presence of dopants [33].

2.4.2.1 P-type diamond

The first attempt to dope IIa diamond by ion implantation was reported by

Vavilov *et al* in 1970 and in 1974 [41]. These pioneering studies, however, suffered from the lack of control experiments; hence effects due to the presence of incompletely annealed implantation related defects could not be properly eliminated. Almost ten years later in 1983 Braunstein *et al* [42] reported on the fabrication of highly conducting thin p-type diamond layers obtained by high dose B implantation (to a dose that exceeded the critical dose for graphitization), which, following high temperature annealing (1450^0C) and graphite removal in boiling acids, resulted in a very thin B doped layer (20 nm) reaching all the way to the surface. This method, of high dose ion-implantation followed by HT annealing and graphite removal, has later been further perfected, and it is now commonly used as a method to obtain a p++ ohmic contact to p-type diamonds [43].

Prins [44] has considered the role of the implantation temperature on the nature of the defects and hence on the resulting electrical properties of the implanted layer. Three distinct implantation- temperature regions were identified: (1) a low temperature region (77 K) where both vacancies and interstitials (intrinsic point defects as well as implanted dopant atoms) are immobile; (2) an intermediate region (300 K<T<800 K) where only interstitials are mobile: in this regime some interstitials recombine with vacancies and some diffuse out of the implanted layer leaving behind a vacancy-rich region; and (3) a high temperature region where both interstitials and vacancies are mobile during the hot-implantation, resulting in a dislocated diamond layer. Following this theory, Prins devised a new implantation/annealing procedure, the so-called cold-implantation-rapid- annealing (CIRA) technique. In this method the diamond is implanted at low temperature, rapidly heated to 800 K, to induce interstitial-vacancy recombination before the interstitial can diffuse away from the implanted layer, and then annealed at high temperature (1700 K) to further reduce the radiation damage and increase the electrical activation of the dopants [33].

The main idea of this method is that the B-interstitials should successfully compete against the self- interstitials to fill in vacancies which is most likely if the B-interstitials are located in a vacancy-rich volume. Two ways of

increasing the dopant-vacancy spatial overlap are suggested [45]: one is to broaden the implanted layer by implanting the dopants at different energies, the other is to use carbon co-implantation to create damaged volume into which the dopant atoms are implanted. These methods, though interesting, did not lead to any significant improvement in the electrical properties of the B implanted sample over those achieved by the CIRA method.

Prawer *et al* [46] have shown that by creating a deeply buried B rich layer in diamond by mega-volt (MeV) ion implantation improved mobilities can be obtained. The reason for this is possibly the improved annealing due to the internal pressure exerted on the damaged layer by the overlying, only lightly damaged, diamond layer. A novel method for making ohmic contacts to the buried layer based on local graphitization by laser pulses was devised. The electrical properties of these B doped, buried layers, reported by Uzan-Saguy *et al* [47], are characterised by high mobilities (600 $cm^2V^{-1}s^{-1}$) and a low compensation ratio (5%). Furthermore, it was shown that the cap layer, overlying the buried, doped layer, is highly insulating, opening the possibility of using such technology for realizing field effect transistor (FET) devices in diamond.

Very high p-type doping (p = 2 x 1019 cm^{-3}) suitable for contacting p-type diamond was achieved by Kalish *et al* [48,49] by B implanting polycrystalline CVD diamond layers by two different methods: (I) high dose B implantations (above the critical dose for graphitization upon annealing), followed by annealing (1300 K) and chemical removal of the graphitized surface layer to expose a thin, highly conductive over-doped layer [33]; (II) high dose high current (current densities up to 500 A/cm^2) B implantations into poorly heat-sunk samples [50], thus heating the sample during implantation to temperatures of the order of 1100^oC. This hot implantation leads, without any further need for annealing, to a highly doped relatively undamaged layer which exhibits high conductivity [33].

B ion implantation is a well controlled process which has been optimized in the last 5 years resulting in doping efficiencies of the order of 2-5%, hole

mobilities of up to 600 $cm^2V^{-1}s^{-1}$ and compensation ratios below 5%. The optimal implantation/annealing scheme comprises a multiple energy cold implantation followed by medium temperature and a high temperature annealing (T>1400°C) stage. The fabrication of over-doped highly conductive layers can be achieved either by hot implantations, or by high dose implantations followed by annealing and graphite removal. These are widely used for realizing ohmic contacts to p-type diamond. Optical characterisation of the B acceptors in substitutional sites is well understood and is a useful tool in the study of defect-dopant interaction [33].

2.4.2.2 N-type diamond

The ion implantation technology was applied for n-type doping using the same collection of donor candidates namely nitrogen, phosphorus and sulphur. Nitrogen as previously mentioned, is the dominant impurity in natural diamond. Both N atoms located in substitutional sites in type Ib diamonds and those accumulated in aggregates in type IaA are donors in diamond with activation energies of 1.7 and 4 eV respectively. Due to these very high ionization energies, N containing diamonds are electrically insulating at room temperature. The N implanted and annealed diamonds were checked by resistivity $\rho(T)$, EPR and CL measurements after implantation and after different annealing stages. It was found that following annealing, almost 50% of the implanted N is located in substitutional sites and that defects found in type Ib diamond exist also in the N implantation-doped diamond. Two important conclusions can be drawn from these results: (i) the CIRA procedure (developed for p-type implantation-doping of diamond) is suitable for N (ii) substitutional N containing diamonds can be obtained by selective area ion-implantation thus enabling us to use the improved field emission properties of N containing CVD diamond also for N implantation doped diamond. Nevertheless, N cannot find application as a standard n-type dopant in diamond in room temperature devices due to its deep level [33].

Phosphorus on a substitutional site in diamond was predicted to act as a shallow donor (0.1 eV) [50]. Recently P containing homoepitaxial diamond

layers were successfully grown by CVD [51] and were shown, by detailed Hall effect measurements, to produce a donor level with an ionization energy of about 0.5 eV below the bottom of the conduction band. The mobility of the P doped layers varies between 30 and 180 $cm^2\ V^{-1}\ s^{-1}$ and typical room temperature carrier concentrations are of the order of 10^{13}—$10^{14}\ cm^{-3}$. This finding provides a guideline for P doping of diamond by ion-implantation. Other potential n-type dopants include lithium and sodium, but there has only been limited success in ion implantation doping of diamond with these elements [33].

2.4.3 Surface Conductivity

Hydrogen-terminated diamond exhibits a high surface conductivity (SC) that is commonly attributed to the direct action of hydrogen-related acceptors. Maier *et al* gave experimental evidence that hydrogen is only a necessary requirement for SC; exposure to air is also essential. A mechanism proposed by Maier *et al* in which a redox reaction in an adsorbed water layer provides the electron sink for the subsurface hole accumulation layer. The model explains the experimental findings including the fact that hydrogenated diamond is unique among all semiconductors in this respect [52]. Undoped diamond with a gap of 5.5 eV is a bona fide insulator. Yet in 1989 Ravi and Landstrass reported a substantial surface conductivity of hydrogenated diamond surfaces, both of single crystals and of films prepared by chemical vapor deposition (CVD), respectively [53]. The surface conductivity of hydrogenated diamond is of the order of 10^{-4} to $10^{-5}\ \Omega^{-1}$ at room temperature (RT). The areal density of the *p*-type carriers responsible for the conductivity is about $\rho_S = 10^{13}\ cm^{-2}$ and it is hardly temperature dependent between RT and 150 K. The Hall mobility of the carriers varies also little with temperature ($\sim T^{1.2}$) [54] and is of the order of 30 $cm^2\ V^{-1}\ s^{-1}$ with a maximum value of 70 $cm^2\ V^{-1}\ s^{-1}$ reported for a carrier density of $1.2 \times 10^{12}\ cm^{-2}$ [55]. It appears that an adsorbate from the atmosphere on the hydrogen-terminated diamond surface is required to induce the surface accumulation layer with $10^{13}\ cm^{-2}$ holes. In order to act as an acceptor, the adsorbate must have its lowest unoccupied electronic level below the VBM of diamond. With an electron

affinity $\chi_{C:H}$ = -1.3 eV for hydrogenated diamond [56], this requirement sets a lower limit for the electron affinity χ_{ad} of the adsorbate: χ_{ad} = Eg – 1.3 eV = 4.2 eV, where Eg = 5.5 eV is the band gap energy of diamond. Thus, direct electron transfer from the diamond into an atmospheric adsorbate appears to be impossible.

However, a thin water layer, as it forms naturally on all surfaces exposed to atmosphere, provides an electron system, which can act as a surface acceptor for diamond. Electron exchange from diamond to the water layer is governed by the redox reaction $2H_3O^+ + 2e^- \Leftrightarrow H_2 + 2H_2O$ [57]. The reaction is driven by the difference in the chemical potential of electrons in the liquid phase (μ_e) and in diamond (Fermi level E_F). As long as μ_e is below E_F, electrons are being transferred from diamond to the water layer and thereby reduce H_3O^+ to H_2 and H_2O. The compensating holes in the diamond form the accumulation layer and the associated space charge induces a potential (surface band bending) that raises μ_e [52]. In equilibrium μ_e and E_F are equal at the interface as shown schematically in Figure 2.18.

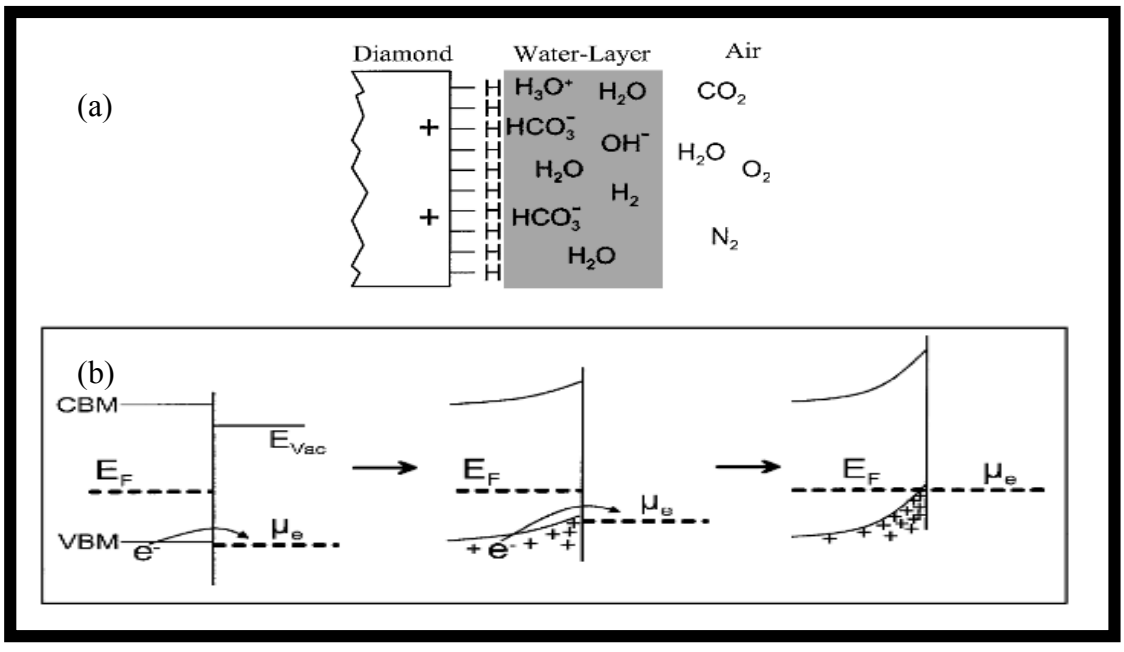

Figure 2.18: (a) Schematic picture of the hydrogenated diamond surface in contact with a water layer as it forms in air. (b) Evolution of band bending during the electron transfer process at the interface between diamond and the water layer [52].

Once surface conductivity has been established, the sample can even be put into vacuum and the wetting layer be removed. As long as the anions remain at the surface the hole accumulation will also be preserved. Thermal desorption of the anions which takes place at much lower temperatures (~300^{o}C) than those necessary for surface dehydrogenation in UHV (~700^{o}C) removes the accumulation layer and leaves a hydrogenated but highly resistive surface [52].

2.5 An overview of applications of diamond

The major advantage of diamond as an electronic material is its high heat conductivity. Solid-state electronic devices generate heat when carriers (electrons and holes) flow through them. The heat has to be dissipated, or else the device will burn out and fail. With the miniaturization of electronic devices to create more efficient and faster chips, this problem is becoming acute. A denser packing of transistors results in a denser generation of heat which has to be conducted away faster. A similar problem is encountered with high-power electronic devices, where large currents and voltages are switched and controlled. In solid-state devices, the maximum powers that can be handled are again coupled to the ability to dissipate the large amount of heat generated. Owing to this, vacuum-tube technology is still regularly used to construct very high-power electronic systems. Diamond is already in use as a substrate on which standard electronic devices and chips are mounted in order to dissipate heat faster. Great improvements in efficiency and reliability have been achieved. For example, solid-state lasers, used as repeaters in optical cables for data transmission, are mounted on diamond substrates. However, if it proves possible to create electronic devices and chips within the diamond substrate itself, far greater improvements are expected.

At low electric fields, the mobilities of electrons and holes in good-quality diamonds are high (in the order of ~2000 $cm^2\ V^{-1}\ s^{-1}$). Coupled to this, diamond has a very high dielectric strength. It can sustain large electric fields and, at such fields, the carriers can move even faster. Transistors that can switch at extremely high frequencies may well therefore be possible.

Owing to its large band gap, it is expected that in high-quality diamonds leakage currents should be small. This bestows many advantages when fabricating electronic devices. For example, in the fast- switching random access memories (RAMS) used in computers, the data is stored as charges within small transistor-controlled capacitors. Owing to leakage currents, the charges need to be refreshed every few milliseconds. For this reason, the data within the RAM is lost when a power failure occurs. By using a suitable large band gap semiconductor, it may be possible for a RAM to keep the stored charges for much longer even up to years, without losing the capability for fast-switching. In such a case continuous refreshing will not be needed, which will lead to lower energy consumption. Furthermore, the data will not be lost when the computer is switched off. For this application, diamond will be competing with other large band gap materials such as silicon carbide.

Transistors fail at temperatures where the densities of the intrinsic and extrinsic-carriers become comparable. In diamond transistors this will only occur at very high temperatures, devices that can operate in high-temperature environments may thus be fabricated. Furthermore, owing to its optical transparency, up to ultraviolet wave- lengths, it could play a role in the field of optoelectronics where electronic and optical devices are integrated within the same chip. Light-emitting diodes have been demonstrated in diamond. Other applications being developed at present are diamond windows for infrared and radiofrequency electromagnetic waves.

Diamond surface displays negative electron affinity (NEA) when appropriately terminated for example with hydrogen. If an electron is placed in the conduction band, and no band bending occurs at the surface that lowers the energy position of this band, the electron will find itself in a higher energy state (-0.5eV) than it would be in when outside of the diamond. Such an electron will “leak out” of the diamond. When enough electrons are available in the conduction band, as would be the case for a suitably doped n-type diamond, the ejection of electrons from the diamond may be sustained by connecting the diamond as a cathode (negatively charged) in a circuit with an

anode (positively charged) that attracts the electrons out of the diamond. To generate this beam of electrons, no heating is required as is needed in the case of a tungsten filament. Replacing all the hot, metal cathodes in existing electronics with cold cathodes will save the large amount of energy expended to heat the cathodes, as well as the cost for the extra electronics required to regulate the heating. Once reliable cold cathodes have been developed, it should be possible to miniaturize vacuum tubes and develop a microvacuum electronics industry. Another attractive application will be the replacement of bulky video displays used for television and computers with flat panel displays in which each pixel is separately activated by electrons emitted from an array of miniature cold cathodes. Aluminum nitride also has NEA, and will be in competition with diamond.

Diamond is more radiation-hard than any other solid. This makes it an ideal material for radiation detectors used in situations where very high fluxes of radiation are encountered. These detectors are planned for the new generation of ultrahigh energy accelerators, or so-called super-colliders. Electronic devices in diamond will also be less prone to failure due to cosmic radiation.

Owing to its high hardness, diamond has a large Young's modulus and can thus transmit acoustic waves with very high frequencies. By depositing a thin layer of a piezoelectric material (a charge generating material under applied stress and vice-versa) such as zinc oxide on the surface of diamond, surface acoustic wave filters have been constructed which operate at much higher frequencies than is possible with other substrates. Diamond is also ideal for other types of transducers which are required to operate at very high frequencies. It will probably find application in the developing field of microelectromechanical (MEM) devices, where small mechanical transducers and actuators are combined with integrated electronic circuits. The idea is to build even more complex devices like micromotors and micropumps. Because living tissue is compatible with carbon, such systems made out of diamond may be implanted in humans for medical purposes [33].

Doped-diamond has been introduced into electrochemistry by Pleskov *et al*. [58]. Since then, mainly the electrochemical behavior of diamond electrodes in aqueous electrolytes has been investigated. The most striking feature here is their very high overpotential for both oxygen and hydrogen evolution [59-67]. This leads to a wide potential window (approx. 3.5 V), which can be used for other electrochemical reactions in aqueous electrolytes. Diamond electrodes have indeed the largest potential window so far measured in aqueous electrolytes. This makes them also totally different to common electrode materials such as gold, platinum or mixed metal oxide DSA® type electrodes. Diamond is also extremely resistant to oxidation and attack by acids even at elevated temperatures. Unlike all other electriode materials, diamond is also resistant to attack by hydrofluoric acid [68]. Diamond also thought to be less prone to fouling [66], although other authors note that deactivitation due to fouling of the diamond does occur ay high potential (E > 2.3V vs standard hydrogen electrode (SHE)). Changing the polarity of the electrodes can also prevent build up of foreign material in the diamond surface [70]. Furthermore, should the diamond surface become fouled in an industrial application, an acid flush can be used to re-activate the surface without degrading the diamond surfaces. This makes diamond an excellent electrode of choice for electrochemistry applications.

2.6 References

[1] L. Ladon, Hybridization of Carbon, Towson University at http://pages.towson.edu/ladon/carbon.html (2001)
[2] H.O. Pierson, Handbook of Carbon, Graphite, Diamond and Fullerenes, Noyes, Park Ridge, NT (1993), 3a.
[3] http://www.chemicool.com/carbon.html (2010)
[4] http://www.mapsofworld.com/referrals/metals/diamond/types-of diamond.html (2010)
[5] S. Sque, Properties of Diamond, University of Exeter at http://newton.ex.ac.uk/research/qsystems/people/sque/diamond/ (2007)

[6] Types of Diamond, Knowledge Base, Corrosion and Materials Technology, CLI Houston at http://www.clihouston.com/knowledge-base/types-of-diamond.html (2010)
[7] C.G. Zoski, Handbook of Electrochemistry, Elsevier B.V., 1st edition (2007)
[8] F.P. Bundy. H.M. Strong, R.H. Wentorf Jr, Chemistry & Physics of Carbon, Vol. 10 (P.L. Walker, Jr and P.A. Thrower, eds), Marcel Dekker Inc (1973)
[9] Adams, D.M, Inorganic Solids, John Wiley & Sons, New York (1981)
[10] Y.L. Orlov, The Minerology of Diamond, John Wiley & Sons, New York (1977)
[11] Hirano, S. and Naka, S., The Ceramics (S. Saito ed), 2-15, Elsevier-Ohmsha, New York (1988)
[12] M. G. Loshak and L. I. Alexandrova , "Rise in the efficiency of the use of cemented carbides as a matrix of diamond-containing studs of rock destruction tool". *Int. J. Refractory Metals and Hard Materials* 19: 5, (2001)
[13] A.R. Badzian, R.C. DeVries , *Mater. Res. Bull. (USA),* vol.23, p.385, (1988)
[14] W.L Hsu, *J.Vac.Sci.Technol*., A(6)3:1803-1811 (1988)
[15] Saito, Y., Sato, K., Tanaka, H., Fujita, K., and Matsuda, S., *J. Mat. Sri, 223(3):842-46* (1988)
[16] Bachmann, P. K., Gartner, G., and Lydtin, H., *MRS Bulletin, 52-5, 9,* Dec, (1988)
[17] P.W. May, Diamond thin films: a 21st-century material, Phil. Trans. R. Soc. Lond. *A* 15, vol. 358, no. 1766, 473-495, January (2000)
[18] Patterson, D. E., *et al*., *Applications of Diamond Films and Related Materials, (Y.* Tzeng, *et al*., eds.), 569-576, Elsevier Science Publishers (1991)
[19] Pickrell, D. J. and Hoover, D. S., *inside ISHM,* 11-15 July/Aug (1991)
[20] Schafer, L., Sattler, M., and Klages, C. P., *Applications of Diamond Films and Related Materials, (Y.* Tzeng, *et al*., eds.), 453-460, Elsevier Science Publishers (1991)
[21] Schafer, L., Sattler, M., and Klages, C. P., *Applications of Diamond Films and Related Materials, (Y.* Tzeng, *et al*., eds.), 453-460, Elsevier Science Publishers (1991)
[22] Spear, K., *J. Amer. Ceram. Soc.* 7(2): 171-91 (1989)

[23] V. Y. Dolmatov, Russian Chemical Reviews 70, 607– 626 (2001)
[24] Shenderova, O. A., Zhirnov, V. V. and Brenner, D. W., 'Carbon Nanostructures', Critical Reviews in Solid State and Materials Sciences, 27: 3, 227 — 356, (2002)
[25] A. L. Vereschagin, Detonation Nanodiamonds (Altai State Technical University, Barnaul, Russian Federation), in Russian (2001)
[26] F.H. Ree, N.W. Winter, J.N. Glosli, *et al*. Physica B 265, 223–229 (1999)
[27] J.A. Viecelli, F.H. Ree, J. Appl. Phys. 88, 683–690 (2000)
[28] J.A. Viecelli, S. Bastea, J.N. Glosli, F.H. Ree, J. Chem. Phys. 115, 2730–2736 (2001)
[29] A.E. Aleksenskii, M.V. Baidakova, A.Y. Vul',Siklitskii, VI, Phys. Sol. State 41, 668–671 (1999)
[30] A. V. Kurdyumov, N. F. Ostrovskaya, V. B. Zelyavskii *et al*., Sverkht. Mater. 23 (1998)
[31] G. P. Bogatyreva, Y. I. Sozin, N. A. Oleynik, Sverkht.,Mater. 5 (1998)
[32] E. Osawa, Pure Appl. Chem., Vol. 80, No. 7, pp. 1365–1379 (2008)
[33] K.H.J. Buschow, R.W. Cahn, M.C. Flemings, B. Ilschner,; E.J. Kramer, S. Mahajan, Encyclopedia of Materials - Science and Technology, Volumes 1-11, Elsevier, (2001)
[34] G.L. Pearson, J. Bardeen, Phys. Rev. (USA) vol.75 p.865 (1949)
[35] J.-P. Lagrange, A. Deneuville, E. Gheeraert, Diamond and Related Materials 7 , 1390–1393 (1998)
[36] H. Sternschulte, K. Thonke, R. Sauer, S. Koizumi, Optical evidence for 630-meV phosphorus donor in synthetic diamond. *Phys. Rec. B. 59,* 12924-7 (1999)
[37] S. Koizumi, M. Kamo , Y. Sato, H. Ozaki H, T. Inuzuka, Growth and characterization of phosphorus-doped (111) homo-epitaxial diamond thin-films. *Appl. Phys. Lett.* 71,1065-7 (1997)
[38] A.T. Collins, *Properties and Growth of Diamond* Ed. G. Davies (INSPEC, IEE, London, UK) ch.9 p.261-88 (1994)
[39] I. Sakaguci *et al*, *Phys. Rev. B (USA)* vol.60, p. 2139-41 (1999)
[40] M.S. Dresselhaus, R. Kalish, *Ion Implantation in Diamond, Graphite and Related Materials* (Springer-Verlag, Berlin Heidelberg) (1992)
[41] V.S. Vavilov, M.A. Gukasyan, M.I. Guseva, T.A. Karatygina, E.A.

Konorova, *Sov. Phys.-Semicond. (USA)* vol.8 , p.471-3 (1974)

[42] G. Braunstein, R. Kalish, *J. Appl Phys. (USA)* vol.54, p.2106-8 (1983)

[43] J.F. Prins, *J. Phys. D (UK)* vol.22, p. 1562 (1989)

[44] J.F. Prins, *Phys. Rev. B (USA)* vol.38, p.5576-84 (1988)

[45] J.F. Prins, *Phys. Rev. B (USA)* vol.39, p.3764-70 (1989)

[46] S. Prawer, K.W. Nugent, D.N. Jamieson, *Diam. Relat. Mater. (Switzerland)* vol.7, p.106 (1997)

[47] C Uzan-Saguy, R. Kalish, R. Walker, D.N. Jamieson, S. Prawer, *Diam. Relat. Mater. (Switzerland)* vol.7, p.1429-32 (1998)

[48] R. Kalish, C Uzan-Saguy, A. Samoiloff, R. Locher, P. Koidl, *Appl. Phys. Lett. (USA)* vol.64, p.2532-4 (1994)

[49] R. Kalish, C Uzan-Saguy, B. Ran, H. Ferber, H. Guettler, R. Zachai, *Diam. Relat. Mater. (Switzerland)* vol.7, p.877-81 (1999)

[50] S.A. Kajihara, A. Antonelli, J. Bernholc, R. Car, *Phys. Rev. Lett. (USA)* vol.66, p.2010-3 (1991)

[51] S. Koizumi *et al*, *Diam. Relat. Mater. (Switzerland)* vol.7, p.540-5 (1998)

[52] F. Maier, M. Riedel, B. Mantel, J. Ristein, and L. Ley, Physical Review Letters, Volume 85, Number 16 (2000)

[53] M. I. Landstrass and K. V. Ravi, Appl. Phys. Lett. 55, 975 (1989); Appl. Phys. Lett. 55, 1391 (1989)

[54] S. G. Ri *et al.,* Jpn. J. Appl. Phys. 38, 3492 (1999)

[55] H.J.Looi, R.B.Jackman, J.S.Foord, Appl.Phys.Lett. 72, 353 (1998)

[56] J. B. Cui, J. Ristein, L. Ley, Phys. Rev. Lett. 81, 429 (1998)

[57] H. Gerischer, in *Physical Chemistry,* edited by H. Eyring (Academic Press, New York), Vol. IX A, p. 463 (1970)

[58] Y .V . Pleskov,A.Y . Sakharova, M.D. Krotova, L.L. Builov and B.V. Spitsyn, *J.Electroanal. Chem.*, 228, 19 (1987)

[59] M. Swain, A.B. Anderson and J.C. Angus, *MRS Bulletin,* Sept. (1998) 56.

[60] M. Fryda, L. Schäfer and I. Tröster, *Recent Res. Devel. Electrochem.,* 4, 85 (2000)

[61] M. Panizza and G. Cerisola, *Electrochim. Acta*, 51, 191 (2005)

[62] M.A.Q. Alfaro, S. Ferro, C.A. Martínez-Huitle and Y.M. Vong, *J. Braz. Chem. Soc.,* 17, 227 (2006)

[63] M. Fryda, T. Matthee, S. Mulcahy, A. Hampel, L. Schäfer and I. Tröster,

Diamond Rel. Mater., 12, 1950 (2003)

[64] H.B. Martin, A. Argoitia, U. Landau, A.B. Anderson and J.C. Angus, *J. Electrochem. Soc.*, 143, L133 (1996)

[65] N. Katsui, E. Takahashi, M. Toyoda, T. Kurosu, M. Iida, S. Wakita, Y. Nishiki and T. Shimamume, *J. Electrochem. Soc.*, 145, 2358 (1998)

[66] F. Beck, H. Krohn, W. Kaiser, M. Fryda, C.P. Klages and L. Schäfer, *Electrochim. Acta*, 44, 525 (1998)

[67] F. Beck, W. Kaiser and H. Krohn, *Electrochim. Acta*, 45, 4691 (2000).

[68] T. Ponnusamy, J. Chen, X. Fei and O Chyan, Analysts, 1268 877-80 (2001)

[69] P.L. Hagans, P.M. Natishan, B.R. Stoner and W.e. O'Grady, J. Electrochem. Soc. 148 E298 (2001)

[70] W. Haenni, P. Rychen, M. Frydaand, C. Comninellis, Thin-Film Diamond II eds CE Nebel and J Ristein (Amsterdam: Elsevier) pp 149-196 (2004)

Chapter 3

A Review On Relevant Diamond Electronics And MEMS Cantilever Devices

3.1 Metal-Diamond Contacts

3.1.1 Ohmic contact

Traditionally, silver paint or a damaged surface [1] and W probe contacts modified by passing a high current [2] have been employed for establishing ohmic contacts on semiconducting diamond for performing electrical measurements. In some cases the painted contacts were annealed to reduce contact resistance [1]. Indium has also been used [3] to make an ohmic contact on diamond; however this metal is unsuitable for high-temperature studies due to its physical softness and relatively low melting point at ~ 157^{o}C. Recently, photolithographically defined contacts of various high melting point metals have been investigated. Moazed *et al*. [4,5] reported the formation of ohmic contacts on diamonds by using metals, e.g., Ti, Ta, Ni, and Mo that form carbides upon annealing. In a typical application, 100 - 150 Å thick layer of Ti followed by a 1500 Å layer of Au was employed. The ohmic contact was obtained following annealing at 885^{o}C for 8 - 16 min in a hydrogen ambient. The surface roughness observed in the Au/Ta, Au/Ti, and Au/Mo contacts is indicative of carbide formation.

A WSiC/diamond multilayer structure has been investigated by Fang *et al.* [6] for its potential as an ohmic contact. These researchers deposited 500 Å of Si on cleaned diamond substrates. This was followed by the implantation of Kr^{+} at an energy of 240 keV, dose and temperature of 2 x 10^{16}/cm^{2} and 700°C respectively, to achieve ion-beam mixing. The samples were then annealed at a temperature 120^{o}C for 1 hr in flowing forming gas. In some samples, they pre-implanted the diamond substrates with Kr^{+} using the conditions of 150 keV, 2 x 10^{16}/cm^{2} and 700^{o}C prior to the deposition of the 500 Å of Si. This implantation step caused the formation of an n-type layer. Following the Si deposition, the structure was annealed in the same manner as the previous case. The post-deposition ion-mixing contributed to a lower contact resistivity of 1 x 10^{-3} Ω-cm^{2} as compared to 5 x 10^{-3} Ω-cm^{2} for the pre-implanted structure.

Geis *et al*. [7] have established ohmic contacts to p-type diamond using surface modification induced by intense argon-fluoride excimer laser radiation. The modified layer was ~500 Å thick and composed of diamond and graphite-like material. It was also stable at high temperatures to 1800^{o}C. Geis [3] also observed that ohmic contacts can be obtained on heavily B doped 10^{21} cm^{-3} diamond with a deposited layer of each of several metals. Similar results have also been reported for polycrystalline diamond films [8]. Surface modification using other techniques has also been employed for the formation of ohmic contacts on diamond surfaces. Childs, Sandhu and Chu [9-11] reported the formation of ohmic contacts by pre-deposition exposure to an Ar sputtering environment prior to the deposition of Au on semiconducting substrates. The pre-sputtering also enhanced the adhesion of the Au film. Normally Au forms rectifying contacts on B doped semiconducting diamond crystals.

Ohmic contact formation by high dose B implantation has been reported by Sandhu *et al*. [11] and Prins [12]. Sandhu *et al*. conducted a selected-area B implantation at room temperature with 65 keV ions to a dose of 3 x 10^{16} cm^{-2} [11] to establish ohmic contact to previously implanted layers in insulating crystals [13,14]. This high-dose implantation step introduced extensive radiation damage leading to graphitization of the surface layer during a subsequent anneal treatment at 950^{o}C in vacuum for 30 min. The graphitized surface was removed by boiling in a solution of $HClO_3$ + HNO_3 + H_2SO_4 (1:4:3). Tungsten probes on the remaining heavily doped film provided ohmic contact. It should be pointed out that Braunstein and Kalish [13], in their earlier work on B implantation-doping of diamond, were also able to establish ohmic contact to their highly conducing film with sharp W probes. Prins [12] obtained ohmic contact on semiconducting crystals using an implantation energy of 35 keV and a B ion dose of 3 X $10^{16}cm^{-2}$ at a substrate temperature of 200°C. Subsequent to annealing at 1200°C the graphitized layer was removed and contact established with a film of metal, such as Ag, Cu, or Au. Metallization at a temperature of ~800^{o}C with an alloy of Ag, Cu, and In provided a strong mechanical bond. A similar study has also been conducted [15] on polycrystalline films deposited on Si and SiAlON. These films were polished [16] prior to ion implantation. In this study, a B dose of 3.5 x 10^{16}

cm^{-2} at 60 keV was employed. An optimum substrate temperature of 100°C was determined empirically. A surface concentration of B of -7 x 10^{20} cm^{-3} in the diamond film was achieved. Using a conventional TLM pattern a specific contact resistance of 3.7 x 10^{-3} Ω cm^2 was obtained with an as-deposited film of Au. Wiih a Au/Ti metallization and subsequent anneal, at a temperature of 850°C and a pressure of 10^{-6} Torr for 30 min, a specific contact resistance of the order of 10^{-6} Ω cm^2 was obtained.

Chromium (Cr) being a carbide-forming metal has been used as the basis of forming ohmic contacts on diamond. Yokoba *et al* had Cr deposited on a boron-doped/undoped bi-layer polycrystalline diamond synthesized by MPECVD and subsequently annealed at 600°C for 10 minutes yielding a contact barrier height of ~0.5eV [17]. Doneddu *et al* carried out similar work on heavily boron-doped single crystal diamond, using X-ray Photoelectron Spectroscopy (XPS) it was discovered that significant interaction between carbon (diamond) and Cr only occurs at annealing temperatures greater than 400°C. After annealing at 800°C, an average value of specific contact resistivity ρ_s = 1.8 x 10^{-4}Ω cm^2 was achieved [18].

3.1.2 Schottky contact

Rectifying contacts have been reported for naturally occurring semi-conducting crystals [19], synthetic B doped crystals [20] and CVD grown homoepitaxial [21,22] and polycrystalline films [23-27]. These contacts have been formed by using point probes [24,27] or by evaporation of films of various metals [20-25], e.g., Al and Au. Rectifying behavior with sputtered platinum on polycrystalline films has also reported by Nishimura *et al* [26]. High breakdown voltages have been reported for polycrystalline films [25]. Shiomi *et al*. [28] have demonstrated that by placing a rectifying contact on an undoped diamond film on a previously deposited doped film, the reverse leakage current is substantially reduced and the breakdown voltage improved. Similar observations have also been reported for polycrystalline films [29]. Introduction of a thin (-20 Å) plasma enhanced CVD (PECVD) SiO_2 film has also been used for improving rectifying characteristics of metal contacts on

both polycrystalline and homoepitaxial films [30]. These improvements in characteristics are probably due to a modification in the barrier height and field distribution and/or to passivation of the surface. Shiomi *et al*. [28] employed an undoped diamond film deposited on a doped film for the fabrication of the gate structure in their MESFETs.

More recently, Humphreys *et al*. [31] have demonstrated that deposited heteroepitaxial films of Ni on semiconducting single crystal diamond exhibit excellent rectifying contacts both at room temperature and 400^{o}C. Moreover, as a result of strong interface bonding, the Ni films exhibit excellent adhesion properties with the underlying diamond substrate. In contrast, metal films deposited at room temperature, e.g., Au, have a tendency to peel from the diamond surface during processing [32].

Contacts formed with $TiSi_2$ deposited by co-evaporation of Ti and Si have also been studied by Humphreys *et al*. [33]. These contacts were nominally rectifying in the as-deposited state. However, following an anneal treatment at a temperature of 1100°C the rectifying properties improved significantly. Excellent rectifying contacts on semiconducting single crystal diamond have also been achieved using a composite film of co-sputtered Ta and Si [34]. At room temperature these contacts showed a reverse leakage current two orders of magnitude lower than the Ni contacts, however, at a measurement temperature of 400^{o}C these had approximately three orders of magnitude higher reverse leakage current. For both $TiSi_2$ and Ta/Si films excellent adhesion on the diamond substrate was reported.

Barrier height measurements for Au and Al contacts on single crystal diamond have been reported by a number of authors [20,35,36]. Most of these studies were conducted on the (111) surface of diamond [34,36]. Both (C-V) and internal photoemission spectroscopy techniques were used. Glover [37] obtained from C-V measurements a barrier height of 1.7 eV for Au on the (100) surface of a chemically cleaned synthetic B doped diamond. Mead and McGill (64) obtained 1.7 - 2.0 eV for Au and 1.9 - 2.0 eV for Al on chemically cleaned semiconducting diamond. The lower values were obtained from C-V

measurements whereas the higher values were from internal photoemission spectroscopy. These measurements probably were taken from the (111) surface of natural crystals. Barrier heights reported by Himpsel *et al*. [36] were significantly different from the above values. They reported barrier heights of 1.3 eV for Au and 1.5 eV for Al employing electron spectroscopy with synchrotron radiation. These results were obtained from the vacuum annealed (111) - (1x1) surface of B doped type IIB diamond. Himpsel *et al*. pointed out that their barrier heights were closer to a second threshold in the internal photoemission measurements of Mead and McGill (35) corresponding to barrier heights of 1.25 and 1.0 eV for Au and Al, respectively.

Hicks *et al*. [38] have measured barrier heights of 1.13 eV for both Al and Au contacts on polycrystalline diamond films, using internal photoemission spectroscopy. Beetz *et al*. [39] performed internal photoemission experiments on Au contacts on CVD diamond to obtain two photoresponse thresholds, one at ~2 eV and the other at ~1.2 - 1.3 eV. It should be noted that barrier heights are difficult to determine from I-V or C-V data on these diamond films since the contacts deviate widely from ideal behavior as a result of the nature of the surface (see Sets. 3.1 and 3.2) the presence of electrically active deep-states and high bulk resistivity. Therefore, internal photoemission and other non-electrical techniques should be preferred for the determination of barrier heights of metal contacts on diamond films. Any pretreatment that affects the nature of the surface, e.g., its deposition history, passivation and the presence of adsorbates, will have an effect on barrier heights, saturation currents, reverse leakage, and device performance. In order to develop a better understanding, surface analytical studies must be conducted in conjunction with terminal electrical characterization of potential device structures.

3.2 MISFET and MESFET

3.2.1 Boron-doped Bulk diamond

Early experimental FET devices in diamond have been demonstrated, primarily in monocrystalline natural or high pressure synthetic wafers or

homoepitaxial layers grown by chemical vapor deposition (CVD) on these wafers. Several groups [28,40-43] have also demonstrated basic field effect transistor (FET) device operation in homoepitaxial diamond films and B doped layers on insulating single crystal diamond substrates.

Geis *et al*. [44] reported a vertical channel FET fabricated in a natural semiconducting diamond substrate. A schematic diagram of the device and its characteristics are shown in Figure 3.1 (a). This device had a transconductance of 30 μS/mm. Gildenblat *et al*. [40] reported a FET device using a 1000 Å sputter-deposited film of SiO, as the gate dielectric. This device with a channel length and width of 60 μm, and 200 μm, respectively, was fabricated on a 1000 Å thick selected area B doped homoepitaxial diamond film grown by microwave plasma CVD on (001) insulating natural type la substrate. An Au/Ti metallization scheme was used for source and drain ohmic contacts with Au as the gate contact metal. The schematic structure of the device and the I-V characteristics measured at 300K are shown in Figure 3.1 (b). Shiomi *et al*. [28] recently reported the characteristics of a circular geometry MESFET (MISFET) device having a 20 μm gate-length. Schematics of the plan-view and the cross-section as well as the characteristics of this device are shown in Figure 3.1 (c). Synthetic type lb substrates were used for the fabrication of these devices. Titanium metal was deposited through a metal mask for the formation of ohmic contacts and the gate metal came in the form of a circular Al design. The drain current tended to saturate at a drain voltage of -50 V. The device had a transconductance of 2.0 μS/mm. The fabrication and characteristics of a depletion mode diamond MESFET was reported by Tsai *et al*. [43]. The device was fabricated on a type IIa insulating diamond crystal. Annealed Au/ Ti source/drain contacts at a separation of 700 pm and an as-deposited Ti/Au gate 150 μm in length and 1 mm in width were employed. A modulation of the drain current was obtained by applying a gate bias and pinch-off was observed at a high positive gate bias. The schematic and the characteristics of the device are shown in Figure 3.1(d). An open channel current of 1.6 pA/mm at a drain bias of 10 V and a transconductance of 0.7 μS/mm were obtained.

An insulated gate field effect transistor was fabricated by Fountain *et al*. [41] using selectively grown B doped homoepitaxial films on type Ia natural crystals. A RPECVD SiO_2 film was used as the gate dielectric. Titanium was used both for gate and source/drain metallization. As-deposited Ti provided ohmic contacts. The device had a gate length of 8 μm and width of 50 μm. The device could not be pinched-off and a transconductance of 38 μS/mm was obtained. Devices fabricated on the Li/B doped films showed better characteristics than those fabricated on B doped films as shown in Figure 3.1 (e). Zeisse *et al*. [42] reported an FET with an implantation doped active layer in a type IIa substrate and a deposited SiO_2 gate insulator. A bilayer Mo/Au metallization was used as source/drain contacts and Ti/Au as the gate contact. The device structure and the reported device characteristics obtained at room temperature are shown in Figure 3.1 (f). Current saturation and pinch-off was observed in these devices; a transconductance of 6.9 μS/ mm was reported.

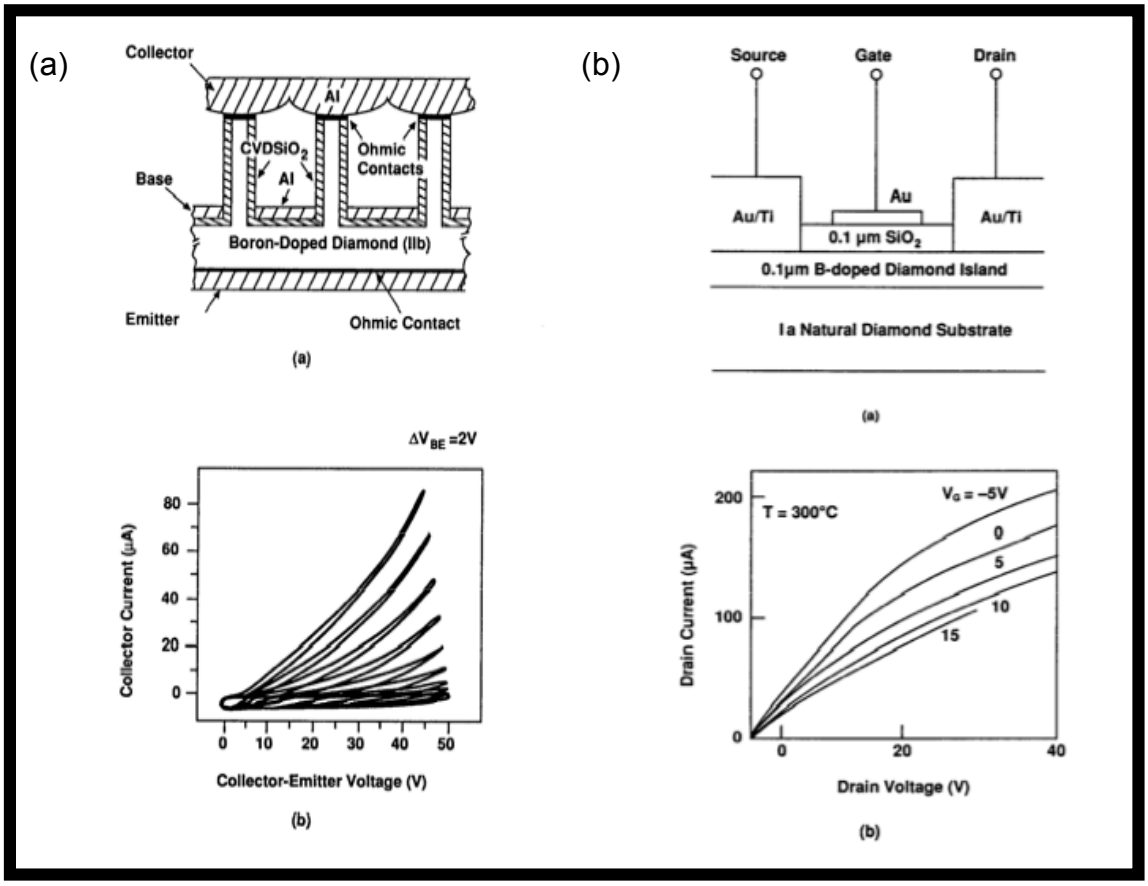

(c)

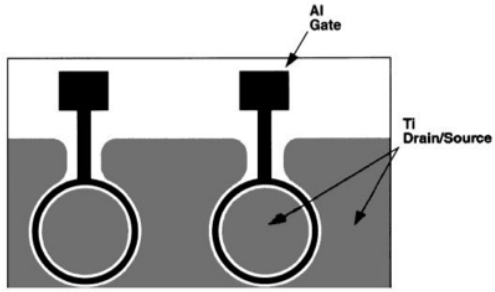
Al
Gate
Ti
Drain/Source

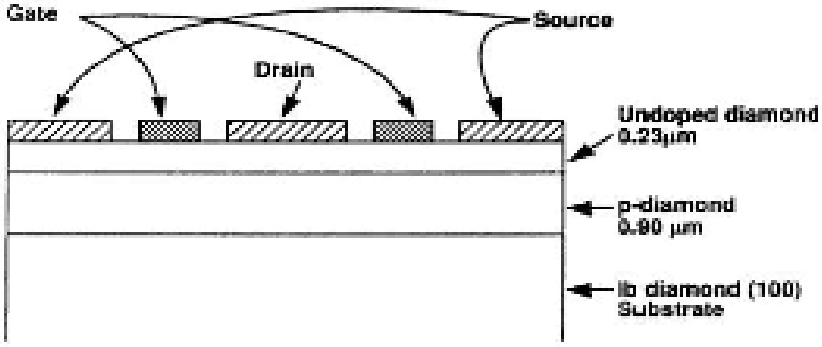
Gate
Source
Drain
Undoped diamond
0.23μm
p-diamond
0.80 μm
Ib diamond (100)
Substrate

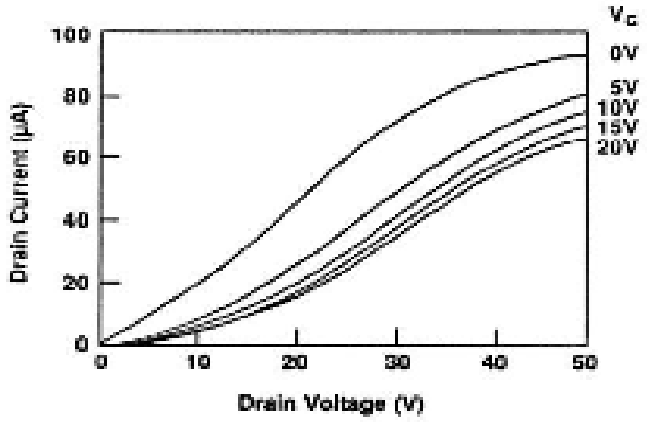
V_G
0V
5V
10V
15V
20V
Drain Current (μA)
Drain Voltage (V)
0
20
40
60
80
100
10
30
50

(d)

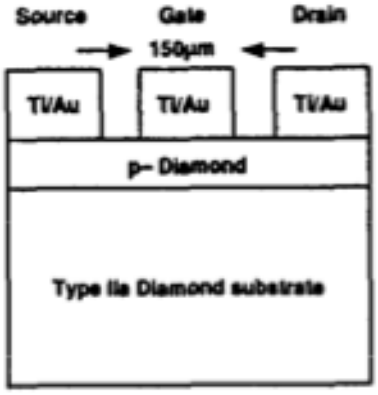
Source
Gate
Drain
150μm
Ti/Au
Ti/Au
Ti/Au
p– Diamond
Type IIa Diamond substrate

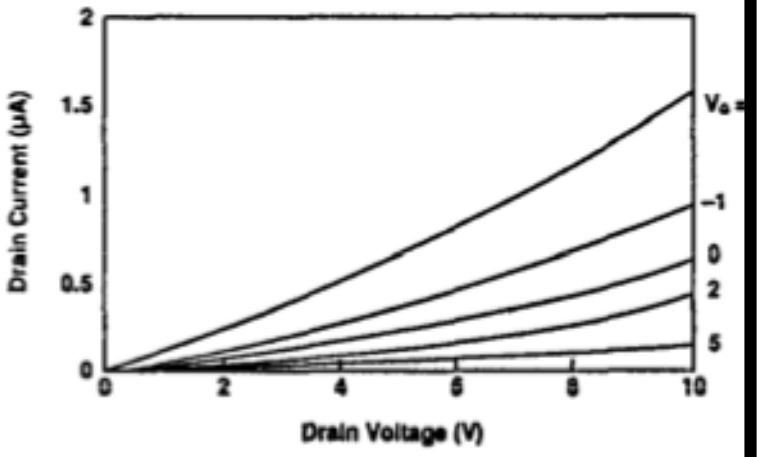
Drain Current (μA)
Drain Voltage (V)
V_G =
–1
0
2
5
0
0.5
1
1.5
2
2
4
6
8
10

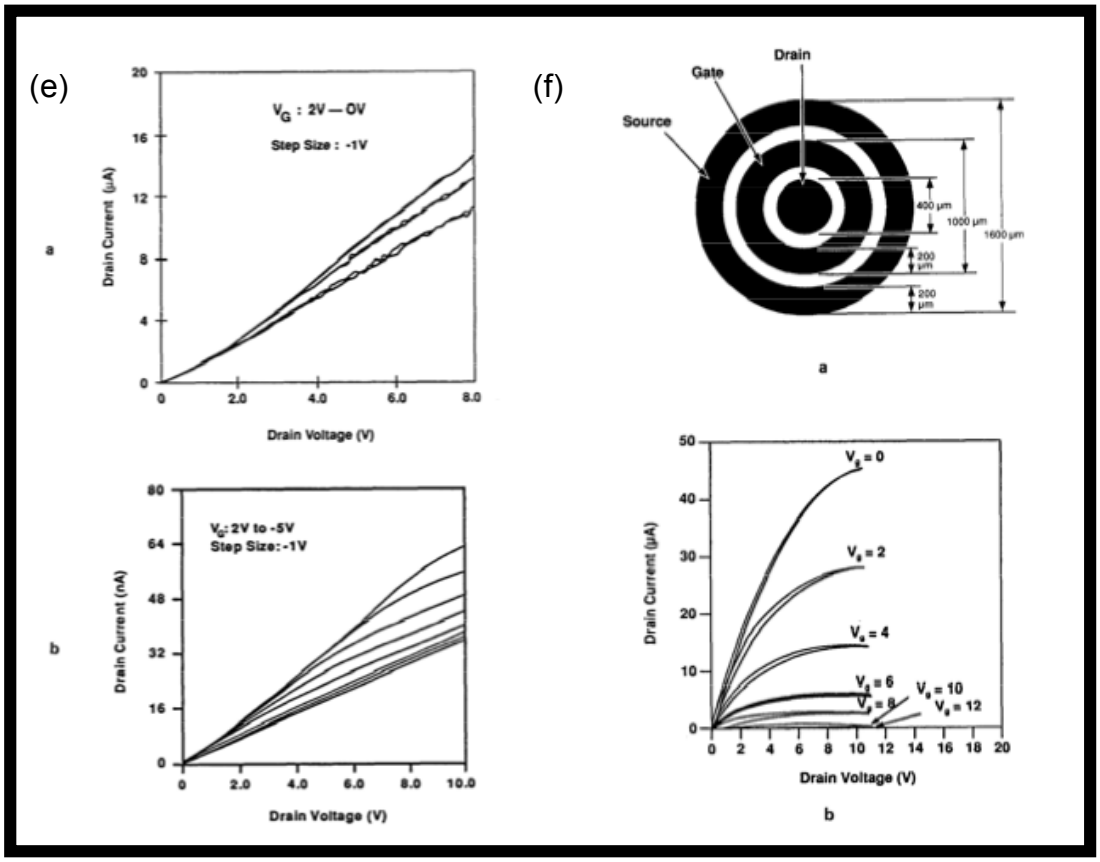

Figure 3.1: (a) Diamond vertical FET: (i) Schematic device structure. (ii) Current-voltage characteristics (b) Insulated gate FET fabricated in selected area homoepitaxial film. (i) Schematic device structure. (ii) Current-voltage characteristics obtained at 300°C (c) Metal-semiconductor FET fabricated on undoped / B doped homoepitaxial diamond film (i) Metal/undoped/B-doped diamond homoepitaxial film device structure. (ii) Current-voltage characteristics. (d) Metal semiconductor FET fabricated in a thin B diffusion doped layer on a type IIa diamond substrate. (i) Device structure. (ii) Current- voltage characteristics. (e) Current-voltage characteristics of insulated gated FET fabricated on selectively grown homoepitaxial films (Ref. 10). (i) Boron doped film. (ii) Lithium/B doped film (f) Insulated gate FET with the active layer formed by multiple B implantation. (i) Schematic device structure. (ii) Current-voltage characteristics obtained at room temperature.

One of the primary reasons for the poor characteristics of the above mentioned devices, apart from the material quality of the currently grown films, is that the device design and process concepts used in their fabrication are yet to be optimized. Major improvements are expected with

short gate lengths of the order of a micron and below. Reduction of source-channel and drain-channel spacings also will improve characteristics further by reducing series resistance of the device. Reduction of these resistances would lead to a better power handling capability and high frequency response.

A depletion-mode metal-insulator-semiconductor field-effect transistor was fabricated by Y.S Pang *et al*, from thin film polycrystalline diamond with a p-type (boron doped) channel and an insulating diamond gate. This device has been successfully operated at 300 °C displaying pinch off when in depletion and high levels of channel current modulation in enhancement. A transconductance value of 174 μS/mm has been measured, the highest reported value to date for this type of device [45].

3.2.2 Hydrogen-terminated diamond FET

Hydrogen-induced surface conductive channels are very attractive for the fabrication of diamond MESFET devices. Surface p-type channel devices show extremely low leakage current and high breakdown voltages. Single-crystal diamond layers show high sheet charge densities in the range of 10^{13} cm^{-2} and carrier mobilities above 100 $cm^2\ V^{-1}s^{-1}$ [46, 47]. The conductivity also seems to follow the surface structure since devices operate on polycrystalline diamond, as well as on single-crystalline diamond, only here the mobility is lower at 70 $cm^2\ V^{-1}s^{-1}$ [48-50]. Since the surface Fermi level of hydrogenated diamond is unpinned [46], Schottky barrier heights depend on the metal work function difference to diamond [46]. Thus, Au is used for ohmic contacts, while Al gives Schottky contacts with a barrier of approximately 0.8 eV [46]. However, due to the unpinned surface Fermi level, the gate surface depletion is also sensitive to adsorbates. Therefore devices on hydrogen-terminated diamond suffer from instabilities.

A hydrogen-terminated surface channel single crystal diamond metal–insulator–semiconductor field-effect transistor (MISFET) with 0.7μm gate length developed by Umezawa *et al* achieved a cutoff frequency of 11 GHz. This value is five times higher than that of 2μm gate metal-semiconductor

MESFETs and the maximum value in diamond FETs at present. Utilizing CaF_2 as an insulator in the MIS structure, the gate-source capacitance is reduced to half that of diamond MESFET because of the gate insulator capacitance being in series to the surface-channel capacitance. This FET also exhibits the highest of 18 GHz and 15 dB of power gain at 2 GHz. The high-frequency equivalent circuits of diamond MISFET are deduced from the parameters obtained from RF measurements[51].

The same research group now led by Miyamoto reduced the gate size down to 0.4-μm of a diamond metal–insulator–semiconductor field-effect transistor (MISFET) using a homoepitaxial diamond films deposited on high-pressure-synthetic type Ib diamond (001) substrates by microwave-plasma-assisted chemical vapor deposition. A cut-off frequency of 15 GHz and a maximum frequency of oscillation of 20 GHz are realized and the former is the highest value for diamond FETs ever reported. The RF characteristics of the MISFETs are higher than those of metal–semiconductor FETs at the same gate lengths. The benefit of the CaF_2 gate insulator such as improvement in the carrier mobility resulting in high RF performance is duplicated in this effort. The source–gate passivation of CaF_2 results in the high DC transconductance because of the reduction of series resistances. A cut-off frequency of more than 30 GHz is expected with the gate minimization and the CaF_2 passivation of source–gate and gate–drain spacings [52].

Saito *et al* employed a hydrogenated surface conductive layer of single-crystal B-doped diamond (111) was employed to fabricate a metal insulator semiconductor field effect transistor (MISFET) using a CaF_2 and Cu stacked gate. The carrier mobility and concentration of the hydrogenated surface on (111) before FET processing were 35 cm^2/V s and $10^{13}/cm^2$, respectively, when bulk carrier concentration and film thickness of the B-doped underlaying diamond was $3 \times 10^{15}/cm^3$ and 1.5 μm, respectively. The DC characteristics of the gate with 1.1 μm length and 50 μm width showed that the maximum measured drain current was 240 mA/mm at − 3.0 V gate voltage, and the maximum transconductance (g_m) was 70 mS/mm. The cut-off frequency of 4 GHz was obtained, which is one of the best values for the RF characteristics

of a diamond homoepitaxial (111) MISFET [53].

A submicrometer-gate (0.2-0.5μm) Cu/CaF_2/diamond metal–insulator–semiconductor field-effect transistors (MISFETs) developed by Matsudaira were fabricated on an H-terminated homoepitaxial diamond films deposited on a high-pressure synthetic Ib (001) substrate. The maximum transconductance in dc mode reaches 165 mS/mm, while the average transconductance is 70 mS/mm in submicrometer-gate diamond MISFETs. The highest cutoff frequency of 23 GHz and the maximum frequency of oscillation of 25 GHz are realized in the 0.2 μm-gate diamond MISFET. From the intrinsic transconductances or the cutoff frequencies, the saturation velocities are estimated to be 4 x 10^6 cm/s in the submicrometer-gate FETs. They are reduced by gate–drain capacitance and source resistance [54].

Hirama *et al* developed a diamond MISFETs on polycrystalline films using alumina gate insulator. A hole accumulation layer has been utilized as hole current channel. The hydrogen-termination was achieved by remote hydrogen plasma. The sheet resistance strongly depends on the substrate temperature during hydrogen-termination process. The polycrystalline diamond MISFETs showed high drain current density of -650 mA/mm and cut-off frequency of 42 GHz. These values are higher than those of single crystal diamond FETs ever reported [55].

The first normally off enhancement mode MESFET structure on hydrogenated CVD polycrystalline diamond was fabricated by H.J. Looi *et al*, with typical carrier concentrations within the range of 10^{17}–10^{19} cm^{-3}. Control over the carrier concentration was achieved by annealing the ‘‘as-grown’’ films in air. For a given annealing temperature a stable carrier concentration was reached. The Hall carrier mobility value of 70 $cm^2 V^{-1}s^{-1}$ has been measured for a film with a carrier concentration of 5 x 10^{17} cm^{-3}, the highest reported for polycrystalline thin film diamond and equivalent to boron doped single crystal diamond. A room temperature transconductance of 0.14 mS/mm has been measured, the highest yet reported for a transistor structure made from polycrystalline material. The devices fully turned off, displayed saturation and

had a low gate leakage current. Al forms a near ideal Schottky barrier on this material (Schottky Barrier Height (SBH) ~ 0.98 eV, ideality factor at 1.1) and was used as the gate metallization within the MESFET. Hirama *et al* fabricated a H-terminated polycrystalline diamond MISFET structure with an alumina gate insulator. The device produced a drain current at 650mA/mm and a cut-off frequency of 42 GHz, which higher than those of single crystal [56].

3.3 Boron-doped delta-layer FET devices

In diamond full activation of the boron acceptor at RT is obtained only for doping concentrations $N_A \geq 10^{20}$ cm^{-3}. In this case, the sheet charge and therefore the thickness of the channel are limited by the breakdown field to $p_S \leq 3 \times 10^{13}$ cm^{-2} and thus $d \leq 3$ nm [57] leading to pulse or delta-doped channels. This represents a challenge for diamond epitaxy, since monolayer precise growth is necessary. Indeed, it is possible to fabricate delta-doped layers with a FWHM of approximately 4 nm and a sheet boron concentration of approximately 1×10^{14} cm^{-2}.

Schwittiers *et al* fabricated the first boron-doped delta-layer MESFET device. A boron-doped delta-layer with a FWHM-thickness of 10 nm was deposited on top of a 250 nm thick intrinsic CVD-diamond buffer-layer overgrown on a high-pressure / high-temperature (HPHT)-grown diamond (100)-substrate. The boron-concentration within the delta-layer is as high as $5x10^{20}$ cm^{-3}. Finally an intrinsic diamond layer with a thickness ~ 20 nm was deposited on top of the delta-layer to form the MESFET structure. Al was used as the Schottky gate contact on a recessed structure at 0.5μm length and WSi as ohmic contacts with gold capping layer. The device produced transistor-like output characteristics with appreciable channel modulation and near-saturation [58].

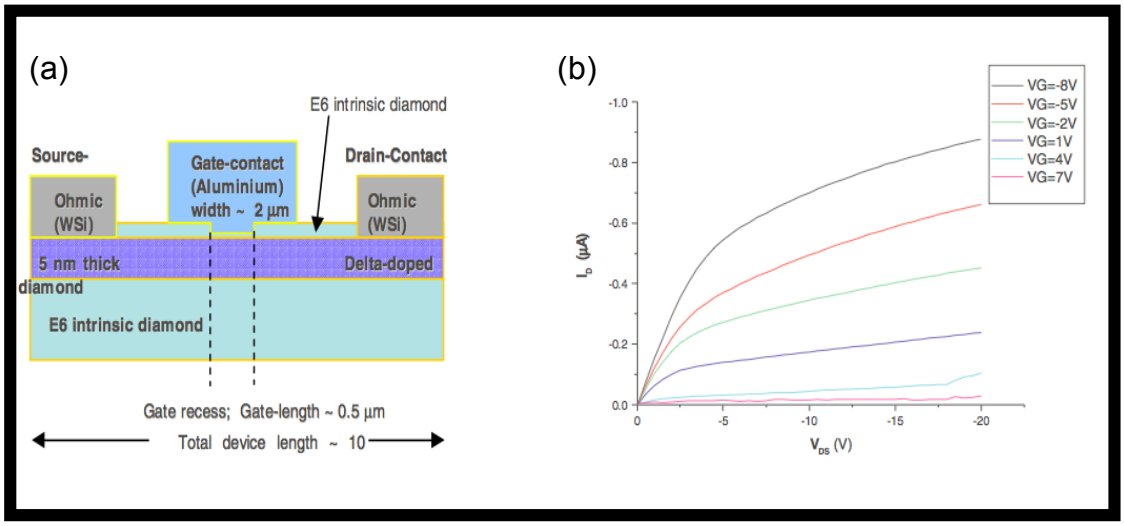

Figure 3.2: (a) Delta-doped MESFET device and (b) transistor-like output characteristics [58]

The delta doping concept with an intrinsic cap layer (nominally undoped) of 25 nm was grown on top of the delta-doped profile has been successfully further applied by El-Hajj *et al* to a diamond metal-insulator-semiconductor field effect transistor (MISFET) structure with an Al_2O_3 gate diode to reduce the gate leakage current, we used an aluminium oxide layer as gate insulator, resulting in full channel carrier activation at room temperature and channel current modulation with complete pinch-off. The effective delta layer thickness is estimated to be around 3-4nm, taken from the CV profiling measurement. Ohmic contact layers consisted of a stack of 4 metallization layers including 5 nm of WSi, 5 nm WSiN, 5 nm of Ti and 250 nm of Au on top. Using a gate recess configuration, a channel current density of 30 mA/mm with a gate length L_G of 0.8 µm has been obtained with semi-enhancement mode operation. First RF measurements have resulted in f_T and f_{max} cut-off frequencies of approx. 1 GHz and 3 GHz respectively [59].

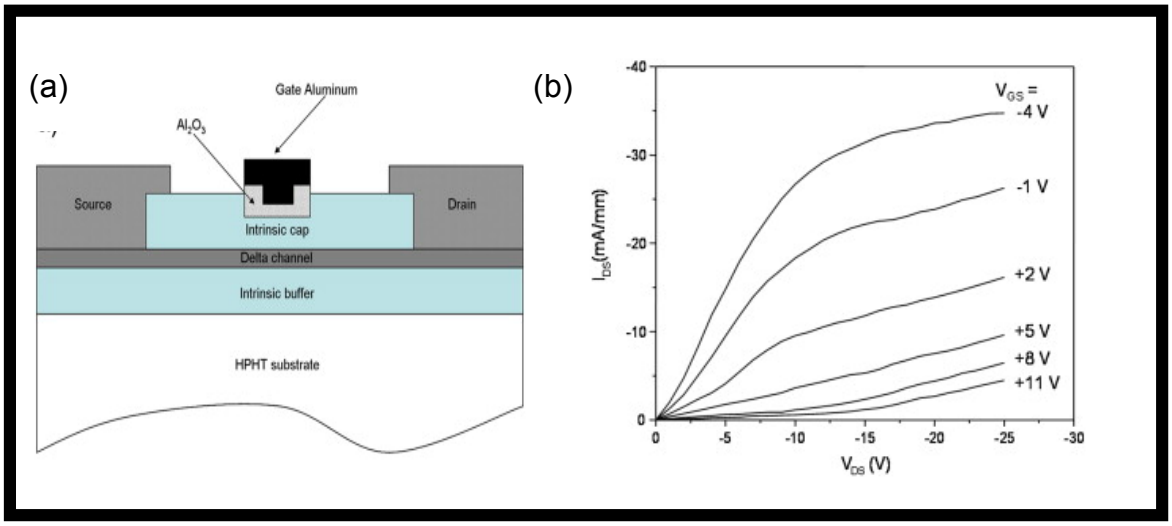

Figure 3.3: (a) delta-doped MISFET device structure and (b) IV output characteristics [59].

3.4 Ion Sensitive Field Effect Transistor

3.4.1 Polycrystalline H-terminated ISFET

Devices were fabricated on hydrogenated non-polished free-standing polycrystalline diamond substrates. Room temperature Hall experiments were performed to evaluate the electronic properties of the surface conductivity [60]. It was found that the surface conductivity is typically characterized by a concentration of holes in the range of 5 x10^{12} – 5 x 10^{13} cm^{-2} with mobilities varying between 10 and 140 cm^2 V^{-1} s^{-1} [61]. Devices were fabricated by standard photolithography processing in combination with oxygen plasma isolation to define the active area, which is about 3 x 3 mm^2. Ti(200Å)/Au(2000Å) contacts were deposited as drain and source contacts using electron-beam evaporation. The processed diamond substrates were mounted in a ceramic holder, and the drain and source metal contacts were bonded to Au metal pads evaporated on the ceramic holder. To prevent any contact between the metal regions and the electrolyte, chemically resistant silicone glue was employed to cover the metal contacts and pads. The gate area exposed to the electrolyte is the same as the active area, i.e., 3 x 3 mm^2. To induce a *p*H sensitivity, H-terminated surfaces were modified by means of

a mild ozone treatment [60].

No pH sensitivity was observed in H-terminated diamond devices, which were not treated with ozone. However, it was also found that nominally H-terminated devices with a poor conductivity which can be attributed to a non-optimum hydrogenation process showed low pH sensitivity, typically about 25 mV/pH. In contrast, the surface modification induced by the ozone treatment gives rise to a clear linear pH sensitivity in the pH range from 2 to 10 curve c in Figure 3.4(c). Further exposure of the device surface to ozone results in an increase of the *p*H sensitivity curve d in Figure 3.4(b). Surprisingly, the pH sensitivities reported in Figure 3.4(b), 63 and 72 mV/pH, are larger than the theoretical maximum predicted by the Nernst limit, which is 59.2 mV/pH. The charged ions from the electrolyte adsorbed on the oxidized surface regions induce a lateral electrostatic modulation of the conductive hole accumulation layer on the surface. In contrast, charged ions are not expected to be adsorbed on the hydrogen-terminated surface, either due to the screening induced by a dense layer of strongly adsorbed counter-ions or by the absence of the proper reactive surface groups. Therefore, the modulation of the surface conductivity is generated by the oxidized regions, which are described as microscopic chemical in-plane gates as depicted in Figure 3.4(a) [60]

(a)

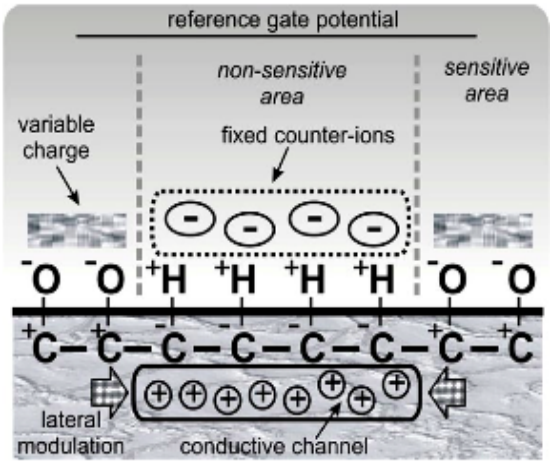

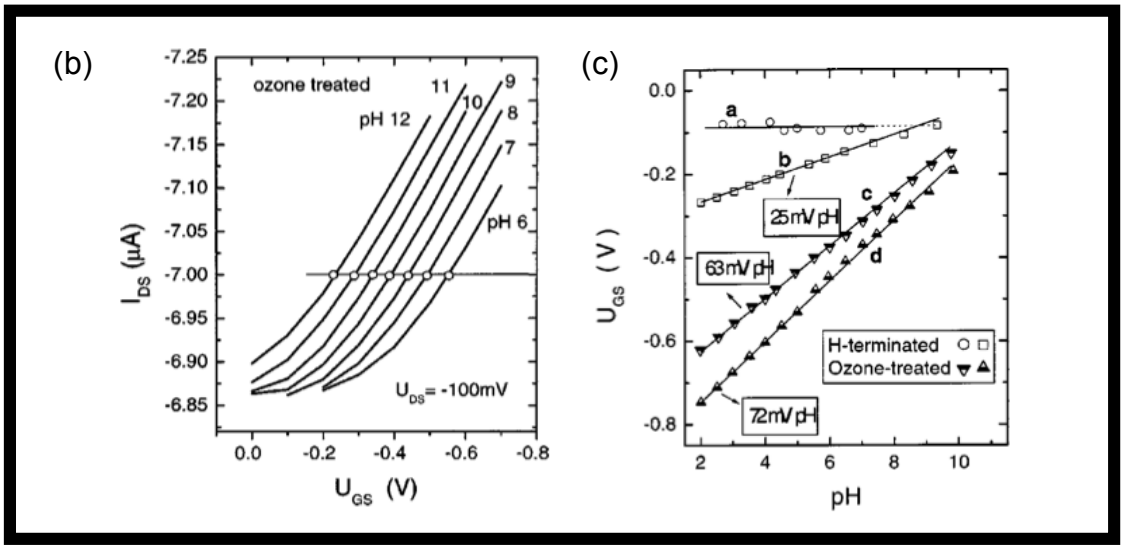

Figure 3.4: (a) Microscopic view of a device cross section in which a H-terminated region is embedded between two O-terminated regions. Holes are only accumulated under the H-terminated diamond surface. Varying the *p*H modifies the adsorbed charge only at the oxidized regions, inducing a lateral modulation of the conductive channel. (b) I_{DS}−U_{GS} curves of an ozone-treated device as a function of the electrolyte pH (c) pH sensitivity (mV/pH) of freshly hydrogenated devices (curve **a** and **b**) compared to ozone–treated diamond devices (curve **c** and **d**).

3.4.2 Single-crystal H-terminated ISFET

Ion-sensitive field-effect transistors (ISFET) are fabricated using intrinsic hydrogen-terminated homoepitaxial diamond layers of 0.2–1.0 µm thickness were grown on synthetic mono-crystalline (100) Ib diamond substrates [62]. The ISFET channels were fabricated in dimensions of (500 µm × 100 µm) using photolithographic masks and soft oxygen plasma. Regions exposed to oxygen plasma become resistive and confine the H-terminated surface areas [63]. Source and drain contacts were deposited by electron beam evaporation of gold, contacted by wire bonding, and encapsulated by a non-conducting chemically resistant lacquer.

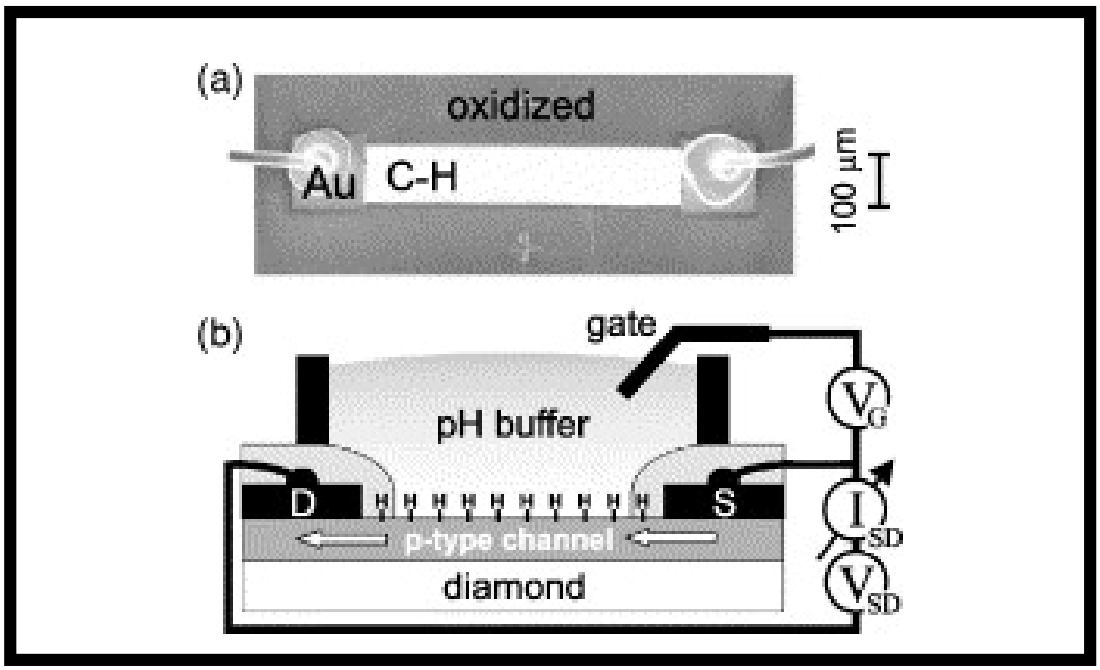

Figure 3.5: (a) Scanning electron microscopy image of the diamond surface with H-terminated ISFET channel. (b) Schematic drawing of the ISFET characterization set-up [62].

The gating is realized by immersing the diamond surface into electrolyte solution, which is contacted by a platinum electrode. Hydrogen termination of diamond surface acts as a gate insulation without any additional oxide layer. The response of gate potential to pH is about −56 mV/pH. The results are discussed in terms of transfer doping mechanism, Nernst equation, and electrochemical properties of diamond surfaces. The decrease of the H-terminated ISFET channel current with increase in pH is correlated with the transfer doping mechanism [64–66]. When the chemical potential of the electrolyte decreases due to an increase in pH the Fermi level in diamond moves upwards to maintain the equilibrium. This leads to a decrease of surface conductivity for higher pH values and vice-versa [62].

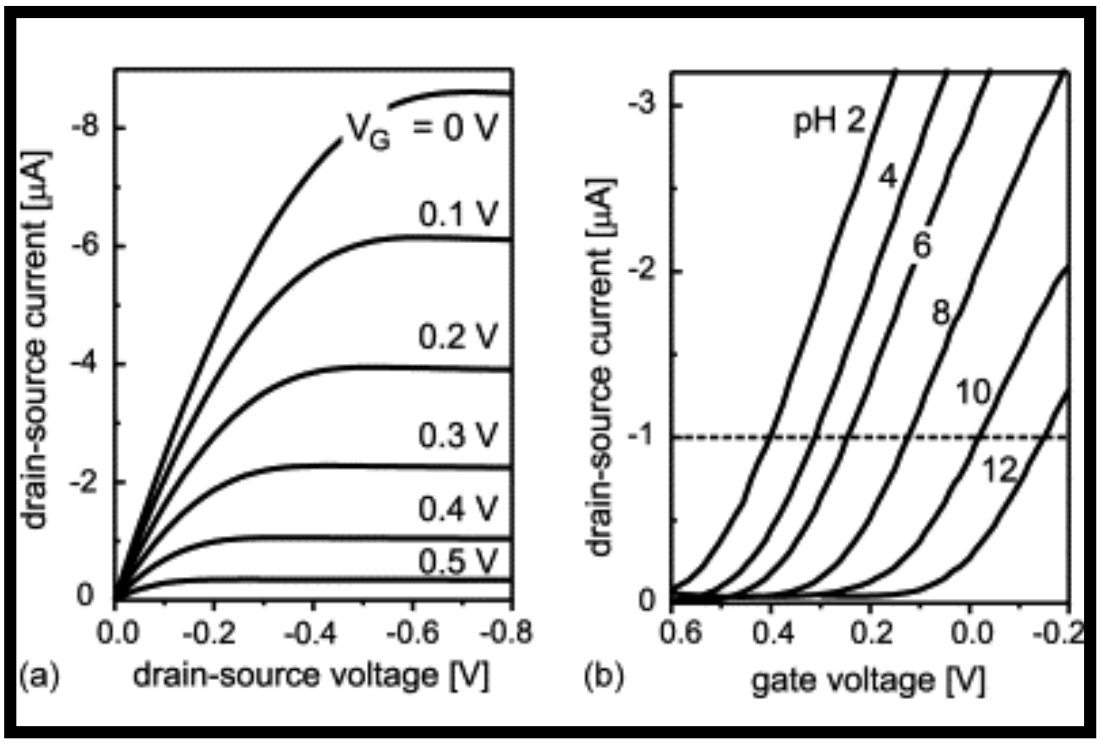

Figure 3.6: (a) Transistor characteristics of H-terminated diamond ISFET at pH 2. (b) Current through the ISFET channel (V_{SD} = -0.2V) as a function of gate voltage in pH 2–12. The horizontal line denotes a constant current level of -1μA [62].

3.4.3 Single crystal uncapped delta-doped ISFET

A concept of an ion sensitive FET (ISFET) on diamond using a thin and highly boron-doped channel is described. The doped channel is in direct contact to the electrolyte solution. The diamond surface is oxygen terminated to provide pH sensitivity and chemical stability. The first set of pH-sensitive ISFET microstructures with the extrinsically doped channel is fabricated on 100-oriented single crystal diamond substrate using a solid doping source technique and a wet chemical oxidation for the O termination. The boron delta-doped layer was grown on the surface of 100-oriented HTHP diamond substrate using the solid doping source technique. Prior to channel growth a 100 nm thick buffer layer of nominally undoped diamond was grown on a polished surface of the HTHP substrate. The individual ISFET structures were formed by mesa-etching using a photoresist mask. The source and drain ohmic contacts to the delta-doped channels were made by Ti/Au metallization.

The open gate areas in the polyamide passivation layer were structured by a lift-off technique. The electrode sample was passivated with a chemically resistant adhesive foil. The open area contacting the electrolyte was about 1 mm^2. The large area ohmic contact to the electrode surface was made with a conductive silver paste [67].

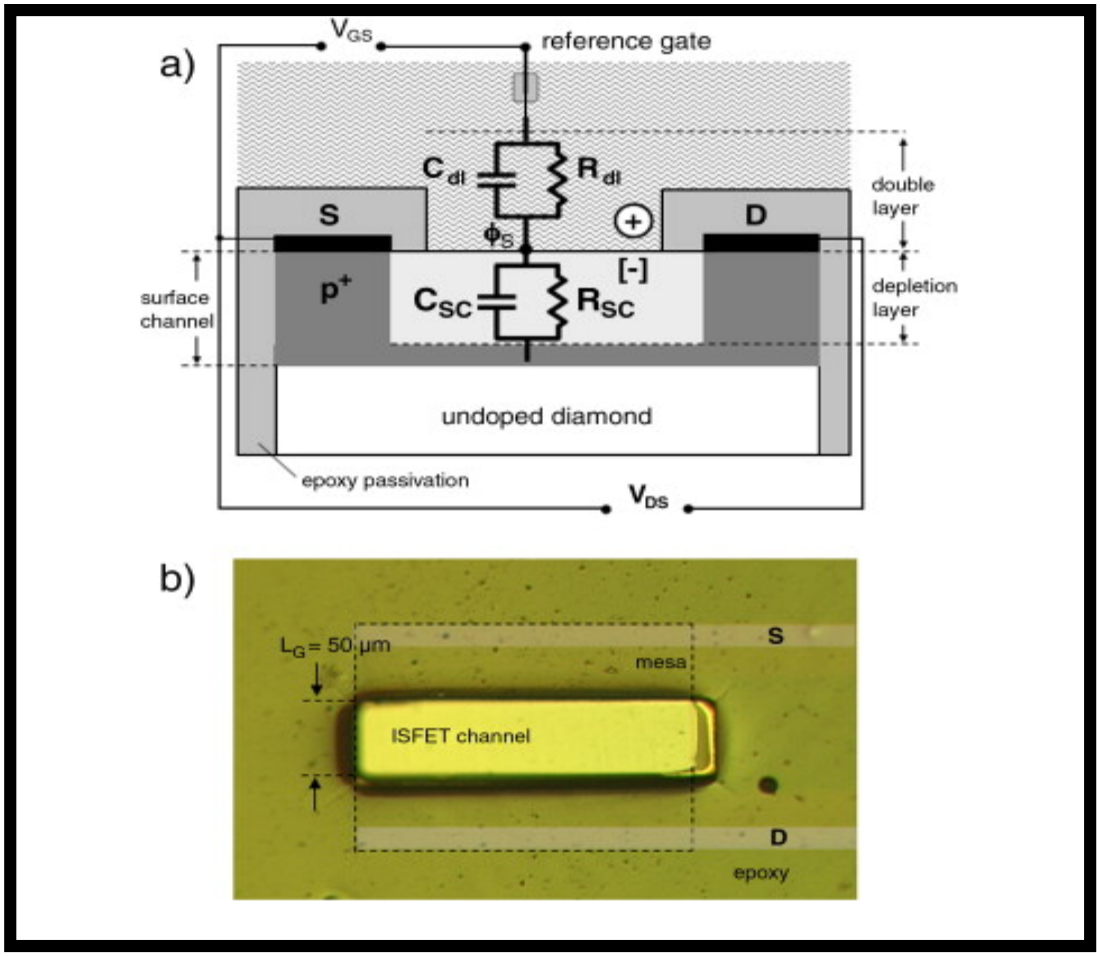

Figure 3.7: (a) Schematic cross-section of the ion sensitive FET with boron-doped channel including the equivalent circuit of the diamond–electrolyte interface, and (b) the layout of a single micro-ISFET fabricated on single crystal diamond substrate.

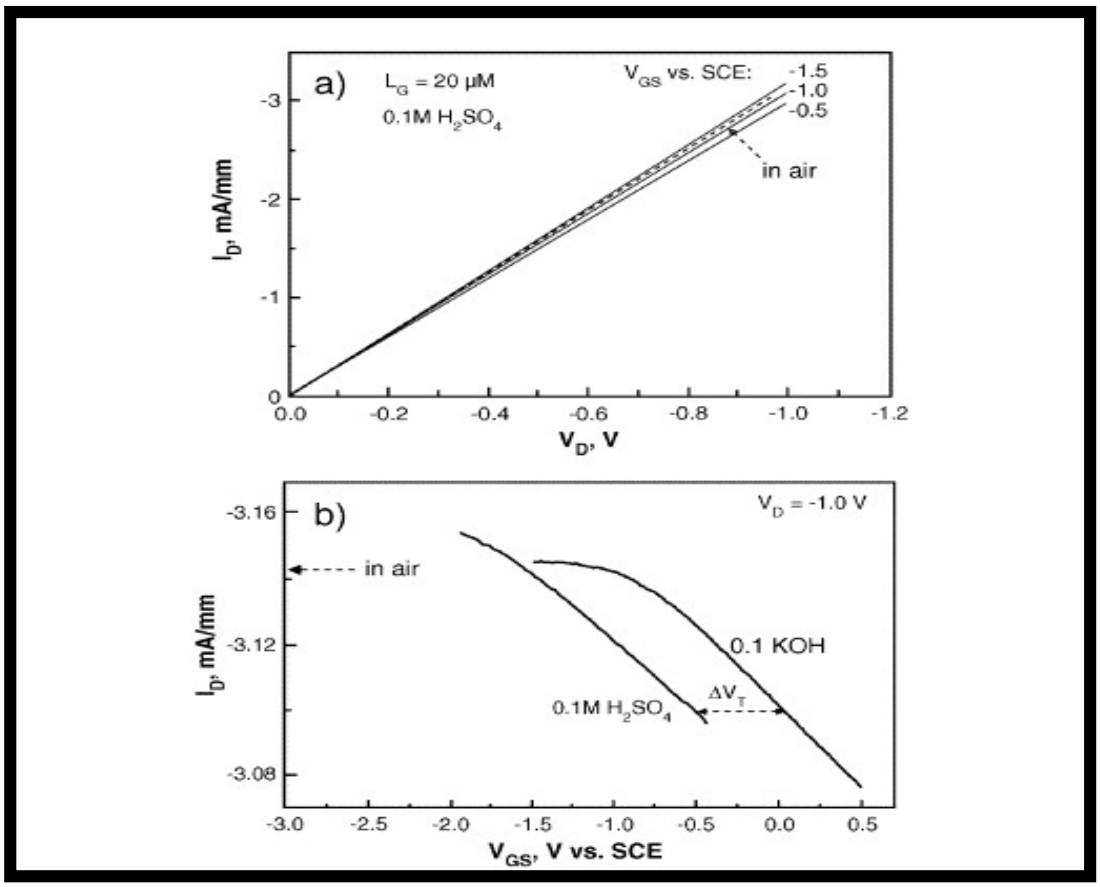

Figure 3.8: The output (a) and the transfer characteristics (b) of a micro-ISFET with boron-doped channel and a gate length of 20 μm. The dashed line shows the conductivity in air.

The fabricated structures show pH sensitivity (50 mV/pH) close to the Nernst's limit of 59 mV/pH. The ISFET characteristics have been reproducible and did not degrade after repeated cycling between 0.1 M H_2SO_4 and 0.1 M KOH solutions. The output characteristics exhibits only 1% current modulation over Δ1V of gate voltage and no saturation (pinch-off). Through electrochemical impedance analysis, it is shown that only a part of the applied gate potential to the diamond–electrolyte interface drops within the delta-doped channel [67].

3.4.4 Nanocrystalline uncapped delta-doped ISFET

The concept of an ion-sensitive FET (ISFET) on diamond with boron delta-doped channel and oxygen-terminated surface for pH sensing has been successfully transferred to large-area nano-crystalline diamond on silicon

substrates. The nano-crystalline diamond layers, including the boron delta-doped channels of the FETs, were grown by hot-filament CVD. The fabricated layers were characterised by their peak concentration of boron of 3 ×10^{20} cm^{-3} and FWHM of about 1 nm. The devices is fabricated by firstly having a pair of 2 × 2 mm Au contacts deposited with a drain-source distance of approx. 500 µm followed by mesa etching performed by an oxygen plasma treatment to define the active device pattern. SU8 (a photosensitive epoxy), which is chemically highly stable and inert, when in contact with the solution, was used to insulate the electrical contacts from the electrolyte solution. The SU8 film has been patterned into three contact openings: two openings at the periphery of the device for electrical source and drain contacts (Au) and one for the gate electrode. The gate electrode width varied from 100 µm to 500 µm. The device was packaged onto a PCB carrier and the complete encapsulation of the ISFET device structure was done using a PTFE foil with a window for the electrochemical gate electrode [68].

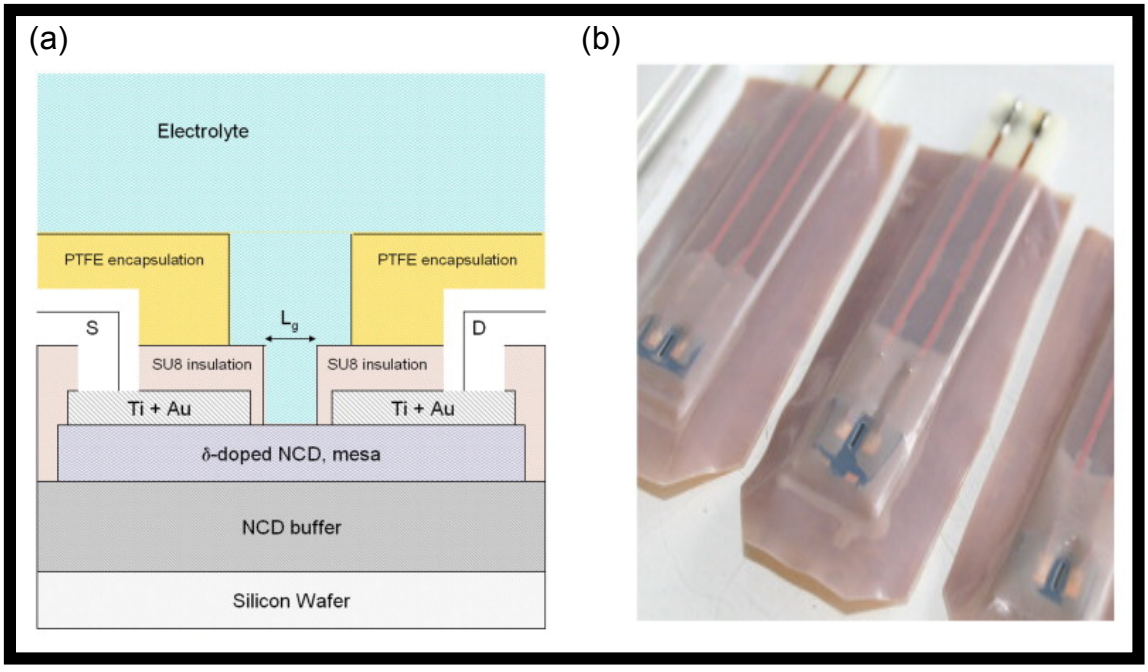

Figure 3.9: (a) Schematic cross section of the ISFET structure on nano-crystalline diamond, (b) Photograph of packaged ISFETs [68].

The O-termination by combination of oxygen-plasma and wet chemical treatments resulted in a pH sensitivity (60 mV/pH) of the ISFETs close to the

Nernst's limit in the range between pH1 and pH13. Current modulation is 50% and there is a very subtle display of non-linearity in the output characteristics. The ISFET characteristics were stable even after anodic treatment in KOH. This allows using nano-crystalline diamond ISFETs with O-termination also as electrodes and even at anodic overpotentials [68].

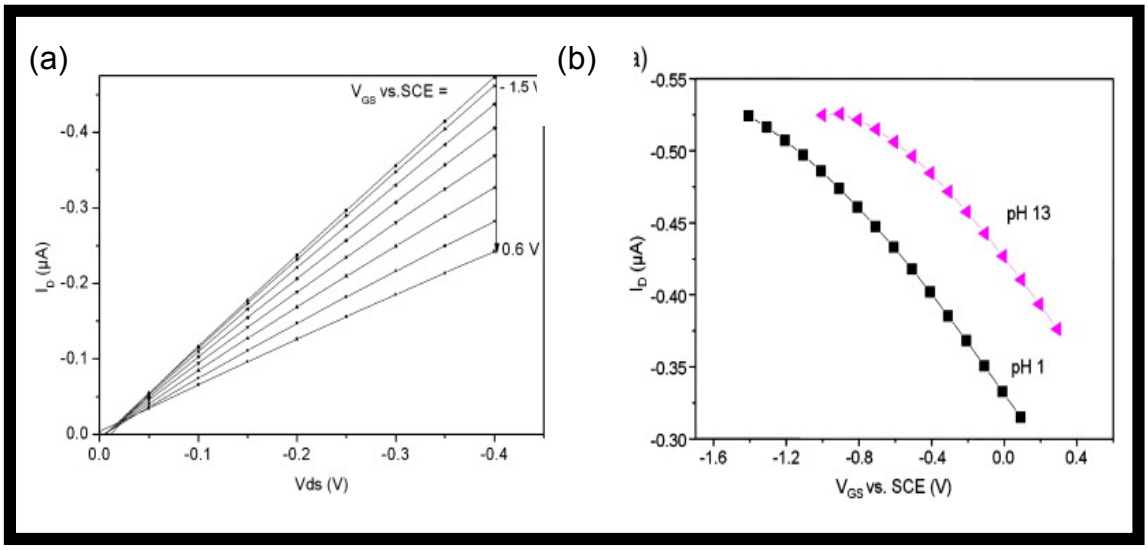

Figure 3.9: (a) Output characteristic of boron δ-doped nanodiamond ISFET with gate length 200 μm, gate width 2.5 mm in 0.1 M H_2SO_4. The gate-source bias is referenced vs. SCE. (b) a) Transfer characteristics at V_{DS} = − 0.5 V of boron δ-doped nanodiamond ISFET in pH1 and pH13.

3.5 Diamond MEMS–Cantilevers

Diamond materials offer great potential for many MEMS and NEMS applications. Amongst the attractive technological properties of diamond materials are the high stiffness, thermal conductivity, optical transparency range, chemical stability and erosion resistance, and dopant controlled variable electrical resistivity. Thin-film diamond offers enhanced mechanical properties, including significantly higher stiffness, strength, hardness, thermal conductivity, and chemical robustness, versus silicon and most other thin-film materials commonly used in microfabrication technologies. Furthermore, the surface chemistry of thin-film diamond lowers the friction and stiction properties of the contracting surfaces in MEMS structures and, thereby,

overcomes a significant reliability problem in many surface micromachined MEMS devices. (MEMS application using thin film diamond) [69]

The friction coefficient of diamond is exceptionally low (0.1–0.01), and the projected wear life is 10 000 times greater than that of Si, making diamond, in principle, an ideal tribomaterial for MEMS components [70,71]. Lubrication poses a major limitation on the design of MEMS devices since the usual methods of delivering lubricant to the interface between contacting parts are very difficult to implement. Additionally, the viscosity of liquid lubricants is sufficient to prevent motion of MEMS components. Diamond is naturally hydrogen or oxygen-terminated, and the passivated surface provides a natural lubricant. [72].

Microcrystalline diamond film application in MEMS have been investigated with structures such as cantilevers, bridge [73], free-standing diamond strings and diamond-based acceleration sensors [74] fabricated. However, the mechanical properties are complicated and not reproducible as well as not being fully understood [75]. Nanocrystalline diamond films whereas have been shown to have high optical quality, high thermal conductivity and a Young's modulus nearly that of single crystal diamond [76]. The nanocrystalline diamond films ranges in thickness from 100 nm to 5 microns sitting on Si based substrates, typically an oxide. The fabrication of the MEMS and NEMS structures are initiated using optical or electron-beam lithography for pattern definition. The pattern is then transferred onto the diamond film using a CF_4/O_2 reactive ion etch with the diamond films protected by a layer of hard mask made of Cr or Al. After removal of the mask, the structures are released in a buffered hydrochloric acid, which removes the underlying oxide layer [76].

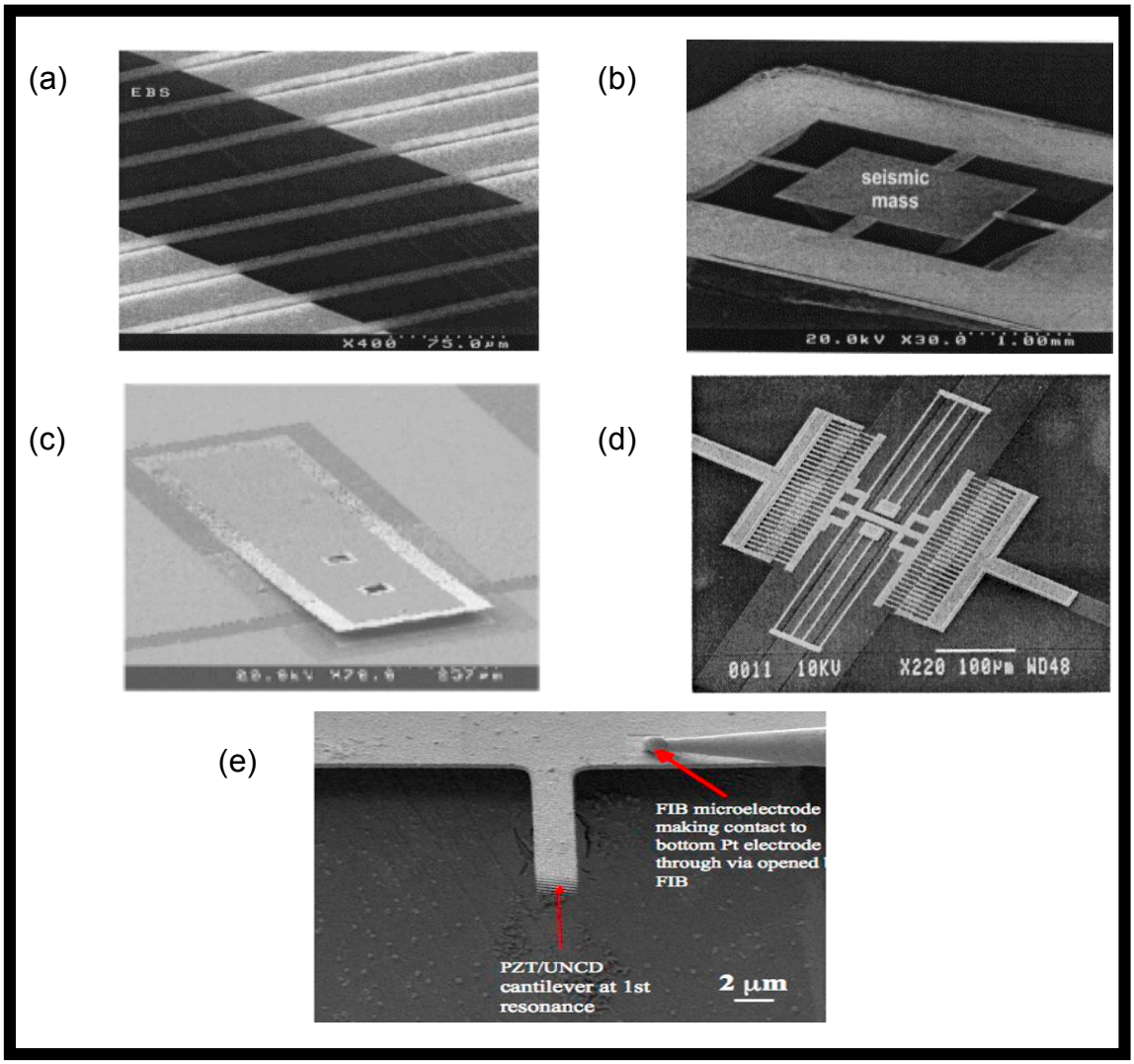

Figure 3.10: (a) Polycrystalline diamond MEMS free-standing diamond strings, (b) acceleration sensor [74] and (c) microswitch device [75] (d) nanocrystalline folded beam MEMS resonator [76], (e) PZT/UNCD MEMS cantilever [77]

Auciello *et al* employed a focused ion beam FIB system with a 30 keV Ga^+ ion beam to define the cantilevers horizontal dimensions on a ~1 µm thick UNCD layer on a Si-100 substrate. Wet-etching the underlying base layer similarly does the release of the cantilever structures [77].

Three-dimensional microstructures including a cantilever have been fabricated in single crystal diamond with a Focused Ion Beam (FIB) assisted lift-off technique [78]. The fabrication method is based on MeV ion implantation, followed by FIB micropatterning and selective chemical etching.

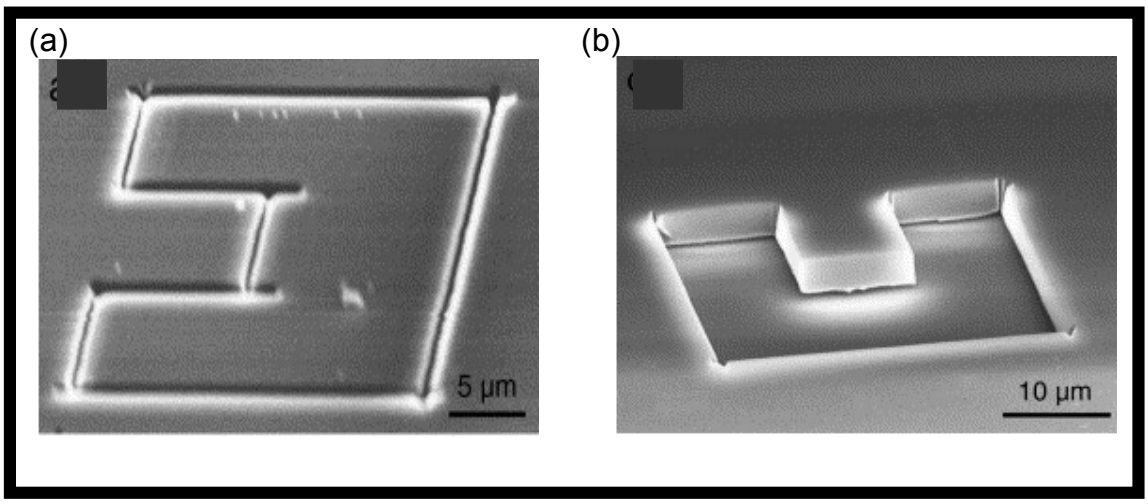

Figure 3.11: SEM images of micro-structures machined in single crystal diamond (a) FIB-patterned regions for the fabrication of a cantilever and (b) the three-dimensional structures in the same samples after the completion of the lift-off step [78].

The crystals were cut and polished from large single-crystals which were synthesized under ultra-high pressure and temperature (HPHT). All sides of the sample have (100) face orientation, and the crystal is classified as type Ib. The nuclear collisions creating lattice defects occur mainly at the end of range of the implanted ions [79], leaving the surface intact. Following ion irradiation, the implanted regions were patterned with a focused 30 keV Ga^+ ion beam. The FIB was employed to mill trenches with sub-micron width, which connected the buried highly damaged layer to the sample surface in shapes defined by the ion beam lithography system. After the FIB patterning, the samples were thermally annealed at a temperature of 550 °C in air for 1 h. When the damage density is above a critical threshold, the diamond crystal structure cannot be recovered upon thermal annealing [80] and [81]. Thus, after annealing, a heavily damaged layer buried at the end of ion range, converts to a non-diamond phase, while in the other regions the crystal structure is partially restored. After the sacrificial buried layer was exposed to the sample surface through the milled trenches, the samples were etched for 1 h in boiling acid (1 : 1 : 1 H_2SO_4 / $HClO_4$ / HNO_3). Buried non-diamond regions connected to a trench, but otherwise covered by diamond, were etched. This allowed unconnected surface layers to lift off, leaving behind the desired cantilever structure, which may include undercut regions [78].

3.6 References:

[1] J. F. Prins, *Appl. Phys. Lett., 41:950 (1982)*

[2] M. W . Geis, D. D. Rathman, D. J. Ehrlich, R. A. Murphy, W. T. Lindley, *IEEE Electron Dev. Lett,, 8341* (1987)

[3] M. W. Geis, *Proc. IEEE, 79:669* (1991)

[4] K. L. Moazed, R. Nguyen, J. R. Zeidler, *IEEE Electron Dev. Lett., 9:350* (1988)

[5] K.L. Moazed, J.R. Zeidler, M.J. Taylor, J, *Appl. Phys.,* 68:2246 (1990)

[6] F. Fang, C.A. Hewett, M.G. Fernandes, S.S. Lau, *IEEE Trans. Electron Dev. 36:1783* (1989)

[7] M.W. Geis, M. Rothschild, R.R. Kunz, R.L. Aggannrall, K.F. Wall, C.D. Parker, K.A. McIntosh, N.N. Efremow, J.J. Zayhowski, D.J. Ehrlich, J.E. Butler, *Appl. Phys. Lett., 552295* (1989)

[8] K. Nishimura, K. Das, M. Iwase, J.T. Glass, K. Kobashi, *Diamond, Silicon Canbide and Related Wide Bandgap Semiwnductors and* (J. T. Glass, R. Messier, and N. Fujimori, eds.), Mat. Res. Soc. Symp. Proc., 162347, Mat. Res. Sot., Pittsburgh (1990)

[9] C.B. Childs, W.K. Chu, US patent application (1989)

[10] C.B. Childs, G.S. Sandhu, W.K. Chu, presented at the 4th SDIO/IST-ONR Diamond Tech. Initiative Symp., Crystal City, Virginia, July (1989)

[11] G.S. Sandhu, Ph.D. thesis, University **of** North Carolina at Chapel Hill (1989)

[12] J.F. Prins, J. Whys., *D: Appl. Phys. 22:1562* (1989)

[13] G. Braunstein, R. Kalish, J. *Appl. Phys., 54:2106* (1983)

[14] J.F. Prins, *Phys. Rev. B, 38:5576* (1988-I)

[15] V. Venkatesan, K. Das, *IEEE Electron Dev. Lett., 13:126* (1991)

[16] G.A. Kim, U. S. Patent number 4,643,161 (1987)

[17] M. Yokoba, Y. Koida, A. Otsuki, F. Ako, T. Oku, M. Murakami, Volume 81, Journal of Applied Physics, Issue 10, pp.6815-6821, May 15 (1997)

[18] D.Doneddu, O.J. Guy, P.R. Dunstan, T.G.G. Maffeis, K.S. Teung, S.P. Wilks, P.Igic, P. Twitchen, R.M. Clement, Surface Science 602, 1135-1140 (2008)

[19] E.C. Lightowlers, A.T. Collins, J. Whys. *D : Appl. Phys., 9:73* (1976)

[20] G.H. Glover, *Solid St. Elect.,* 16:973 (1973)

[21] S.A. Grot, G.S. Gildenblat, C.W. Hatfield, C.R. Wronski, A.R. Badzian, T. Badzian, R. Messier, IEEE Electron *Dev. Lett.,* 11:100 (1990)

[22] H. Shiomi, H. Nakahata, T. Imai, Y. Nishibayashi, N. Fujimori, *Jpn. J. Appl. Phys.,* 28:758 (1989)

[23] G.S. Gildenblat, S.A. Grot, C.R. Wronski, A.R. Badzian, T. Badzian, R. Messier, App. *Phys. Lett. 53:586* (1988)

[24] Y. Mori, H. Kawarada, A. Hiraki, *Diamond, Silicon Carbide and Related WideBandgap Semiconductors,* (J. T. Glass, R. Messier, and N. Fujimori, eds.), Mat. Res. Soc. Symp. Proc. 162:353 (1990)

[25] D. G. K. Jeng, H.S. Tuan, R.F. Salat, G.J. Fricano, *Proc. 2nd Intl. Conf. Electronic Mat.,* (R. P. H. Chang, M. Geis, B Meyerson, D. A. B. Miller, and R. Ramesh, eds.), p. 577, Mat. Res. Soc., Pittsburgh (1990)

[26] K. Nishimura, K. Das, J.T. Glass, J. *Appl Phys.,* 69:3142 (1991)

[27] K. Miyata, Y. Matsui, K. Kumagai, S. Miyauchi, K. Kobashi, A. Nakaue, Proc. 2nd Int. Conf. *New Diamond Sci. Tech., (R.* Messier, J. T. Glass, J. E. Butler, and R. Roy, eds.), p. 981, Mat. Res. Soc., Pittsburgh (1991)

[28] H. Shiomi, Y. Nishibayashi, N. Fujimori, *Proc. 2nd Int. Conf. New Diamond Sci. Tech.,* (R. Messier, J. T. Glass, J. E. Butler, and R. Roy, eds.), p. 975, Mat. Res. Soc., Pittsburgh (1991)

[29] K. Miyata, D.L. Dreifus, K. Das, J.T. Glass, K. Kobashi, Electrochem. Soc. Meeting, Washington, D. C., May 6 - 10 (1991)

[30] V. Venkatesan, K. Das, D.L. Dreifus, J.T. Glass, G.G. Fountain, R.A. Rudder, J.B. Posthill, R.J. Markunas, Electrochem. Soc. Meeting, Washington, D. C., May 6 - 10 (1991)

[31] T.P. Humphreys, J.V. LaBrasca, R.J. Nemanich, K. Das, J.B. Posthill, *Jpn. J. Apple Phys.,* 30:L1409 (1991)

[32] K. Das, K., unpublished work (1990)

[33] T.P. Humphreys, J.V. LaBrasca, R.J. Nemanich, K. Das, J.B. Posthill, *Electron. Lett.,* 27:1515 (1991)

[34] S.R. Sahaida, D.G. Thompson, in Mater. Res. Soc. Symp. Proc., (T. D. Moustakos, J. I. Pankoveand, Y. Hamakawa, eds.), (1992)

[35] G.H. Glover, *Solid St. Elect.,* 16:973 (1973)

[35] C.A. Mead, T.C. McGill, Phys. Lett. 58A:249 (1976)

[36] F.J. Himpsel, P. Heimann, D.E. Eastman, *Solid State Comm.* 36:631 (1980)

[37] N. Fujimori, T. Imai, A. Doi, *Vacuum, 36:99* (1986)

[38] M.C. Hicks, C.R. Wronski, S.A. Grot, G.S. Gildenblat, A.R. Badzian, T. Badzian, R. Messier, *J. Appl. Phys.,* 65:2139 (1989)

[39] C.P. Beetz, Jr., B.A. Lincoln, D.Ft. Winn, Diamond Optics III (A. Feldman and S. Holly, ed.) 1325:241, SPIE (1990)

[40] G.S. Gildenblat, G. A. Grot, C.W. Hatfield, A.R. Badzian, *IEEE Electron Dev. Lett,* 12:37 (1991)

[41] G.G. Fountain, R.A. Rudder, D.P. Malta, S.V. Hattangady, R. Alley, G.C. Hudson, J.B. Posthill, R.J. Markunas, T.P. Humphreys, R.J. Nemanich, V. Venkatesan, K. Das, Electrochem. Soc. Meeting, Washington, D. C., (May 6 - 10, 1991)

[42] C. Zeisse IX, C.A. Hewett, R. Nguyen, J.R. Zeidler, R.G Wilson, IEEE *Electron Dev. Lett.,* 12:602 (1991)

[43] W. Tsai, M. Delfino, D. Dodul, M. Riaziat, Y. Chiang, G. Reynolds, C.B. Cooper III, *IEEE Electron Dev. Lett.,* 12:157 (1991)

[44] M.W. Geis, N.N. Efremow, D.D. Rathman, *J. Vac. Sci. Tech.,* A6:1853 (1988)

[45] L.Y.S. Pang, S.S.M. Chan, R.B. Jackman, C. Johnston, and P.R. Chalker, Appl. Phys. Lett. 70, 339 (1997);

[46] A. Vescan, P. Gluche, W. Ebert, E. Kohn, *IEEE Electron Device Lett.,* 18, 556, (1997)

[47] K. Hayashi, S. Yamanaka, H. Okushi, K. Kajimura, *Appl. Phys. Lett.,* 68**,** 376 (1996)

[48] H.J. Looi, R.B. Jackman, J.S. Foord, *Appl. Phys. Lett.,* 72, 353 (1998)

[49] Y. Mizuoshi, H. Nagasawa, H. Kawarada, *Diam.Relat.Mater.,* 6, 277 (1997)

[50] H.Y. Looi, L.Y.S. Pang, Y. Wang, M.D. Whitfield, R.B. Jackman, *IEEE Electron Device Lett.,* 19, 112 (1998)
[51] H. Umezawa, H. Taniuchi, H. Ishizaka, T. Arima, N. Fujihara, M. Tachiki, H. Kawarada, IEEE Electron Device Letters, Vol. 23, No. 3, March (2002)
[52] S. Miyamoto, H. Matsudaira, H. Ishizaka, K. Nakazawa, H. Taniuchi, H. Umezawa, M. Tachiki and H. Kawarada**,** Diamond and Related Materials Volume 12, Issues 3-7 (2003)
[53] T. Saito, K. Park, K. Hirama, H. Umezawa, M. Satoh, H. Kawarada, H. Okushi, Diamond & Related Materials, 14, 2043 – 2046 (2005)
[54] H. Matsudaira, A. Takuya, H. Umezawa, S. Miyamoto, H. Ishizaka, M. Tachiki, H. Kawarada, Diamond and Related Materials, Volume 12, No. 10, 1814-1818(5), October (2003)
[55] K. Hirama, Y. Jingu, M. Ichikawa, H. Umezawa, H. Kawarada, Silicon Carbide and Related Materials , Materials Science Forum, (Vol. 600 - 603), 1349-1351, (2007)
[56] H.J. Looi, L.Y.S. Pang, Y. Wang, M.D. Whitfield,R.B. Jackman, IEEE Electron Device Letters, Vol. 19, No. 4, April (1998)
[57] A. Aleksov *et al*, IEEE - EDL, 23(8), p488 (2002)
[58] M. Schwitters, M.P. Dixon, A. Tajani, D.J. Twitchen and S.E. Coe, H. El-Haji, M. Kubovic, M. Neuburger, A. Kaiser and E. Kohn, 2nd EMRS DTC Technical Conference – Edinburgh 2005
[59] H. El-Hajj, A. Denisenko, A. Kaiser, R.S. Balmer and E. Kohn, Diamond and Related Materials, Vol. 17, Issue 7-10, p.1259-1263, July-October (2008)
[60] J.A.Garrido, A.K. Hartl, M.S. Stutzmann, O.A. Williams, R.B. Jackman, Appl. Phys. Lett. 86, 073504 (2005)
[61] O. A. Williams and R. B. Jackman, Semicond. Sci. Technol. **18**, S34 (2003)
[62] B. Rezek,1, D. Shin, H. Watanabe, C. E. Nebel, Sensors and Actuators B 122, 596–599, (2007)
[63] B. Rezek, J. Garrido, C.E. Nebel, M. Stutzmann, E. Snidero and P. Bergonzo, *Phys. Status Solidi A* 193**,** p. 523, (2002)
[64] S.G. Ri, T. Mizumasa, Y. Akiba, Y. Hirose, T. Kurosu and M. Iida, *Jpn. J. Appl. Phys.* 34**,** p. 5550, (1995)

[65] F. Maier, M. Riedel, B. Mantel, J. Ristein and L. Ley, *Phys. Rev. Lett.* 85, p. 3472, (2000)

[66] D. Shin, H. Watanabe and C.E. Nebel, *J. Am. Chem. Soc.* 127**,** p. 11236, (2005)

[67] A. Denisenko, G. Jamornmarn, H. El-Hajj, E. Kohn, Diamond & Related Materials,16, 905–910, (2007)

[68] M. Dipalo**,** C. Pietzka**,** A. Denisenko**,** H. El-Hajj and E. Kohn**,** Diamond and Related Materials, Vol. 17, Issues 7-10, p. 1241-1247, July-October (2008)

[69] M.A. Huff, D.A. Aidala, J.E. Butler, MEMS applications using diamond thin films, Solid State Technology, vol. 49, issue 4 (2006)

[70] M.N. Gardos In: B. Bushan, Editor, *Tribology Issues and Opportunities in MEMS*, Kluwer Scientific Publishers, The Netherlands, p. 341, (1998)

[71] M.N. Gardos *Surf. Coat. Technol.* 113**,** p. 183, (1999)

[72] A. R. Krauss, O. Auciello, D. M. Gruen, A. Jayatissa, A. Sumant, J. Tucek, D. C. Mancini, N. Moldovan, A. Erdemir, D. Ersoy, M. N. Gardos, H. G. Busmannf, E. M. Meyerg and M. Q. Ding, Diamond and Related Materials, Vol. 10, Issue 11, p. 1952-1961, November (2001)

[73] J.L. Davidson, R. Ramesham and C. Ellis. J. Electrochem. Soc. 137, pp. 3206–3210, (1990)

[74] E. Kohn, P. Gluche and M. Adamschik, Diamond and Related Materials Volume 8, Issues 2-5, Pages 934-940, March (1999)

[75] P. Schmid, M. Adamschik, S. Ertl, P. Gluche, E. Kohn, "Modelling Approach for CVD-Diamond based mechanical structure", *Proceedings of the Second International Conference on Modeling and Simulation of Microsystems, San Juan,* pp. 636–639, *April* (1999)

[76] J.E. Butler, T. Feygelson, L. Sekaric, H. Craighead, J. Wang and C.T.-C. Nguyen, Technical Proceedings of the 2003 Nanotechnology Conference and Trade Show, Vol. 1, Chpt. 12, p. 560 (2003)

[77] S. Srinivasan, J. Hiller, B. Kabius', O. Auciello, Applied Physics Letters 90, 134101 (2007)

[78] P. Olivero, S. Rubanov, P. Reichart, B.C. Gibson, S.T. Huntington, J.R. Rabeau, Andrew D. Greentree, J. Salzman, D. Moore, D.N. Jamieson and S.

Prawer, Diamond and Related Materials, Volume 15, Issue 10, p. 1614-1621, October (2006)

[79] M.B.H. Breese, D.N. Jamieson and P.J.C. King, Material Analysis Using a Nuclear Microprobe, John Wiley and Sons Inc, New York (1996).

[80] N.R. Parikh, J.D. Hunn, E. McGucken, M.L. Swanson, C.W. White and R. Zuhr, Laser and Ion Beam Modification of Materials, Elsevier Science Publishers B.V, Amsterdam (1994).

[81] C. Uzan-Saguy, C. Cytermann, R. Brener, V. Richter, M. Shaanan and R. Kalish, *Appl. Phys. Lett.*, 67, p. 1194, (1999)

Chapter 4

Experimental Methods

4.1 Substrate cleaning and preparation

The purpose of this treatment is to remove any graphite and other non-diamond carbon from the surface of a sample as a prelude to device fabrication with high levels of stability. This surface cleaning process was developed in UCL in 1994 [1]. The method described here using strongly oxidizing solutions involving ammonium persulfate – sulfuric acid generates low concentration of surface sulfur together with an oxide phase. It was reported that this cleaning technique produces the Auger features of polycrystalline diamond surfaces resembling those of single crystal material [1] thus suggesting this treatment may offer better performance when used during fabrication of diamond electronic devices.

Essentially, the cleaning process can be broken down to the following stages such as the initial de-greasing, acid bath stage, rinsing and the final de-greasing. The collection of chemicals includes the degrease solvents, acids and bases such as 1,1,1 trichloroethane, acetone, 2-propanol (isopropanol, IPA), sulphuric acid (H_2SO_4), ammonium persulphate ($(NH_4)_2S_2O_8$), hydrogen peroxide (H_2O_2) and ammonium hydroxyde (NH_4OH). It should be noted that all processes here are to be carried out in a fume cupboard.

4.1.1 Initial de-grease

1. Sample is submerged in a warm Trichloroethane solution at 60^{o}C for 5 minutes.
2. Full immersion in Acetone, followed by in IPA and drying by N_2 at room temperature.
3. Place the sample on a hotplate at 85^{o}C for 5 minutes to remove moisture from the surface.
4. Cool the sample down to room temperature.

It is critical to prevent the solvent from forming a residual layer on the sample surface, which is insoluble in the solvent in the following cleaning stage.

4.1.2 Acid bath process

1. Mixing the Etching Solution:
    i. Measure 30ml concentrated Sulphuric Acid (H_2SO_4) into a clean glass “sugar bowl”
    ii. Add about 6 teaspoons of Ammonium Persulphate ($(NH_4)_2S_2O_8$) to create a super-saturated solution.
    iii. The sugar bowl must be covered with a lid.
2. Mixing the Rinse solution:
    i. 10ml Hydrogen Peroxide (H_2O_2) into a glass dish
    ii. 10 ml Ammonium Hydroxide (NH_4OH)
    iii. The sugar bowl must be covered with a lid
3. The lid is removed from the Etching solution and the bowl is placed in the heater set to 200^oC
4. When the temperature reaches 85^oC, the diamond sample is dropped in the Etching solution
5. The temperature is kept at ~ 200^oC, a 20 minute countdown is initiated
6. At the end of the 20 minute countdown, the heater is turned off and the solution must be allowed to cool down to ~50^oC.
7. The diamond sample is transferred to the Rinse solution and for a period of 10 minute. Extra care is needed as there will be some heavy fizzing as the acid is neutralized.
8. The diamond sample is rinsed in de-ionized (DI) water and blow-dried with N_2
9. The de-greasing method is repeated as the final stage.

4.2 Lithography

It is defined as the process of transferring shapes or patterns onto substrates or materials. The process generally employs a pre-fabricated mask of which the shape or pattern is derived from.

The simplest form of lithography is the use of a shadow-mask which simply is a solid thin piece of metal with apertures defining the desired patterns. The window on the mask allows the deposition of a layer of new material typically metal electrical contacts or protective masks for etching. The diagram below illustrates the process of shadow-mask based lithography technique.

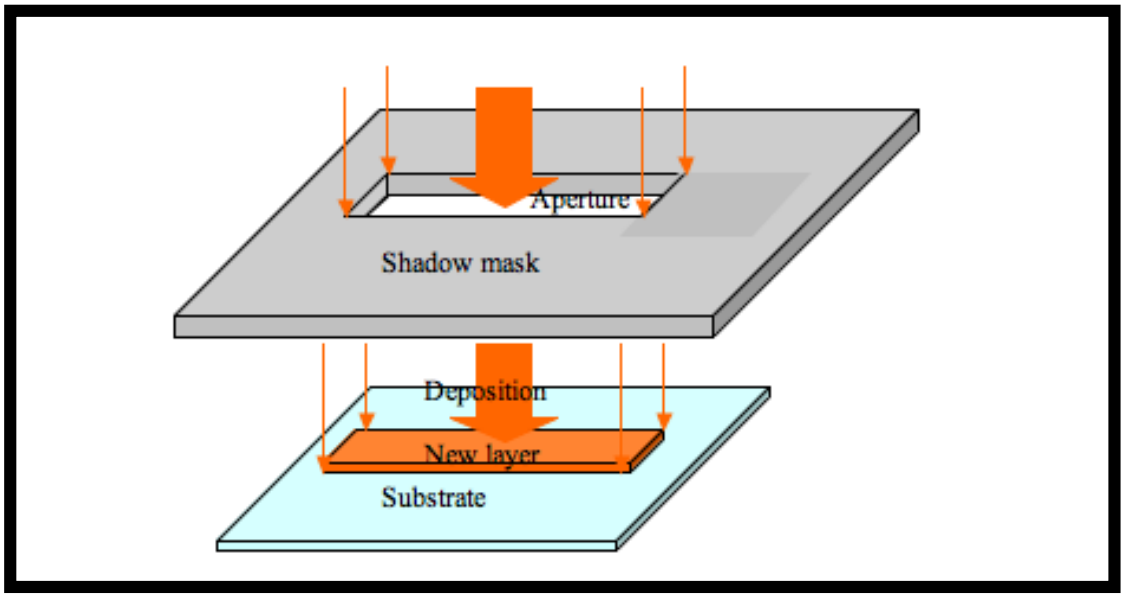

Figure 4.1: Shadow-mask based lithography technique.

4.3 Metal contacts deposition

The technique used is here is fundamentally called the filament evaporation where metals are raised to their melting point in vacuum by resistive heating. Typically, metal pieces are placed on a filament that acts as a resistor as shown in the diagram below.

The metal pieces give off a vapor and the atoms travel in a straight line away from the source until they strike the target sample. The heating filament that accommodates the metal source comes in 3 basic shapes spiral, basket and boat, are made from refractory metals such as tungsten (for the first two design) or molybdenum (for the boat). The start and stop of the deposition is controlled by a mechanical shutter which is in turn can be controlled automatically by presetting the machine or manually at a push of a button. Evaporation takes place in a vacuum, typically at chamber pressure between

~ 10^{-7} to 10^{-6} mbar i.e. vapors other than the source material are almost entirely removed before the process begins. In high vacuum (with a long mean free path), evaporated particles can travel directly to the deposition target without colliding with the background gas [2].

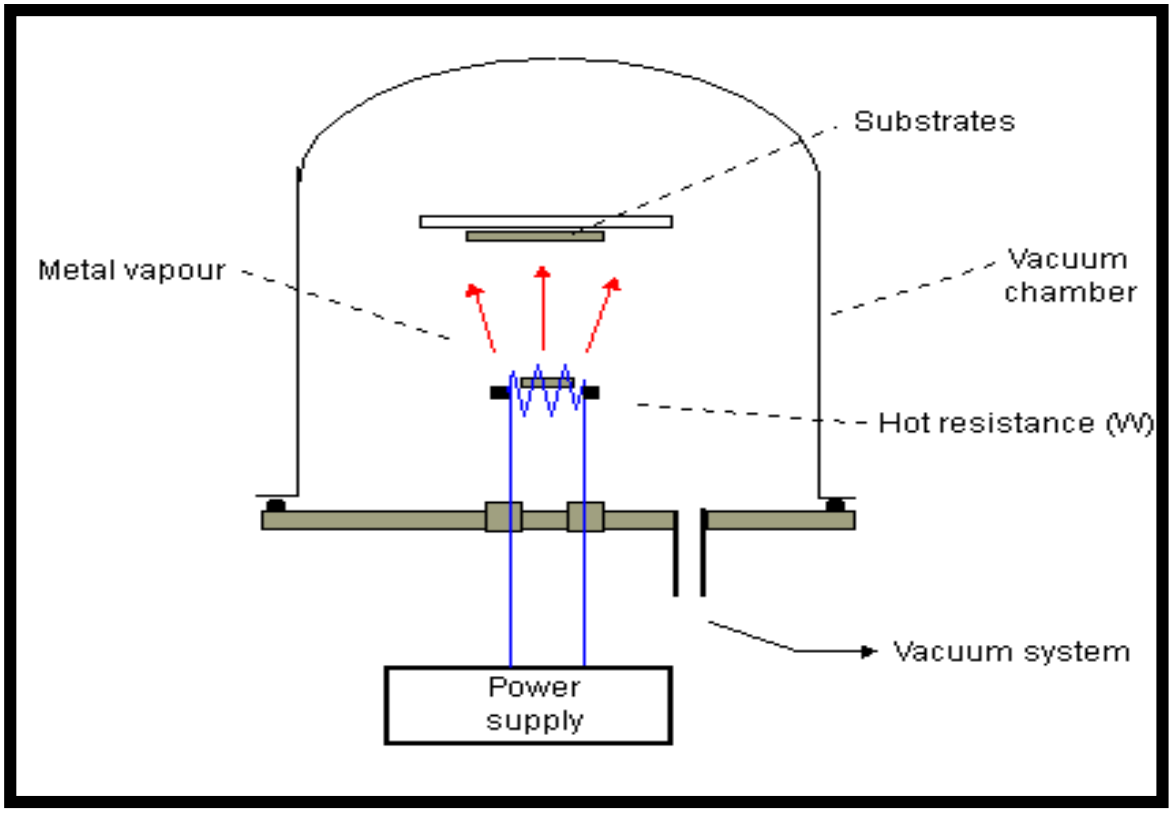

Figure 4.2: Schematic diagram of thermal evaporator system [3]

The system in use here is the Thermal Evaporator II Bell Jar A306 allowing metals such as Cr, Au, Ag, Ni, Al, Ti, Sn & Ge to be deposited on target substrates.

4.4 Reactive Ion Etching

Dry etching generally uses plasma, which are partially ionized gases to etch the target area. Plasma-based etching requires Radio Frequency (RF) power to activate the chemical reactions for removal of a surface of a material. Plasma is a collection of equal free moving electrons and ions. It is considered to be the fourth state and the most common form of matter. An

ion-electron pair is continuously created and destroyed by ionization and recombination respectively. A lot of energy (thermal, electrical, or ultra violet and visible light) is needed to remove the electrons from the atoms to form plasma and without sufficient energy, plasma recombine into neutral gas. Plasma can be accelerated and manoeuvred by electrical and magnetic fields where it can be controlled.

Reactive Ion Etching (RIE) is a method of dry etching and is defined as plasma etching under conditions where the etched surface is subjected to energetic (i.e. greater than about 50eV) positive ion bombardment. The main purpose of RIE is to create an anisotropic etch where the etch will be uni-directional. When plasma is formed by the applied RF potentials, the gas molecules are broken down into a number of fragments and radicals. A significant number of these molecular fragments may become ionized in the plasma and may be accelerated to the various electrode surfaces within the discharge chamber. In many cases, ion bombardment is very useful in maintaining the directionality, or anisotropy, of the etching process. There are two parts of reactive ion etching; chemical and physical. In the former, the sample substrate is placed inside a chamber reactor where several gases are introduced, depending on the recipe. An RF power source strikes the plasma in the gas mixture; breaking the gas particles into ions. The ions are then accelerated towards the surface of the material being etched, which in this case is diamond and reacts with the surface forming another sort of gaseous material.

It is a very intricate task to develop dry etching processes that balance chemical and physical etching, since there are a number of parameters to adjust. By changing the balance it is possible to manipulate the anisotropy of the etching, since the chemical part is isotropic and the physical part is highly anisotropic, the combination of both can form sidewalls that have shapes from rounded to vertical. An anisotropic etch is vital for high-fidelity pattern transfer. A hard mask which has a much slower etch rate then the material being etched is used to protect certain areas from etching, exposing only the concentrated areas desired to be etched.

Specifically, the technique employed in the research activities outlined in this thesis is called the inductively coupled reactive ion etching (ICP-RIE). The plasma is contained inside a chamber, which is induced by an inductive coil wrapped around a quartz chamber. The RF coils located in front of the RF transducer induces an alternating magnetic field, and this helps to produce high-density plasma due to confinement of electrons and ions. Very high plasma densities typically in the range of 10^{15} cm^{-3} can be achieved, though etch profiles tend to be more isotropic. However, an RF source or DC bias can be applied onto the sample stage to extract and accelerate the reactive species from the plasma to achieve anisotropy and deep etching. An ICP etching system requires the use of two RF power sources usually at 13.56 MHz, the ICP that creates and enhances the amount of reactive gases in the chamber and one that forms the plasma potential at the surface of the substrate. Hence, control over the coil (ICP) and platen (substrate biasing) power determines the etch rate and degree of anisotropy [4].

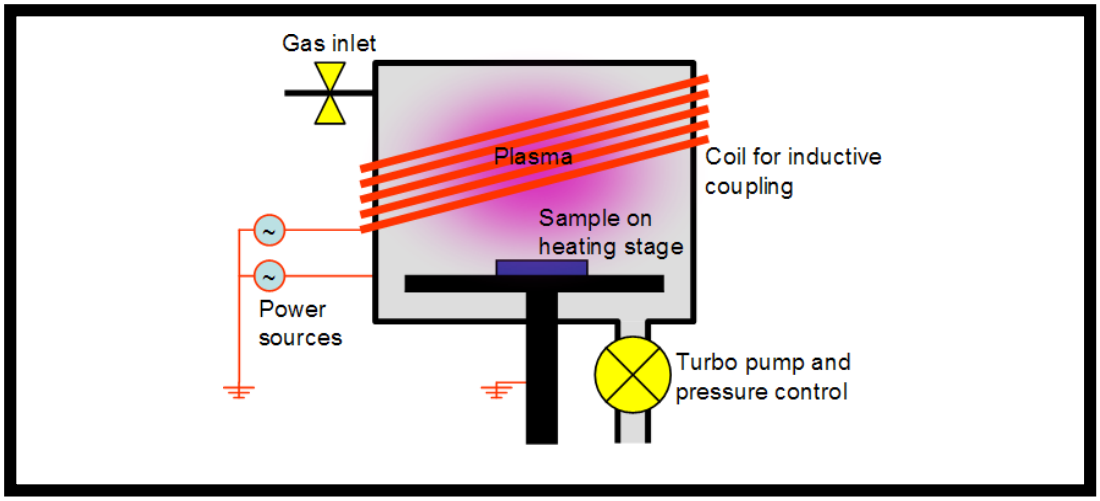

Figure 4.3: Schematic diagram of an ICP-RIE system [4]

4.5 Current-Voltage Characterisation

The relationship between charge carrier flow through an electronic device under the influence of an external DC potential applied between its terminals is called the current-voltage characteristics. It is prevalently used to determine the device basic parameters and model its behaviour in electrical circuits.

Electronic devices will each have a single or a set of signature I-V characteristics. The simplest version being that of the 2-terminal resistor whereby the current varies linearly with the applied voltage, following Ohm's Law. Devices such as the transistor having more than 2 terminals will exhibit a current dependency on more than one terminal voltage difference. Typical I-V characteristics of a resistor (ohmic), diode (rectifying) and transistor are shown in the diagrams below.

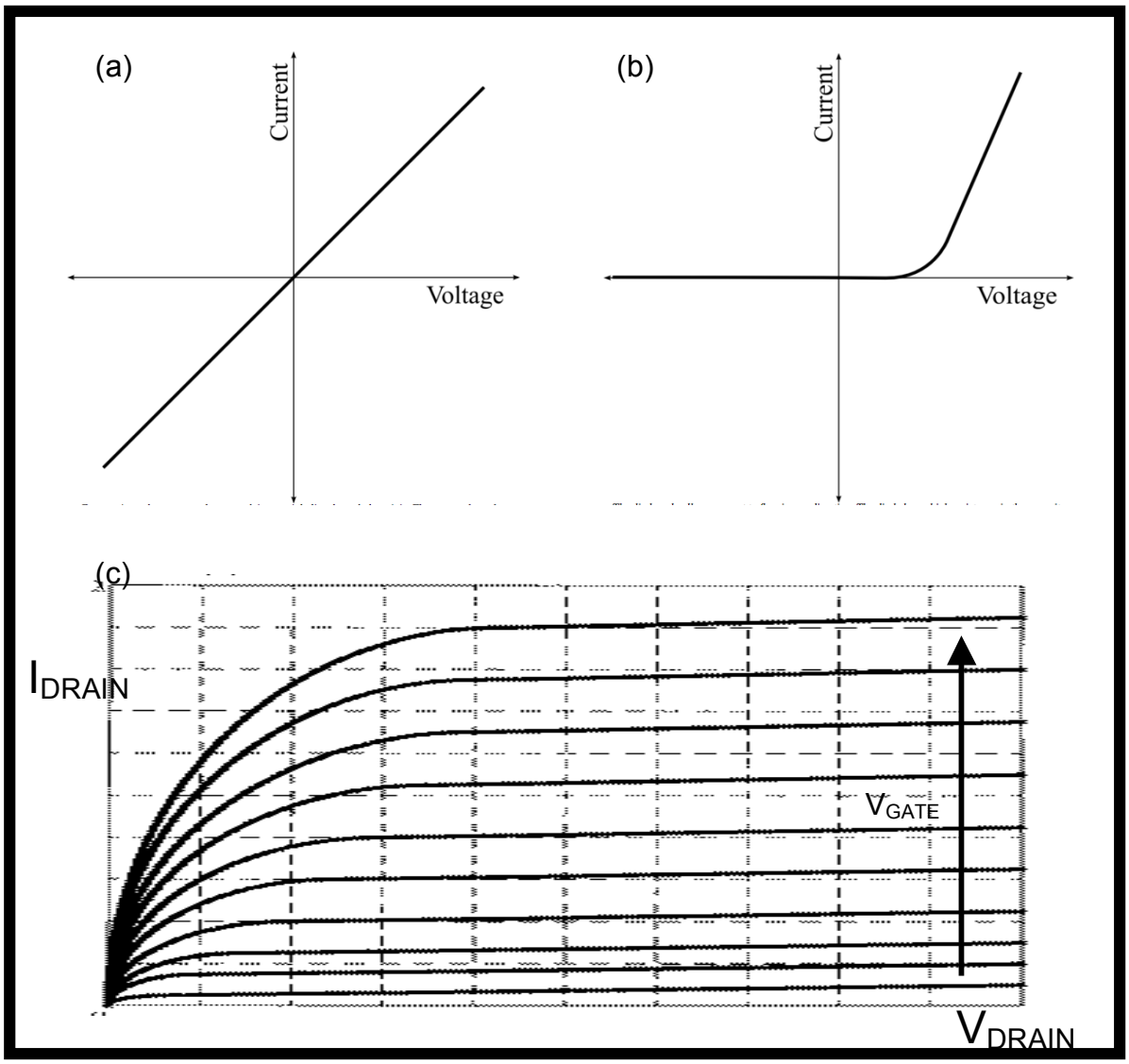

Figure 4.4: I-V characteristic of (a) a linear device (resistor) (b) a non-linear device (diode) [5] and (c) a field effect transistor [6]

4.6 Cyclic Voltammetry

Cyclic voltammetry (CV) has become an important and widely used electroanalytical technique in many areas of chemistry. It is rarely used for quantitative determinations, but it is widely used for the study of redox processes, for understanding reaction intermediates, and for obtaining stability of reaction products. [7] In general, cyclic voltammetry is used to study the electrochemical properties of an analyte in solution [8-10] and is obtained by measuring the current as the potential is varied. Cyclic Voltammetry technique on the other hand is based on varying the applied potential at a working electrode in both forward and reverse directions (at some scan rate) while monitoring the current. For example, the initial scan could be in the negative direction to the switching potential. At that point the scan would be reversed and run in the positive direction. Depending on the analysis, one full cycle, a partial cycle, or a series of cycles can be performed [7].

The electrochemical cell, where the voltammetric experiment is carried out, consists of a working (indicator) electrode, a reference electrode, and usually a counter (auxiliary) electrode. The working electrode, which makes contact with the analyte, must apply the desired potential in a controlled way and facilitate the transfer of charge to and from the analyte. The reduction or oxidation of a substance at the surface of a working electrode, at the appropriate applied potential, results in the mass transport of new material to the electrode surface and the generation of a current. A second electrode with a known potential is used to gauge the potential of the working electrode, furthermore it must balance the charge added or removed by the working electrode. It is however extremely difficult for a single electrode to maintain a constant potential while passing current to counter redox events at the working electrode. Solving this problem, the role of supplying electrons and referencing potential has been divided between two separate electrodes. The reference electrode is a half-cell with a known reduction potential. Its only role is to act as reference in measuring and controlling the working electrodes

potential and at no point does it pass any current. The auxiliary electrode passes all the current needed to balance the current observed at the working electrode. To achieve this current, the auxiliary will often swing to extreme potentials at the edges of the solvent window, where it oxidizes or reduces the solvent or supporting electrolyte. These electrodes, the working, reference, and auxiliary make up the modern three-electrode system [8,11-14].

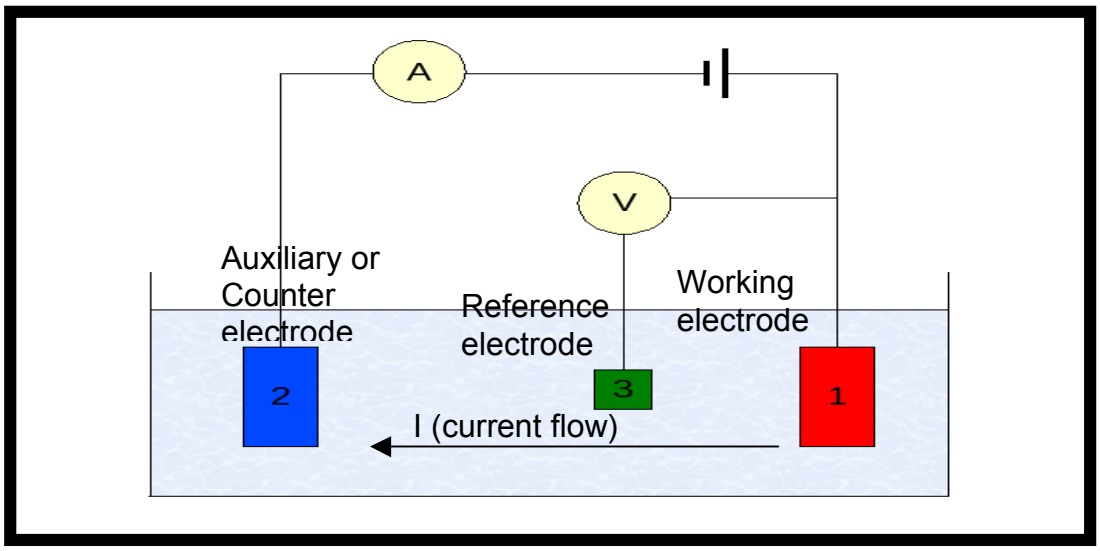

Figure 4.5: The 3-electrode system [15]

Analytical chemists routinely use voltammetric techniques for the quantitative determination of a variety of dissolved inorganic and organic substances. Inorganic, physical, and biological chemists widely use voltammetric techniques for a variety of purposes, including fundamental studies of oxidation and reduction processes in various media, adsorption processes on surfaces, electron transfer and reaction mechanisms, kinetics of electron transfer processes, and transport, speciation, and thermodynamic properties of solvated species [7]. In the absence of redox-active species in the electrolyte, the cyclic voltammetry technique is used to define the useable non-redox working range of applied external potential (potential window) of a working electrode (the active area of the diamond device). Such information is critical to ensure ISFET operation is biased without hitting both hydrogen and oxygen evolution overpotentials.

The basic components of a modern electroanalytical system for voltammetry are a potentiostat, computer, and the electrochemical cell. In some cases the potentiostat and computer are bundled into one package, whereas in other systems the computer and the A/D and D/A converters and micro-controller are separate, and the potentiostat can operate independently.

4.7 Mott-Schottky Plots

The interface between a semiconductor electrode and an electrolyte solution. In order for the two phases to be in equilibrium, their electrochemical potential must be the same. The electrochemical potential of the solution is determined by the redox potential of the electrolyte solution, and the redox potential of the semiconductor is determined by the Fermi level. If the redox potential of the solution and the Fermi level do not lie at the same energy, a movement of charge between the semiconductor and the solution is required in order to equilibrate the two phases. The excess charge that is now located on the semiconductor does not lie at the surface, as it would for a metallic electrode, but extends into the electrode for a significant distance (100- 10,000 Å). This region is referred to as the *space charge region*, and has an associated electrical field. Hence, there are two double layers to consider: the interfacial (electrode/electrolyte) double layer, and the space charge double layer [16].

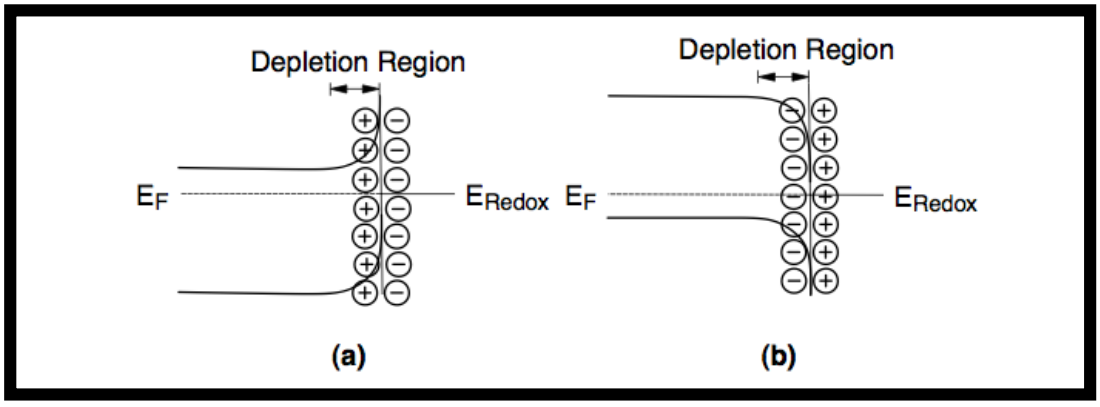

Figure 4.6: Band-bending of (a) n-type (b) p-type semiconductor at equilibrium with an electrolyte [16]

For an *n*-type semiconductor electrode at open circuit, the Fermi level is typically higher than the redox potential of the electrolyte, and hence electrons will be transferred from the electrode into the solution. Therefore, there is a positive charge associated with the space charge region, and this is reflected in an upward bending of the band edges **(**Figure 4.6a and 4.7ai**)**. Since the majority charge carrier of the semiconductor has been removed from this region, this region is also referred to as a *depletion* layer. For a *p*-type semiconductor, the Fermi layer is generally lower than the redox potential, and hence electrons must transfer from the solution to the electrode to attain equilibrium. This generates a negative charge in the space charge region, which causes a downward bending in the band edges (Figure 4.6b and 4.7ciii). Since the holes in the space charge region are removed by this process, this region is again a depletion layer. The band edges in the interior of the semiconductor (i.e., away from the depletion region) also vary with the applied potential in the same way as the Fermi level. However, the energies of the band edges at the interface are not affected by changes in the applied potential. Therefore, the change in the energies of the band edges on going from the interior of the semiconductor to the interface, and hence the magnitude and direction of band bending, varies with the applied potential. There are three different situations to be considered:

a) At a certain potential, the Fermi energy lies at the same energy as the solution redox potential (Figure 4.7(bi) and 4.7(bii)). There is no net transfer of charge, and hence there is no band bending. This potential is therefore referred to as the *flatband potential*, E_{fb}.
b) Depletion regions arise at potentials positive of the flatband potential for an *n*-type semiconductor (Figure 4.6(a) and 4.7(ai)) and at potentials negative of the flatband potential for a *p*-type semiconductor (Figure 4.6(b) and 4.7(cii)).
c) At potentials negative of the flat- band potential for an *n*-type semiconductor, there is now an excess of the majority charge carrier (electrons) in this space charge region, which is referred to as an *accumulation* region (Figure 4.7ci). An accumulation

region arises in a *p*-type semiconductor at potentials more positive than the flatband potential (Figure 4.7aii).

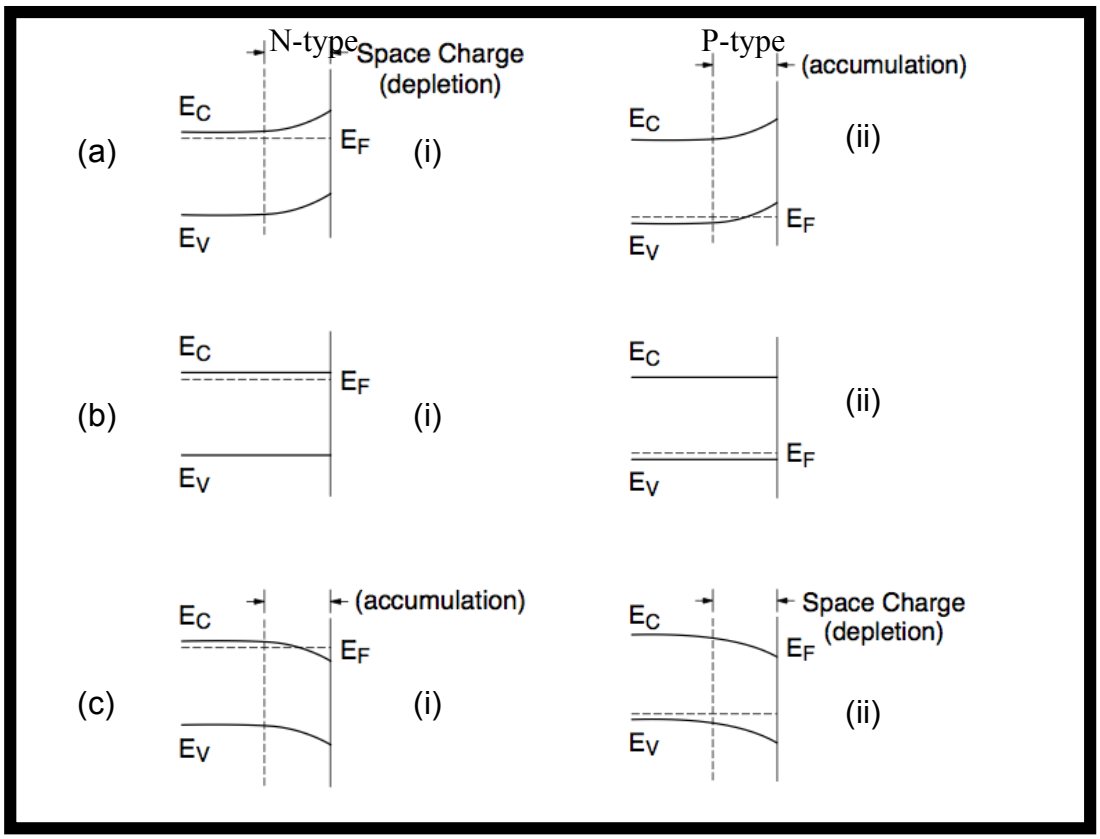

Figure 4.7 Effect of varying the applied potential (E) on the band edges in the interior of n-type and p-type semiconductor (a) E > Ef_b (b) E = E_{fb} (c) E < E_{fb}. [16]

The charge transfer abilities of a semiconductor electrode depend on whether there is an accumulation layer or a depletion layer. If there is an accumulation layer, the behavior of a semiconductor electrode is similar to that of a metallic electrode, since there is an excess of the majority of charge carrier available for charge transfer. In contrast, if there is a depletion layer, then there are few charge carriers available for charge transfer, and electron transfer reactions occur slowly, if at all. The flat-band voltage can be determined using a method that involves measuring the apparent capacitance as a function of potential under depletion condition and is based on the Mott- Schottky relationship:

$$\frac{1}{C_{sc}^2} = \frac{2}{e\varepsilon\varepsilon_o N}\left(E - E_{FB} - \frac{kT}{e}\right) \qquad (4.1)$$

where C_{sc} = capacitance of the space charge region, ε= dielectric constant of the semiconductor, ε_o= permittivity of free space, N = donor density (electron donor concentration for an *n*-type semiconductor or hole acceptor concentration for a *p*-type semiconductor), E = applied potential and E_{fb} = flatband potential

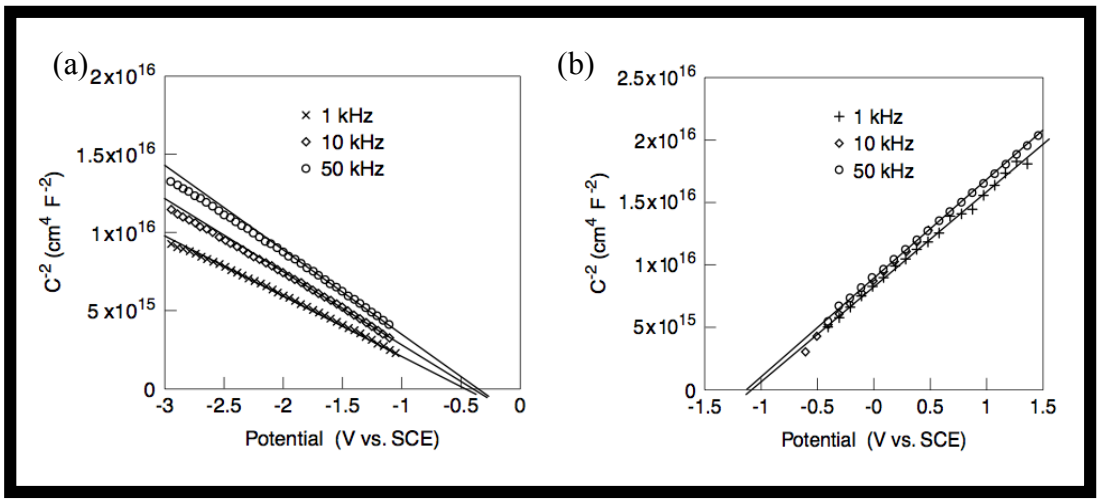

Figure 4.8: Mott-Schottky plots for (a) p-type and (b) n-type semiconductor [16]

Mott-Schottky plots ($1/C^2$ vs. E) are shown for a *p*-type silicon semi-conductor and an *n*-type silicon semiconductor in Figure 4.8(a) and Figure 4.8(b), respectively using Equation 4.1. The donor or acceptor density can be calculated from the slope, and the flatband potential can be determined by extrapolation to C = 0. The capacitance values are calculated from impedance measurements [16] of which technique is described in the following section.

4.8 Electrochemical Impedance Spectroscopy

Electrochemical Impedance Spectroscopy (EIS) or ac impedance methods have seen tremendous increase in popularity in recent years. Initially applied to the determination of the double-layer capacitance [17-20] and in ac polarography [21,22] they are now applied to the characterization of electrode

processes and complex interfaces. EIS studies the system (typically an electrochemical cell) response to the application of a periodic small amplitude ac signal. These measurements are carried out at different ac frequencies in the range of 1mHz to 10MHz and, thus, the name impedance spectroscopy was later adopted. The technique may be used to investigate the dynamics of bound or mobile charges in bulk or interface regions of any kind of ionic solids, or liquid materials, semiconductors, mixed ionic-electronic materials and insulators (dielectrics) [23]. Analysis of the system response contains information about the interface, its structure and reactions taking place there [24].

Electrochemical impedance is the frequency-dependent complex valued proportionality factor, which is a ratio between the applied potential and current signal. For the sake of simplicity, the impedance plots for the resistor network will be considered in some detail. The reason for choosing this circuit is because many of the electrochemical systems encountered in practice are actually modeled or based using this network [23].

The term resistance and impedance both imply an obstruction to current or electron flow. When dealing with a direct current (DC), only resistors provide this effect. However, for the case of an alternating current (AC), circuit elements such as capacitors and inductors can also influence the electron flow. These elements can affect not only the magnitude of an AC wave form, but also its time-dependent characteristics or phase [25]. In DC theory, where the frequency equals 0 Hz, a resistance is defined by the Ohm's Law:

$$E = I.R \qquad (4.2)$$

Where E = applied potential, I = resulting current and R = resistance. For an AC current, where the frequency exceeds zero, this is represented by

$$E= I.Z \qquad (4.3)$$

Where E = applied potential, I = resulting current and Z = impedance, the AC equivalent of resistance.

The mathematical contribution of the plot is based on a vector diagram, corresponding to a sine wave E and a sine wave I. This is because sine wave analysis is the most appropriate for electrochemical impedance studies to date. The current sine wave can be described by the following equation:

$$E_t = E_0 \sin(wt) \quad (4.4)$$

$$I_t = I_0 \sin(wt + \phi) \quad (4.5)$$

Where $w = 2\pi f$, E_0, I_0 = maximum amplitudes respectively, w = frequency in radians/sec, f = frequency in Hz and ϕ = phase shift in radians. Using Ohm's law,

$$Z_t = E_t/I_t = E_0 \sin(wt)/I_0\sin(wt + \phi) = Z_0 \sin(wt)/\sin(wt + \phi) \quad (4.6)$$

The impedance is therefore expressed in terms of magnitude Z_0 and phase shift ϕ. With Euler's relationship,

$$\exp(j\phi) = \cos\phi + j\sin\phi \quad (4.7)$$

It is possible to express the impedance as a complex function,

$$Z(w) = E/I = Z_0 \exp(j\phi) = Z_0 (\cos\phi + j\sin\phi) = Z_0 \cos\phi + j\, Z_0 \sin\phi \quad (4.8)$$

$$\text{Or,} \quad Z(w) = ReZ + j\, ImZ \quad (4.9)$$

Where ReZ and ImZ are the real and imaginary part of the impedance, respectively. The relationship between these quantities are:

$$|Z|^2 = (ReZ)^2 + (ImZ)^2 \quad (4.10)$$

$$\phi = \tan^{-1} (ImZ)/(ReZ) \qquad (4.11)$$

The result of the equation may be represented graphically using two types of plots: complex plane (also known as Cole-Cole or Nyquist plots) and Bode plots. The complex plane plot is a plot of Z" versus Z', that is, the imaginary versus the real components, plotted for various frequencies. A complex plane plot for a Randles circuit (R+R//C) is shown in Figure 4.9. It is a typical equivalent circuit of an electrochemical interface. Another type of graph is the Bode plot i.e. log |Z| (magnitude) and phase-angle ϕ, versus log frequency.

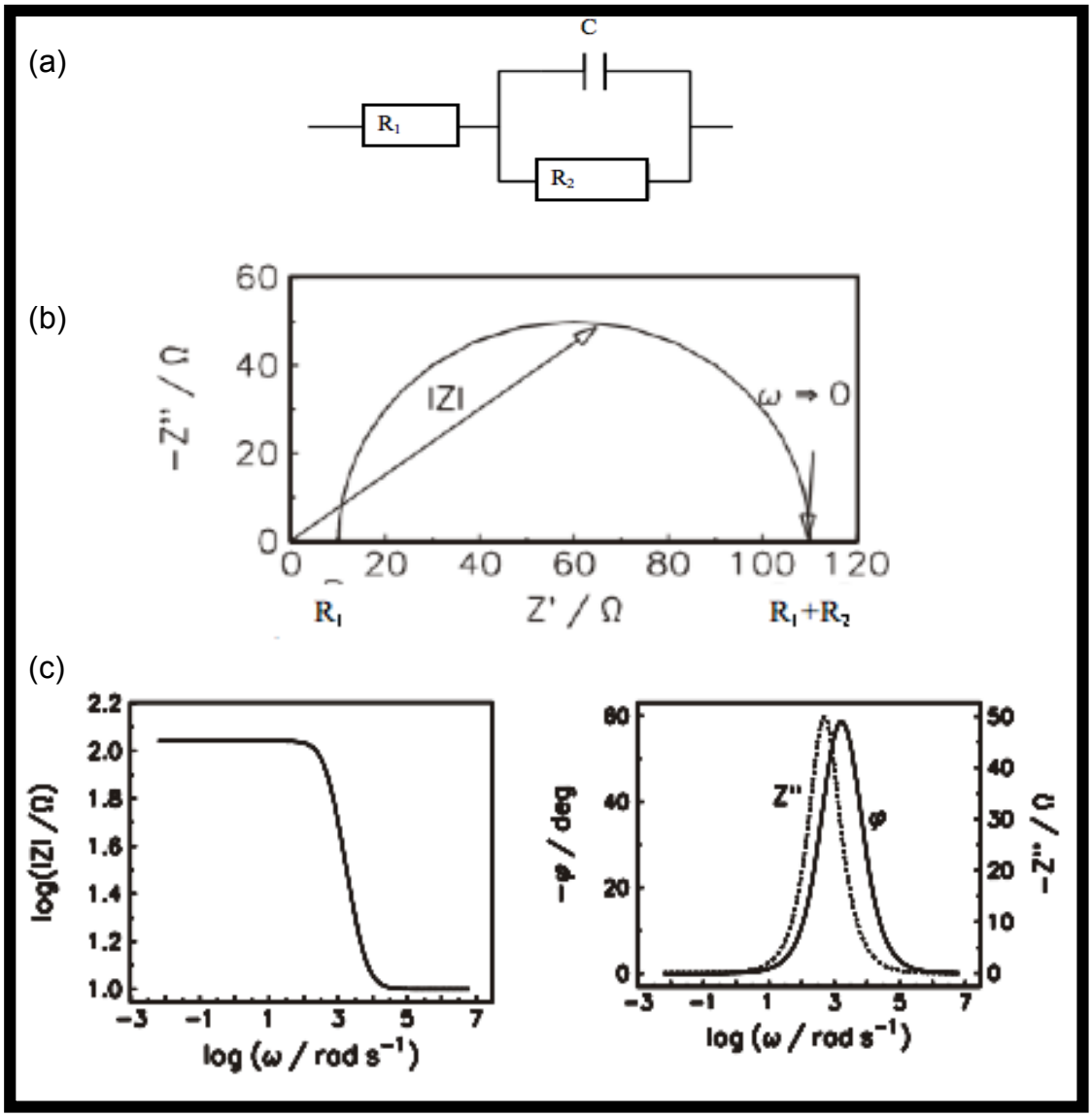

Figure 4.9: (a) RC circuit representing an electrochemical interface (b) Cole-Cole plot (c) Bode plots

Its corresponding impedance for the RC circuit in Figure 4.9 is:

$$Z(w) = E/I$$
$$= R_1 + 1/(1/R_2 + jCw)$$
$$= R_1 + R_2/(1+w^2C^2R_2^2) – jwC^2R_2^2/(1+w^2C^2R_2^2) \quad (4.12)$$

Where E = voltage, I = current, R_1 and R_2 = resistance values and C = capacitance.
Furthermore,

$$|Z(w)| = \sqrt{[R_1 + R_2/(1+w^2C^2R_2^2)] + wCR_2^2/(1+w^2C^2R_2^2)} \quad (4.13)$$

When w tends to zero, |Z(w)| equals to (R_1 + R_2). And as w approaches infinity, |Z(w)| equals to R_1.

At high frequencies, the capacitor conducts current easily making R1 the sole contributor to the total impedance. When the frequencies are low, the capacitor acts more like an open circuit forcing current to flow through R2 thus making the effective total impedance equals to R_1 + R_2. At intermediate frequencies, the impedance takes a value between R_1 and R_1 + R_2, having both real and imaginary components. This gives rise to the Cole-Cole plot having semicircular shapes, which corresponds to the equation:

$$[Z' – (R_1+ R_2/2)]^2 + Z''^2 = (R_2/2)^2 \quad (4.14)$$

It has been shown that the above equation is analogous to the equation of a circle, with a radius of $R_2/2$ and a centre at (R_1+ R_2/2,0). With w, R1 and R2 all greater than zero, a semicircle is formed on the axis when plotted as function of frequency. Z(w) is plotted in figure 4.9(b) in terms of a Cole-Cole plot in the complex plane with the negative imaginary parts above the real axis, as is usually used in electrochemistry.

At the peak of the semicircle, the following condition is obtained:

$$w_{max}R_2C = 1 \quad (4.15)$$

and hence,

$$C = 1/2\pi f_{max}R_2 \quad (4.16)$$

Knowing the value of R_2 and the frequency f_{max}, the value of the capacitance can be determined. It is possible to obtain all the three parameters (R_1,R_2 and C) from the Cole-Cole plot as shown in Figure 4.9(b), provided sufficient frequency is investigated.

Physical Electrochemistry	**Equivalent Circuit Elements**
Electrolyte resistance: The resistance of an ionic solution depends on the ionic concentration, type of ions, temperature and the geometry of the area in which current is carried.	**$R = \rho 1/A$**
Double layer capacitance: An electrical double layer exists on the interface between an electrode and its surrounding electrolyte. This double layer is formed as ion from the solution "stick on" the electrode surface. The charged electrode is separated from the charged ions and this separation is very small, often on the order of angstroms. Charges separated by an insulator form a capacitor. On a bare metal immersed in an electrolyte, there will be 20 to 60 μF capacitance for every 1cm^2 of electrode area.	**C_{dl}**
Polarization Resistance: Whenever the potential of an electrode is forced away from its value at open-circuit, that is referred to as "polarizing" the electrode. When an electrode is	**R_p**

polarized, it can cause current to flow through electrochemical reactions that occur at the electrode surface. The amount of current is controlled by the kinetics of the reactions and the diffusion of reactants both towards and away from the electrode.	
Charge Transfer Resistance: A resistance is formed by a single kinetically-controlled electrochemical reaction. For a metal electrode, electrons can enter the metal and metal ions diffuse into the electrolyte and vice-versa. Charge can then be transferred. This charge transfer reaction speed depends on the kinds of reaction, the temperature, the concentration of the reaction products and potential.	R_{ct}
Diffusion: Diffusion also can create an impedance called a Warburg impedance. This depends on the frequency of the potential perturbation. At high frequencies, the Warburg impedance is small since diffusing reactants do not have to move very far. At low frequencies the reactants have to diffuse farther, increasing the Warburg impedance.	**W**

Table 4.1: Common physical electrochemistry elements [25]

Analysis of the system response contains information about the interface; its structure and reactions taking place there. However, EIS is a very sensitive technique and it must be used with great care. Besides, it is not always well understood. This may be connected with the fact that existing reviews on EIS are very often difficult to understand by non-specialists and, frequently, they do not show the complete mathematical developments of equations connecting the impedance with the physico-chemical parameters. It should be stressed that EIS cannot give all the answers. It is a complementary technique and other methods must also be used to elucidate the interfacial processes [24].

4.9 Scanning Electron Microscopy

The scanning electron microscope (SEM) is a type of electron microscope that images the sample surface by scanning it with a high-energy beam of electrons in a raster scan pattern. The electrons interact with the atoms that make up the sample producing signals that contain information about the sample's surface topography, composition and other properties such as electrical conductivity.

The types of signals produced by an SEM include secondary electrons, back-scattered electrons (BSE), characteristic X-rays, light (cathodoluminescence), specimen current and transmitted electrons. Secondary electron detectors are common in all SEMs, but it is rare that a single machine would have detectors for all possible signals. The signals result from interactions of the electron beam with atoms at or near the surface of the sample. In the most common or standard detection mode, secondary electron imaging or SEI, the SEM can produce very high-resolution images of a sample surface, revealing details about less than 1 to 5 nm in size. Due to the very narrow electron beam, SEM micrographs have a large depth of field yielding a characteristic three-dimensional appearance useful for understanding the surface structure of a sample.

In a typical SEM, an electron beam is thermionically emitted from an electron gun fitted with a tungsten filament cathode. Tungsten is normally used in thermionic electron guns because it has the highest melting point and lowest vapour pressure of all metals, thereby allowing it to be heated for electron emission, and because of its low cost.

The electron beam, which typically has an energy ranging from 0.5 keV to 40 keV, is focused by one or two condenser lenses to a spot about 0.4 nm to 5 nm in diameter. The beam passes through pairs of scanning coils or pairs of deflector plates in the electron column, typically in the final lens, which deflect the beam in the x and y axes so that it scans in a raster fashion over a

rectangular area of the sample surface. When the primary electron beam interacts with the sample, the electrons lose energy by repeated random scattering and absorption within a teardrop-shaped volume of the specimen known as the interaction volume, which extends from less than 100 nm to around 5 µm into the surface. The size of the interaction volume depends on the electron's landing energy, the atomic number of the specimen and the specimen's density. The energy exchange between the electron beam and the sample results in the reflection of high-energy electrons by elastic scattering, emission of secondary electrons by inelastic scattering and the emission of electromagnetic radiation, each of which can be detected by specialized detectors. The beam current absorbed by the specimen can also be detected and used to create images of the distribution of specimen current. Electronic amplifiers of various types are used to amplify the signals which are displayed as variations in brightness on a cathode ray tube. The raster scanning of the CRT display is synchronised with that of the beam on the specimen in the microscope, and the resulting image is therefore a distribution map of the intensity of the signal being emitted from the scanned area of the specimen. The image may be captured by photography from a high-resolution cathode ray tube, but in modern machines is digitally captured.

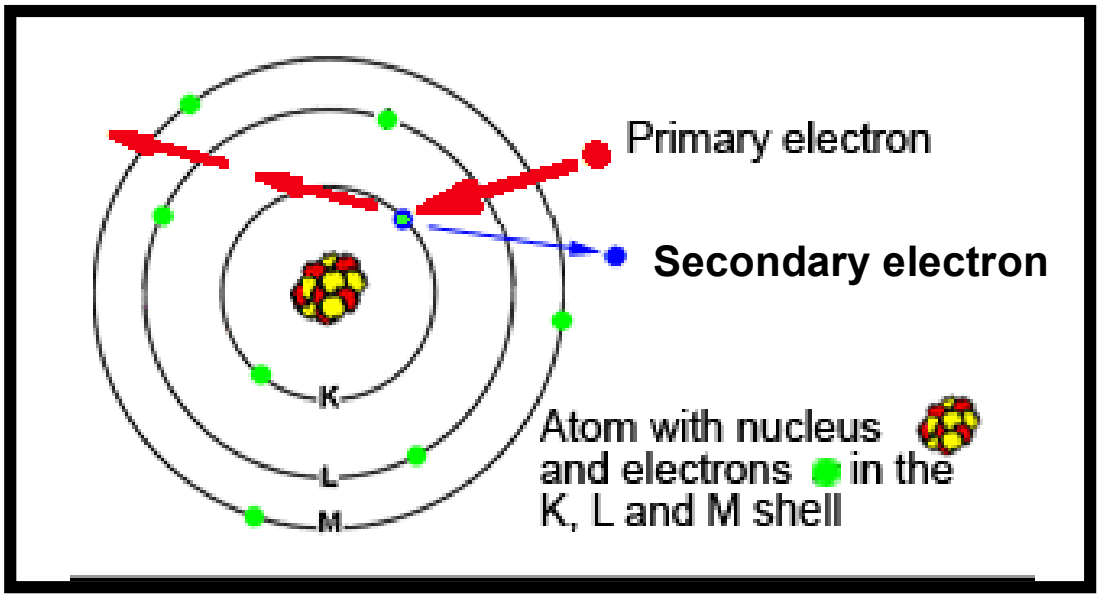

Figure 4.10: Electron beam interaction with an atom [26]

In more detail, the electron beam interacts with the electrons present in the atom rather than the nucleus. Since all electrons are negatively charged, the beam electrons will repel the electrons present in the sample. This interaction causes the beam electrons to slow down as it repels the specimen electrons, the repulsion may be so great that the specimen electrons are pushed out of the atom, and exit the surface of the sample, these are called secondary electrons (Figure 4.10). The secondary electrons are moving very slowly when they leave the sample. Since they are moving so slowly, and are negatively charged, they can be attracted to a detector, which has a positive charge on it. This attraction force allows you to pull in electrons from a wide area and from around corners in much the same way that a vacuum pulls in dust particles. The secondary electron current reaching the detector is recorded, and the microscope image consists of a "plot" of this current I against probe position on the surface. The contrast in the micrograph arises from several mechanisms, but first and foremost from variations in the surface topography. Consequently, the secondary electron micrograph is virtually a direct image of the real surface structure. The ability to pull in electrons from around corners is what gives secondary electron images a 3-dimensional look.

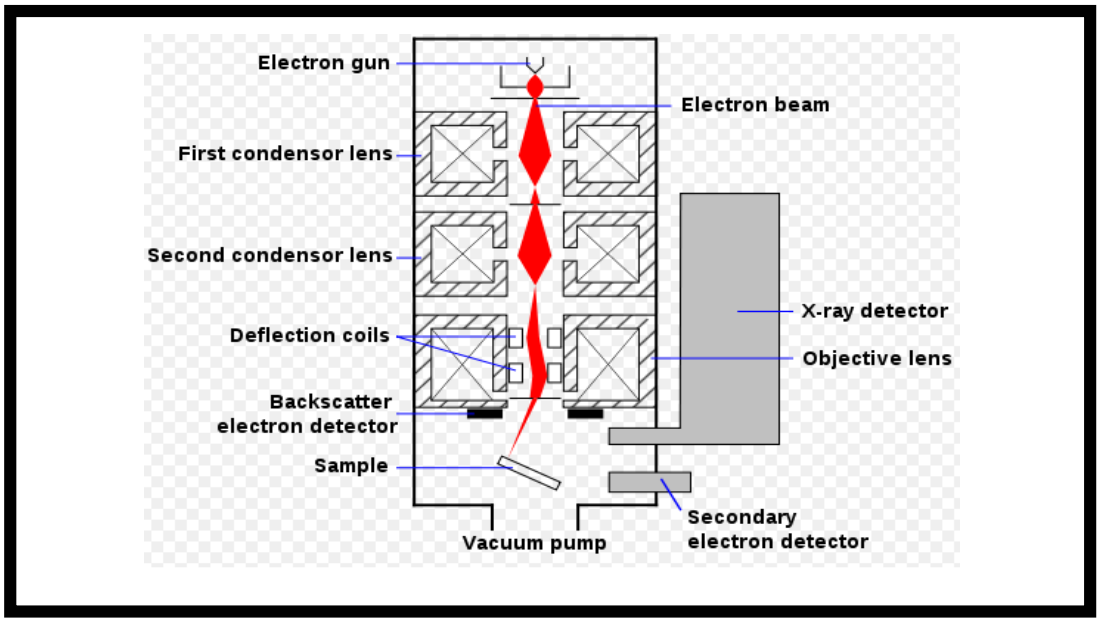

Figure 4.11: Schematic set-up of a SEM system [27]

The attainable resolution of the technique is limited by the minimum spot size that can be obtained with the incident electron beam, and ultimately by the scattering of this beam as it interacts with the substrate. With modern instruments, a resolution of better than 5 nm is achievable. This is more than adequate for imaging semiconductor device structures.

4.10 Focus Ion Beam Milling

A focused ion beam system is an effective combination of a scanning ion microscope and a precision machining tool. The modern focused ion beam system utilizes a liquid metal ion source (LMIS) at the top of its column to produce ions, usually Ga+. From here the ions are pulled out and focused into a beam by an electric field and subsequently passed through apertures, then scanned over the sample surface (Figure 4.12).

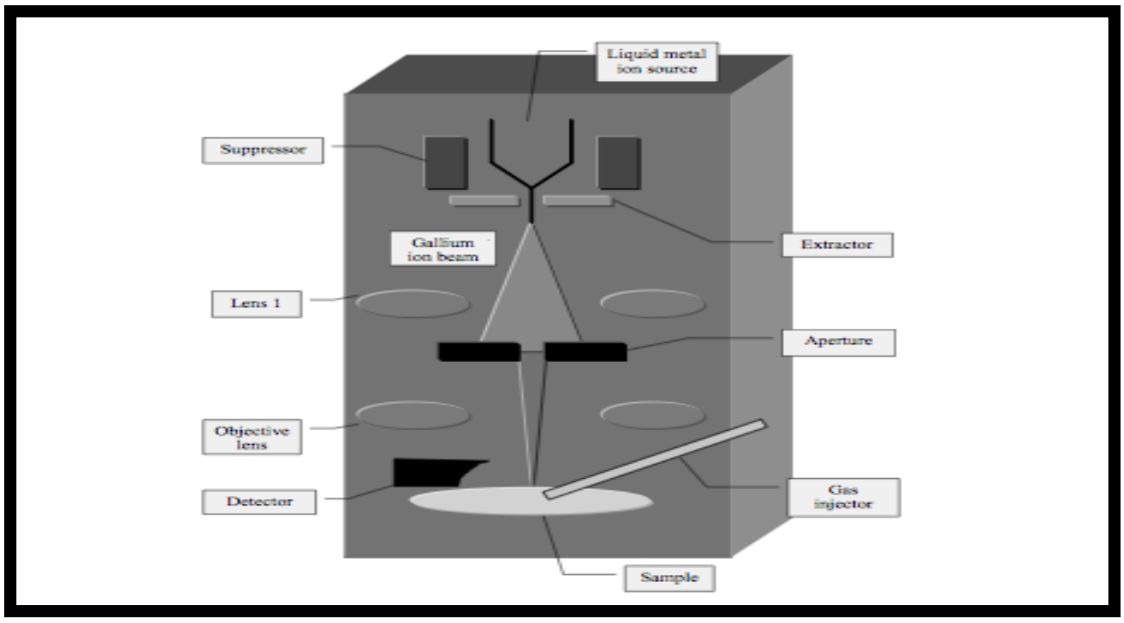

Figure 4.12: A schematic representation of a Focused Ion Beam system [29]

Upon impact, the ion-atom collision is either elastic or inelastic in nature. Elastic collisions result in the excavation of surface atoms—a term called sputtering—and are the primary cause of the actual modification of the material surface (Figure 4.13). Inelastic collisions occur when the ions transfer some of their energy to either the surface atoms or electrons. This process

produces secondary electrons (electrons which become excited and are able to escape from their shell), along with X rays (the energy released when an electron drops down into a lower shell). Since the inner electrons of the sample cannot be reached by the incoming ion beam inner shell excitation does not occur, and as a result, usable X-rays are not likely to be generated as is the case when using an electron beam. Secondary ions are also produced through the collision, seemingly after secondary electrons have been emitted.

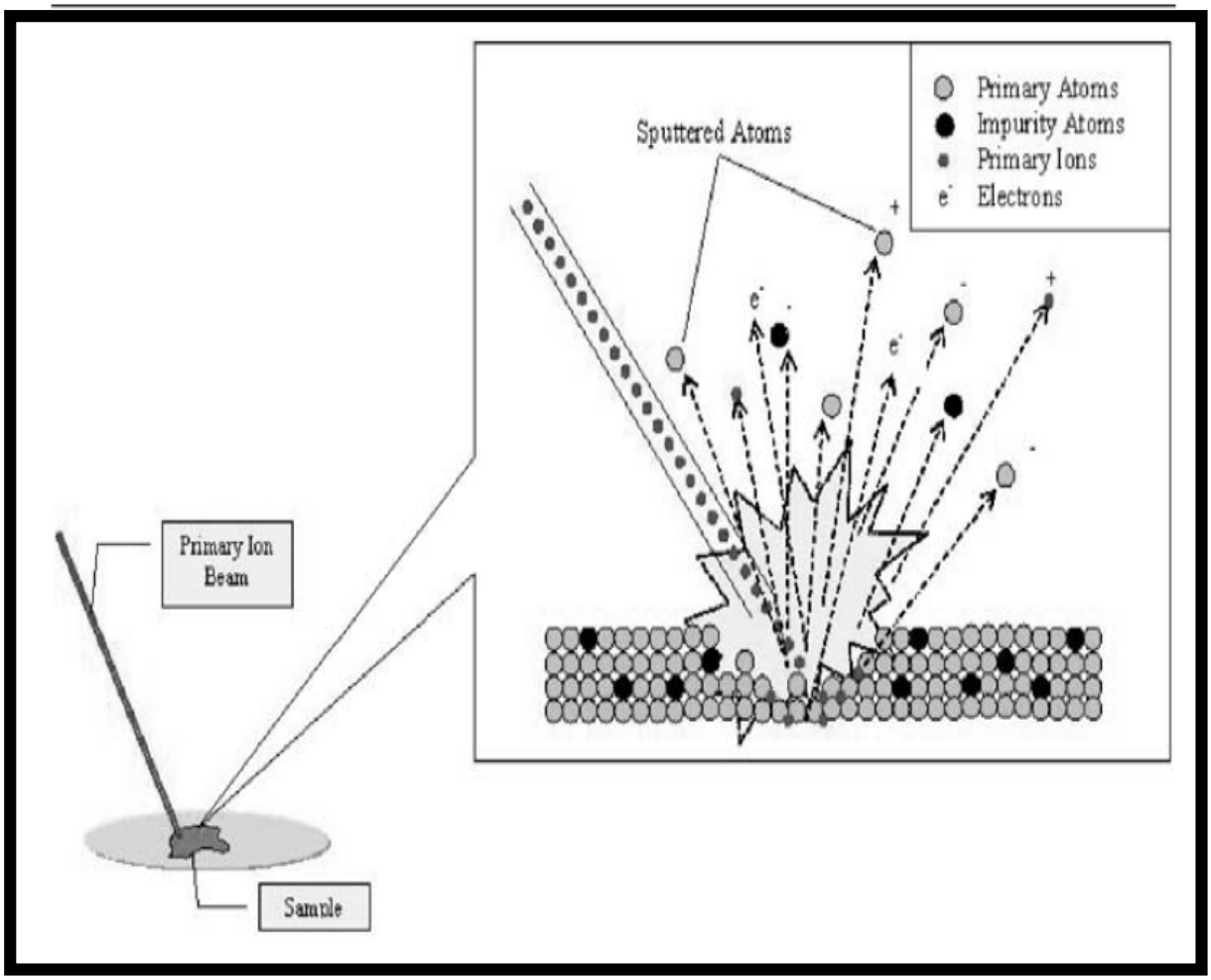

Figure 4.13: Schematic diagram of ion-beam sputtering process [29]

Valuable information can be gathered from all emission, depending on the capabilities of the machine. The signals from the ejected ions, once collected, can be amplified and displayed to show the detailed structure of the sample

surface. Beyond its imaging capabilities, the FIB can be used as a deposition tool by injecting an organometallic gas in the path of the ion beam, just above the sample surface. This technique proves to be practical for certain material repair applications. In addition, by containing the ion beam over a specific region of the sample for an extended length of time, the continuous sputtering process will lead to noticeable removal of material, which is useful for probing and milling applications. The underlying factor in the physics behind the FIB is the fact that Ga^+ ions are significantly more massive than electrons (1.2×10^{-25} kg and 9.1×10^{-31} kg respectively), a remarkably enhancing feature. The collisions between the large primary ions and the substrate atoms cause surface alterations at various levels depending on dosage, overlap, dwell time, and many other variables, in a way that electrons cannot achieve [28].

The relatively large ions have a difficult time penetrating the sample by passing between individual atoms. Their size increases the probability of interaction with atoms, causing a rapid loss of energy. As a result, ion-atom interaction mainly involves the outer shell, resulting in atomic ionization and breaking of the chemical bonds of the surface atoms. This is the source of secondary electrons and the cause of changes in the chemical state of the material. The total length the ion travels is known as its “penetration depth,” a term which also applies to electrons. The moving ion recoils one of the atoms in the sample, which then causes another constituent atom to recoil. As a result, the ions create many atomic defects along their path. This generation of defects plays an important role when using an ion beam for material modifications.

As for the difference in mass, ions—being many times heavier—can carry about 370 times the momentum of electrons. Upon contact, this momentum can be transferred to the atoms in the sample, causing enough motion to remove the atoms from their aligned positions. This sputtering effect, not present when an electron beam is used, has important milling applications. In particular, gallium (Ga+) ions are used in the FIB for several reasons. Firstly, its low melting point makes gallium convenient in that it requires only limited heating, and therefore is in the liquid phase during operation. Also, its mass is

just about ideal, as it is heavy enough to allow milling of the heavier elements, but not so heavy that it will destroy a sample immediately. Finally, since some of the ions used in the beam will be implanted into the sample, it is important to use an element that will not interfere with the analysis of the sample. Gallium can easily be distinguished from other elements, and therefore does not cause trouble in this regard. Although gallium is not the only possible choice, it has become the popular ion for use in the FIB system [29].

4.11 Raman Spectroscopy

Raman scattering is a powerful light scattering technique used to diagnose the internal structure of molecules and crystals. Raman spectroscopy relies on inelastic scattering of monochromatic light, usually from a laser source. Inelastic scattering happens when there is energy transfer between the photons and the molecules during their interaction. In a light scattering experiment, light of a known frequency and polarization is scattered from a sample. The scattered light is then analyzed for frequency and polarization. The interaction between the laser light and molecular vibration results in the energy or frequency of the photons to be shifted up or down relative to the original monochromatic energy or frequency.

The impingement of light upon a molecule generates an interaction with the electron cloud and the bonds of that molecule. Consequently, the molecule is excited from the ground state to a virtual energy state. The relaxation of the molecule causes a photon emission rendering it in a different rotational or vibrational state. The energy differential leads to a shift in the emitted photon's frequency relative the excitation wavelength. If the final vibrational state of the molecule holds higher energy than the initial state, then the frequency of the emitted photon will be down-shifted for the conservation of energy of the system. This shift in frequency is defined as a Stokes shift. If the final vibrational state experienced a reduction in energy than the initial state, then the emitted photon will be shifted to a higher frequency, and this is called as an Anti-Stokes shift. The shift gives information about vibrational, rotational

and other low frequency transitions in molecules. The magnitude of the shift is independent of the excitation frequency. This "Raman shift" is therefore an intrinsic property of the sample.

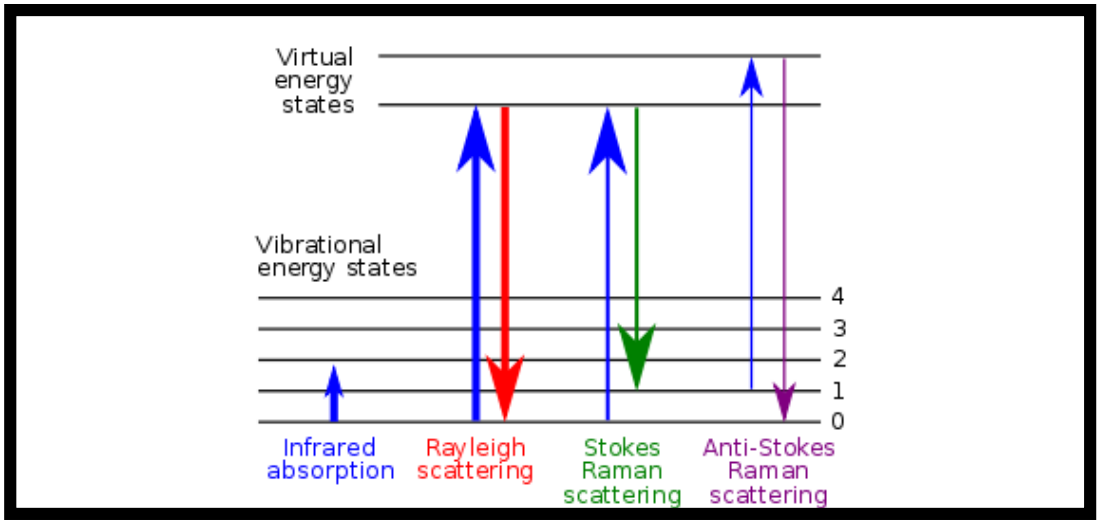

Figure 4.14: A simple Stokes & Anti-Stokes Shift diagram [30]

For Raman effect to take place, a change in the molecular polarization potential or amount of deformation of the electron cloud with respect to the vibrational coordinate is required. The quantity of the polarizability change dictates the Raman scattering intensity. The pattern of shifted frequencies is determined by the rotational and vibrational states of the sample. The mechanism by which the Raman effect occurs can be understood classically, although a quantum mechanical derivation is necessary for understanding the variation in line intensities and developing selection rules for predicting which vibrational modes are Raman active. Both descriptions are based upon an interaction between the oscillating induced polarization or dipole moment of the molecule (P) and the time-dependent electric field vector of the incident radiation (E).

$$E_i = E_i^o \cos 2\pi c\omega_o t, \qquad (4.17)$$

where E^0_i is the ith component of the time- dependent electric field amplitude and w_0 is the frequency of the electric field (Ei). The time-dependent induced

polarization (P) is also caused by the electric field (E) which interacts through the molecular polarizability α.

$$P = \alpha E \tag{4.18}$$

As the molecule vibrates (undergoes atom displacements), the electronic charge distribution and, hence, the polarizability (α) varies in time. The polarizability is related to the electron density of the molecule and is often visualized in three dimensions as an ellipsoid and represented mathematically as a symmetric second-rank tensor. The time-dependent amplitude (Qk) of a normal vibrational mode executing simple harmonic motion is written in terms of the equilibrium amplitude Q^0_k the normal mode frequency w_k, and time (t).

$$Q_k = Q_k^o \cos 2\pi c\omega_k t \tag{4.19}$$

An expression for the induced polarization can be derived in terms of the normal coordinate and electric field by writing the polarizability as a Taylor series in the normal coordinate and retaining only the linear terms. For the ij component, then,

$$\alpha_{ij} = \alpha_{ij}^o + \sum_{k=1}^{3n-6} \left(\frac{\partial \alpha_{ij}}{\partial Q_k}\right) Q_k + \cdots \tag{4.20}$$

The combination of equations (4.17-4.20) shows that the induced polarization is composed of nine terms similar to the $\alpha_{ij}E_i$ component depicted in equation (4.21).

$$\alpha_{ij}E_i = \alpha_{ij}^o E_i^o \cos 2\pi c\omega_o t + E_i^o \sum_{k=1}^{3n-6} \tfrac{1}{2}\left(\frac{\partial \alpha_{ij}}{\partial Q_k}\right)_e Q_k^o \times [\cos 2\pi c(\omega_o+\omega_k)t + \cos 2\pi c(\omega_o-\omega_k)t]. \tag{4.21}$$

The first term in equation (4.20) corresponds to the elastic component of the scattered light (Rayleigh scattering), while the second term corresponds to the inelastically scattered Raman component. Equation (4.20) also indicates that Raman scattered light can occur at two new frequencies different from the incident light frequency. These correspond to Stokes (w_0-w_k) and anti-Stokes (w_0+w_k) scattering processes. The partial derivative factor, $(\partial\alpha_{ij}/\partial Q_k)_e$, evaluated at the equilibrium position of the normal coordinate comprises a necessary condition for Raman activity of the normal mode Q_k. Raman effects occur only for those normal modes that cause the molecule to undergo a net change in polarizability during the course of the vibration. While equation (7) implies that both Stokes and anti-Stokes components ,should appear with equal intensity, quantum mechanical derivation shows that the Stokes/anti-Stokes intensity ratio is proportional to the Boltzmann factor (7), and can be used to determine the molecular temperature of a collection of molecules. The statistical derivation is based upon the thermal population of ground and excited molecular vibrational states according to a Boltzmann distribution.

These results can be generalized to describe the Raman scattering process in solids. Interaction between incident electromagnetic radiation and the electrons in a solid can occur to yield scattering because the time-varying electric field of the radiation can induce a dipole moment (M) in the solid. The induced dipole moment will vary with the frequency of the incident field and generate elastic scattering (Rayleigh) at the same frequency as the incident radiation, but scattered over 360^o. For inelastic scattering, energy can be "removed" from the induced dipole moment if a vibrational excitation (phonon) can be produced in the solid. This excitation is characterized by a time-varying dipole moment during vibration of the normal mode, associated with that phonon. As with a single molecule, this vibrational mode must exhibit a change in polarizability during the vibration to exhibit Raman activity. Following a Raman scattering process, the system will be left in a higher vibrational level corresponding to a Stokes process and emission of red-shifted light, or a lower level resulting from anti-Stokes scattering and

emission of blue-shifted light from the wavelength of the incident excitation. Figure 1 depicts these two scattering processes and shows the relationship between the Stokes/anti-Stokes intensity ratio and the Boltzmann factor [31].

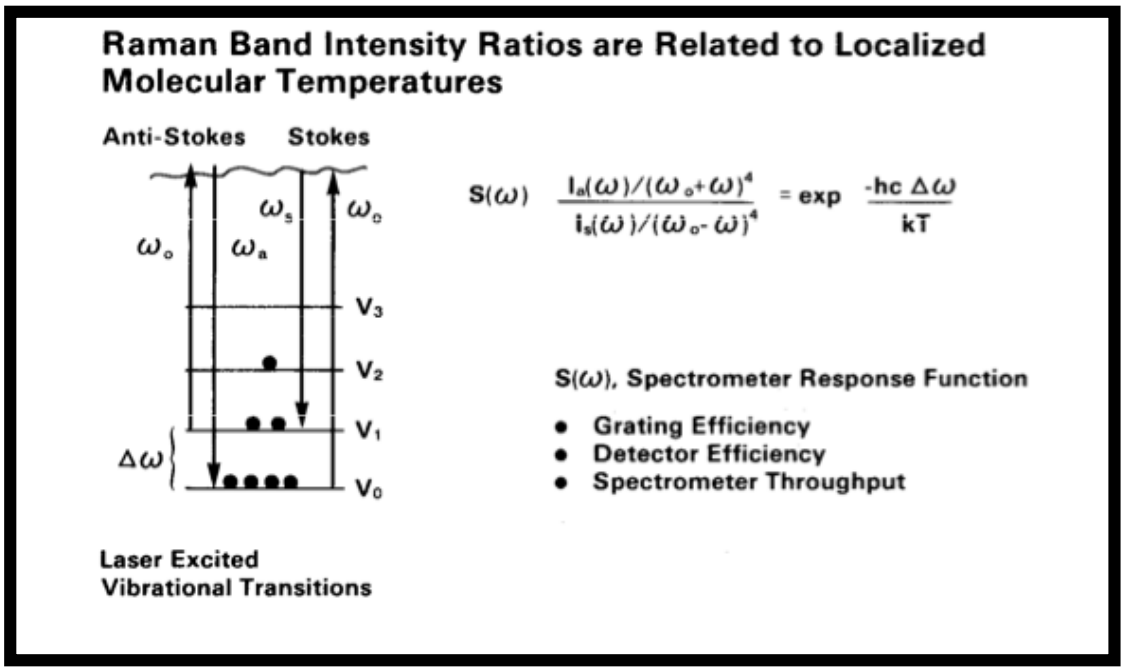

Figure 4.14(b): Laser-excited vibrational transitions and the relationship of Stokes/Anti-Stokes band intensity ratios to temperature [31].

4.12 Fourier Transform Infra-Red Spectroscopy

The energy of most molecular vibrations corresponds to that of the infrared region of the electromagnetic spectrum. Molecular vibrations may be detected and measured either in an infrared spectrum or indirectly in a Raman Spectrum. The position of an absorption band in the spectrum may be expressed in microns or commonly the reciprocal of the wavelength, cm^{-1}. The usual range of an infrared spectrum is typically between 4000 cm^{-1} and 625 cm^{-1}[32].

Functional groups have natural vibration frequencies, characteristic of that functional group. . The resonant frequencies can be in a first approach related to the strength of the bond, and the mass of the atom at either end of it. Thus, the frequency of the vibrations can be associated with a particular bond type.

The fact that many functional groups can identified by their characteristic vibration or resonant frequencies makes infrared spectrum the simplest, most rapid and often most means of assigning a compound to its class.

Infrared light is absorbed when the oscillating dipole moment (due to molecular vibration) interacts with the oscillating electric field vector of the infrared beam. A simple rule for deciding if this interaction (and hence absorption of light) occurs is that the dipole moment at one extreme must be different from the dipole moment at the other extreme of the vibration. In the Raman effect a corresponding interaction occurs between light and the molecule's polarizability, resulting in different selection rules.

The most important consequence of these selection rules is that in a molecule with a centre of symmetry those vibrations symmetrical about the centre of symmetry are active in Raman and inactive in the infrared; those vibrations which are not centrosymmetric are inactive in the Raman and usually active in the infrared. This is doubly useful, for it means that the two types of spectrum are complementary and the more easily obtained, the infrared, is the most informative for organic chemists because most functional groups are not centrosymmetric [32].

A complex molecule has a large number of vibrational mdes which involve the whole molecule. To a good approximation, however, some of these molecular vibrations are associated with the vibrations of the individual bonds or functional groups (localized vibrations) while others must be considered as vibrations of the whole molecule. The localized vibrations are either stretching, bending, rocking, twisting or wagging. To illustrate this, the methylene group is used as below

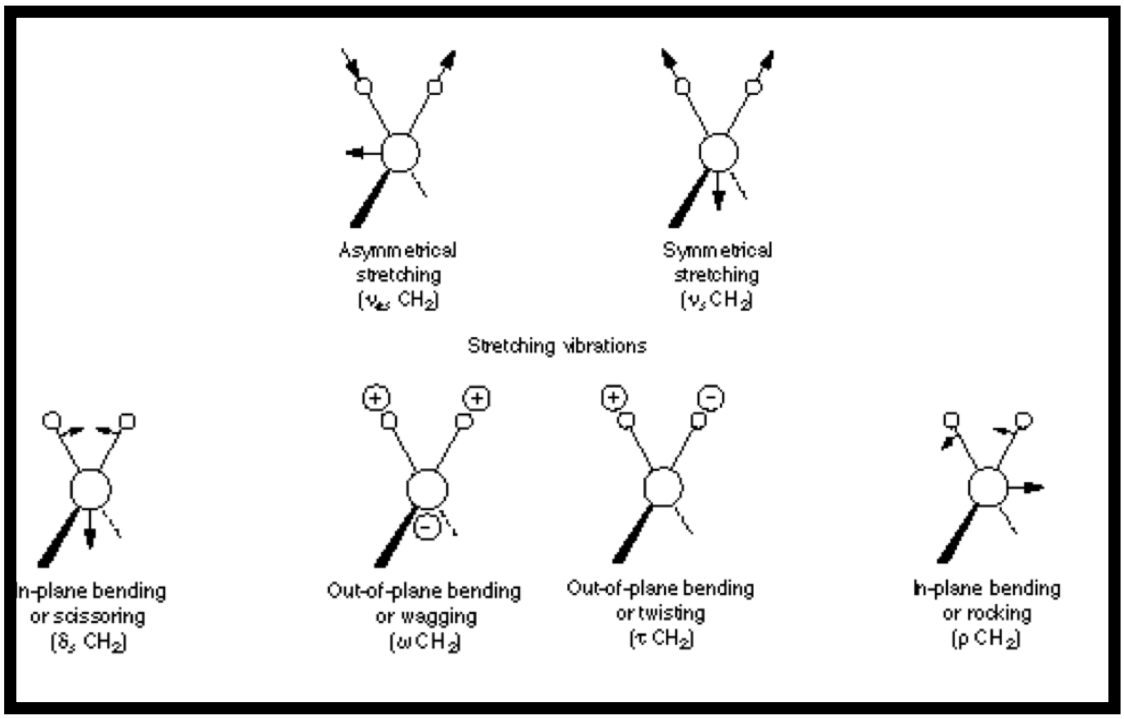

Figure 4.15: Major vibrational mode for a non-linear group, CH_2 [33]

Many localized vibrations are very useful for the identification of functional groups.

The infrared spectrum of a sample is recorded by passing a beam of infrared light through the sample. Examination of the transmitted light reveals how much energy was absorbed at each wavelength. This can be done with a monochromatic beam, which changes in wavelength over time, or by using a Fourier transform instrument to measure all wavelengths at once. From this, a transmittance or absorbance spectrum can be produced, showing at which IR wavelengths the sample absorbs. Analysis of these absorption characteristics reveals details about the molecular structure of the sample. When the frequency of the IR is the same as the vibrational frequency of a bond, absorption occurs.

4.13 Energy-dispersive X-ray Spectroscopy

Energy dispersive X-ray spectroscopy (EDS) is an analytical technique used for the elemental analysis or chemical characterization of a sample. It is a chemical microanalysis technique performed in conjunction with a scanning

electron micro- scope (SEM). The technique utilizes X-rays that are emitted from the sample during bombardment by the electron beam to characterize the elemental composition of the analyzed volume. Features or phases as small as about 1 mm can be analyzed [34].

EDS works by using an electron microscope to focus an electron beam to interact with the atoms in a sample. As the electron beam displaces electrons in the sample, a detector converts the electrons scattered by the electron beam into a microscopic image. This also causes the generation of characteristic X-rays. In order to return the atom to its normal state, an electron from an outer atomic shell drops into the vacancy in the inner shell. This drop results in the loss of a specific amount of energy, namely, the difference in energy between the vacant shell and the shell contributing the electron. This energy is given up in the form of electromagnetic radiation X-rays [34].

The wavelength of this X-ray can be calculated from

$$\lambda = \frac{hc}{\Delta E} \tag{4.22}$$

Where h is Planck's constant, c is the speed of light and ΔE is the energy between excited states. Since energy levels in all elements are characteristic to that element, X-rays are generated. The accumulation of energy counts creates a spectrum representing the analysis of the sample. Therefore, while the electron microscope produces an image of the sample topography, energy dispersive X-ray microanalysis tells the microscopist what elements are present in the sample.

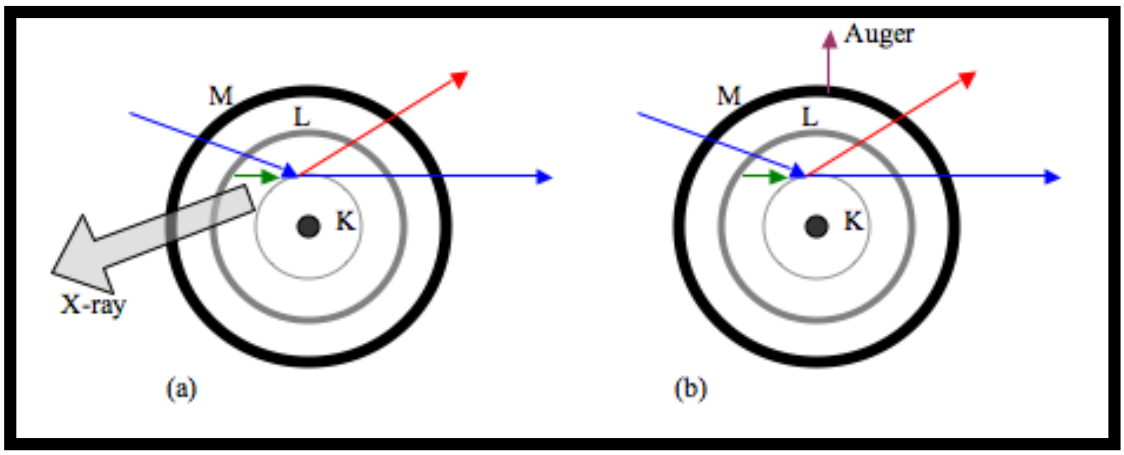

Figure 4.16: The two in which ways an inner shell-excited atom can relax. In both cases a K-shell electron has been knocked out – in (a) a characteristic (K_{α}) X-ray is emitted while in (b) an Auger electron (KLM) is ejected [35]

Before one can use the X-rays for analytical purposes, one needs to know which of the many characteristic X-ray lines for each element is the most intense, this enables us to chose the best line to use as an index of how much of each element is present in the sample.

In the K series, the lines $K_{\alpha 1}$ and $K_{\alpha 2}$ are seven to eight more intense than $K_{\beta 1}$ and $K_{\beta 2}$ (another close pair). Consequently the K 'doublet', as it is called, is most frequently used for analysis. However, it is not always possible to excite the K series lines in an electron beam instrument since, as the atomic number of the emitting element increases, the energy required to knock out a K-shell electron also increases. For example, the elements heavier than tin (Z=50) need electrons of more than 25keV to excite any K lines at all, and are not efficient producers of K X-rays until the incident electron energy is about 75keV. Since we would like to be able to analyze a specimen in an SEM,, where electron energies of perhaps only 30keV are available, we must look for other characteristic X-rays that are more easily excited in order to detect heavy elements. Fortunately the L series of lines shown in Figure 4.17, or even the M series for very heavy elements, has very suitable properties. Again it turns out that of the vast number of possible lines, $L_{\alpha 1}$ and $L_{\alpha 2}$ are far stronger than the remainder, which can normally be ignored. A similar effect

narrows the M series down to a few useful lines. Table X shows the energy and associated wavelength of X-rays generally occurs when the bombarding electrons have about three times the X-ray energy. A study of Table X will show that the selected elements have at least one strong X-ray line with energy less than 10keV and therefore should be no difficulty in analyzing all the elements, using a scanning electron microscope operating at 25-30keV.

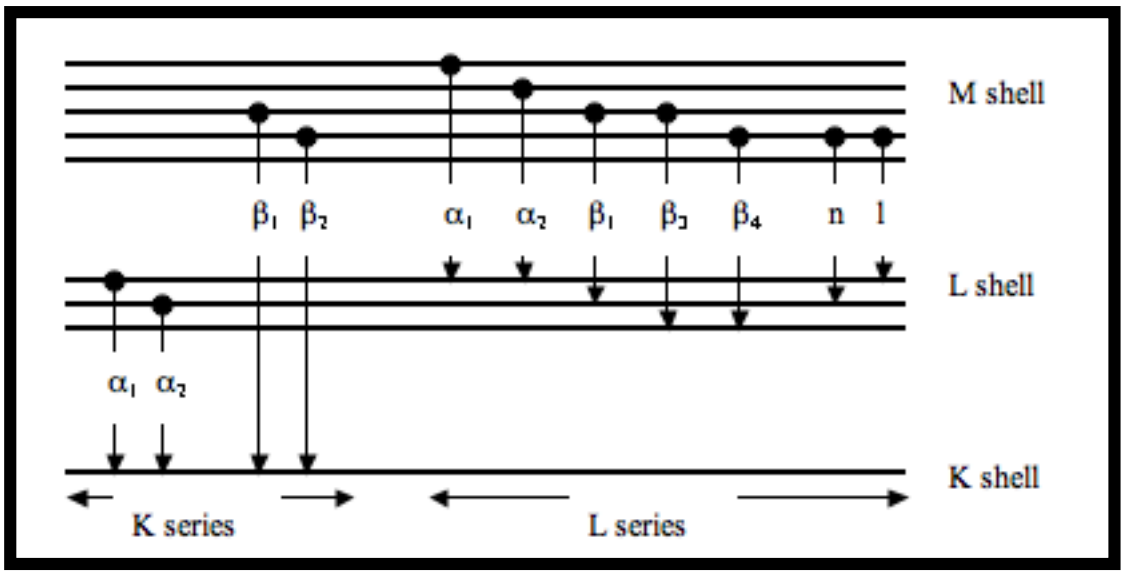

Figure 4.17: Some of the more common transitions between the K,L and M shells of an atom that lead to the X-ray lines indicated (35)

Statistical rules predict that the smallest concentration of an element that can be detected with an EDX system. If one is trying to detect a very minor element, very long acquiring times are required. In this instance more sensitive techniques can be employed such as ion mass spectroscopy (SIMS).

The minimum detection limit (m_{dl}) or lower limit of detection (l_{ld}) is given by:

$$m_{dl} = \frac{k\sqrt{2}}{c'}\sqrt{\frac{N_b}{T}} \qquad (4.23)$$

where N_b = background intensity (under the peak of interest), T = counting lifetime for the experiment nd c' = counts per sec per wt% of the element in question.

$$c' = \frac{N_p - N_b}{c} \tag{4.24}$$

Where c = wt% concentration of the element in question, k =1 when the peak is identified at 68.3% confidence, k = 2 when the peak is identified at 95.4% confidence and k = 3 when the peak is identified at 99.7% confidence of the selected elements. Most EDX analysis programs operate at 95.4% (k = 2) confidence levels. EDX detection limits are therefore ~ 0.2% for every elements and 4-5% for light elements, when T<300 seconds [35].

Element	*Atomic Number Z*	*Relative Actomic Mass A_r*	$K_{\alpha 1}$		$L_{\alpha 1}$		$M_{\alpha 1}$	
			E(keV)	*λ(nm)*	*E(keV)*	*λ(nm)*	*E(keV)*	*λ(nm)*
			(a)	*(b)*	*(a)*	*(b)*	*(a)*	*(b)*
Hydrogen	1	1.0						
Helium	2	4.0						
Lithium	3	6.9	0.05					
Beryllium	4	9.0	0.11	11.40				
Boron	5	10.8	0.18	6.76				
Carbon	6	12.0	0.28	4.47				
Nitrogen	7	14.0	0.39	3.16				
Oxygen	8	16.0	0.52	2.36				
Fluorine	9	19.0	0.68	1.83				
Neon	10	20.2	0.85	1.46				
Sodium	11	23.0	1.04	1.19				
Magnesium	12	24.3	1.25	0.99				
Aluminium	13	27.0	1.49	0.83				
Silicon	14	28.1	1.74	0.71				
Phosphorus	15	31.0	2.01	0.61				
Sulphur	16	32.1	2.31	0.54				
Chlorine	17	35.5	2.62	0.47				
Argon	18	39.9	2.96	0.42				
Potassium	19	39.1	3.31	0.37				
Calcium	20	40.1	3.69	0.34	0.34	3.63		
Scandium	21	45.0	4.09	0.30	0.39	3.13		
Titanium	22	47.9	4.51	0.27	0.45	2.74		
Vanadium	23	50.9	4.95	0.25	0.51	2.42		
Chromium	24	52.0	5.41	0.23	0.57	2.16		
Manganese	25	54.9	5.90	0.21	0.64	1.94		
Iron	26	55.8	6.40	0.19	0.70	1.76		
Cobalt	27	58.9	6.93	0.18	0.77	1.60		
Nickel	28	58.7	7.48	0.17	0.85	1.46		
Copper	29	63.5	8.05	0.15	0.93	1.33		
Zinc	30	65.4	8.64	0.14	1.01	1.23		

Table 4.2*:* The energy and associated wavelength of the strongest K, L and M shells [35]

4.14 Atomic Force Microscopy

The atomic force microscope (AFM) uses a stylus in the form of a sharp probe mounted near to the end of a flexible microcantilever arm, which interacts directly with the surface, probing the repulsive and attractive forces which exist between the probe and the sample surface to produce a high-resolution three-dimensional topographic image of the surface. The AFM has a number of advantages over electron microscope techniques, primarily its versatility in being able to take measurements in air or fluid environments rather than in high vacuum, which allows the imaging of polymeric and biological samples in their native state.

By raster-scanning this probe across a surface of interest and simultaneously monitoring the deflection of this arm as it meets the topographic features present on the surface, a three-dimensional picture can be built up of the surface of the sample to a high resolution. Many different variations of this basic technique are currently used to image surfaces using the AFM, depending upon the properties of the sample and the information to be extracted from it. These variations include ‘static’ techniques such as contact mode, where the probe remains in constant contact with the sample, and ‘dynamic’ modes, where the cantilever may be oscillated, such as with the intermittent or non-contact modes. The forces of interaction between the probe and the sample may also be measured as a function of distance by the monitoring of the deflection of the cantilever, providing that the spring constant of the lever arm is sufficiently calibrated.

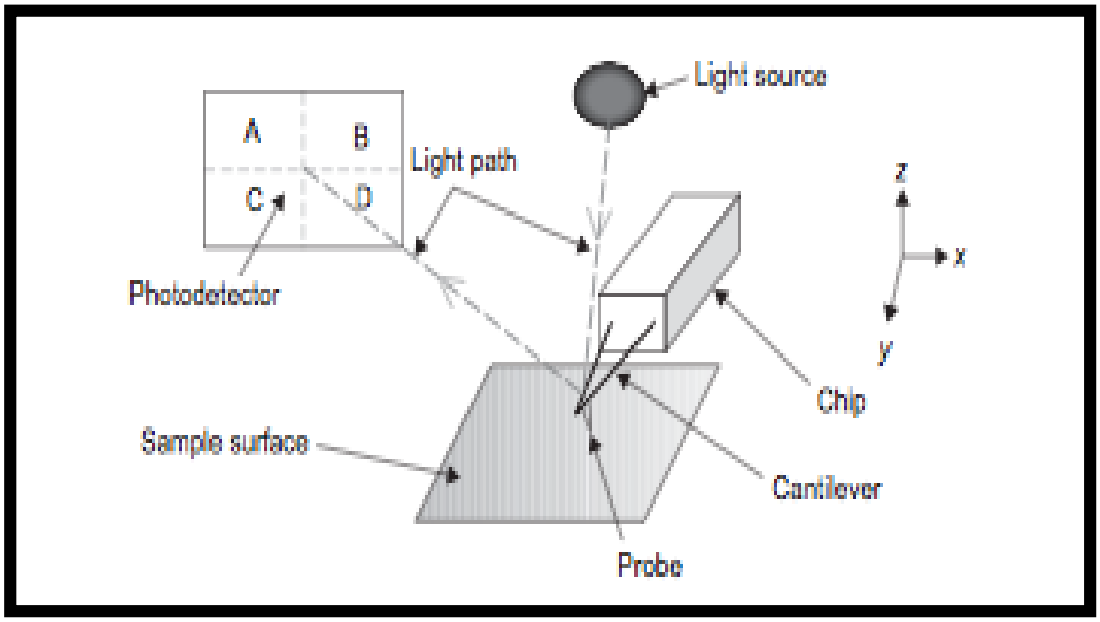

Figure 4.18: A schematic diagram of typical AFM system [36]

In Figure 4.18 the basic set-up of a typical AFM is shown. Cantilevers are commonly either V-shaped, as shown, or a rectangular, 'diving board' shaped and either made of silicon or silicon nitride. The cantilever has at its free end a sharp tip, which acts as the probe of interactions. This probe is most commonly in the form of a square-based pyramid or a cylindrical cone. Typically the upper surface of the cantilever, opposite to the tip, is coated with a thin reflective surface, usually of either gold (Au) or aluminium (Al). A few examples of different configurations for levers and probes are shown in Figure 4.19.

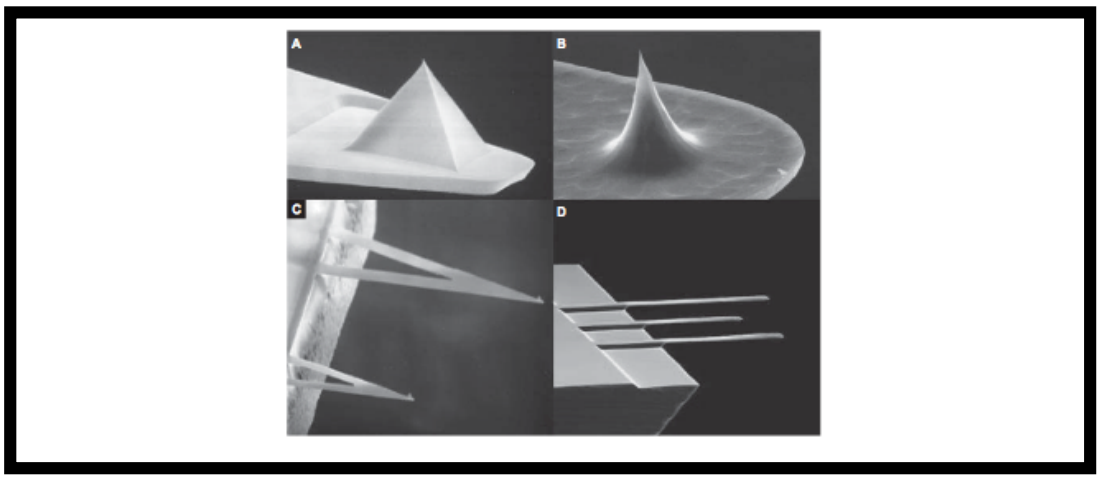

Figure 4.19: Different configurations for AFM cantilevers [36]

The probe is brought into and out of contact with the sample surface by the use of a piezocrystal upon which either the cantilever chip or the surface itself is mounted, depending upon the particular system being used (these two configurations are referred to as tip-scanning or surface- scanning, respectively). Movement in this direction is conventionally referred to as the *z*-axis. A beam of laser light is reflected from the reverse (uppermost) side of the cantilever onto a position-sensitive photodetector. Any deflection of the cantilever will produce a change in the position of the laser spot on the photodetector, allowing changes to the deflection to be monitored.

In Figure 4.20 the force regimes under which the main imaging modes occur are illustrated schematically. At large separations there are no net forces acting between the probe and the sample surface. As probe and surface approach each other, attractive van der Waals interactions begin to pull the probe towards the surface. As contact is made, the net interaction becomes repulsive as electron shells in atoms in the opposing surfaces repel each other. In this figure, the repulsive forces are shown as being positive and attractive forces negative.

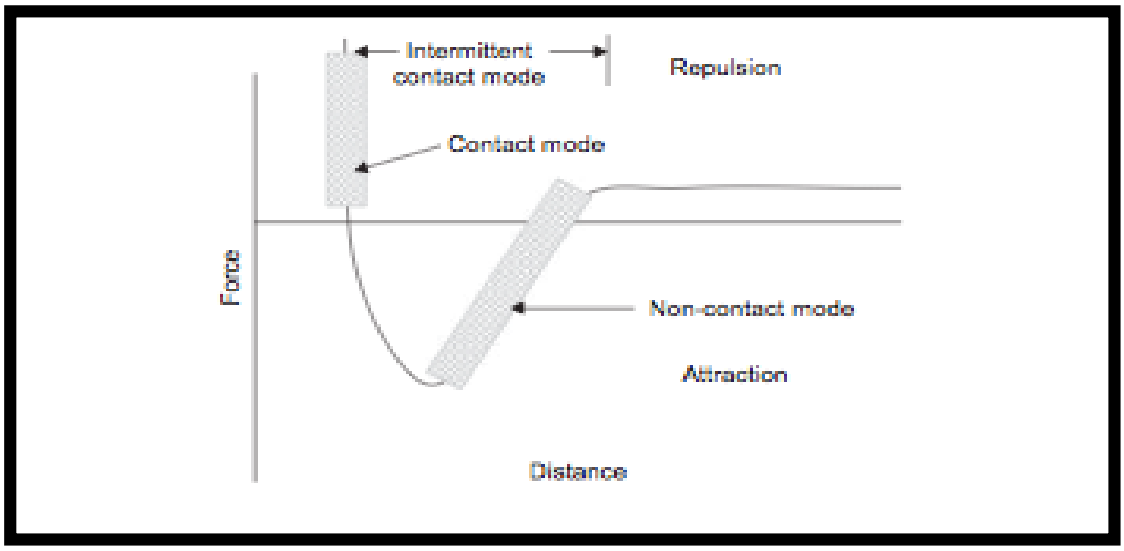

Figure 4.20: Relationship between force and probe distance from sample surface [36]

Contact mode imaging is so called because the probe remains in contact with the sample at all times. There are two variations on this technique: constant force and variable force. With constant force mode, a feedback mechanism is utilised to keep the deflection, and hence force, of the cantilever constant. As the cantilever is deflected the *z*-height is altered to cause a return to the original deflection or ‘ set point ’. The change in *z*-position is monitored and this information as a function of the *x*,*y*-position is used to create a topographical image of the sample surface. For variable force imaging, the feedback mechanisms are switched off so that *z*-height remains constant and the deflection is monitored to produce a topographic image. This mode can be used only on samples which are relatively smooth with low lying surface features, but for surfaces to which it is applicable, it can provide images with a sharper resolution than constant force mode.

Contact mode is often the mode of choice when imaging a hard and relatively flat surface due to its simplicity of operation. Several drawbacks include lateral forces may cause damage to the probe or the sample, or also result from adhesive or frictional forces between the probe and the sample. This can also lead to a decrease in the resolution of images and can cause deformation of the sample, leading to an underestimation of the height of surface features, as well as causing an increase in the area of contact between the probe and the surface.

In the tapping mode, the cantilever is allowed to oscillate at a value close to its resonant frequency. When the oscillations occur close to a sample surface, the probe will repeatedly engage and disengage with the surface, restricting the amplitude of oscillation. As the surface is scanned, the oscillatory amplitude of the cantilever will change as it encounters differing topography. By using a feedback mechanism to alter the *z*-height of the piezocrystal and maintain constant amplitude, an image of the surface topography may be obtained in a similar manner as with contact mode imaging. In this way as the probe is scanned across the surface, lateral forces are greatly reduced compared with the contact mode. When using tapping mode in air, capillary forces due to thin layers of adsorbed water on surfaces, as well as any other

adhesive forces, which may be present, have to be overcome. If the restoring force of the cantilever due to its deflection is insufficient to overcome adhesion between the probe and the surface, then the probe will be dragged along the surface in an inadvertent contact mode. As a result, for this mode in air the spring constants of AFM cantilevers are by necessity several orders of magnitude greater than those used for either tapping mode in liquid or contact mode (typically in the range of 0.01–2 Nm^{-1} for contact mode to 20–75 Nm^{-1} for tapping in air) [36].

4.14.1 AFM for Cantilever Calibration

By measuring the resonance behaviour of cantilevers, the manufacturing variability in the material properties of the cantilevers can be at least to some extent taken into account. This leads to a more reliable calculation for the spring constant of a cantilever surrounded by a fluid environment, such as air, from the following relationship [37, 38]:

$$k = 0.1906\rho_f b^2 l Q \Gamma_i(\omega_f)\omega^2 \quad (1.5) \qquad (4.25)$$

where ρ_f is the density of the surrounding fluid; Q the quality factor (a measure of the sharpness of the resonance peak); Γi the imaginary component of the hydrodynamic function, dependent upon the Reynolds number of the fluid; and ω_f the fundamental resonance frequency of the cantilever.

A very simple and straightforward method of calibrating the cantilever spring constant is to press the cantilever to be calibrated against another, reference, cantilever of known k (Figure 4.21), generating a force versus deflection graph also knows as the force curve. The cantilever behaves linearly or like a Hookean spring, thus the formula F=kx is applicable and the slope from the force curve can be used to determine the spring constant of the cantilever.

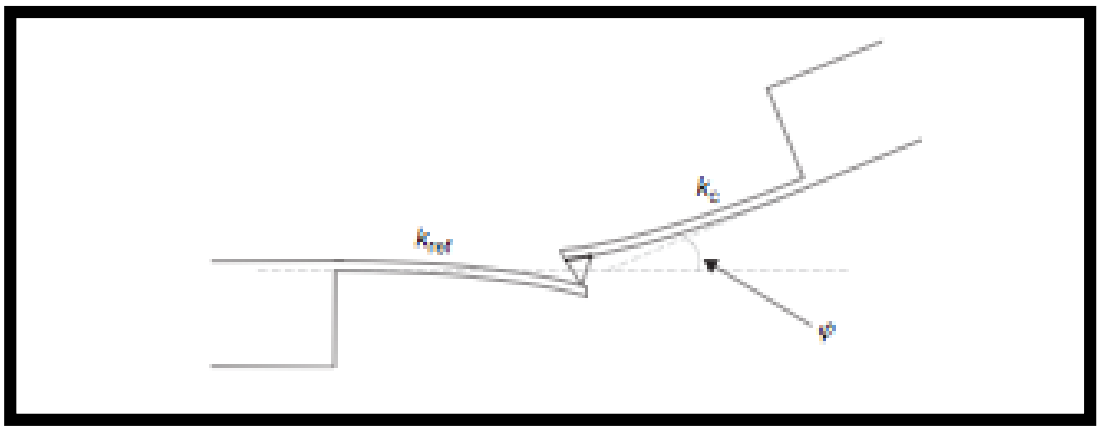

Figure 4.21: The pressing method to calibrate the AFM cantilever spring constant [36]

When the two levers are pressed together, the slope of the contact region on the force curve will be the result of the deflection of both levers. As a result, comparison of this slope with the slope obtained when pressed against a hard surface, which will not appreciably deform under the pressure exerted upon it, will allow the calculation of the unknown spring constant, providing that the same optical lever set-up and hence its sensitivity remains unchanged between each set of measurements:

$$k_c = k_{ref}\left(\frac{\delta_{hard} - \delta_{ref}}{\delta_{ref} \times \cos\varphi}\right) \tag{4.26}$$

$$k_c = k_{ref}\left(\frac{\delta_{hard}}{\delta_{ref}} - 1\right) \tag{4.27}$$

where k_c and k_{ref} are the spring constants of the unknown and known reference levers, δ_{hard} and δ_{ref} the gradients of the contact regions of force curves against a hard surface and the reference lever, respectively, φ the angle between the two levers. Typically levers are mounted onto the AFM with an in-built tilt angle of approximately 10–12°, which is liable to give a value of

k varying from the true value by less than the experimental uncertainty. In addition, if care is taken to maintain the same angle between the lever and the experimental sample when calibrating the lever, then the apparent spring constant calculated by this method will be identical to the effective spring constant. As such the term cos φ can be ignored (Equation (4.27)). This is a quick and simple method to use and can be carried out where the instrumentation being used does not allow the measurement of the resonance spectrum of the cantilever.

One area where caution must be taken with the reference lever method is in the precise positioning of the two levers (Figure 4.21). Based on the equation

$$k = \frac{Et^2w}{4l^3} \tag{4.28}$$

where E is the Young's modulus of the lever and t,w, and l the thickness, width and length of the lever, respectively, *k* will vary inversely in relation to l^3. This means that if the cantilever to be calibrated overlaps with the reference lever, effectively reducing the length of the reference, the measurements obtained will be as though taken against a stiffer reference lever, leading to an underestimation of k_c. Another important factor to consider is that the stiffness of the unknown cantilever and the reference must be similar in order to get a truly accurate result. If one cantilever is much stiffer than the other, then the slope obtained from a force curve of the cantilevers pressed together will be dominated by the deflection of the softer lever. It has been suggested that one lever should not have a spring constant greater than the other by more than a factor of three [39] for this method to be effective [36].

4.15 References

[1] B. Baral, S.S.M Chan and R.B. Jackman, J, Vac. Sci. Technol. A14 2303 (1996)

[2] R.C. Jaeger, "Film Deposition". *Introduction to Microelectronic Fabrication*. Upper Saddle River: Prentice Hall, (2002)

[3] http://www.icmm.csic.es/fis/english/evaporacion_resistencia.html, (2010)

[4] http://www.photonics.ethz.ch/research/core_competences/technology/processing/etching, (2010)

[5] http://thephysicstutor.com/notes/html/p2-current-electricity.html, (2010)

[6] http://www.ece.gatech.edu/research/labs/vc/processes/devChar.html, (2010)

[7] S.P. Kounaves, Voltammetry Techniques, Dept. of Chemistry, Tufts University, (Ch. 37), p. 717, Settle, F.A. (ed.) Prentice Hall Publishers, 20 June (1997)

[8] A.J. Bard, L.R. Faulkner, *Electrochemical Methods: Fundamentals and Applications* (2 ed.). Wiley (2000)

[9] R.S. Nicholson, S. Irving, "Theory of Stationary Electrode Polarography. Single Scan and Cyclic Methods Applied to Reversible, Irreversible, and Kinetic Systems.". *Analytical Chemistry* **36** (4): 706–723 (1964)

[10] J. Heinze, "Cyclic Voltammetry-"Electrochemical Spectroscopy". New Analytical Methods (25)". *Angewandte Chemie International Edition in English* **23** (11): 831–847 (1984)

[11] P. Kissinger, W.R. Heineman, *Laboratory Techniques in Electroanalytical Chemistry, Second Edition, Revised and Expanded* (2 ed.). CRC (1996)

[12] Zoski, Cynthia G., *Handbook of Electrochemistry*. Elsevier Science (2007)

[13] R.S. Nicholson, S. Irving, "Theory of Stationary Electrode Polarography. Single Scan and Cyclic Methods Applied to Reversible, Irreversible, and Kinetic Systems". *Analytical Chemistry* **36** (4): 706–723 (1964)

[14] A. Hickling, "Studies in electrode polarisation. Part IV.-The automatic control of the potential of a working electrode". *Transactions of the Faraday Society* **38**: 27–33 (1942)

[15] http://en.wikipedia.org/wiki/Voltammetry, (2010)

[16] A.W. Bott, Electrochemistry of Semiconductors, *Current Separations 17:3, p. 87-91 (1998)*

[17] D.C. Graham, *Chem. Rev*., **41,** 441-2, (1947)

[18] R. Parsons, *Modern Aspects of Electrochemistry*, Vol. 1, p. 103. 3 (1954)

[19] P. Delahay, *Double Layer and Electrode Kinetics*, Wiley-Interscience, New York, 4 (1965)
[20] D.M. Mohilner in *Electroanalytical Chemistry*, A.J. Bard, Ed., Dekker, New York, p 241 (1966)
[21] B. Breyer and H.H. Bauer, *Alternating Current Polarography and Tensammetry*, *Chemical Analysis Series*, P.J. Elving and I.M. Kolthoff, Eds., Wiley-Interscience, New York, (1963)
[22] A.M. Bond, *Modern Polarographic Techniques in Analytical Chemistry*, Dekker, New York (1980)
[23] J.R. Macdonald, Impedance Spectroscopy, Wiley, New York (1987)
[24] A. Lasia, Electrochemical Impedance Spectroscopy and Its Applications, Modern Aspects of Electrochemistry, B. E. Conway, J. Bockris, and R.E. White, Edts., Kluwer Academic/Plenum Publishers, New York, Vol. 32, p. 143-248. Département de chimie, Université de Sherbrooke, Sherbrooke Québec (1999)
[25] Basics of Electrochemical Impedance Spectroscopy, Application Notes, Gamry Instruments, p.1-17, Sept (2010)
[26] http://www.vcbio.science.ru.nl/en/fesem/eds/ (2010)
[27] http://en.wikipedia.org/wiki/Scanning_electron_microscope (2010)
[28] J. Orloff, M. Utlaut, L. Swanson, High Resolution Focused Ion Beams: FIB and Its Applications, Kluwer Academic/Plenum Publishers, New York, NY (2003)
[29] N. Yao, Z.L. Wang, Chpt 9 Focused Ion Beam System—A Multifunctional Tool For Nanotechnology, Handbook of Microscopy for Nanotechnology, Springer – Verlag p. 250-254 (2005)
[30] http://en.wikipedia.org/wiki/Raman_spectroscopy (2010)
[31] G.J.Exarhos, G.E. McGuirre, Characterization of Semiconductor Materials – Principles and Methods, Chpt 5 p.244-248, Volume 1. William Andrew Publishing/Noyes (1989)
[32] D.H. Williams, I. Fleming, 'Spectroscopic methods in organic chemistry', p. 35-73, Third Edition, McGraw-Hill (UK), (1980)
[33] *R. M. Silverstein, G. C. Bassler, and T. C. Morrill,* Spectrometric Identification of Organic Compounds, *4th edition. New York: John Wiley & Sons, 1981, p. 166, by permission of John Wiley & Sons, Inc., (1981)*

[34] R. Kohli, K.L. Mittal, Developments in Surface Contamination and Cleaning - Fundamentals and Applied Aspects, p. 662-663, William Andrew Publishing (2008)
[35] P.J. Goodhew, J. Humphreys, R. Beanland, “Electron Microscopy and Analysis”, Third Edition, Taylor & Francis (2004)
[36] D. Johnson, H. Nidal, W.R. Bowen, “Basic Principles of Atomic Force Microscopy”, Chpt 1, p. 2-21, Elsevier (2009)
[37] J.E. Sader, Frequency response of cantilever beams immersed in viscous fluids with applications to the atomic force microscope, J. Appl. Phys. 84 (1) 64–76 (1998)
[38] J.E. Sader, J.W.N. Chon, P. Mulvaney, Calibration of rectangular atomic force microscopy cantilevers, Rev. Sci. Instrum. 70 (10), 3967–3969 (1999)
[39] C.T. Gibson, G.S. Watson, S. Myra, Determination of the spring constants of probes for force microscopy/spectroscopy, Nanotechnology 7, 259–262 (1996)

Chapter 5

Single Crystal Boron-doped i-δ-i Diamond Ion-Sensitive Field-Effect Transistor

5.1 Introduction

An ISFET resembles a metal-oxide-semiconductor FET (MOSFET) structure that has had the metal gate region removed, being replaced by an ionic solution and a partially immersed reference electrode. The introduction of an ion-sensitive layer onto the solution-device interface can lead to a measurable signal being generated in reaction to chemical stimuli. The site-binding model for ISFET operation involves modification of hydroxyl (OH) sites created when the device is immersed in aqueous solutions. The originally neutral hydroxyl OH site is considered to assume a positive charge (OH_2^+) when protonated and negative (O^-) when it donates a proton to the solution. The concentration level of the adsorbed H^+ ions i.e. the resulting state of charge on the surface, is then responsible for modulating the underlying drain-to-source current within the channel-region of the FET at fixed gate biases.

Advances in medical diagnostics are creating the need for novel miniaturised pH sensors, which can be used for *in-vivo* patient monitoring [1]. Requirements for such a device are materials biocompatibility, high measurement precision (sensitivity and stability) and sub-second response times. Ion-sensitive field effect transistors (ISFETs) have been explored in this context [2]. ISFETs have also been usefully deployed for cellular recording from living tissue [3]. However, when fabricated from conventional semiconductors complex issues relating to biocompatibility arise, and sensitivity is often a problem. Diamond may offer a solution here being biocompatible [4-12] and a wide band-gap semiconductor, a property that offers the prospect of improved signal-to-noise ratios in devices [13]. Diamond-based ISFETs that have been reported to date largely rely on so-called 'surface conductivity', where an adsorbate covered hydrogen-terminated surface leads to the generation of a p-type surface [14], for the formation of the active channel region of the transistor [15-26]. However, the H-terminated diamond surface used is not chemically stable and can be oxidised in electrolyte solutions under anodic polarization [27].

Attempts to use a more conventional approach for carrier generation are somewhat undermined by activation energy required by available dopants; boron is readily incorporated into diamond, but forms an acceptor state some 0.37eV away from the valence band edge, meaning few free carriers exist at room temperature [28]. At high doping levels an impurity band emerges, removing the need for significant thermal activation, but conductivity then results through carrier 'hopping' with the associated low carrier mobility values [28]. A possible solution to this problem is to use the concept of δ-doping that has been widely used within III-V semiconductor technology [29]. This involves the formation of very thin, highly doped regions within a homostructure. Provided the doped, or δ, layer is only a few atom layers thick, carriers will move in a region close to, but outside, this layer. The resultant separation between carriers and the donor or acceptor atoms that created them leads to enhanced mobility. From a quantum perspective the δ-layer distribution must be less than the free carrier de Broglie wavelength, thereby creating a V-shaped Coulomb potential well in the conduction band, leading to sub-band formation [29]; as the sub-band index increases so does the spatial extent of the wavefunction (Figure 5.1), further reducing the strength of ionized impurity scattering. Since the δ-layer is ideally heavily doped, in the case of diamond the problem associated with the otherwise high activation energy is overcome, with the prospect of high mobility hole transport outside of the δ-layer itself. The use of diamond δ-doping for the realisation of high frequency FETs has recently been reviewed [30].

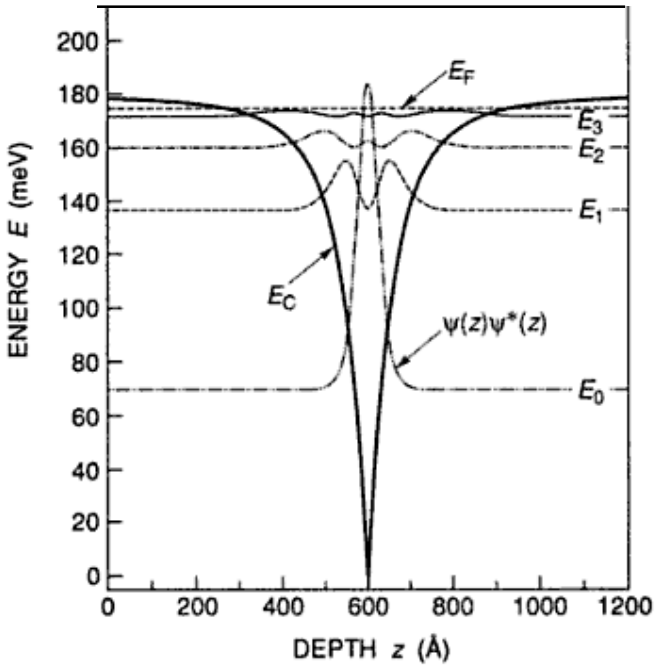

Figure 5.1: Self-consistently calculated sub-band energies and wavefunctions of δ-doped GaAs with a sheet donor concentration of 5.0 x 10^{12} cm^{-2} (Schubert *et al*. [29]). The δ-doped layer here is 600Å or 60nm below the surface.

To date no reports on the use of single crystal capped δ-doped layers for the fabrication of ISFETs have been made. Denisenko and co-workers [31] used an uncapped ~5nm δ-layer for the ISFET structure but electrochemical characterization was done on a heavily boron doped diamond at some 400nm thick and both in direct contact with the solution. The high doping level used for the diamond electrode was to avoid the problem associated with the otherwise high activation energy of the acceptor state and to mimic the uncapped δ-doped ISFET electrolyte-semiconductor interface. The same team used nanocrystalline diamond (NCD) substrates with an NCD δ-doped boron layer, which C-V measurements suggested to be of the order of 1nm wide (FWHM) [32]. ISFET measurements were again made with the doped layer in direct contact with the solution. In both cases the ISFET structures showed sensitivity to the pH of the test solutions, with a shift in the threshold voltage of 50mV/pH, which is close to Nernst's limit. However, the channel currents measured did not saturate with the highest drain-source voltages used, indicating that the condition of 'pinch-off' could not be achieved. This

chapter presents upon the fabrication and characterisation of single crystal **δ**-doped diamond ISFETs with an intrinsic cap between the **δ**-layer of thickness 5nm and 3.2nm and the solution. These devices are labelled as δ3-ISFET and δ4-ISFET respectively. An uncapped ISFET based on a thinner **δ**-layer (3.2nm) substrate was also fabricated as a benchmarking measure and is referred to as δ2-ISFET.

5.2 Device fabrication

Microwave plasma-enhanced CVD was used to produce both intrinsic and boron-doped layers on type Ib synthetic single crystal diamond samples by Element Six Ltd, using growth conditions similar to those described previously [33]. Following the growth of a 100nm thick i-layer on the Ib substrate, a δ-layer was grown, which in the case of the three samples used in this study have FWHM thicknesses of 5nm and 3.2nm as judged by SIMS. Onto the 5nm and 3.2nm δ-layers was then grown an intrinsic capping layer of 15-20nm thicknesses whilst one 3.2nm δ-layers was removed and kept uncapped. The boron δ-layer was grown in a separate MPECVD system to avoid residual background boron doping the intrinsic diamond layers. Hall effect measurements and SIMS analysis showed the δ-layer to have boron concentrations of 4 to 7 x 10^{20} atoms cm^{-3}. Relevant Hall effect data are also presented in Table 3.1. Prior to use all samples were subjected to wet chemical treatments as described in Chapter 2. Such aggressive cleaning methods are known to leave the surface free from organic contaminants and in a strongly oxidised state [34], removing any unintentional or residual hydrogen-termination thus avoiding so-called 'surface conductivity' [35]. This was then followed by the standard de-greasing procedure involving acetone, isopropanol and de-ionized water.

Device	Carrier Density (cm^{-2}) (300K)	δ-layer thickness (FWHM)	Carrier concentrations (cm^{-3})	SIMS – carrier concentrations (cm^{-3})	Mobilty (cm^2/V-s) (300K)
δ2-ISFET	2.5×10^{14}	3.2nm	6×10^{20}	N/A	0.8
δ3-ISFET	1.8×10^{14}	5nm	4×10^{20}	4×10^{20}	3-4
δ4-ISFET	2.3×10^{14}	3.2nm	7×10^{20}	7×10^{20}	2-3

Table 5.1: Carrier concentrations (Hall effect) and chemically attained boron concentrations (SIMS) of δ-structure diamond ISFETs [36]

The transistor structure was realised with the formation of a 0.5mm wide, 2.5mm long and an elevation of ~40nm conductive mesa-like channel etched by pure Argon plasma in the ICP-RIE (STS Shallow Etcher) chamber using Al as an etch mask; patterned by means of a shadow mask. The Argon plasma was formed under a coil power of 300W and platen power set at 100W, gas flow rate of 45sccm and in a vacuum pressure of 10mTorr, producing an etch rate of ~0.7-1nm/min. The substrate was kept at constant temperature of 20^{O}C. A pair of Cr/Au bi-layers on the opposing end of the capping layer act as drain and source contacts were deposited using the Bell Jar A306 thermal evaporator unit. The ohmic characteristics were then formed by annealing at a temperature of 750^{o}C for 10 minutes in 10^{-6} Torr vacuum condition [37], allowing the formation of a thin carbide layer penetrating the intrinsic cap accessing the **δ-**layer and all available conduction paths therein.

Fabrication steps

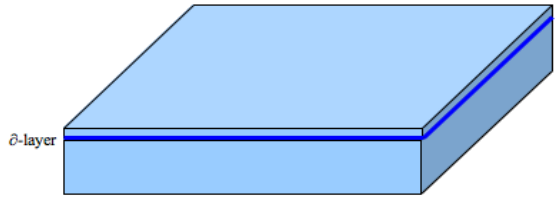

E6 Capped δ substrates

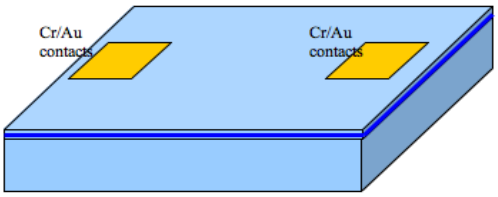

Cr/Au ohmic contact metal deposition by thermal evaporation

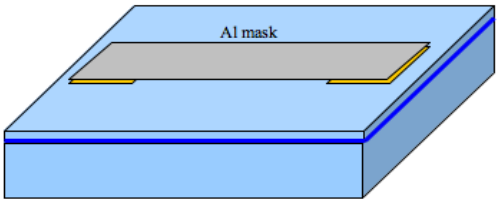

Al Etch Mask deposition by thermal evaporation

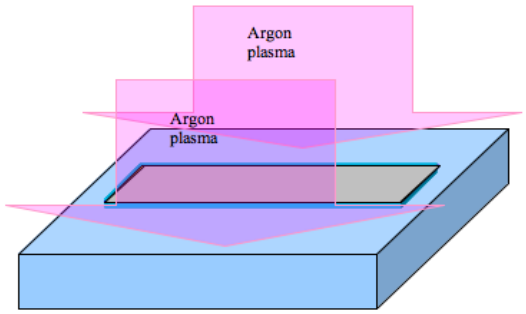

Argon plasma ICP-RIE mesa-etching

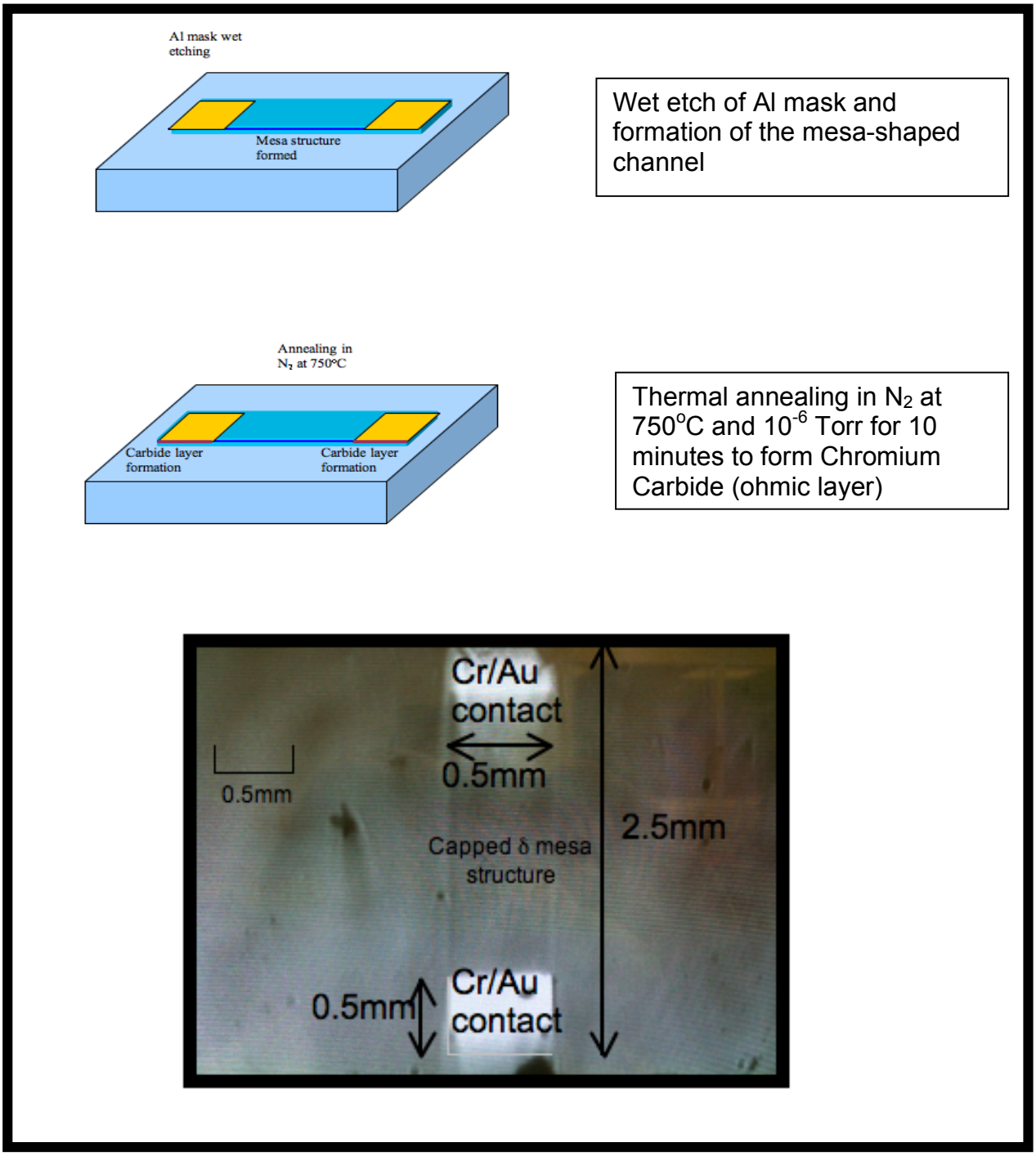

Figure 5.2: (a) Schematic illustration of the fabrication steps for both capped and uncapped ISFET structures (b) a magnified optical image of the real device.

A polytetrafluoroethylene (PTFE) 2-part housing with a sealing silicone rubber gasket was used to support the ISFET enabling large and robust electrical contacts to be made with the aid of thin gold wires pressed to the source and drain contacts surface which remained isolated from the exposed gate region

of the device, above which solutions could be placed (Figure 5.3). The effective gate area is designed to be 0.5mm^2. An Ag/AgCl reference electrode was positioned in the solution above the intrinsic diamond gate.

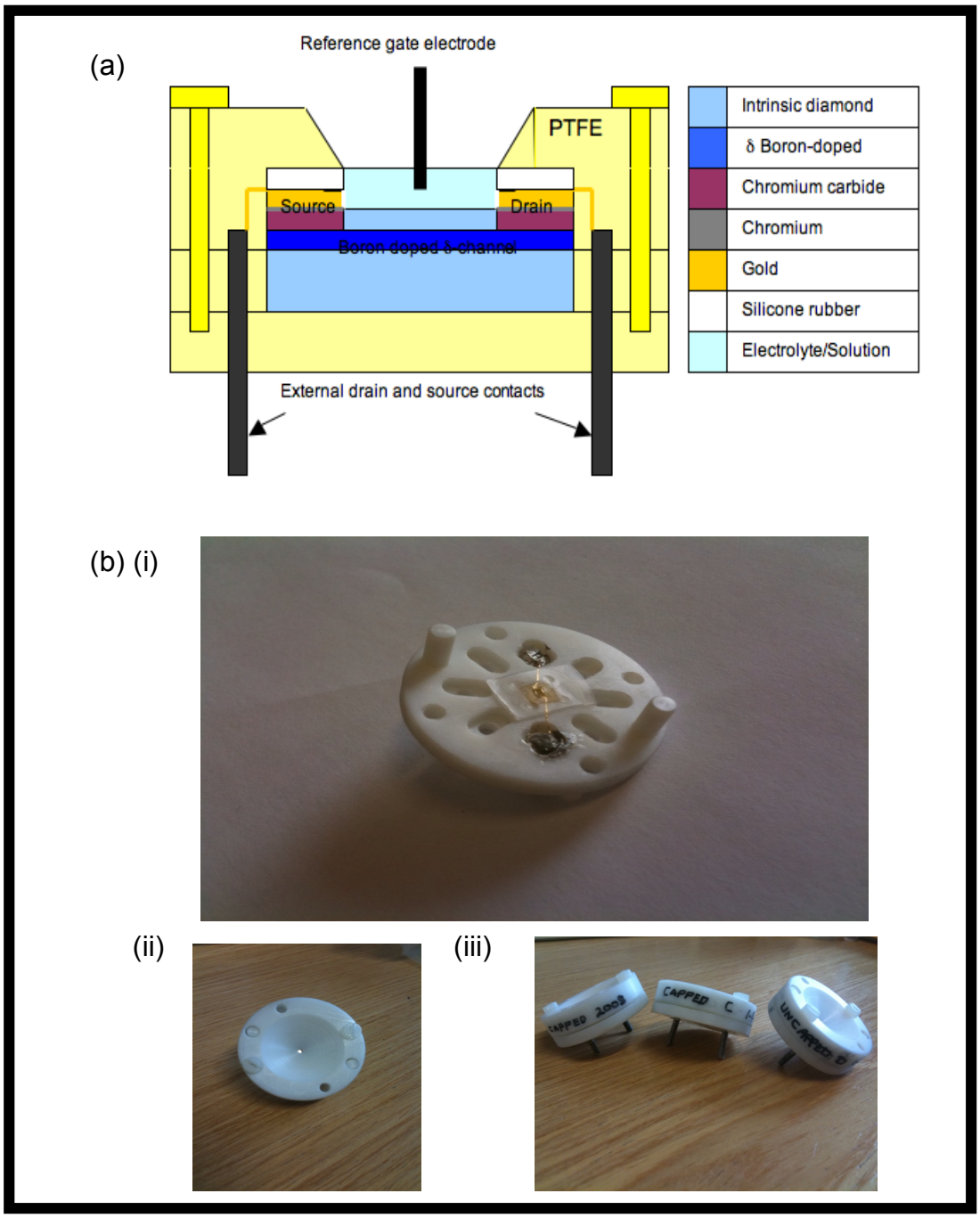

Figure 5.3: (a) A cross sectional schematic of the robust PTFE-cased ISFET design (b) the real devices (i) device mounted (ii) and (iii) enclosed casing

5.3 Experimental methods

Cyclic voltammetry, electrochemical impedance spectroscopy (Mott-Schottky, and Bode plots) and current-voltage measurements ('dry' resistive, output, transfer and cyclic pH I-V characteristics) were used to comprehensively determine the electrochemical and electrical characteristics of the ISFETs; a 956 Autolab III/Fr2 Potentiostat (Eco-Chemie) and a Keithley 4200 I-V kit were respectively used throughout. A 0.1M HNO_3 solution was used for cyclic voltammetry and electrochemical impedance spectroscopy using the 3-electrode electrochemical cell arrangement (as illustrated in Chapter 4) consisting the Ag/AgCl reference electrode (0.205 V vs Normal Hydrogen Electrode (NHE)), a platinum counter electrode and the diamond ISFET as the working electrode. Electrical characteristics and pH sensitivity measurements were done in buffer solutions of pH 2 and pH 10 with the Ag/AgCl reference electrode assuming the gating role. In reference to the potential window revealed by the cyclic voltammetry, the range of the applied external drain and gate voltages were determined. The uncapped ISFET was only electrically characterized here.

5.4 Results

Cyclic voltammetry measurements were performed on the capped ISFET structures in 0.1M H_2NO_3 solution. In cyclic voltammetry, the electrode potential ramps linearly versus time. The potential is measured between the reference electrode and the working electrode and the current is measured between the working electrode and the counter electrode. This data is then plotted as current density (I/cm^2) vs. potential (V), as shown in Figure 5.4(a), (b) and (c); no significant current flow occurs between the values of +1.5 and -0.5V producing an effective potential window of ~2V for ISFET operation. Beyond these values the current is seen to sharply increase. The curves are similar for both forward and reverse direction voltage scans.

Application of a drain-source voltage (V_{DS}) creates a drain-source current (I_{DS}), which can be modulated by application of a gate voltage, via the

reference electrode (V_{GS}). The resulting output characteristics are shown in Figure 5.5(a), (b) and (c). In all cases I_{DS} increases with V_{DS} in a slightly non-linear fashion, with the exception of δ2-ISFET, which remains virtually ohmic. All output characteristics are referenced against measurements made in air. Typically transistors are operated in the saturation regime, where further increases in V_{DS} no longer affect the value of I_{DS}; there is evidence showing the device is approaching the saturation regime within the allowable bias window as indicated by the decrease of the gradients on the I_{DS} vs V_{DS} graph, which is limited by the onset of a redox current in the FET gate area. The drain currents for δ4-ISFET, δ3-ISFET and δ2-ISFET are dependent on the gate bias at a rate of 24%, 20% and 4.4% for every ΔV_G of 1V in pH 2 respectively and shows increase in magnitude with more negative potential. The pH sensitivities of the devices are demonstrated in Figure 5.6(a) (b) and (c), where the drain current (I_{DS}) is plotted against the gate potential (V_{GS}) for pH levels of 2 and 10. A shift of 0.44, 0.42 and 0.38V over eight pH levels can be observed, approximating to 55.2, 52.5 and 47mV/pH. Reproducibility of the IV characteristics within 2% for the capped δ-ISFETs was evident over 3 cycles between pH 2 and pH 10 as seen in Figure 5.7. The IV characteristics of the uncapped δ2-ISFET reached stability only after an initial drift between the first and second cycle.

In addition to I-V characterization, it can be informative to measure the changes in capacitance with voltage of the capped ISFET in solution. A small ac signal is applied on top of the gate voltage and a plot of $1/C^2$ vs V_{GS} made (Mott-Schottky plot); this is shown in Figure 5.8 for an ac frequency of 1kHz. The linear projection of the plots shown by the dotted line on Figure 5.8(a) and (b) gives flat-band voltages (V_{FB}) equal to +4.74V and +3.76V vs Ag/AgCl in the (0.1M) HNO_3 solution for δ3-ISFET and δ4-ISFET respectively There are three or four capacitances may be considered, that of the double layer, capping layer, the cap-δ interface and the space charge region. Since these capacitance values are in series, the total capacitance is the sum of their reciprocals.

Further insight into the operation of the ISFET devices can come from impedance measurements. In a so-called 'Bode' plot the impedance is plotted with log frequency on the x-axis and both the absolute value of the impedance ($|Z| = Z_0$) and phase-shift on the y-axis. This information for measurement in 0.1M H_2NO_3 solution is shown in Figure 5.9(a) and (b); whilst the phase angle can be seen to peak at a given frequency, the impedance value decreases with increasing frequency.

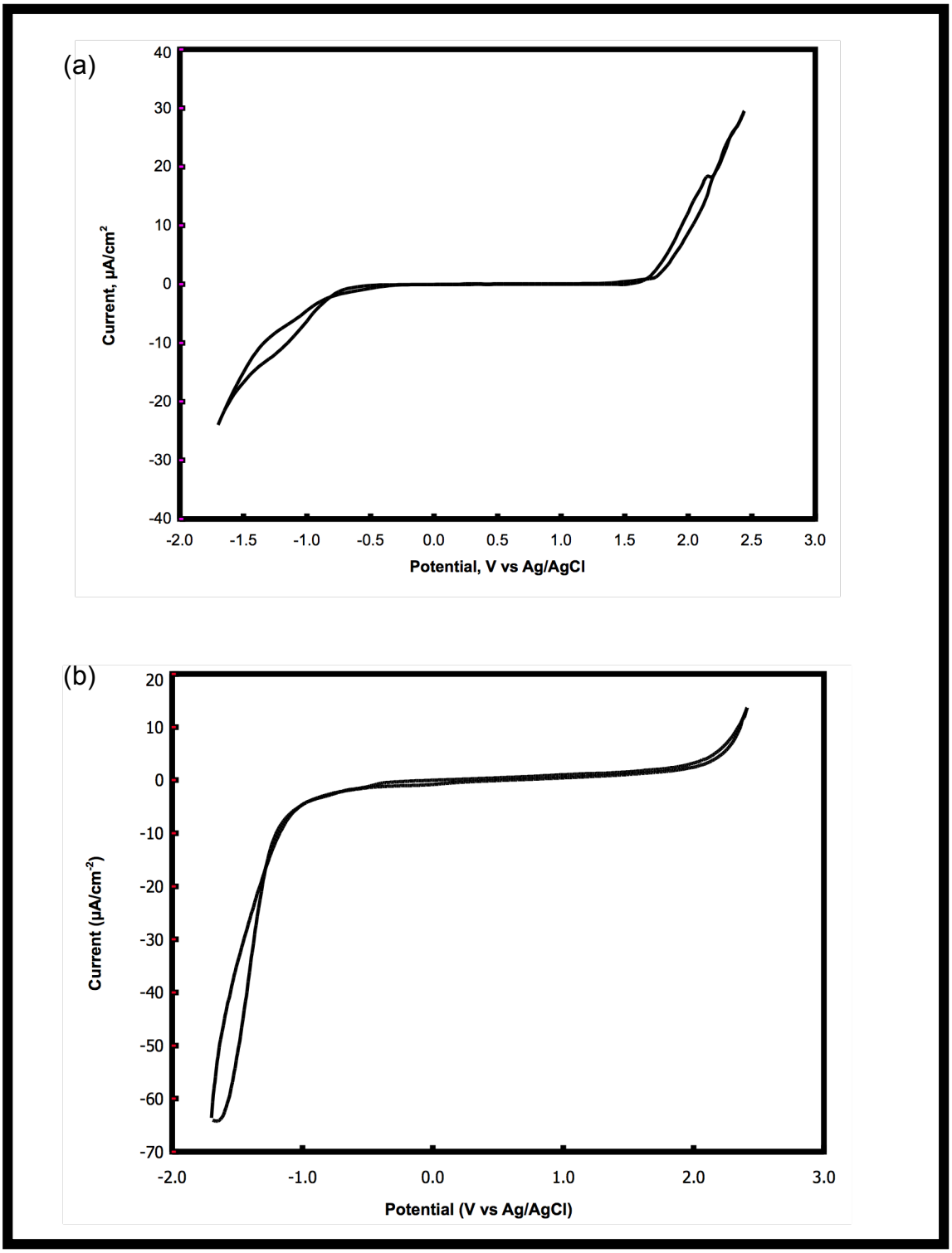

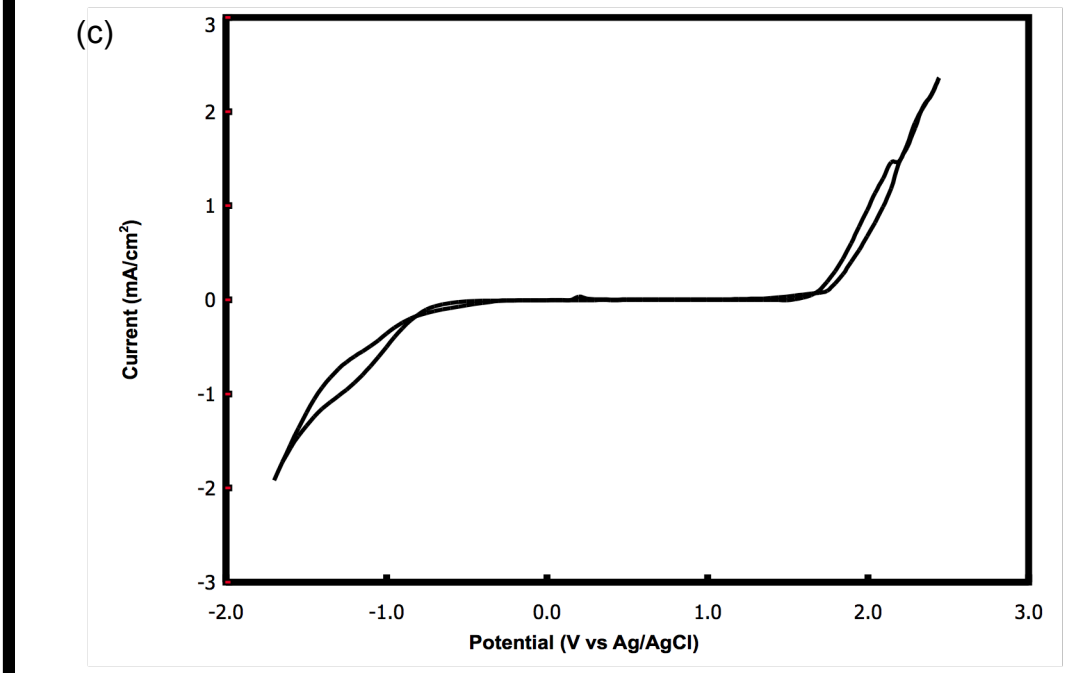

Figure 5.4: Cyclic voltammetry of (a) δ3-ISFET, (b) δ4-ISFET and (c) δ2-ISFET in 0.1M H_2NO_3 solution

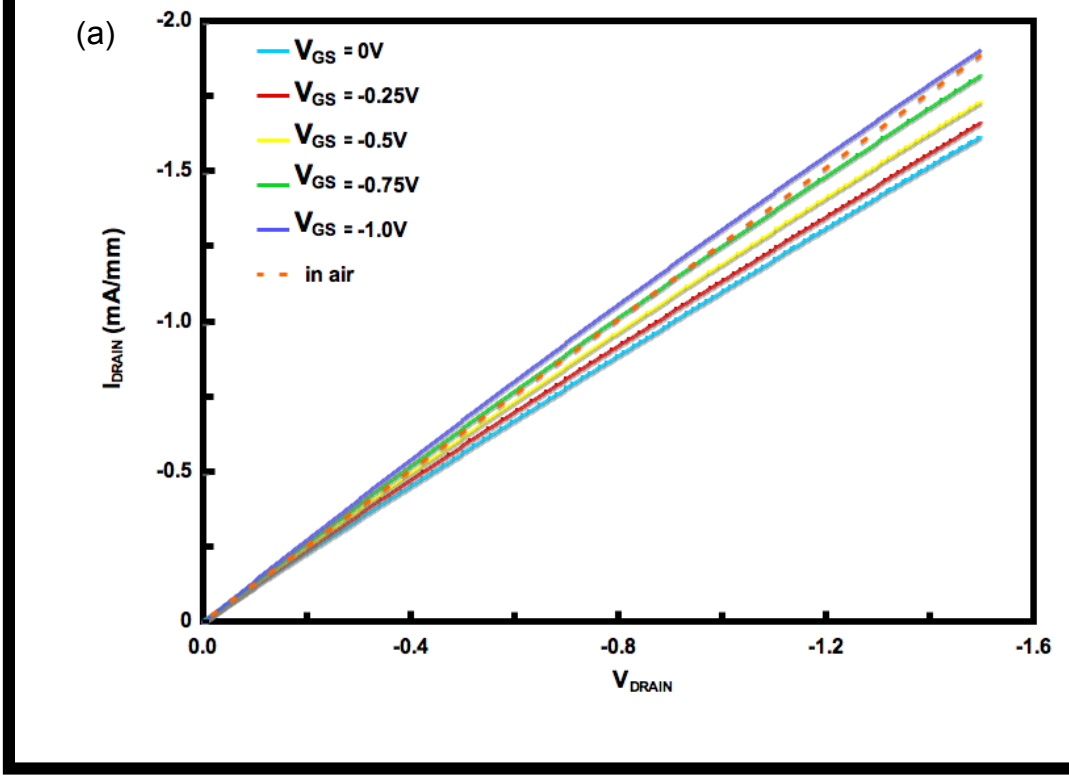

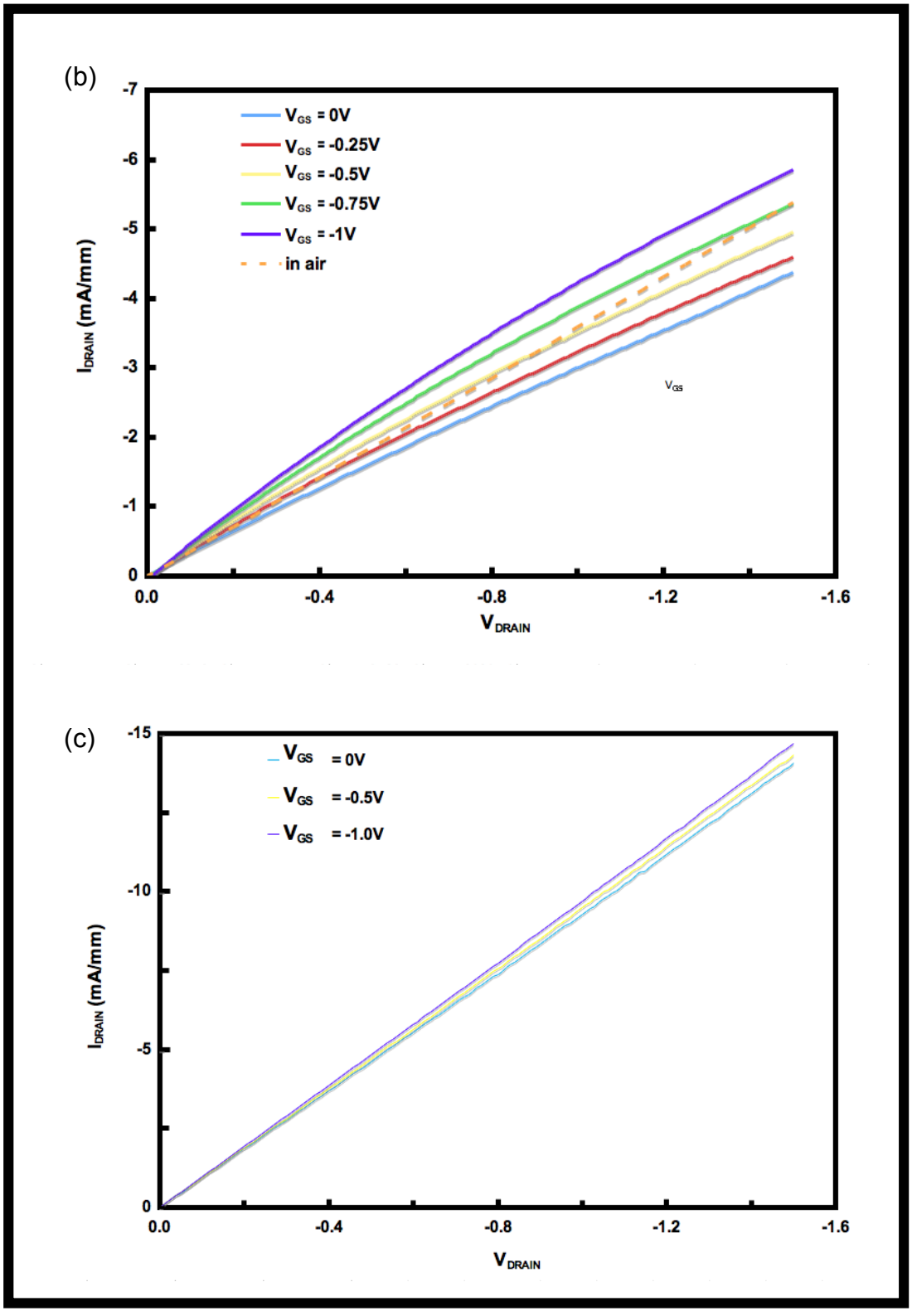

Figure 5.5: The output characteristics of (a) δ3-ISFET (b) δ4-ISFET (c) δ2-ISFET in pH2 buffer solution

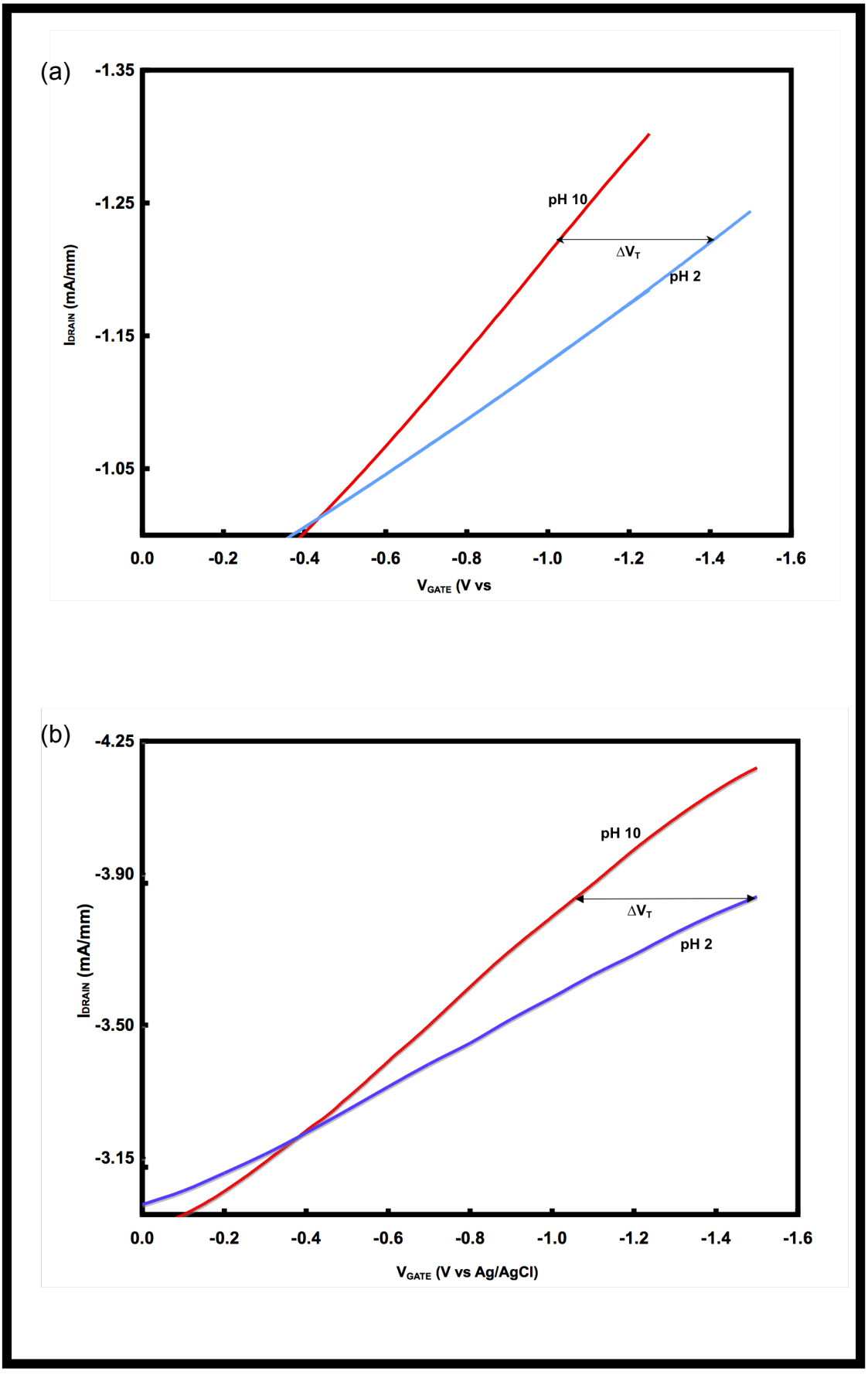
(a)
-1.35
-1.25
-1.15
-1.05
I_{DRAIN} (mA/mm)
pH 10
ΔV_T
pH 2
0.0
-0.2
-0.4
-0.6
-0.8
-1.0
-1.2
-1.4
-1.6
V_{GATE} (V vs
(b)
-4.25
-3.90
-3.50
-3.15
I_{DRAIN} (mA/mm)
pH 10
ΔV_T
pH 2
0.0
-0.2
-0.4
-0.6
-0.8
-1.0
-1.2
-1.4
-1.6
V_{GATE} (V vs Ag/AgCl)

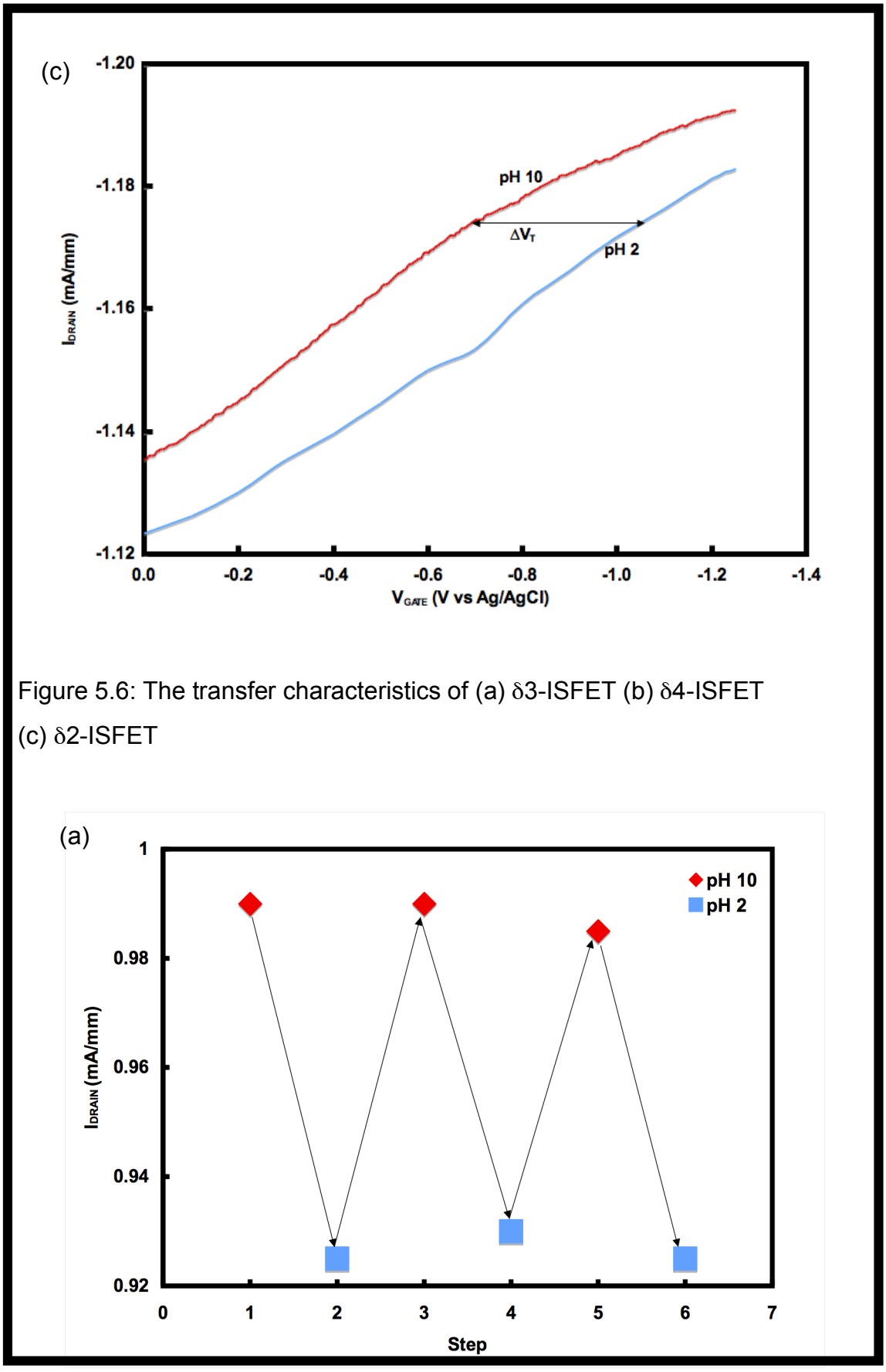

Figure 5.6: The transfer characteristics of (a) δ3-ISFET (b) δ4-ISFET (c) δ2-ISFET

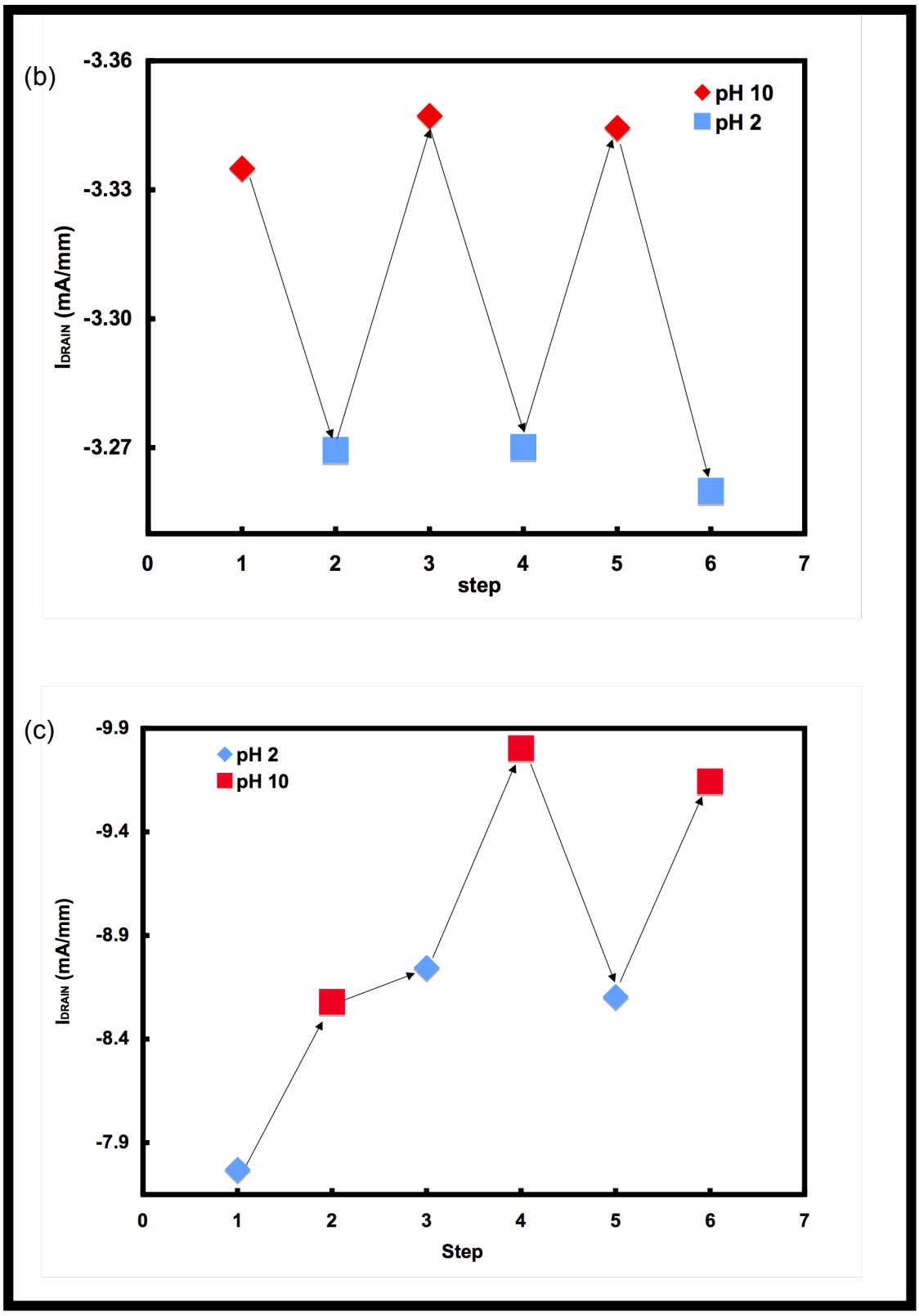

Figure 5.7: Sequence of pH tests with (a) δ3-ISFET (b) δ4-ISFET (c) δ2-ISFET

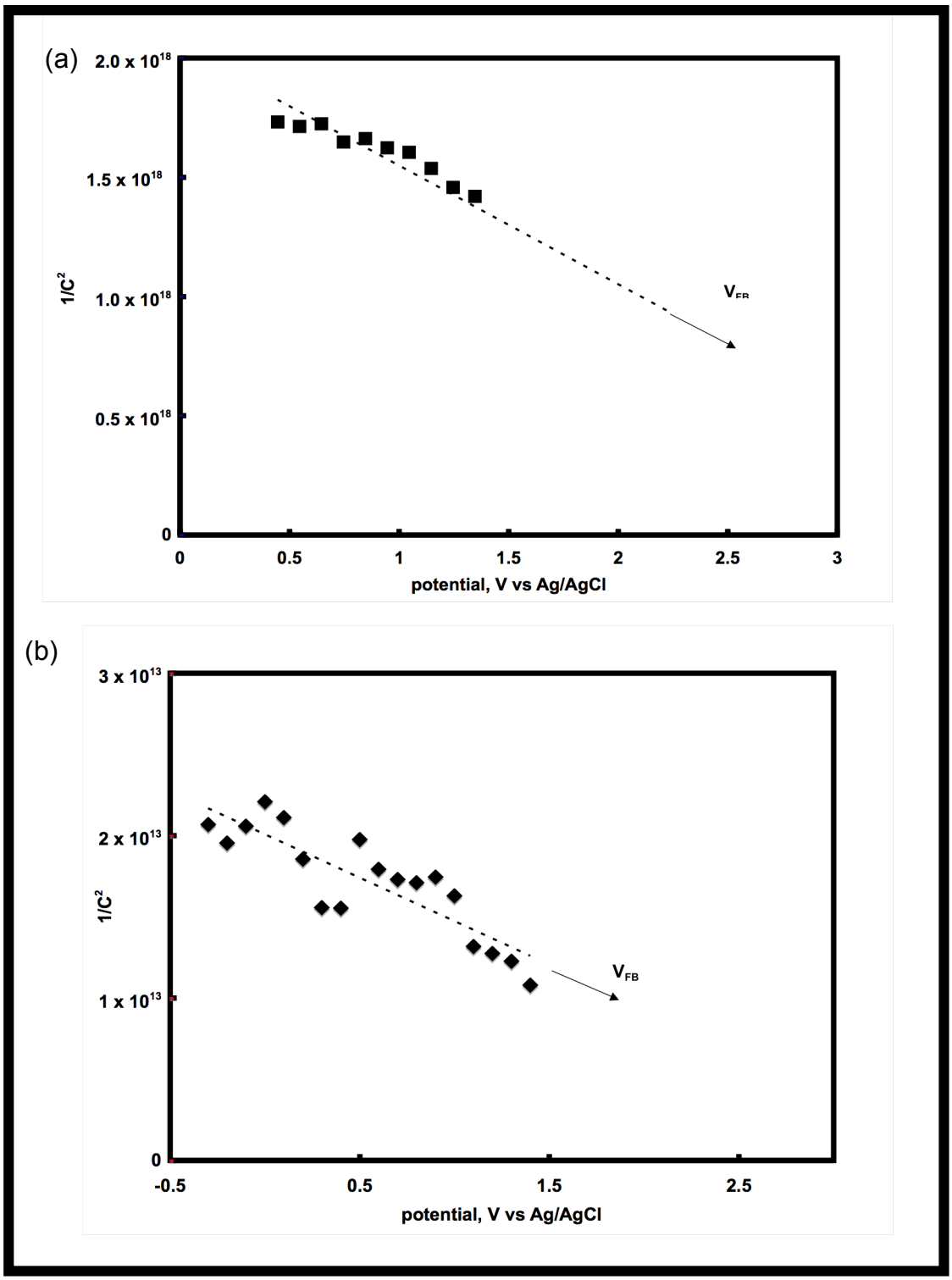

Figure 5.8: Capacitance-voltage plot of (a) δ3-ISFET and (b) δ3-ISFET in 0.1M H_2NO_3 solution. The V_{FB} is projected to be 4.72 V and 3.74V respectively.

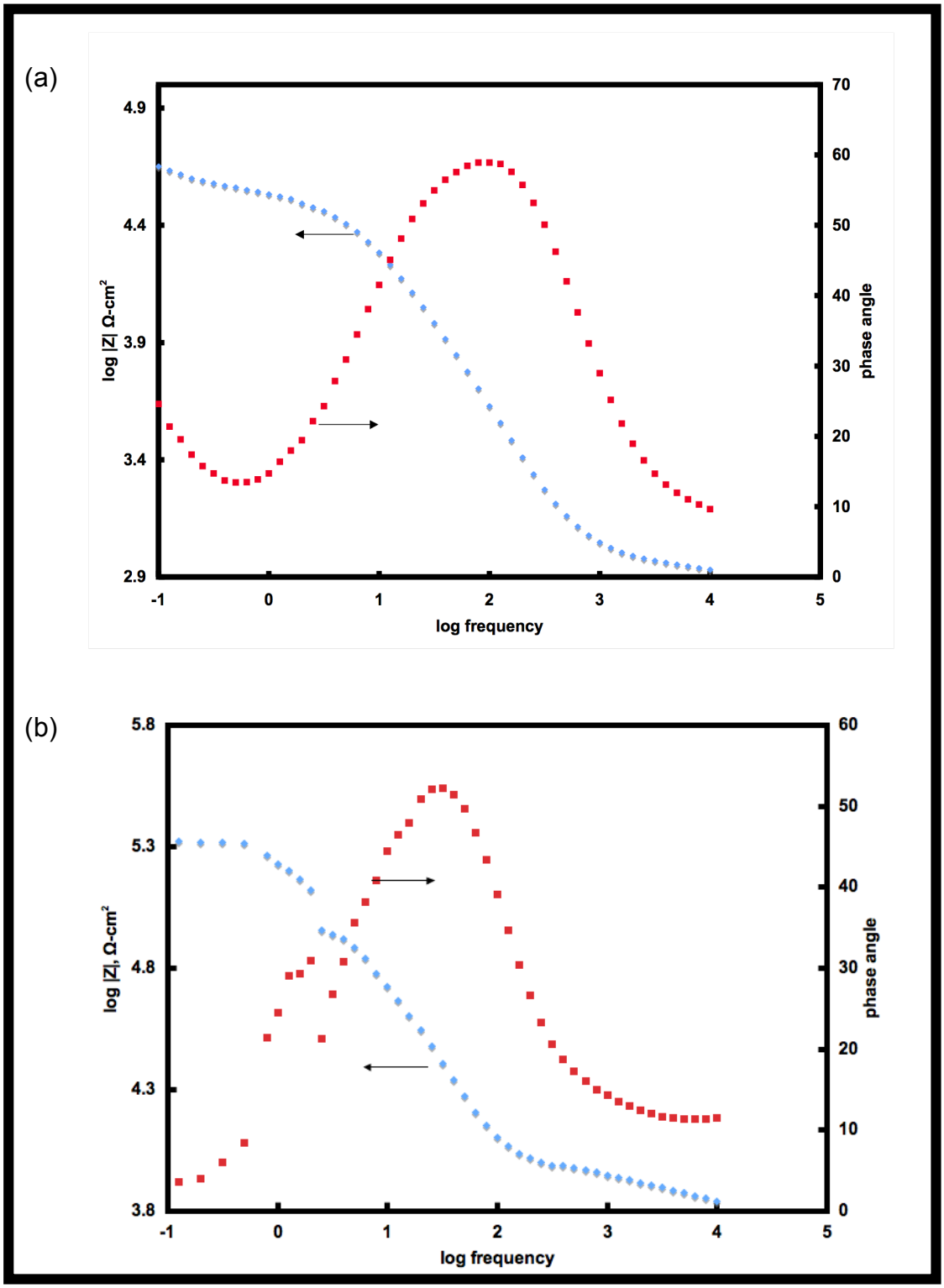

Figure 5.9 Bode plot for (a) δ4-ISFET and (b) δ3-ISFET in a 0.1M HNO_3 solution at 0V potential vs Ag/AgCl. The fitting parameters are listed in Table 5.2.

5.5 Discussion

The linear cyclic-voltammetry characteristics shown in figure 5.4(a), (b) and (c) indicate a usable potential window in aqueous solutions of ΔV_G^{max} = 2V, with current blocking at levels between 10^{-9} – 10^{-8} A/cm^2 over the potential window. At large positive and negative biases, the anodic and cathodic current can be observed. The exponential current spikes are manifestation of the oxygen and hydrogen evolutions involving electron transfer between the ions in the solution and the diamond electrodes occurring at applied overpotentials.

Observing the output characteristics, the drain currents for δ4-ISFET and δ3-ISFET exhibit hints of saturating with increasing drain-source voltage, indicating non-ohmic channel conductance within the non-redox operating voltages here (Figure 5.5(a) and (b)). The non-linearity in the output characteristics of δ4-ISFET is more pronounced indicating better depleting action by the applied gate voltage that in turn is placated by the improved interface between δ-layer and the intrinsic capping layer [38]. In normal FET operation asymmetry in the conductive region of the channel caused by high V_{DS} values causes channel 'pinch-off' and saturation of the drain current; over the values of V_{DS} used here the process or the onset of 'pinching-off' has been observed. Duplicating the shortcomings displayed by the uncapped ISFET fabricated and tested by Denisenko *et al* [31], δ2-ISFET shows only a modulation of linear characteristics with no signs of channel pinching. The sheet charge density of the channel was determined to be 2.5, 1.8 and 2.3 x 10^{14} cm^{-2} for δ2-ISFET, δ3-ISFET, and δ4-ISFET [36] are around 2.8, 2 and 2.6 times higher than the previously reported un-capped ISFET device [31] respectively. When this fact is considered alongside the limited value of V_{DS} that can be applied due to redox reactions within the aqueous solution (Figure 5.4(a)), the lack of real saturation can be understood.

It is also worth highlighting that the conductivity of the ISFET channels could be increased beyond the value measured in air. This is clearly seen for

gate voltages from as low as -0.5V all the way to -1V. Such observation points to the idea of the creation of a new conduction channel, existing outside the interface and δ-layers revealed by the dry impedance spectroscopy [38]. Following the lower drain current values observed for gate voltages between 0V to -0.25V where the I-V curves are more pronounced, it can be surmised that the non-linearity or near-saturation of the drain current observed is the depletion of carriers in the capping intrinsic layer or gradual increase in channel resistance through the movement of charge carriers from the a high mobility region in the intrinsic capping layer to the low mobility traps-infested and high impurity scattering interface and δ-layers [38] provoked by the interplaying action between the applied drain and gate bias. In the case for δ4-ISFET, the improved transition between the δ-layer and the intrinsic cap [38] may be the difference here in accommodating smoother and more effective eviction of holes from the conducting channel under the applied gate and drain biases, generating better non-linearity on its output characteristics. As expected, δ4-ISFET's higher drain current values are a direct result of more released carriers as determined and predicted by the Hall measurements data (Table 5.1). It is also interesting to note that the drain current levels for δ4-ISFET and δ2-ISFET are comparable, a further corroborating evidence.

With marked improvement, the transconductance (a measure of gate control over the channel current) of the capped-ISFETs studied here is significantly higher than that of both the previous ISFETS of uncapped [31] structure. The variation of the gate bias ΔV_G of 1V in pH 2 buffer solution produced a drain current modulation sensitivity of 20% and 24% for δ3-ISFET and δ4-ISFET respectively. Based on the MESFET equation,

$$V_{pinch-off} = V_{FB} - \frac{qN_a.d_{max}^2}{\varepsilon_s\varepsilon_0} \qquad (5.1)$$

with a peak concentration of 4 and 7 x 10^{20} cm^{-3} and channel thickness d_{max} = 5 and 3.2 nm respectively and assuming the conduction takes place in the δ-

channel, the sheet charge densities were expected to change by ~4.7 and 2.72 x 10^{13} cm^{-2} or 13% and 12% for every ΔV_G of 1V, from a base value of 1.8 and 2.3 x 10^{14} cm^{-2}. In other words, the δ-channels were predicted to be softly pinched by 0.65 and 0.38nm respectively over an applied voltage of 1V. Judging from the experimental values being close to double those of the expected, the idea of a new conduction path forming in the intrinsic capping layer at higher gate voltages seems plausible. The higher than predicted current modulation could also be attributed to higher mobilities expected in the capping layer due to the absence of the scattering effect by ionized impurities in the δ-channel. Under the same set of applied potentials and with similar mobility values in the 2 cap-structured devices, δ4-ISFET's greater carrier density released or available for conduction and modulation may have played a supporting role in the larger transconductance exhibited. Further supporting hypothesis are presented in the following paragraphs.

The uncapped δ2-ISF*Et al*ows a change of 4.4% of its drain current to change per Δ1V of applied gate voltage while underperforming against a pre-calculated value of 12%, it shows superior performance to that of the reported ~5nm uncapped δ-ISFET standing at only 1% [31]. Juxtaposing with the δ4-ISFET and δ3-ISFET, the transconductance is even relatively poorer. Besides having semi-metallic characteristic [39], the low carrier mobility of δ2-ISFET at 0.8cm^2/Vs at 300K compared to 3 and 4 cm^2/Vs for δ4 and δ3-ISFET is likely to be responsible for the low current modulation in response to applied external gate bias and absence of non-linearity drain current response. Interestingly, the mobility ratio of the uncapped and capped structures at 3:0.8 approximately tallies with that of the transconductance being 24:4.4. Emphatically, this analysis implies that for δ3-ISFET and δ4-ISFET pinching does not occur in δ-layer but in the conducting channel supported in the cap instead. Current instability or drift is an issue for δ2-ISFET as observed in the pH cyclic sequence I-V measurements. A probable cause is uncontrollable drifting of carriers into the buffer layer beneath the δ-channel. Thus the concept of having an intrinsic capping layer to provide more stable and

sensitive devices is justified. The following analyses will explore this assertion further.

The 5nm and 3.2nm i-δ-i ISFETs display higher pH sensitivity of 52 and 55 mV/pH respectively compared to the 50 mV/pH reported in previous work [31]; closer to the limit of the Nernstian dependency at 59.2 mV/pH. The uncapped 3.2nm δ2-ISFET possesses a pH sensitivity of 47mV/pH though not improvement, it is still in agreement of the Nernstian limit. Expectedly from basic electrostatic, the shift of the threshold voltage was in tandem with the change in H^+ concentration thus in compliance with the surface polarization based on the Site-Binding Model [40]. The presence of OH^- or scarcity of H^+ at high pH values causes the deprotonation of the C-OH group on the surface, effectively reducing it to the negatively charged $C\text{-}O^-$ thus electrostatically forces the positive charge carriers out from the δ-channel and interface and into the capping i-layer. Conversely, at low pH levels the high concentration of H^+ ions site-bond with the originally neutral C-OH sites converting them to the positively charged $C\text{-}OH_2^+$. Through the force of repulsion, holes are pushed away leaving the channel slightly depleted. As a result, V_{FB} shifts and the transfer characteristic is correspondingly displaced along the x-axis. And the drain current therefore is duly modulated in tandem with the pH change.

The corresponding Hall measurements [36] assigned higher sheet carrier density at 300K to the 3.2nm substrate at 2.3×10^{14} cm^{-2}, compared to the substrate having a δ-layer of thickness 5nm at 1.8×10^{14} cm^{-2}. Prior to device fabrication, the substrates for δ3-ISFET and δ4-ISFET were subjected to 'dry' impedance spectroscopy measurements. It was revealed that δ3-ISFET and δ4-ISFET both support 3 conduction paths, δ layer itself (ii) the interface between the δ layer and the intrinsic buffer and (iii) the interface between the δ layer and the intrinsic capping layer [38]. Sample δ3 showed complex features with the conduction path (iii) exhibiting two activation energy at ~0.25eV and ~1.75eV, indicative of thermally activated defects and trap sites present influencing carrier transport [38]. In the case of the δ4, the situation appears to be improved with conduction path (iii) possessing a single

activation energy of ~0.25eV [38]. It is likely that with the aid of surface polarization courtesy of H^+ or OH^- ions in the electrolytes and the applied gate potential, a portion of the positively charged holes are presumably released into the 20nm-thick capping i-layer. The modulation or movement of higher carrier density in capping layer of the δ4-ISFET is thought to have induced larger channel resistance change and consequently, bigger potentiometric shift. Larger carrier density would correspondingly allow greater accumulation and stronger polarization of the channel or the sub-surface region in the cap. This leads to a 'bigger potential gap' between the state of depletion and accumulation, and slightly higher pH sensitivity. A similar argument can be put forward for the higher transconductance, of which the conductive state of the channel is dependent on the applied gate potential since mobility values for the two devices are very similar. Furthermore, the improved conduction paths could have facilitated for the better carrier movement or modulation through pH-induced surface polarization. In support, Huang *et al* fabricated a number of gateless Al_xGa_{x-1N}/GaN HEMT pH sensors with varying Al and Ga content to generate different carrier concentrations. Similarly, it was observed that the HEMT pH sensor with the highest carrier concentration displayed the biggest reaction in device current in response to pH changes. Carrying a structural resemblance to the capped δ-ISFETs here, this HEMT pH sensor supports an oxide – intrinsic-semiconductor capping bi-layer separating the conducting channel and the electrolyte [41].

The Mott-Schottky plots [figure 5.8(a) and (b)] revealed trends of linearity over the potential window range. The flat-band voltage of the oxidized diamond surface is usually located in the positive potential range close to the onset of the oxygen evolution reaction. The V_{FB} values obtained here are in good agreement with the reported values 3 – 4 V vs SCE for epitaxial single crystal diamond electrodes [42]. They are also significantly less than the flat-band voltage at +8.8V previously reported for the ISFET, with the boron-doped channel in direct contact with the solution [31]. This effectively means less applied voltage is required to permit carrier accumulation on the surface thus could be a contributing factor to the better drain current modulation sensitivity. However, the gap of 1V between the two flatband voltages fairly

commensurates with the drain current level advantage enjoyed by δ4-ISFET over δ3-ISFET.

The resolved slope of the Mott-Schottky plot can be further exploited to calculate the concentration of uncompensated acceptor ions, N_a. In this case the value N_a should correspond to the positive charge carriers or holes in the 15-20nm capping layer 'sandwiched' between the electrolyte and the heavily boron-doped δ layer. Using the following equation

$$N_a = \frac{-2}{q\ \varepsilon_s\varepsilon_0} \frac{dC^{-2}}{dV} \qquad (5.2)$$

The hole concentration can be assumed to be 3.4 x 10^{18} and 3.55 x 10^{19} cm^{-3} for δ3-ISFET and δ4-ISFET. Though the values determined here are only 5% of the levels revealed by SIMS and Hall effect measurements, it is possible that they reflect the carrier density released and available for modulation in the capping layer, lending more credibility to the formation of a conduction path outside the δ-channel under ISFET operating conditions presented here. This experimental observation is in agreement with a simulation study on carrier confinement in boron δ-doped diamond devices, which predicts a δ-layer thickness of 3nm achieving 30% delocalization of free holes outside of the doped region [43]. Less than abrupt or imperfect interface to δ-doped layer may hold the explanation behind such aberration between experimental and theoretical values.

The frequency dependent measurements (Figure 3) enable a model to be proposed for the behaviour for each of the capped ISFETs. A simple Randle's circuit equivalent of the series solution resistance, R_{ser}, in series with the R-C parallel network of the polarization resistance, R_p and the double layer capacitance, C_{dl} in the form of a constant phase element (CPE) was initially fitted. However, this was proven to be inadequate to account for the changes of effective impedance values measured over the range of frequency used. The best model representing the Frequency Response Analysis (FRA)

data for δ3-ISFET, is a $(R_1//C_1)+(R_2//C_2)+(R_3//C_3)+(R_4//C_{c4})$ network with the best fitting parameters as tabulated below.

Device	$Q_1 = 1/Z = Q_o(jw)^n$ and $C_1 = Q_o.(w = 1 rad)^n$ ($\mu F/cm^2$)	R_1 ($M\Omega$ cm^2)	C_2 ($\mu F/cm^2$)	R_2 ($M\Omega$ cm^2)	C_3 ($\mu F/cm^2$)	R_3 ($k\Omega$ cm^2)	C4 (nF/cm^2)	R4 ($k\Omega$ cm^2)
δ3-ISFET	33	19.6	0.62	0.18	0.38	17.64	1.58	8.92
δ4-ISFET	56	10.0			1.34	33.92	1.03	0.91

Table 5.2: Fitting parameters of the equivalent circuits representing the capped ISFETs in 0.1M HNO_3 solution in the potential of 0V vs Ag/AgCl

The RC network modelled includes a constant phase element CPE: $Q_1 = 1/Z = Q_o(jw)^n$ in the form of a nominal capacitance C_1 = 33 $\mu F/cm^2$ taken as the numerical value of the CPE Q_1 at w = 1: $C_1 = Q_o.(w = 1 rad)^n$ with the n-factor at about 0.95 (phase angle of 85°) in parallel with the polarisation resistor R_1 = 19.6 MΩ-cm^2. C_1 is representative of the electrolyte double-layer C_{dl} on the diamond surface and is in the same range to the reported double layer capacitance of ~ 20$\mu F/cm^2$ for O-terminated boron-doped diamond in redox solutions [44]. Assigning the high value of R_1 to the polarisation resistance of the diamond-electrolyte interface tallies with the 'blocking' mode within the potential window of the ISFET, suppressing leakage current to as low as 10^{-8}-10^{-9} A/cm^2. C_4 = 1.58 nF/cm^2 is likely to represent the 'intrinsic' capping layer supporting a conduction path in the form of R_4 = 8.92 kΩ-cm^2. The resistive component of the remaining RC network pairs of C_2 = 0.62 $\mu F/cm^2$ and R_2 = 0.18 MΩ-cm^2 and of C_3 = 0.382 $\mu F/cm^2$ and R_3 = 17.64 kΩ-cm^2 are associated with the interface layer and delta channel, agreeing with the Hall effect measurement data made previously on these samples [36]. It is also reasonable to designate the partnering capacitive components to that of the interface layer and delta channel respectively.

As previously stated the 20 nm capping i-layer here is in direct contact with the electrolyte. The C_4 value at 1.58 nF/cm^2 or its absolute value of 3.1 x 10^{-10} F factoring in the device dimensions is a substantial departure from the typical capacitance value for an intrinsic single crystal diamond falling in the pF range (C_{dia}). One possible explanation could be the formation of a conduction path through the rearrangement of holes in the cap layer producing a diffusion capacitance (C_{diff}) running in parallel with the true intrinsic capacitance. Since the total capacitance in parallel is simply the arithmetic sum, the much smaller pF value of the intrinsic capacitance would be relatively rendered insignificant (C_{dia}//C_{diff} => C_{dia}+ C_{diff} ≈ C_{diff}), C_4 ≈ C_{diff}. Correspondingly, the much lower resistivity (8.92 kΩ-cm^2) of a p-channel in the capping layer provides the effective or 'preferred' path over the highly resistive 'surrounding' intrinsic diamond. The third RC network is assigned to the interface between the cap and δ-layer with R_{int} = 0.18 MΩ-cm^2 being close to value revealed by the 'dry' impedance spectroscopy measurements of ~10^5 Ω-cm^2 [38]. The Hall measurements made on an uncapped δ structure produced a sheet resistivity of ~ 10^3 – 10^4 Ω-cm^2 [36] thus allowing R_3 to represent that of the δ-layer itself. C_2 and C_3 values are within reasonable agreement to reported values of the capacitance of the space charge region for a boron-doping concentration of ~10^{20} cm^{-3}, standing at about 2μF/cm^2 [42,44].

The 3.2 nm δ4-ISFET presents a simpler equivalent circuit model with only 3 RC bridges fitted. The C_1-R_1 network is representative of the double-layer capacitance and the polarisation resistance with both values in agreement with those reported [31,42,44] and leakage current blocking characteristic within the potential window. Specifically, the representing the double layer capacitance is the CPE value of 56 μF/cm^2 with the n-factor equivalent to 0.83 (phase angle of 75^o). R_2 = 33.92 kΩ-cm^2 and R_3 = 0.91 kΩ-cm^2 could be assigned to the conductive channels supported in the interface and capping layers. The values of C_2 = 1.34 μF/cm^2 duly attributed to the depletion region in the δ-layer, implies an improvement in the transition region between the δ and the capping layer being much closer to reported values. Similar to δ3-ISFET, C_3 = 1.03 nF/cm^2 in turn underpins the idea of

rearrangement or movement of charge carriers in the intrinsic diamond. The effect of the released of more charge carriers into the capping and interface layers is thought to obscure the presence of the δ-layer which is duly absent from this circuit fitting.

With the fitted polarisation resistance R_p values were in the MΩ-cm^2 range, the equivalent circuit models could be reduced to just capacitances in series (Figure 5.10). The ratio of the double layer to the 20 nm "intrinsic" cap and δ-layer capacitances $C_{double\text{-}layer}$:(C_{cap}:$C_{interface}$:$C_{space\text{-}charge}$) provides an adjustment factor for δ3-ISFET and δ4-ISFET of ~0.98 and 0.97 respectively to the applied voltage covering all conductive channels in the i-δ structure; becoming a major contributing factor in the high transconductance sensitivity observed. The capping structure allows almost full monopoly of the applied voltage on the available conduction paths in the ISFET.

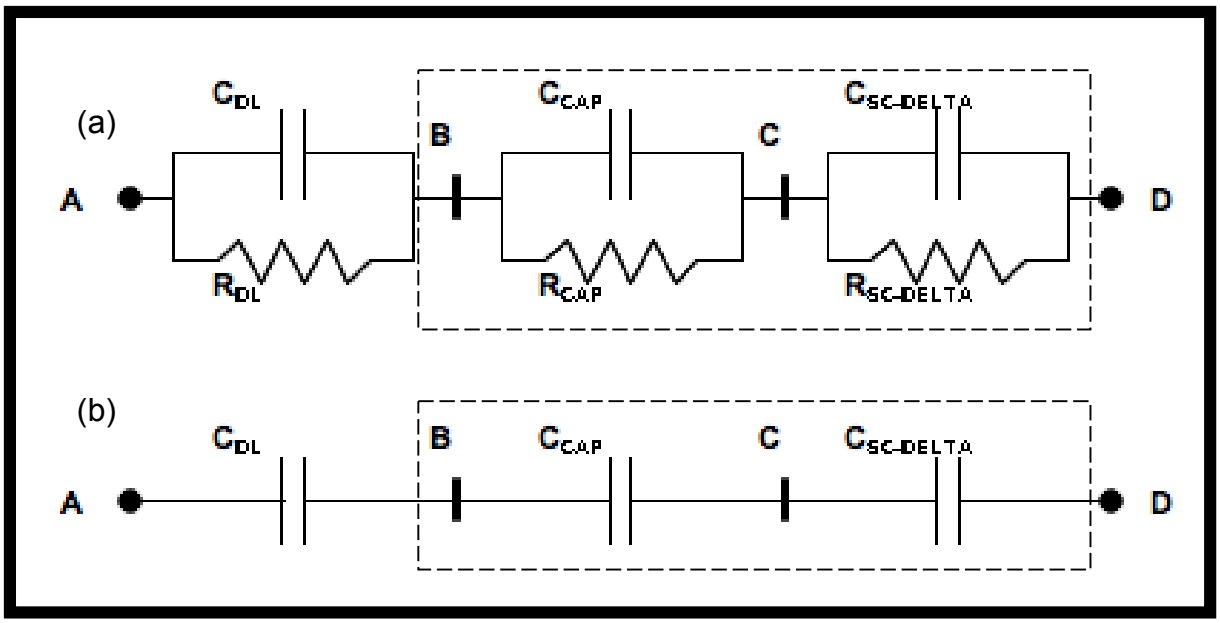

Figure 5.10: (a) Equivalent circuit of the electrolyte-diamond interface (b) Simplified equivalent circuit valid in the potential window

Having undergone the same surface chemical cleaning process and carrying near identical applied potential adjustment factor, the better transistor characteristics shown by δ4-ISFET (3.2nm) over δ3-ISFET (5nm) therefore must be attributed to the quality of the device internal structure, namely the δ-

layer, its thickness and interfaces and the corresponding higher density of released charge carriers.

5.6 Conclusion

The ISFET's drain current showed signs of 'pinching' but did not reach saturation within the bias window and its modulation sensitivity was found to be within only 3% of error. Also, the measured values of the flat band voltage and transconductance were a considerable improvement over previous work. It is again clear that from the impedance measurements that the insulating cap layer supports free carrier density, as is expected for an effective delta device, where carriers originating from the delta layer are transporting in the adjacent undoped regions. It is therefore again confirmed that the O-terminated i-δ-i ISFET structure is the correct design to provide stable and reliable robust chemical sensors. The performance advantages enjoyed by δ4-ISFET presumably comes down to the thinner δ-layer which allows more carriers released to be modulated, evidently shown by the higher current magnitudes in the I-V output characteristics, lower flat-bland voltage, higher transconductance and importantly, better pH sensitivity. However, a larger potential window or a much thinner δ-layer (~1–2nm) is required to completely deplete the conducting channel and achieve full drain current saturation. Based on the improvements achieved here, the author will pursue to further optimize the delta layer profile and diamond-electrolyte interface to realise ISFETs with full pinch-off characteristics.

5.7 References

[1] O. Korostynska, K. Arshak, E. Gill, and A. Arshak, IEEE Sensors Journal, 8, 20 (2008)

[2] S. Bermejo, C. Jutten and J. Cabestany, Sensors and Actuators B, 113, 222 (2006)

[3] A. Poghossian, S. Ingebrandt, A. Offenhäusser and M.J. Schöning, Seminars in Cell & Developmental Biology, (In Press), 20, (2009)

[4] C.G. Specht, O.A. Williams, R.B. Jackman, R. Schoepfer, Biomaterials, 25, 4073 (2004)

[5] X. Xiao, J. Wang, C. Liu, J.A. Carlisle, B. Mech, R. Greenberg, D. Guven, R. Freda, M.S. Humayun, J. Weiland and O. Auciello, J. Biomed. Mater. Res. B, 77, 273 (2006)

[6] P. Bajaj, D. Akin, A. Gupta, D. Sherman, B. Shi, O. Auciello and R. Bashir, Biomedical Microdevices, 9, 787 (2007)

[7] K.K. Liu, C.L. Cheng, C.C. Chang, Nanotech., 18, 325102 (2007)

[8] A.M. Schrand, L. Dai, J.J. Schlager, S.M. Hussain, E. Osawa, Diamond & Related Materials 16, 2118 (2007)

[9] M. Amaral, P.S. Gomes, M.A. Lopes, J.D. Santos, R.F. Silva, M.H. Fernandes, J. Nanomaterials, 894352 (2008)

[10] M. Amaral, P.S. Gomes, M.A. Lopes, J.D. Santos, R.F. Silva, M.H. Fernandes, J. Biomed. Mater. Res. A, 87, 91 (2008)

[11] W.C. Clema, S. Chowdhurya, S.A. Catledgea, J.J. Weimerd, F.M. Shaikh, K.M. Hennessy, V.V. Konovalova, M.R. Hilla, A. Waterfeld, S.L. Bellisa and Y.K. Vohra, Biomaterials, 29, 3461 (2008)

[12] M. Amaral, P.S. Gomes, M.A. Lopes, J.D. Santos, R.F. Silva and M.H. Fernandes, Acta Biomaterialla, 5, 755 (2009)

[13] I. M. Buckley-Golder and A. T. Collins, Diam. & Relat. Mater., 1, 1083 (1992)

[14] E. Snidero, D. Tromson, C. Mer, P. Bergonzo, J.S. Foord, O.A. Williams and R.B. Jackman, J. Appl. Phys., 93, 2700 (2003)

[15] A. Denisenko, A. Aleksov, E. Kohn, Diamond Relat. Mater. 10, 667 (2001)

[16] H. Kawarada, Y. Araki, T. Saki, T. Oqawa, H. Umezawa, Phys. Status Solidi, A Appl. Res. 185, 79 (2001)

[17] R. Muller, A. Denisenko, M. Adamschik and E. Kohn, Diam. & Relat. Mater., 11, 651 (2002)

[18] T. Sakai, Y. Araki, H. Kanazawa, H. Umezawa, M. Tachiki and H. Kawarada, Jap. J. Appl. Phys. Part 1, 41, 2595 (2002)

[19] R. Muller, A. Denisenko and E. Kohn, Diam. & Relat. Mater., 12, 554 (2003)

[20] W. Yang, R. Hamers, Appl. Phys. Lett. 85, 3626 (2004)

[21] J.A. Garrido, A. Haertl, S. Kuch, M. Stutzmann, O.A. Williams, R.B. Jackman, Appl. Phys. Lett. 86, 073504 (2005)

[22] K.S. Song, G.J. Zhang, Y. Nakamura, K. Furukawa, T. Hiraki, J.H. Yang, T. Funatsu, I. Ohdomari and H. Kawarada H, Phys. Rev. E, 74, 041919 (2006)

[23] B. Rezek, H. Watanabe, D. Shin, T. Yamamoto, C. Nebel, Diamond & Relat. Mater. 15, 1007 (2006)

[24] C.E. Nebel, H. Kato, B. Rezek, D. Shin, D. Takeuchi, H. Watanabe, and T. Yamamoto, Diam. & Relat. Mater., 15, 264 (2006)

[25] A. Bennet,O. Gaudin, O.A. Williams, J.S. Foord,R.B. Jackman, Proc. Mat. Res. Soc., 956, 221 (2007)

[26] B. Rezek, D. Shin, H. Watanabe H, C.E. Nebel, Sens. & Actuators B, 122, 596 (2007)

[27] T. Kondo, K. Honda, D. Tryk, A. Fujishima, J. Electrochem. Soc. 152, E18 (2005)

[28] T.H. Borst and O. Weiss, Physica Status Solidi, A154, 423 (1996)

[29] E.F. Schubert (Ed.), “Delta-doping of Semiconductors”, Cambridge University Press, (1996)

[30] R.S. Balmer, I. Friel, S.M. Woollard, C.J.H. Wort, G.A. Scarsbrook, S.E. Coe, H. El- Haj, A. Kaiser, A. Denisenko, E. Kohn and J. Isberg, Phil. Trans. R. Soc. A366, 251 (2008)

[31] A. Denisenko, G. Jamornmarn, H. El-Hajj, E. Kohn, Diam. & Relat. Mat. 16, 905 (2007)

[32] M. Dipalo, C. Pietzka , A. Denisenko, H. El-Hajj , E. Kohn, Diam. & Relat. Mat. 17, 1241 (2008)

[33] H. El-Hajj, A. Denisenko, A. Bergmaier, G. Dollinger, M. Kubovic R.S. Balmer and E Kohn. Diam. & Relat. Mater., 17, 1259 (2008)

[34] B. Baral, S.S.M. Chan and R.B. Jackman, J. Vac. Sci. Technol. A 14, 2303 (1996)

[35] O.A. Williams and R.B. Jackman, J. Appl. Phys., 96, 3742 (2004)

[36] N. Timulty, ‘Diamond Based Nanostructures for Electronic Applications’, p. 153-165, Doctoral Thesis, University College London (2010)

[37] Y. Zhu, L. Wang, W. Yao and L. Cao, Appl. Surface Science 171, 143-150 (2001)

[38] N. Timulty, J. Welch, H. Ye, R.S. Balmer, C. Wort, R. Lang, R.B. Jackman, Appl. Phys. Letter, 94, 051207 (2009)

[39] Bustarret, E. , Gheeraert, F. & Watanabe, K.. Phys. Rev. Lett. 93, 237005 (2004)

[40] D. E. Yates, S. Levine, and T.W. Healy. J. Chem. Soc. Fraday Trans. 1, (1974).

[41] H.S. Huang, C.W. Lin, H.C. Chiu, 978-1-4244-2540-2/08/, IEEE (2008)

[42] J. Lagemaat, D. Vanmaekelbergh, J. Kelly, J. Electroanal. Chem., 139, 475 (1999)

[43] A. Fiori, J. Pernot, E. Gheeraert, E. Bustarret, Phys. Status Solidi A 207, No. 9, 2084–2087 (2010)

[44] D. Becker, K. Juttinger, J. Appl. Electrochem., 33, 959 (2003)

Chapter 6

Nanodiamond-gated Silicon Ion-sensitive Field Effect Transistor

6.1 Introduction

Ion Sensitive Field Effect Transistor (ISFET) technology has become widespread within chemical sensing applications, typically detecting hydrogen ion (H^+) concentration related to the pH of chemicals [1]. The useful performance that may be achieved using ISFET-based sensors is demonstrated by their applications in medical diagnostics, monitoring clinical or environmental samples, fermentation and bioprocess control and testing pharmaceutical or food products [2,3]. In the potentiometric configuration, changes in the carrier concentration in the conducting channel effectively change the potential difference between the active area and the gate electrode, which in turn is recorded by a voltage-sensing system.

ISFETs are typically made of single-crystal silicon due to the mature and reliable fabrication technology available with this material. The Si itself must be overlayed with a pH sensitive region, typically its oxide SiO_2, to offer suitable surface chemical properties for H^+ sensing applications [1]. However, to enable such an ISFET to sense other species, alternative sensitising layers are required [4]. An increasingly important class of materials that require improved small and robust sensors are explosive vapours or vapours of precursor species. Recently, tri-nitrotoluene (TNT) detection with an ISFET was demonstrated using complex chemical procedures to attach either hydroxydopamine or aminothiophenol groups to the active region of an Al_2O_3 gated Si ISFET device [5]. This letter reports a simple method for modifying Si-based ISFETs with a coating of diamond on its active area, and shows how highly effective chemical sensing of explosive vapours and precursors may be achieved using this approach.

Diamond possesses properties favourable for chemical and biological sensing since as a material it can display exceptional chemical inertness and natural biocompatibility [6-8], whilst be readily chemically functionalised for sensing purposes. For example, photochemical chlorination, amination and carboxylic functionalisation processes have been widely demonstrated [9,10]. These functionalized surfaces have also been modified with DNA, enzymes and

proteins [11] for biological sensing. Diamond ISFETS have been successfully fabricated through the use of hydrogen-based surface transfer doping [12-14] and boron-doped δ-profile FETs [15,16]. Partially oxidised H-terminated and boron-doped δ-profile ISFETs rely on carbon-based hydroxyl (C-OH) sites for pH sensing [13,15,16]. In contrast, a single crystal diamond ISFET employing a conductive fully H-terminated surface channel is modulated through chemical potential equilibrium shifts at different pH levels [14]. However, the immaturity of diamond device technology limits the near-term commercial prospects for such an approach to sensor fabrication. Here a hybrid-solution is proposed, where inexpensive pre-fabricated Si ISFETs can be coated with nanodiamond particles offering the benefits of established Si technology with the properties of a diamond surface for sensing applications.

6.2 Device Fabrication

Nano-diamonds produced by a detonation process [17] (DNDs) were used throughout (New Metals & Chemicals Corporation, Japan). DNDs in the size range 5-15nm were suspended in de-ionised water and attached to a Si ISFET (Hach, USA) using sonication. The Si ISFET sensor came with a digital meter having both 'pH' and 'mV' readout options. Firstly, the DND-containing solution was diluted using de-ionized water at a ratio of 0.5ml: 6.5ml respectively. Attachment of the DND particles onto the Si ISFET silicon chip sensor was done by immersing the gate active area in the DND solution (Figure 6.1) and sonicated for 10 minutes, a technique developed by Williams and co-workers [18]. To avoid the built-in reference electrode layered with DND particles, it was duly protectively sealed during sonication. After sonication, the ND-coated Si ISFET was dried on a hot plate at 40-50^{o}C for a period of ~15 minutes. This attachment technique should produce an ND layer of ~100nm thick, based on AFM scans on various post-sonication drying techniques carried out by the Diamond Electronics Group in UCL.

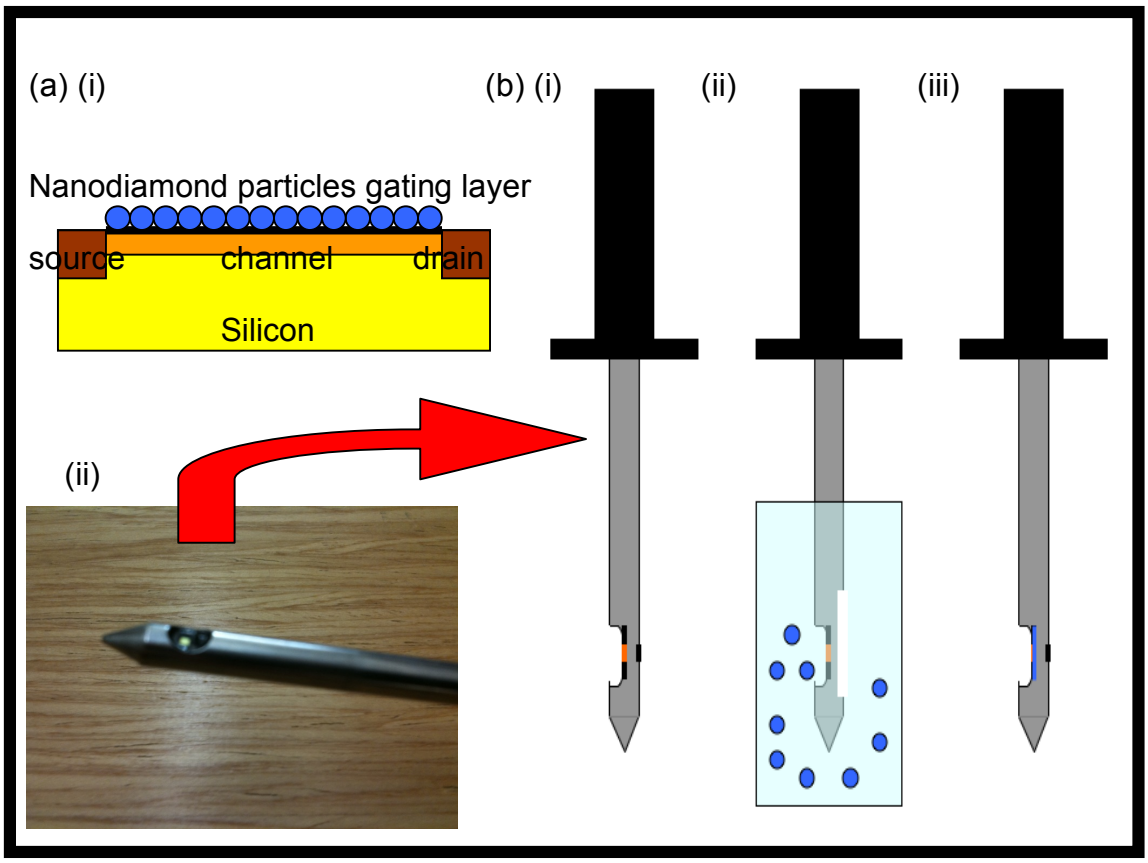

Figure 6.1: DND attachment on Si ISFET by sonication (a) (i) device concept (ii) real as-received device. (b) (i) ISFET device (ii) immersed and sonicated in DND containing solution (iii) ND-coated Si ISFET

6.3 Experimental Methods

Atomic force microscopy (AFM, Veeco Dimension V) was used to image the Si ISFET active area before and after DND coating. An identical but uncoated ISFET was employed throughout as a control. For voltage response and pH sensitivity calibration purposes, both the ND-coated and uncoated ISFETs were immersed in buffer solutions of pH 2,4,7,10 and 12 (Sigma-Aldrich). The corresponding outputs were recorded against the labelled pHs of the solutions. For the liquid phase sensing work, both ISFETs were immersed in ionic solutions of $NaNO_2$ (Sigma-Aldrich) and $NaClO_3$ (Sigma-Aldrich) of varying concentration from 0.1 to 0.0001M by means of proportional dilution using de-ionised water.

Exposure to 2,4-dinitrotoluene (Sigma-Aldrich) and ammonia (NH_3) at five concentration levels in the vapour phase were made and changes in the gate-source voltage by potentiometry were taken as measurement of detection. The polarity and trend of the voltage response for NH_3 detection was used as a clear reference for those of 2,4 DNT vapour due the former's established basicity. The vapour phase masurement was made in a temperature-controlled air-tight glass container (Figure 5.2).

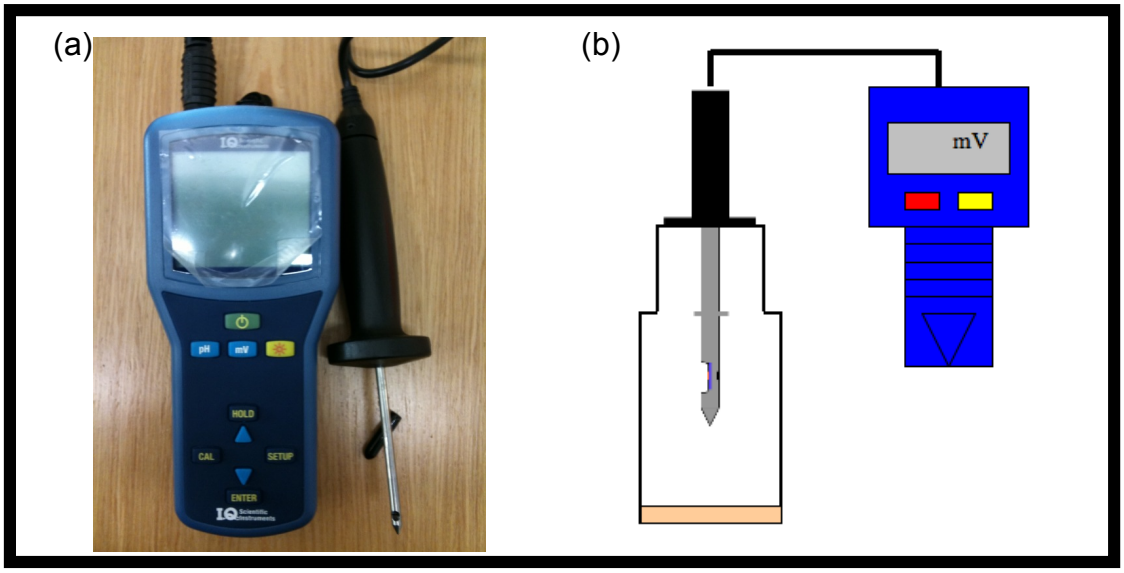

Figure 6.2:(a) Actual ISFET probe and meter (b) a schematic diagram of the basic experimental cell arrangement

To control the 2,4 DNT vapour concentration, thermal energy was applied to the glass container by means of refrigeration and a hot-plate over a temperature range of 6 – 24^{o}C monitored by an external thermocouple. The vapour pressure curve as a function of temperature (~270-340K) for 2,4-initrotuolene can be expressed using the Clausius-Clapeyron relationship:

$$\log_{10} P\,(\text{Torr}) = a - b/T(\text{K}) \qquad (1)$$

where a and b coefficients are equivalent to 13.16 ± 0.40 and 4948 ± 20 respectively as determined in an experiment carried out by Freedman *et al* [19]. With the chosen controllable temperatures at 6,13,15,17 and 23^{o}C, the

generated 2,4 DNT vapour concentrations in parts per billion (ppb) are tabulated below

Temperature (^{o}C)	Vapour Pressure (Torr)	Concentration (ppb)
6.4	2.822×10^{-5}	37.137
13.0	7.233×10^{-5}	95.167
15.0	9.538×10^{-5}	125.496
17.1	12.700×10^{-5}	167.109
23.4	29.265×10^{-5}	385.061

Table 6.1: Expected 2,4 DNT concentration (ppb) as a function of temperature

Ammonium hydroxide (NH_4OH) or ammonia water readily gives off NH_3 vapour at room temperature of which partial pressure and concentration are a function of the dilution level of the ammonium hydroxide solution.

Molal Concentration of NH_3 in the Solutions in Percentages	Temperature = 290K		
	Partial Pressures of NH_3 above aqua ammonia (psi)	Partial Pressures of H_2O Vapor above aqua ammonia (psi)	Vapour Concentration (x 10^3 ppm)
5	0.83	0.34	52.30
10	1.32	0.32	80.78
15	2.69	0.30	152.06
20	4.28	0.28	222.22
25	6.67	0.26	308.37
30	10.76	0.25	418.51
35	16.33	0.23	522.39
40	23.84	0.21	615.23
45	33.20	0.19	690.37
50	44.25	0.17	748.47

Table 6.2: Partial pressures of ammonia above aqua ammonia [20]

Referencing Table 6.2, five molal concentrations of NH_3 at 5%, 10%, 20%, 30% and 40% were made and stored in separate test cells or containers from the a 50% NH_4OH solution source by proportional dilution.

Solid-state devices for the detection of threat signatures are an active area for research; in the current case 2,4 DNT and $NaNO_2$ were chosen as safe analogues for the detection of the explosive tri-nitrotoluene (TNT) and, RDX and HMX respectively [21]. $NaClO_3$ and also $NaNO_2$ being highly oxidizing chemicals are often used in explosive mixtures and internationally classified as explosive precursors [22]. Sharing a common cationic element, the ISFET's electrical responses should quantitatively allow the discrimination of the anions, NO_2^- and ClO_3^-. On the side, the sensing of NH_3 is also of wide importance due to its high toxicity and numerous applications where the gas is used or generated, which includes environmental protection, clinical diagnosis, industrial processes, food processing and power plants [23-27].

6.4 Results

AFM images for uncoated and nanodiamond (ND) coated ISFET active area surfaces are shown in Figure 6.3(a) and (b). Few features are apparent on the uncoated ISFET, as would be expected. On the ND coated active area, 5-15nm DND particles can be discerned, but these have aggregated to form clusters of particles in the size range 20-100nm. The particles are strongly adherent, not being removed by routine physical abrasion or cleaning. The pH sensitivity calibration step produced linear responses as illustrated in Figure 6.4, with identical gradient of 55.3mV/pH for both ND-coated and bare Si ISFETs, albeit a uniform shift of +20mV separating the former from the latter. The modulation of the surface potential, which is induced by ion adsorption, is governed by the Nernst equation [28]. The theoretical maximum response of an ISFET is known as the Nernst limit, which is 59.2 mV / *p*H.

Figure 6.5 shows the voltage response to different molarities of $NaNO_2$ and $NaClO_3$ for both ND-coated and bare Si ISFETs. It can be observed that

larger voltage gaps are generated between 0.1M and 0.01M of $NaClO_3$ and $NaNO_2$ at 17.2mV and 62.3 mV compared to that of the uncoated ISFET at 1.3mV and 36.7mV. The ND-coated ISFET demonstrates the capability to rationally react to the changing molarities of explosive precursors, namely $NaNO_2$ and $NaClO_3$. The Si ISFET fails to resolve between pure de-ionised water and solutions of the salt-based precursors of different molarities. The output voltages at 23mV and 40mV responding to de-ionised water generated by the Si ISFET is equivalent to a 0.05M $NaNO_2$ and super-concentrate $NaClO_3$ (>>1M) respectively. The 2,4 DNT vapour exposure yielded corresponding potential shifts to varying concentrations expressed in parts per billion (ppb) illustrated in Figure 6.6. A resolved linear relationship is established by the ND-coated ISFET between the voltage response and vapour concentration of 2,4-DNT over a potential difference of 17.8mV whereas the Si ISFET only gave a much smaller voltage response at 2.5mV over a single concentration step exposure of 2,4-DNT at 385ppb. From the Figures 6.5 and 6.6, it can be seen that the voltage responses are increasing in the negative direction with increasing target molecules concentrations. This correlates with the output voltage of the device in reaction to increasing NH_3 vapour concentration as shown in Figure 6.7. The control Si ISFET was unable to display any sensing action against NH_3; recording unstable readings corresponding to a state of non-detection.

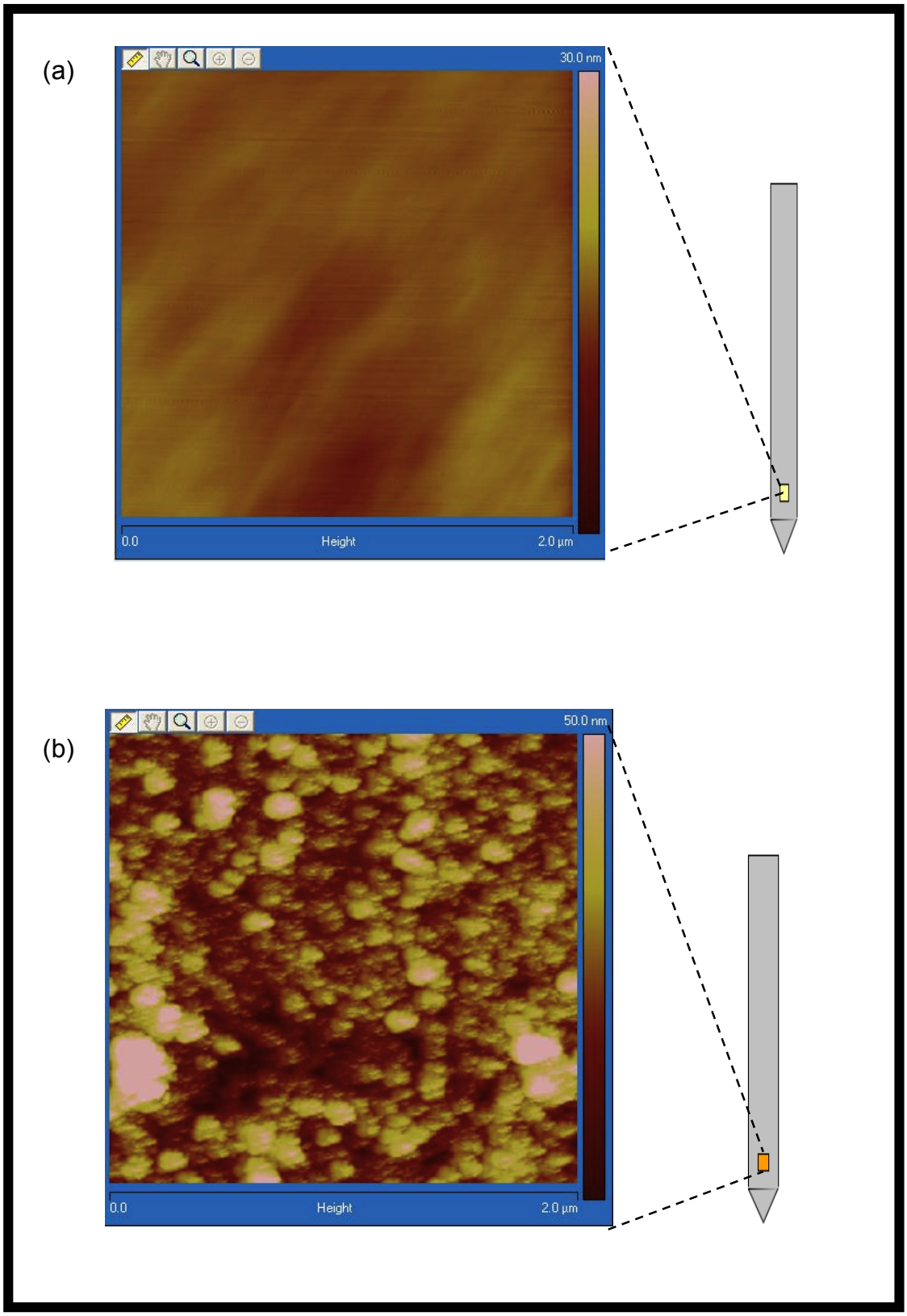

Figure 6.3: AFM images from the Si ISFET (a) before and (b) after coating with detonation nanodiamonds (DNDs). The length scale is the same for both x and y axis. The height scale is indicated at the top of each colour scale bar.

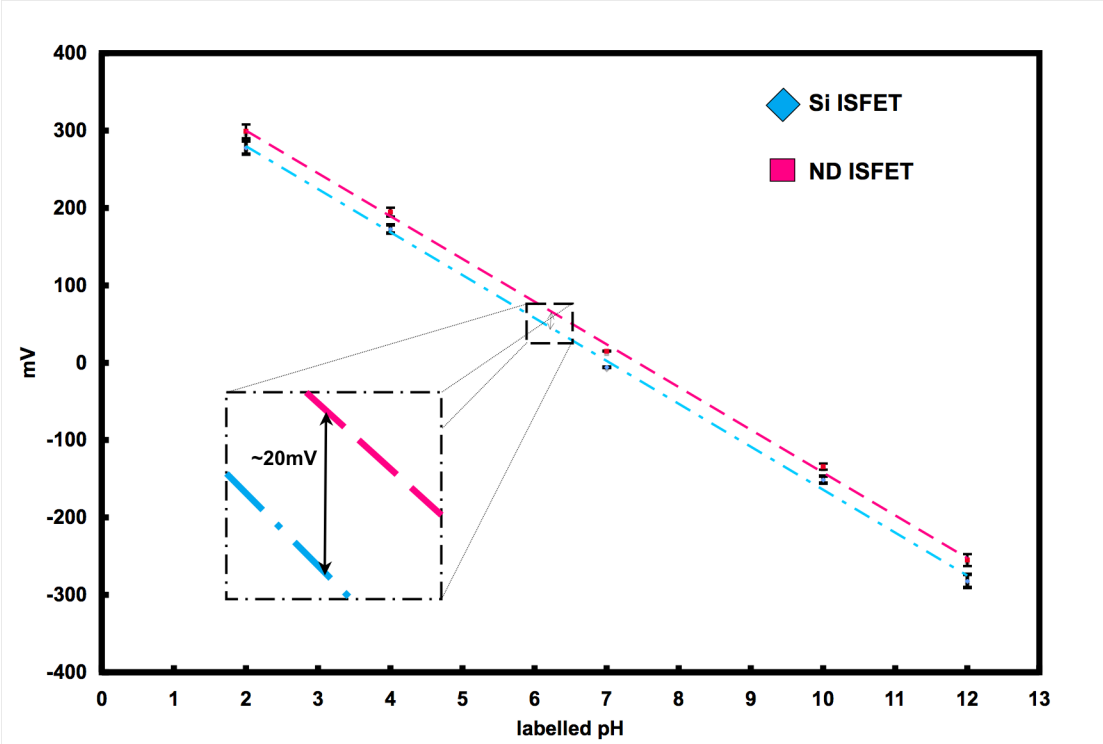

Figure 6.4: The ISFET calibration curve produced by immersing both devices (ND-coated and uncoated) in pH 2,4,7,10,12 buffer solutions.

(a)

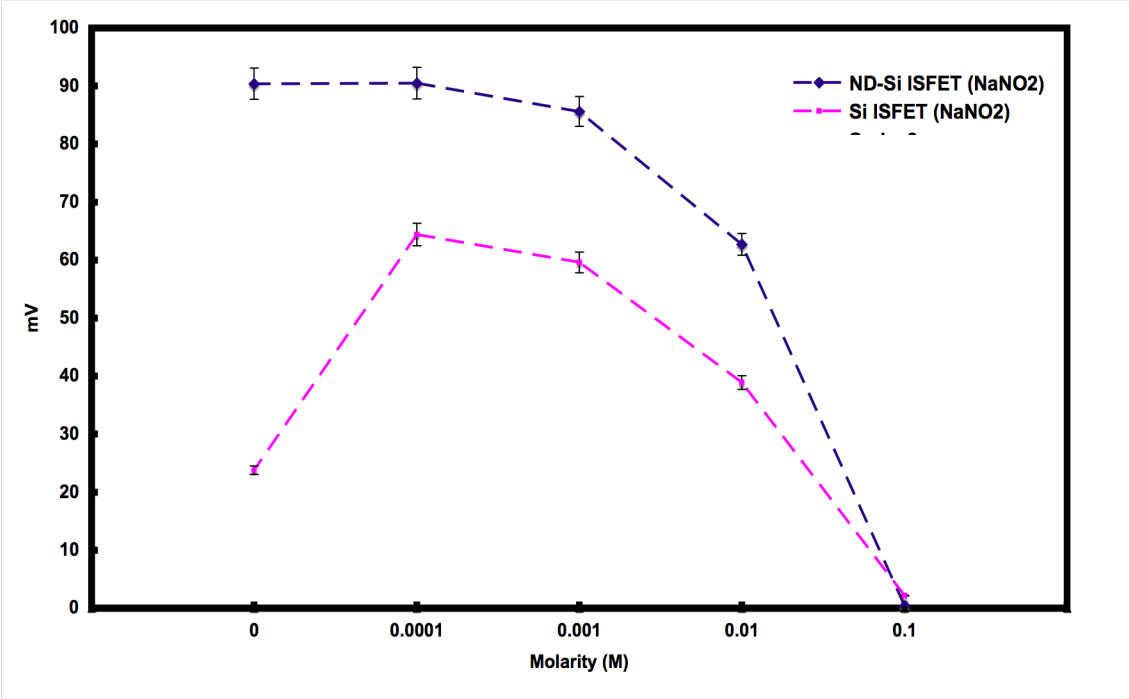

(b)

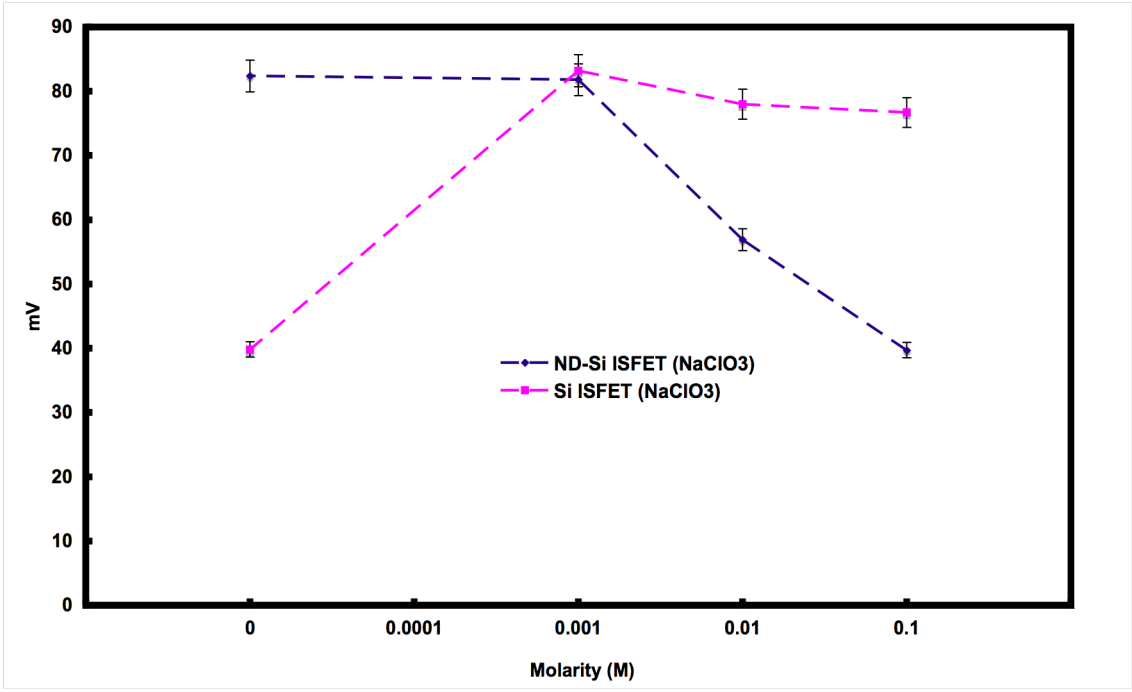

Figure 6.5: Voltage responses to (a) NO_2^- and (b) ClO_3^- solutions at different concentrations (0.1M to 0.0001M) for ND-coated and uncoated Si ISFETS.

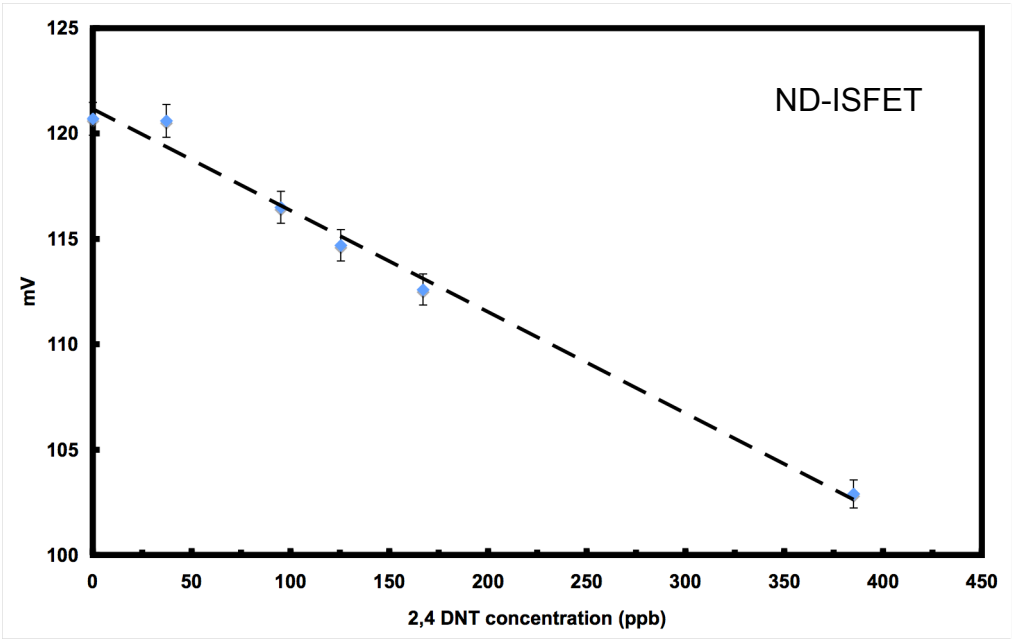

Figure 6.6: ND-coated Si ISFET's output voltage in reaction to 2,4-DNT exposure at 5 concentration levels in parts per billion (ppb).

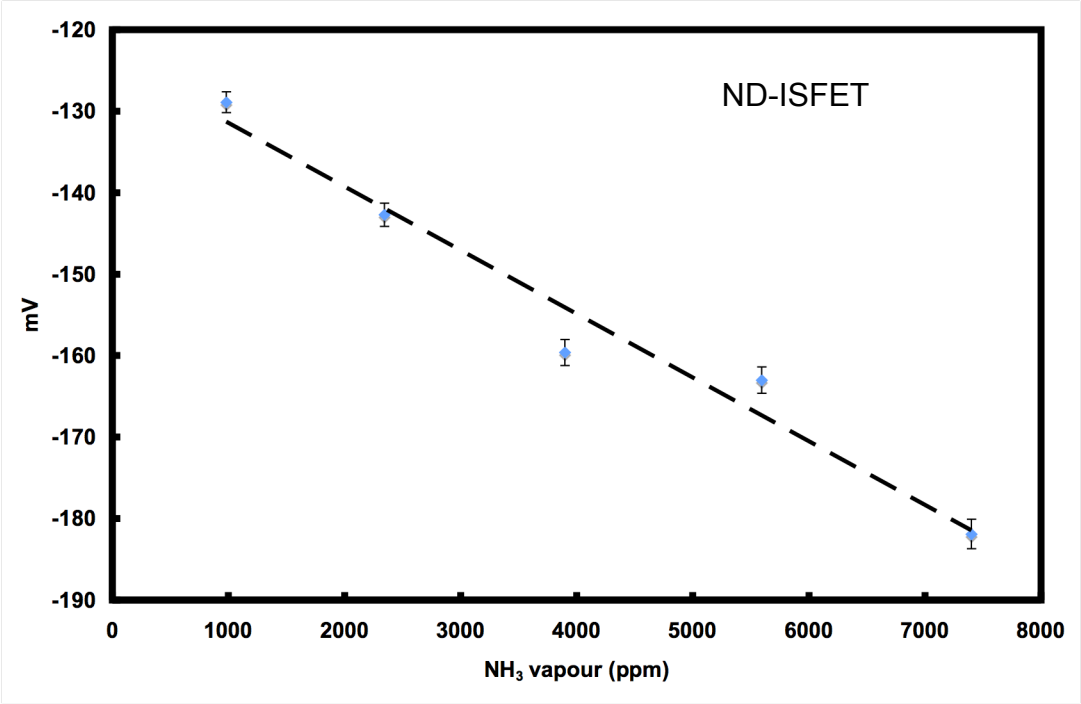

Figure 6.7: The output voltage generated by the ND-ISFET in varying concentration of NH_3 vapour in parts per million (ppm)

6.5 Discussion

Nanodiamond particles are normally left partially functionalised with hydroxyl (OH) and carboxyl (COOH) groups after a thorough chemical oxidising process (Figure 6.8) [29]. Attachment of NDs on the pH sensitive negatively charged oxide layer of the ISFET was made possible through electrostatic attraction by the positive zeta potential (ζ) characteristic of the NDs [36]. Oxygen having superior electronegativity values renders SiO_2, Ta_2O_5 and Al_2O_3 surfaces negative. The ND-coated ISFET's duplication of the linear pH response of the Si ISFET albeit up-shifted by 20mV confirms the presumed highly-oxidized surface of the DND, which should be pH sensitive [15,16,30]. As suggested by the site-binding model proposed by Yates *et al* in 1983, the pH sensitive OH part of hydroxyl and carboxyl sites on the ND surface experiences protonation and deprotonation in solutions containing high and low H^+ ions concentration respectively, altering the semiconductor surface potential Ψ_0 and correspondingly modulate the source-drain current [31]. The near-uniform +20mV displacement of the pH sensitivity slope confirms the stability of the positive zeta (ζ) potential of the predominantly carboxylated

nanodiamond surface in pH 2-12 as demonstrated in a previous work [32]. Zeta potential is the potential difference between the dispersion or host medium (in this case, liquid) and the stationary layer of fluid attached to the dispersed particle.

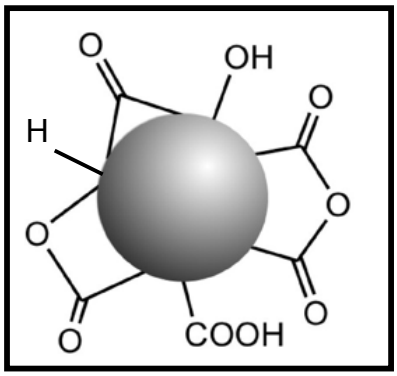

Figure 6.8: Surface terminations of nanodiamond core particles [29]

With the details of the as-received ISFET's internal semiconductor technology and circuitry system unknown (not supplied), analysis of the systematic output voltage response to the pH changes proposes that the device should be a p-channel ISFET. The following analyses will elucidate this inference. P-channel MOSFET is typically biased in the negative voltage regime. A rated negative voltage is required to create the p-type inversion layer in an n-type bulk semiconductor. Likewise, the polarity of the drain voltage needs to be negative to allow the extraction of positively charged carrier or holes from the source region and interplay with the gate voltage to deplete the channel near the drain region achieving 'pinch-off' condition and drain current saturation. As a function of the gate voltage, the drain current increases exponentially beyond the FET threshold voltage. The relationship between the drain current and the modulating gate voltage is defined as the transfer characteristic as illustrated in the Figure 6.9 below, and fundamental to the principle of potentiometry.

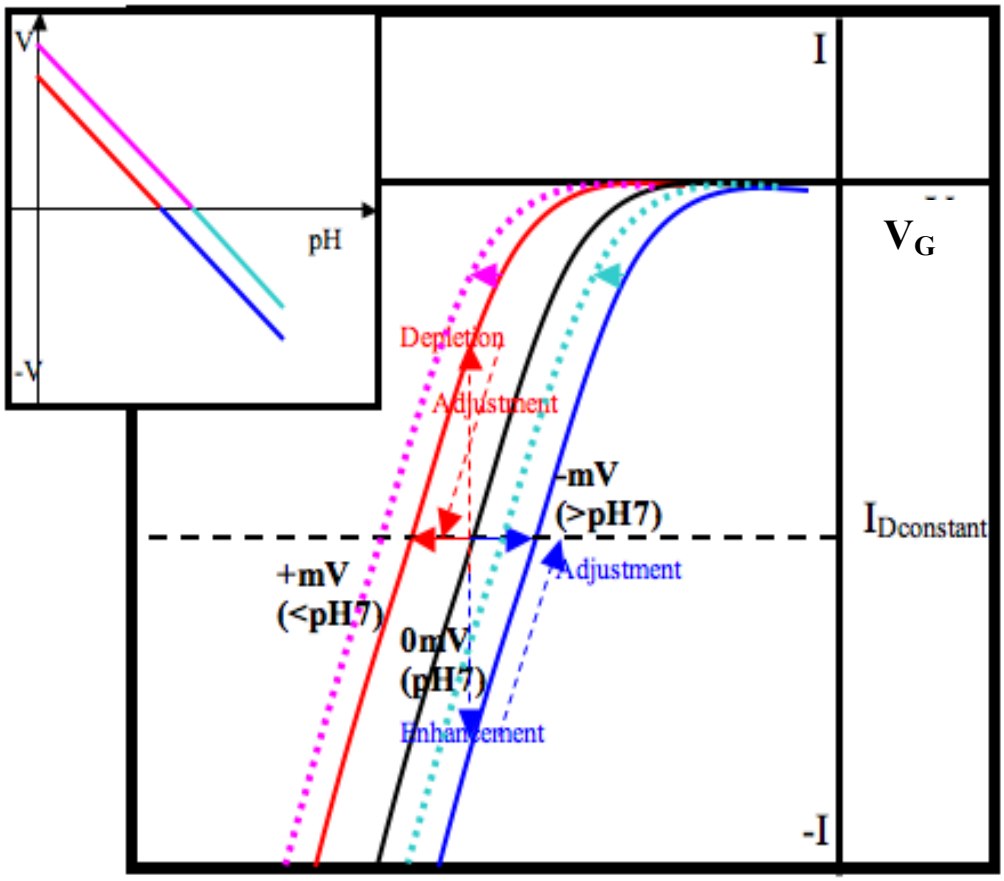

Figure 6.9: Transfer characteristics, drain current (I) versus gate voltage (V_G) and pH-induced shifts - the proposed potentiometry p-type ISFET system

With the effective surface charge modified by the varying H^+ concentration, the carrier concentration hence the drain current is modulated accordingly. The ISFET is likely to be arranged as a potentiometry-based sensor where changes in the carrier concentration in the channel triggers the potentiometry system to restore the original source-drain current level by adjusting the gate-source voltage. Assuming the ISFET is biased such that the transfer characteristic curve for pH 7 (black) sits as shown in Figure 6.9 and is interpreted as '0mV' as the output. At fixed gate and drain voltages, the pH sensitive sites, –COOH and –OH sites on the DND-covered gate of the ISFET are protonated ($–COOH_2^+$ and $–OH_2^+$) at low pH levels the holes concentration in the channel is reduced or partially depleted, resulting in higher threshold voltage (V_T) and the transfer characteristic curve is shifted to the left (red arrows and curve) to keep the drain current constant. Conversely,

in high pH conditions the deprotonation of the pH sensitive sites ($–COO^-$ and $–O^-$) lowers V_T and the transfer characteristic will move to the right (blue arrows and curve). Referencing the negative polarity of the applied external bias and the '0mV' output for pH 7, the negative or left-shift (red curve) being 'in-line' with bias polarity is computed by the system as 'positive' increment whilst the antagonistic right-shift (blue curve) as 'negative'. This operation model explains the negative slope profile extending from positive values for pH<7 to negative values for pH>7 for the ISFET (Figure 6.4) and also shown as inset in Figure 6.8. In such potentiometric configuration, the internal electronic circuitry interprets the adjusted voltage and displays it as a pH level or its accumulative absolute value in 'mV'. Importantly, the fact that the ND-coated ISFET retains the same, near-to-ideal, value as the bare Si device at 55.3mV/pH against the theoretical Nernstian limit of 59.2mV/pH is encouraging, suggesting that the device remains highly responsive to pH changes. It can be surmised here that NDs are an effective gate material for ISFETs in terms of H^+ ions or pH level detection.

Carboxyl (COOH) groups amongst others contribute to the acidic character to carbon materials [33]. Therefore the attachment of the partially carboxylated ND particles on the gate area has the likely depleting effect on the p-type channel beneath. An overall displacement of the transfer characteristics to the left would then be predicted and consequently up-shifting the linear mV-pH response as colour-coded in Figure 6.8. Hence, the +20mV shift of the gate voltage observed on the mV-pH response line in Figure 5.4 could represent the potentiometric reaction restoring the preset constant drain current.

It can also be argued that the additional dielectric layer formed by the ND possessing capacitance of ~11pF [34] may have played a supporting role in the 20mV upward uniform displacement of the mV/pH slope. The extra dielectric layer that is the ND coating results in two capacitors connected in series and the total value of the capacitive elements C_T of the original pH sensitive oxide layer and the ND coating is the sum of their reciprocals. This phenomenon is illustrated in Figure 6.10.

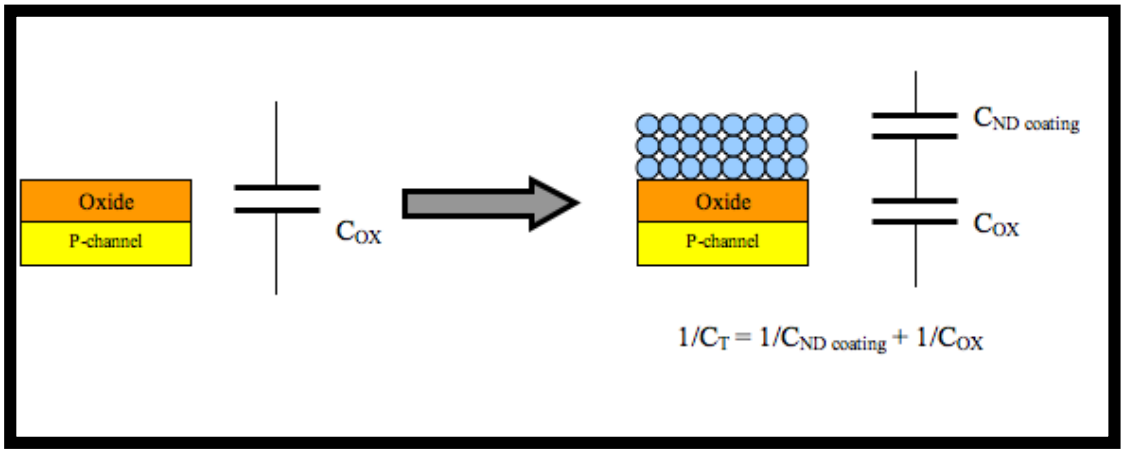

Figure 6.10: Capacitive layers on the (a) as-received (b) ND-coated Si ISFET structures

Based on the equation $C_{ox} = \varepsilon_{ox}/d$ where ε_{ox} and d are relative permittivity and oxide thickness respectively, and the active area of the ISFET at 4mm x 4mm, commercially used pH sensitive materials such as SiO_2, Ta_2O_5 and Al_2O_3 display capacitance values in the range of ~10^{-7} to 10^{-6} F/cm^2. Therefore, adding a 'capacitor' of value ~10^{-11} F/cm^2 in series pulls the effective total capacitance down to the 10^{-11} F/cm^2 range. Based on a computational study made, nanodiamonds of sizes similar to the ones deployed here are also likely to carry a strong net positive charge and potential [35]. With the capacitive characteristic of the ND layer dominating and applying V = Q/C, the probable presence of the strongly positive charge and potential could also play a role in repelling holes away from the channel hence forcing the ISFET to turn on at a higher voltage i.e. larger V_T and an up-shifted pH response slope. From capacitive potential divider network theory, It can also be predicted that the ND layer with a capacitance of 10^{-11} F/cm^2 takes a greater share of the applied potential, reducing the portion received by the semiconductor and as a result, the inversion channel is left slightly pinched and more resistive and in turn, forces the potentiometry to apply a higher voltage to restore the original state of the channel.

Additional to that, the post-synthesis purification method applied and processing technique developed by Osawa *et al* are known to render the individual nanodiamond particles having positive (ζ) zeta potentials of value +40 – 50mV (Table 2.5, Chapter 2) [36], which is critical for DND attachment

on negatively charged oxide surfaces such as SiO_2 via electrostatic attractive force. The +20mV shift could be an approximate measure of the positive (ζ) zeta potential, which may also imply a similar depleting effect on the p-type inversion channel below thus provoking identical potentiometric restoration as mentioned previously. Reviewing the schemes of potentiometric reaction stimulation, it seems plausible to infer that the +20mV shift observed is the combination of the carboxyl group's acidic presence on the nanodiamond surfaces and the comparable values of the positive (ζ) zeta potentials of value 40 – 50mV. It is also worth mentioning that Jee *et al* reported positive (ζ) zeta potential values between +8-40mV in pH 2-12 solutions [32] for DNDs of similar size and identical purification method. The capacitive effect considered could have had still played a contributing role but the consequent voltage shift is expected to be much higher than +20mV due to the near monopoly of the ND dielectric layer.

The DND particles used are partially carboxylated and hydroxylated (Figure 6.8) [29]. Such functional groups are typically responsible for ion and particularly nitro-group molecular adsorption [37-44]. It should also be noted that the C-COOH bond existing between COOH and the diamond surface is expected to be stronger than Si-COOH [45,46] or on any other surface. This implies that the nanodiamond sensing surface will display greater stability than those based on other materials. It has been demonstrated that the basic lone pairs of the nitro-groups on 2,4-DNT bind to strongly acidic polymers [47]. Hence, it can be considered that the hydrogen-bond acidic sites of the carboxylated termination region of the DNDs interact with the weakly basic lone pairs found on the oxygen atoms of the nitro-groups of the 2,4-DNT in the present case. Carboxylic groups being Brønsted-Lowry acids are proton donors, and the likely scenario would be proton transfer from the COOH termination on the DNDs to the aromatic nitro-groups of the 2,4-DNT. This leaves the ND surface negatively charged causing channel to be more conductive through accumulation of holes thus reducing the gate-source voltage. As with the mV-pH response, the system will record and display decreasing gate-source voltage with increasing vapour concentration. Evidencing the chemisorption of the 2,4-DNT on ND surface via FTIR scans

on the ND surface is presented in Chapter 7 of this thesis. The absence of the crucial -OH part of the carboxyl group on the bare Si ISFET is deduced to be responsible for the device's insensitivity towards 2,4-DNT.

The acid-base interaction being fundamental to the sensing mechanism here is duplicated between COOH and ionic nitro-groups in the nitrite solution such as the NO_2^-; proton (H^+) transfer from the acidic (OH) part of COOH to the slightly basic NO_2^-. Essentially, the proton transfer reduces the 'positivity' of the acidic COOH termination and consequently, the DND surface. Based on the H^+ calibration curve (Figure 6.4), the effective decrease of total positive charge on the active area of the ISFET should shift down the gate-source voltage and this is clearly demonstrated by the ND-coated ISFET's decreasing output voltages with increasing concentration of NO_2^- as was observed with DNT. By the same token, the basic presence of the ClO_3^- in $NaClO_3$ is purportedly detected by the same functional group COOH, again necessitating the transfer of H^+ to the basic ClO_3^- rendering the surface of the nanodiamond layer more negative, thus similarly decreasing the ISFET output voltage. The output trends further suggest that the chemisorption affinity of the salt solutions' cationic element Na^+ had a minor or insignificant real adsorption on the nanodiamond surface corroborated by work done on the ion selectivity of imperfectly hydrogenated polycrystalline diamond surface to K^+ and Mg^{2+} [48]. The downward trend of the output voltage with increasing concentration confirms the chemical interaction is solely between the nanodiamonds and the anions, NO_2^- and ClO_3^-.

Exposure to NH_3 vapour at 5 levels of concentration generated an output trend that corroborates the ND-coated Si ISFET's general response to particles containing levels of basicity. The basic NH_3 molecule was expected to reduce each acidic carboxyl group site to an effective COO^- by withdrawing a proton (H^+) and forming NH_4^+ [49], rendering the ND surface negatively charged and consequently, depleting the FET channel of electrons. Such condition would provoke the potentiometry to generate and display a more negative voltage to maintain a constant drain-source current. Without the COOH on the uncoated Si ISFET, the acid-base interaction could not be

supported hence inability to detect and rationalise the presence of varying NH_3 vapour.

In the vapour phase detection, a gate-less FET operation is assumed with the open gate area modulating the channel below upon the chemisorption of admolecules. With the absence of the reference electrode acting through a liquid medium, control of the potentiometry is thought to be taken over by the drain-to-source voltage. Enhancement or depletion of the FET channel from the adsorption of respective gas molecules therefore signals the drain voltage to change accordingly for drain current regulation. Such model adequately explains the observed output trend in response to 2,4-DNT and NH_3 exposure.

Polarization of the ND surface due to 2,4-DNT chemisorption was reproduced when a nanodiamond layered hydrogen-terminated diamond resistance-based sensor fabricated by Ahmad *et al* [50]. The decreasing resistance of the p-type channel upon exposure to increasing 2,4-DNT vapour further corroborates the ISFET response model proposed here.

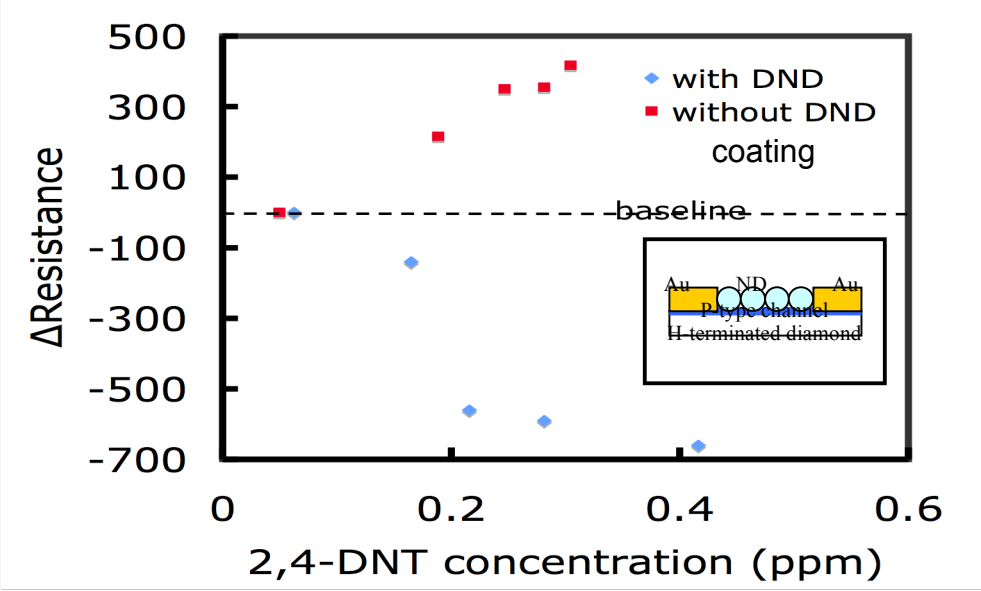

Figure 6.11: Changes in surface conductivity (expressed in ∆resistance) of bare and DND-coatd HD resistor sensor in response to exposure to 2,4-DNT vapour[50]

An important point of observation is the large sensitivity advantage of the ND-coated ISFET against the control unit over a decade molarity change of $NaNO_2$ and $NaClO_3$, and at low concentrations of 2,4 DNT vapour at 37ppb and 385ppb. The voltage gaps between 0.1M and 0.01M of $NaClO_3$ and $NaNO_2$ are 17.2mV and 62.3 mV for ND-coated ISFETs, compared to that of the uncoated ISFET at 1.3mV and 36.7mV. The detection of 2,4 DNT covers a potential difference of 17.8mV on the ND-coated ISFET compared to only 2.5mV by the Si ISFET over the range from zero to 385ppb. The superior sensitivity may arise through the nanodiamond coating presenting a high surface area : volume ratio, therefore offering more exposed COOH sensing sites. There is also evidence of discrimination between the cationic species NO_2^- and ClO_3^- based on the output voltages generated. In the concentration regime of 0.01 and 0.0001M, the adsorption of ClO_3^- produced greater voltage increases (Figure 6.5). The larger dipole moment possessed by ClO_3^- at 2.2 Debye [51] compared to that of NO_2^- at 0.21 Debye [52] could possibly account for this phenomena.

6.6 Conclusions

To conclude, the concept of an effective hybrid ISFET by nano-diamond coating commercially available silicon devices has been demonstrated. The mechanism of sensing utilizes the electronic transduction of the alteration of the characteristic surface charge of the nanodiamonds induced by chemisorption provoking the corresponding modulation of the channel current and shifts in the threshold voltage. Promisingly, the high sensitivity exhibited following the chemisorption of $NaNO_2$ (RDX and HMX precursor), $NaClO_3$ and 2,4 DNT at low molarities and vapour concentrations respectively shows this to be an inexpensive and uncomplicated approach for the detection of threat signatures. By extension, fully COOH functionalised DND particles should present a greater sensitive platform and is a natural step forward from this work. Other functional groups may be attached or the DN surface treated for selectivity studies. Based on the given manufacturer's information, the active area of the Si ISFET is covered with a membrane layer

enhancing sensitivity to H^+. This layer did not impede the operation of the hybrid device, but further work to compare devices in the absence of such a layer should be performed in future work.

6.7 References

[1] P. Bergveld, "ISFET, theory and practice," in Proc. IEEE Sensor Conf., Toronto, ON, Canada, pp. 1–26, Oct. (2003)

[2] P. Bergveld, Sensors and Actuators B, 88, 1 (2003)

[3] K. Y. Park, S. B. Choi, M. Lee, B. K. Sohn, S. Y. Choi, Sensors and Actuators B, 87, 1 (2002)

[4] A. Izquierdo, M. D. L.de Custro, Electroanalysis, 7, 505 (1995)

[5] E. Sharon, R. Freeman, I. Willner, Electroanalysis, 21, 2185 (2009)

[6] L. Tang, C. Tsai, W.W. Gerberich, L. Kruckeberg, D.R. Kania Biomaterials 16, 483 (1995)

[7] H.J Mathieu Surf. Interface Anal. 32, 3 (2001)

[8] F.Z. Cui, D.J. Li Surf. Coat. Technol. 131, 481 (2000)

[9] K. Takahashi, M. Tanga, O. Takai, H. Okamura, Bio Indust. 17, 44 (2000)

[10] K. Takahashi, M. Tanga, O. Takai, H. Okamura Diamond Relat. Mater. 12, 572 (2003)

[11] W. Yang, O. Auciello, J.E. Butler, W. Cai, J.A. Carlisle, J.E. Gerbi, D.M. Gruen, T. Knickerbocker, T.L. Lasseter, J.N. Russell, Jr, L.M. Smith, R.J. Hamers, Nature Mater. 1, 253 (2002)

[12] J.A. Garrido, A. Härtl, S. Kuch, M. Stutzmann, O.A. Williams, R. B. Jackman, Appl. Phys. Letts., 86, 073504 (2005)

[13] C. E. Nebel, B. Rezek, D. Shin, H. Watanabe, T. Yamamoto,

J. Appl. Phys., 99, 033711 (2006)

[14] B. Rezek, H. Watanabe, D. Shin, T. Yamamoto, C.E. Nebel, Diam. & Relat. Mater., 15, 673 (2006)

[15] M. Dipalo, C. Pietzka, A. Denisenko, H. El-Hajj, E. Kohn, Diam. & Relat. Mater., 17, 1241 (2008)

[16] A. Denisenko, G. Jamornmarn, H. El-Hajj, E. Kohn, Diam. & Relat. Mater., 16, 905 (2007)

[17] O.A. Shenderova, V.V. Zhirnov and D.W. Brenner, *C*rit. Rev. Solid State Mater. Sci. 27, 227 (2002)

[18] O.A. Williams, O. Douheret, M. Daenen, K. Haenen, E. Osawa, M. Takahashi, Chemical Physics Letters 445, 255 (2007)

[19] A. Friedman, P.L. Kebabian, Z. Li, W.A. Robinson, J.C. Wormhoudt, Meas. Sci. Technol. 19, 125012 (2008)

[20] T.A Wilson, 'The Total and Partial Vapor Pressures Of Aqueous Ammonia Solutions', University Of Illinois Engineering Experiment Station, Bulletin No. 146, February (1925)

[21] G.V. Mozjoukhine, Appl. Magn Reson. 18, 527 (2000)

[22] J. Ledgard, "The Preparatory Manual of Explosives", Third Edition, English, ISBN: 0615142907, (2007)

[23] B. Timmer, W. Olthuis and A. Van Den Berg, Sens. Actuators, B, 107, 666 (2005)

[24] M. Vidotti, L. H. Dall, S. I. Cordoba de Torresi, K. Bergamaski and F. C. Nart, Anal. Chim. Acta, 489, 207 (2003)

[25] B.A. Lopez de Mishima, D. Lescano, T. Molina Holgado and H. T. Mishima, Electrochim. Acta, 43, 395 (1998)

[26] A. C. A. de Vooys, M. T. M. Koper, R. A. van Santen and J. A. R. van Veen, J. Electroanal. Chem., 506, 127 (2001)

[27] D. Giovanelli, M. C. Buzzeo, N. S. Lawrence, C. Hardacre, K. R. Seddon and R. G. Compton, Talanta, 62, 904 (2004)

[28] W. M. Siu and R. S. C. Cobbold, IEEE Trans. Electron Devices 26, 1805 (1979)

[29] A. Krueger, J. Stegk, Y. Liang, L. Lu, G. Jarre, Langmuir 24, 4200 (2008)

[30] A. Poghossian, M.H. Abouzara, A. Razavia, M. Bäckera, N. Bijnensc, O.A. Williams, K. Haenen, W. Moritze, P. Wagner, M.J. Schöning, Electrochimica Acta 54, 5981 (2009)

[31] D. E. Yates, S. Livine and T. W. Healy, Site-binding model of the electrial double layer at the oxide/water interface, J. Chem. Soc., Faraday Trans. I, 70, 1807- 1818 (1974)

[32] A.Y. Jee, M. Lee, Current Applied Physics, Vol. 9, 2, 1 (2009)

[33] O.A Shenderova, S.A. Ciftan Hens, D. Ho, 'Nanodiamonds: Applications in Biology and Nanoscale Medicine', ISBN 978-1-4419-0530-7, p.93 Springer (2010)

[34] A. Chaudhary, J.O. Welch, R.B. Jackman, Appl. Phys. Lett. 96, 242903 (2010)

[35] W.K. Liu, D. Ho, 'Nanodiamonds: Applications in Biology and Nanoscale Medicine', ISBN 978-1-4419-0530-7, p.264-269 Springer (2010)

[36] E. Osawa, Pure Appl. Chem., Vol. 80, No. 7, pp. 1365–1379 (2008)

[37] H. Benhima, National Doctorate of the Faculty of Sciences, Agadir, Morocco. (2002)

[38] H. Benhima, M. Chiban, F. Sinan, P. Seta, M. Persin, Colloid and Surface B: Biointerfaces. 61, 10 (2008)

[39] H. Benhima, M. Chiban, F. Sinan, P. Seta, Récents Progrès en Génie des Procédés, Lavoisier, Ed Tec et Doc, Paris, No. 89, p.353 (2003)

[40] F. Sinan, Doctorat of state, Faculty of Sciences, Agadir, Morocco. (1995)

[41] F. Chiban, H. Benhima, B. Saadi, A. Nounah, F. Sinan, J. de Physique IV. 123, 393 (2005)

[42] M. Chiban, A. Amzeghal, H. Benhima, F. Sinan, S. Tahrouch, P. Seta, Reviews in Biology and Biotechnology, 6, 40 (2007)

[43] N. Kuyucak, B. Volesky, Biotechnol. Lett. 2, 137 (1988)

[44] M. Friedman, A.C. Waiss, Environ. Sci. Tech. 6, 457 (1972)

[45] R.T.Sanderson, *Polar Covalence*, 1983, Academic Pr; First Printing edition, ISBN 978-0126180800, (March 1983)

[46] R. T. Sanderson, Chemical Bonds and Bond Energy, Academic Press, New York (1971)

[47] E.J Houser, T.E. Mlsna, V.K. Nguyen, R.Chung, R.L. Mowery, R.A. McGill, Talanta 54, 469 (2002)

[48] A. Härtl, J.A. Garrido, S. Nowy, R. Zimmermann, C. Werner, D. Horinek, R. Netz, M. Stutzmann, J. Am. Chem. Soc., 129 (5), pp 1287–1292 (2007)

[49] L. Sun, R.M. Crooks, Langmuir, 9, 1775-1780 (1993)

[50] Rezal K. Ahmad, Ana Carolina Parada, Niall Tumilty, Richard B. Jackman, Appl. Phys. Lett. 97, 203503 (2010)

[51] L.J.A. Siquiera, S. M. Urahara, M.C.C. Ribeiro, Journal of Chemical Physics, Vol. 119, No. 15, pp. 8002-8012 (2003)

[52] S. Flugge, K.V. Meyenn, Z. Physik 253, 369 (1972)

Chapter 7

Fabrication and Characterisation of Triangle-faced Single Crystal Diamond Micro-Cantilevers

7.1 Introduction

Cantilever sensors fall under the category of microelectromechanical systems (MEMS) that rely primarily on mechanical phenomena and involve the transduction of the mechanical energy [1]. These so-called MEMS sensors operate on the deformations of their micromachined parts such as singly and doubly supported beams i.e. cantilevers and bridges or diaphragm respectively. Typically, sensors based on the cantilever design fits the definition of a chemical sensor consisting of a physical transducer and a chemically selective layer so that an appreciably measurable signal can be generated in reaction to chemical stimuli [2]. The interest in MEMS transducers is demonstrated by their latent applications in telecommunications [3-5], optical imaging [6,7] and data storage [8-13]. However, in recent times extensive research effort has been focused on innovative group of physical, chemical and biological sensors based on the cantilever design of which its physical configuration is very much suited for the conversion of afore-mentioned stimuli into readable signals [14-15] using optical [16], piezoresistance [17], piezoelectric [18-21], capacitive [22-24] and electron tunnelling methods [25].

In the static mode of operation, the bending of the cantilever takes place in response to the gradient of the mechanical stress generated in the device. Typically, the induced surface stresses are created by the adsorption of the targeted analyte on the chemically selective surface of the cantilever. Importantly, one of the sides of the cantilever must be kept inert to the targeted adsorbates because the cantilever can only deflect when there is a difference of surface stress between the top and bottom surfaces of the beam. Cantilever transducers can also be operated in the dynamic mode that means the beam is constantly in oscillation only to be mechanically damped by the adsorption of chemical or biological species. The resonating motion can be generated by an ac source and electromagnetic or even acoustic field excitation. The micro-sized static-mode and dynamic-mode cantilevers might

carry an inherent surface stress that would render them in pre-bent state and receptive to thermally induced noise respectively.

Cantilevers are typically made of single-crystal silicon due to the achieved economy of scale, and its matured and reliable fabrication technology. The advent of chemical vapour deposited (CVD) diamond as a material platform for chemical and biological sensing devices produced the concept of diamond cantilevers carrying identical sensing purposes to that of silicon micro-beams. Diamond possesses extreme properties such as high mechanical strength, exceptional chemical inertness and outstanding thermal stability. Favourably, diamond's friction coefficient is very low at ~0.1-0.01 compared to silicon's value of 0.45 and its projected wear life and brittle fracture strength is respectively 10^4 and 23 times greater than that of silicon, making diamond tribologically an ideal material for MEMS devices [26,27]. Additionally, diamond can be hydrogen or oxygen terminated, offering both hydrophobic and hydrophilic properties, and the passivated surface provides a natural lubricant between contacting MEMS components [28].

Diamond is also naturally biocompatible [29-31] therefore has a potential for 'in-vivo' sensing. To generate chemical and biologically selective diamond surfaces, a photochemical chlorination / amination / carboxylation process on H-terminated surfaces has been used [32,33]. Further progress in the form of a photochemical method using alkene to modify the nano-crystalline diamond (NCD) surface [34], electrochemical reduction of diazonium salts to functionalize boron-doped ultra-NCD [35], and the introduction of direct amination process of diamond [36] encourages more diamond-based sensor research activities. These functionalized surfaces have also been modified with DNA, enzymes and protein [34] to complete the biological and chemical sensing portfolio of the much-needed diamond sensors, in this case the cantilever type.

Diamond cantilever structures have been successfully fabricated using NCD-on-Si by lithographic techniques for patterning followed by either the growth phase (for the seeding method) or reactive ion etching on an existing NCD

layer to fully form the cantilever shapes [28]. The free-standing beams are released by the use of an undercutting selective silicon wet etch process. However, NCDs' mechanical properties are reported to be dependent on the grain size, and are always inferior to single crystal diamond [37]. For example, Young's modulus and mechanical hardness for NCDs are typically in the range 800-980 GPa and 45-90 GPa, compared to values of 1050 GPa and 96 GPa for single crystal material. Single crystal diamond also offers more consistency surface morphology thus creating the possibility of having an array of single crystal diamond cantilevers carrying identical mechanical properties. Since single crystal HPHT and CVD diamond has now become a commercially accessible material, it is timely to consider its use as the platform material for diamond MEMS.

A single crystal diamond-based cantilever structure as previously been reported, was fabricated by a focused ion beam (FIB)-assisted lift-off technique which employed MeV ion implantation, followed by FIB micro-patterning and selective chemical etching [38]. The undercut clearance below the cantilever was reported to be approximately 0.2μm. This makes it inaccessible to micro-capillary tube insertion for diamond surface functionalisation that is expected to be required for subsequent sensing applications. In this article, a more simple process is demonstrated, using a technique solely based on the application of the FIB to mill and pattern a free-standing cantilever in a single crystal diamond plate, which is expected to provide a solution to the problem associated with limited clearance under the cantilever previously reported. Various annealing procedures have been used to remove residual damage and contamination. Raman characterisation and Energy Dispersive Spectroscopy (EDS) on the fabricated beam structures have been carried out.

7.2 Experimental and theoretical design considerations

The basic design approach adopted is depicted in Figure 7.1. The FIB tool comprises a beam of energetic Ga^+ ions, which physically sputter the

diamond in the direction of the impinging beam; use of the beam at two angles can be used to create a triangular 'trench' (Figure 7.1(i), (ii)), with a third cut being used to release the cantilever (Figure 7.1(iii), (iv)). The resulting triangular structure represents the simplest way of constructing a cantilever using only FIB milling as compared to a conventional rectangle cross-sectioned cantilever. This is is a clear departure from the conventional shape used so the potential of a triangular cantilever for MEMS applications must be considered.

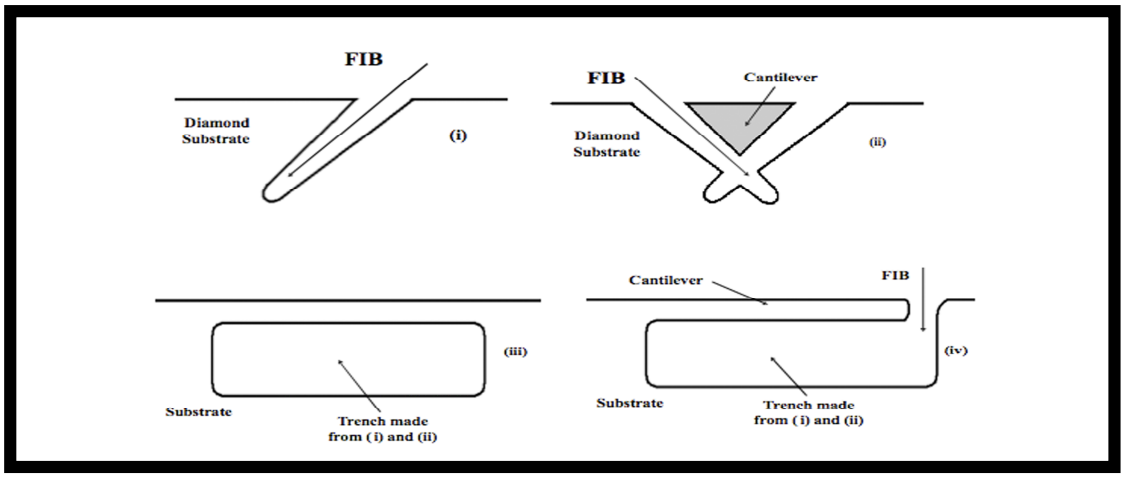

Figure 7.1: Cantilever Fabrication using FIB. (i) A long FIB cut is applied at an angle on to the substrate. (ii) A second FIB cut of the same length then applied on the opposite side, resulting in a triangular cross sectioned cantilever being formed. (iii) The side view after the long trenches in (i) and (ii) are applied. A final cut at the end results in the cantilever being made (iv).

Considering the non-extreme case that the force applied is a uniformly distributed load (UDL), a load that is applied evenly over the entire cantilever, The maximum bending a cantilever would suffer is given by [39],

Maximum deflection, $$\delta = \frac{Fl^4}{8EJ} \qquad (1)$$

Where l is the length of the cantilever, F is the force being applied on the cantilever, E the Young's Modulus of the material and J is the 2nd moment of

inertia of the cantilever cross section. The latter term defines the resistance of the shape (cross section) to bending, as shown in figure 2, with definitions for the relevant dimensions which will give different second moments of inertias given by Equations (2) and (3).

$$I_{rectangle} = \frac{tw^3}{12} \qquad (2) \qquad\qquad I_{triangle} = \frac{tw^3}{36} \qquad (3)$$

The bending of the cantilever causes sheer stress on the cantilever acting in parallel to the beam, which is given by,

Stress on cantilever, $$\varepsilon = \frac{M\delta}{J} \qquad (4)$$

Where **M** is the moment from the bending (Force × distance). Stoney's Equation [39] is another equation that is important in describing cantilever properties, that is

Deflection, $$\delta = \frac{3\sigma\,(1-v)}{E}\left(\frac{l}{t}\right)^2 \qquad (5)$$

Where the terms are as defined previously, whilst σ is the surface stress and v represents Poisson's ratio of the cantilever material. Poisson's ratio is the ratio of the relative contraction strain, or transverse strain normal to the applied load, to the relative extension strain, or axial strain in the direction of the applied load.

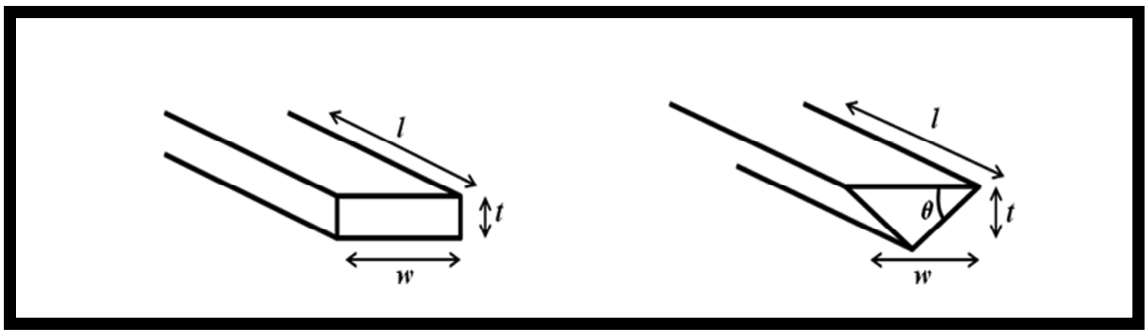

Figure 7.2: The cross sectional view of the 2 types of cantilevers as well as notations for its dimensions. *l, h* and *b* are the length, height and base size of the cantilever. θ is the angle between the base and side of the triangle.

It is essential that the cantilever to have very good deflection capabilities as this would correlate to good signal readouts. It can be seen from equations (1), (2) and (3) that the strongest factors that influence this property are the dimensions ***l,*** length and ***w***, width of the cantilever. So to have a good bendy cantilever, it would need to be long and thin. Stoney's equation suggests that a cantilever of the same material and deflection will have a surface stress that depends on the square ratio of the length to thickness of the cantilever. Surface stress, ***σ*** is the amount of work per unit area required to stretch a surface.

To model the bending, it was important to first determine the magnitude of force the cantilever could possibly be subjected to when trying to function. As mentioned, most of the established cantilever research some with functionalized surfaces are on silicon cantilevers. Though made from different materials, the forces that these cantilevers undergo would still be similar when the surfaces are functionalized similarly. As an example, the differential surface stress of some silicon cantilevers functionalized with non-ionizable hexadecanethiol self assembled monolayers used to ionic hydrogen bond formation gave a mean tensile differential surface stress of +1.2 ± 0.3 mN/m to -14.5 ± 0.5 mN/m for a silicon cantilever of 500μm length, 100 μm width and 0.9μm thickness (500 × 100 × 0.9) μm [40]. This gave an absolute deflection of about 350 nm. The sign (positive or negative) of the mean tensile differential surface stress, ***σ*** indicates (tensile or compressive respectively)

the direction the cantilever will bend, upwards or downwards. The uniform force on this silicon cantilever (500 × 100 × 0.9) μm with a 350nm deflection can be calculated using equation (1) to be 0.504 N.

Taking a rectangle cross section diamond cantilever with arbitrary dimensions of ***l*** = 10 μm, ***w*** = 2 μm and ***t*** = 1 μm (10 × 2 × 1) μm the amount of force it would undergo would be proportional to the area, resulting in a value of 2 x 10^{-4} N. This gives a deflection, stress and surface stress for the diamond cantilever (10 × 2 × 1) μm of 1.3pm, 7620 N and 6.3 x 10^{-3} N/m using the above equations. Again using these equations, the deflection of a diamond cantilever with these dimensions was modelled for both rectangular and triangular cross sections, and is plotted against force applied in figure 3.

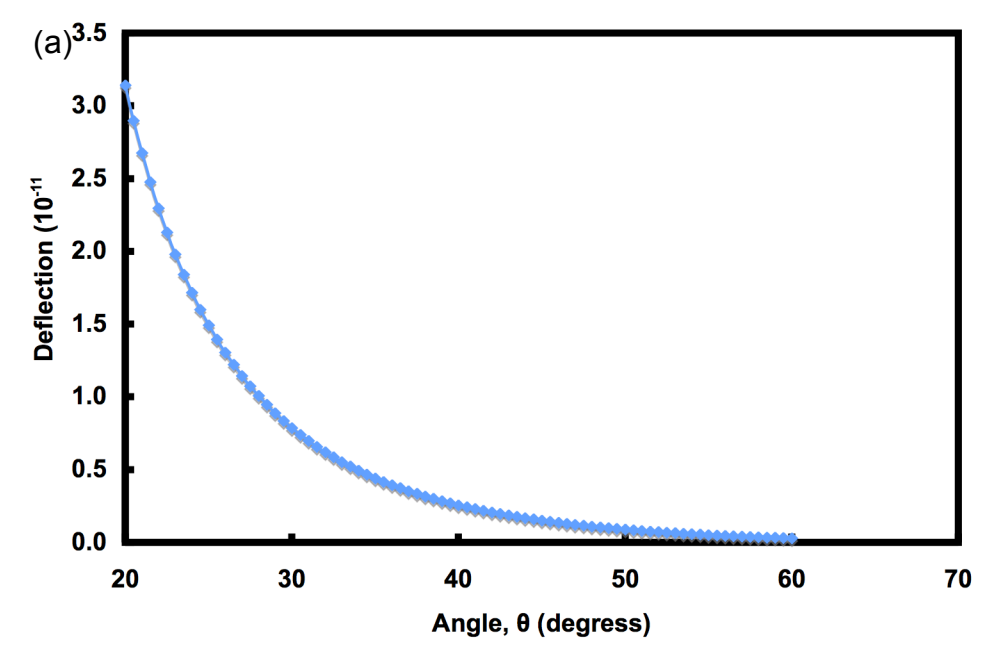

(b)

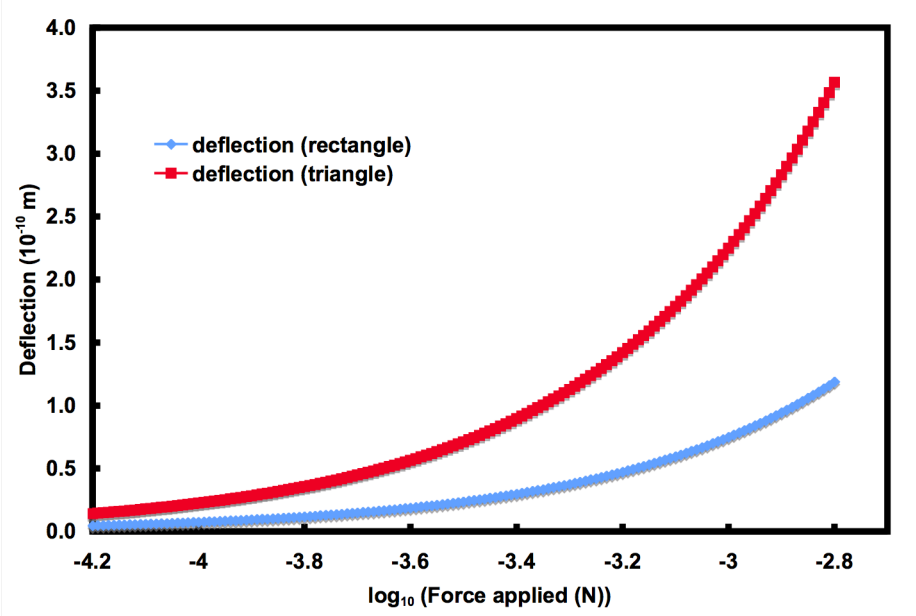

Figure 7.3: (a) The graph of Deflection Vs Force Applied on the cantilever that compares the deflection between a triangular and a rectangular cross sectioned (10 × 2 × 1) μm cantilevers (b) The graph of Deflection Vs Angle, θ between the side and base of a the triangle cross section

It can be seen from figure 7.3(b), that the deflection of the triangular cantilever is significantly more, by a factor of three, than a given rectangular cantilever with the same dimensions. Intuitively, this concurs with the equations (1) and (3) that the triangular cantilever, having a 2nd moment of inertia 3 times smaller than that of the rectangle, would be 3 times easier to bend given identical dimensions as compared to the rectangular cantilever and hence this would give out 3 times the magnitude of signal output. It can therefore be concluded that having a triangular cross section cantilever could actually be a positive design attribute. For the triangular cantilever the thickness, would depend on angle at which the FIB milling is will also be important. The modelling shown in Figure 7.3(a) indicates more important to avoid large angles beam milling (>50^{o}) during fabrication which would result in little deflection.

7.3 Experimental methods

An FIB system equipped with *in-situ* SEM imaging (Carl Zeiss XB1540 "Cross-Beam" focussed-ion-beam microscope) was used throughout with Ga^+ ions at energy of 30 KeV, and beam currents in the 2-5 nA range. Single crystal CVD and HPHT diamond samples ((100) and Ib plates, Element Six Ltd) were degreased and cleaned in strongly oxidising solutions before use. A thin (~50nm) Au coating was applied using the Bell Jar A360 thermal evaporator, before carrying out FIB experiments to avoid sample charging. The samples were prepared onto the FIB stage with the gold surface grounded in the corner using silver paint through the FIB stage. The working distance in the vacuumed FIB chamber was 5mm in a vacuum of about 0.2-0.3 mPa. The area, angle of incidence, gun current and duration of the ion beam were varied. This ion beam can be manipulated to focus in various accurate ways. The area of focus can be varied from large rectangles to thin lines. The depth of milling can also be controlled by varying the current used to launch the ions, from nanoamperes to miliamperes and the duration of the milling.

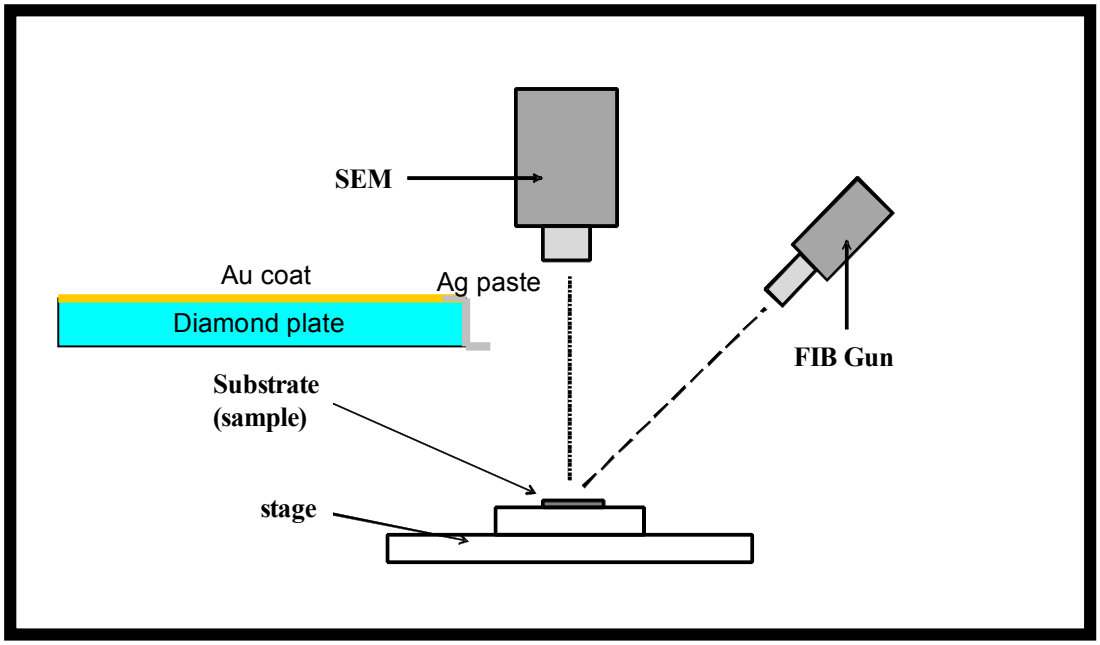

Figure 7.4: A simplified diagram of the inside of the vacuum chamber in a FIB machine

It would be practically impossible to get really small angles using the FIB so the lower range (< 25°) of good deflection is unattainable. At the same time, it is more important to avoid the large angles (>50°) during fabrication which would result in little deflection. . To make the cantilever have as little height, ***h*** as possible, the angle (90º - θ) at which the FIB milling is done has to be as large as possible to result in θ to be as small as possible (Figure 7.5).

So,

$$\text{Height of cantilever, } \boldsymbol{h} = \frac{b}{2}.\tan\theta$$

The angle θ, is set to be 34° which is the lowest possible angle that can be achieved using the given FIB machine that has a maximum milling angle of 54°. So for this cantilever with a base of 3 μm and the smallest possible FIB incident angle being 54º (θ = 36º),

$$h = \frac{3}{2}\tan(90° - 56°)$$
$$= 1.0898\ \mu m$$

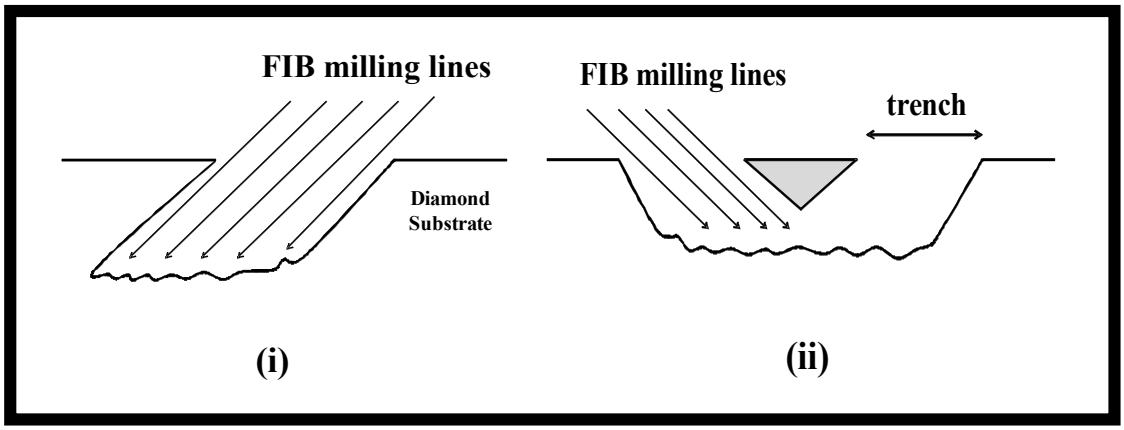

Figure 7.5: The multiple-line milling approach used to successful construct the cantilevers

To get the required depth when milling, the area of the FIB had to be reduced to mere lines as this focused all of the ions on to a small area leading to

sufficient penetration. These small FIB milling lines put together were required to achieve a large enough trench for the structure to be free standing. These lines were typically 15-20μm long using 2nA of FIB gun current for time durations in the range 300-500s.

FIB milled samples underwent a number of annealing steps at 500^{o} C, 750^{o} C and 1000^{o} C in flowing N_2 atmosphere at a vacuum pressure of ~10^{-6} Torr to remove possible residual damage and contamination by FIB-micromachining. A Renishaw Raman micro-spectroscopy system (model) was used to extract Raman spectra by the means of an Ar laser at 514nm with a spot diameter of ~5μm and intensity of ~ 200kWcm^{-2}. EDS spectra were acquired by a Hitachi S-4800 Energy-dispersive X-ray Spectroscopy system, which includes spectral imaging, qualitative and quantitative analysis of contamination levels. For the very purpose of characterisation, a set of wide cantilevers (w ~5μm) was fabricated to accommodate the Renishaw's smallest laser spot focus. Both Raman and EDS spectra were collected at each annealing steps described above.

7.4 Results

A large number of FIB structures were created; representative SEM images are shown here. Figure 7.6(a) shows a cantilever with dimensions of around 16 × 3 × 2 μm (cantilever I, indicated by arrow). Sloping sidewalls can be seen either side of the cantilever, with significant roughness or debris being evident. Multiple FIB milling lines were used. Figure 7.6(b) shows another cantilever (cantilever II), now with dimensions of ~32μm long with a width of ~2μm; similar structuring on the surrounding side walls can be seen. Further milling of cantilever II, lead to the structure shown in Figure 7.6(c), where the beam is now thinner being 575nm

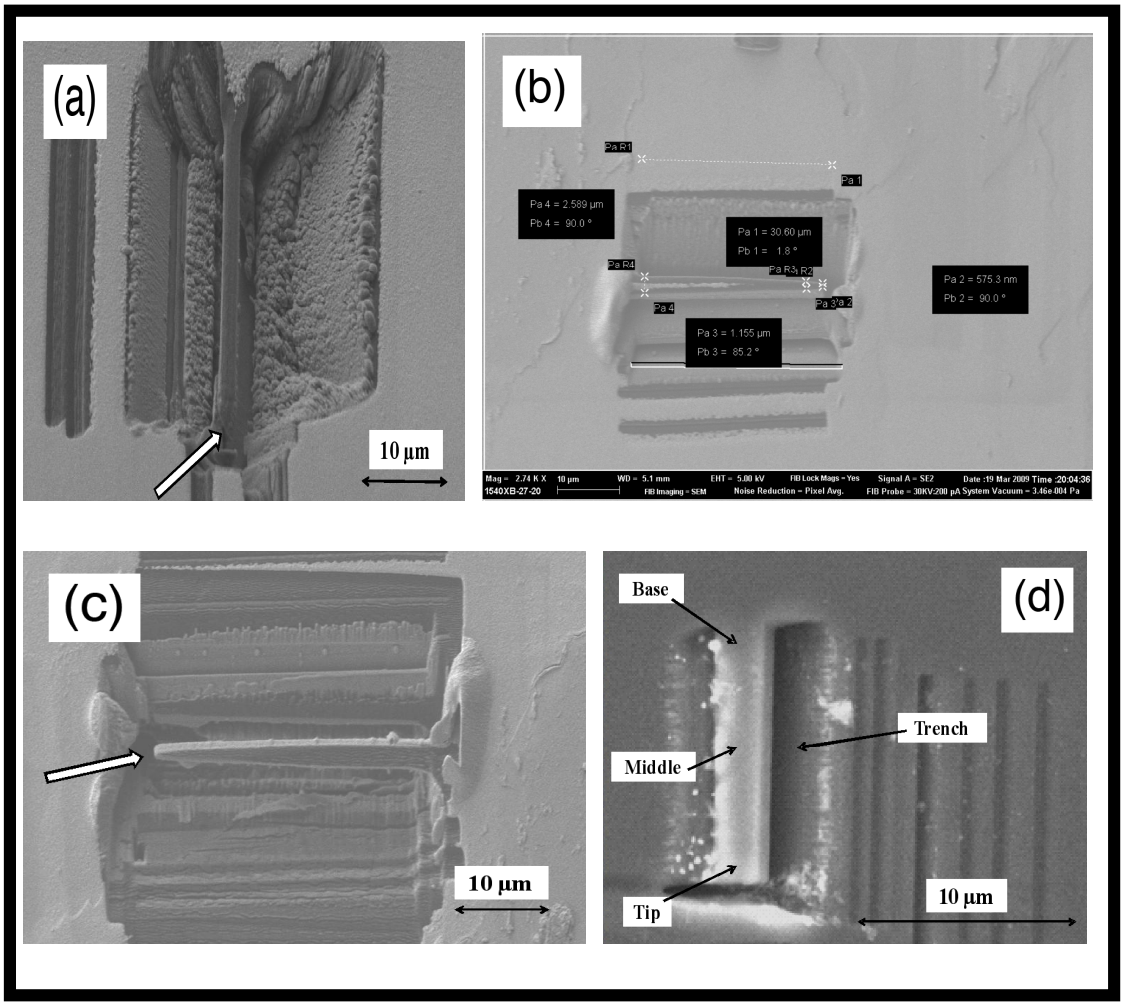

Figure 7.6: (a) Cantilever I was made using multiple FIB milling lines (b) The dimensions of this cantilever are 16.17 × 3.36 ×2.17 µm (c) A smaller width cantilever (originally larger Cantilever II) thinned down by gradually applying FIB milling lines and (d) cantilever IV used for analysis (Figure 7.7).

Raman spectroscopy was used to characterise the chemical nature of the carbon structures after FIB milling had been performed. Figure 4(d) shows an SEM image of a cantilever structure with arrows indicating the position of the Raman analysis. Figure 7.7(a) shows Raman spectra taken from the middle of the cantilever (i) of sample 1 and (ii) sample 2, itself as a function of post-fabrication annealing (in N_2 flowing gas ambient). Sample 2 was only given the 1000^{o}C anneal treatment. The prominent 1332cm^{-1} peak associated with diamond (sp^3) carbon is clearly seen in all cases, but other features are also present depending on the annealing process used. Figure 7.7(b)

concentrates on changes to the diamond peak itself; slight shifts in the peak position and width can be seen. The wavenumber and width of the diamond peak is plotted in figures 7.7(c) and (d) for the different regions identified in the SEM in figure 7.6(d). Considerable variation is apparent in both. The results of EDS on this sample are shown in figure 7.7(e), where the overall percentage of carbon within the sampled area is plotted against annealing treatment. Only in the case of 1000^0C annealing is the sampled area within the EDS measurement solely carbon.

(a) (i)

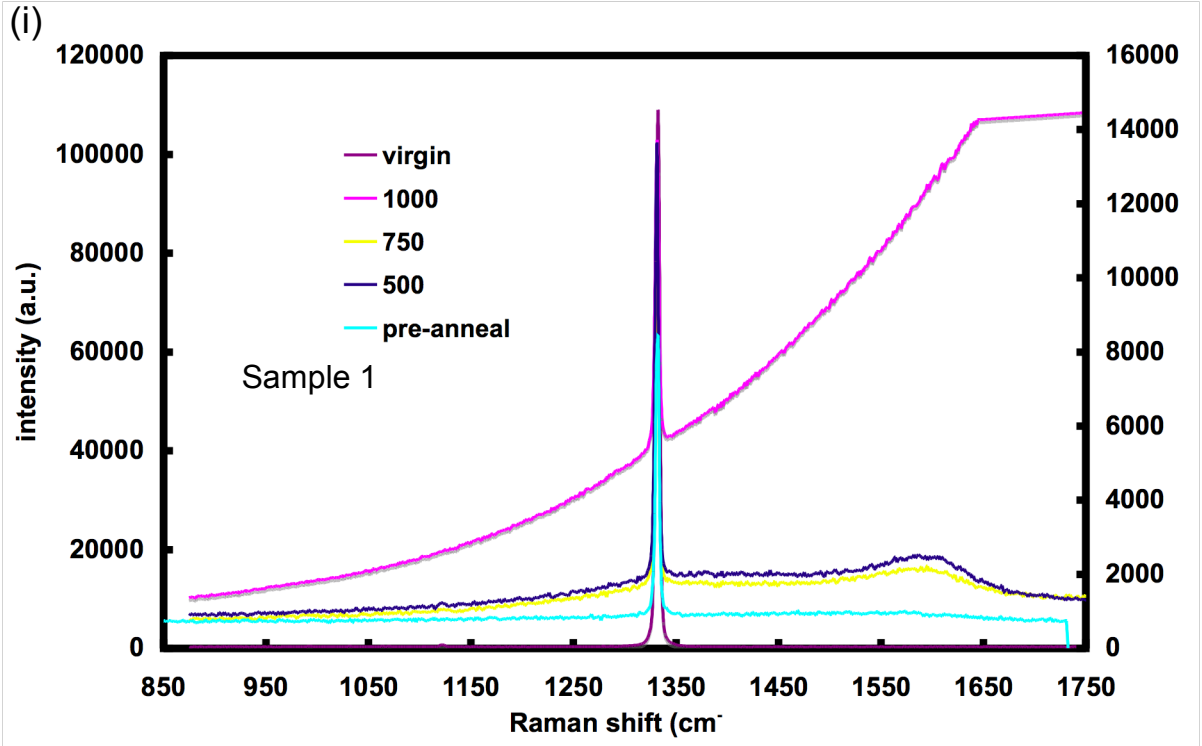

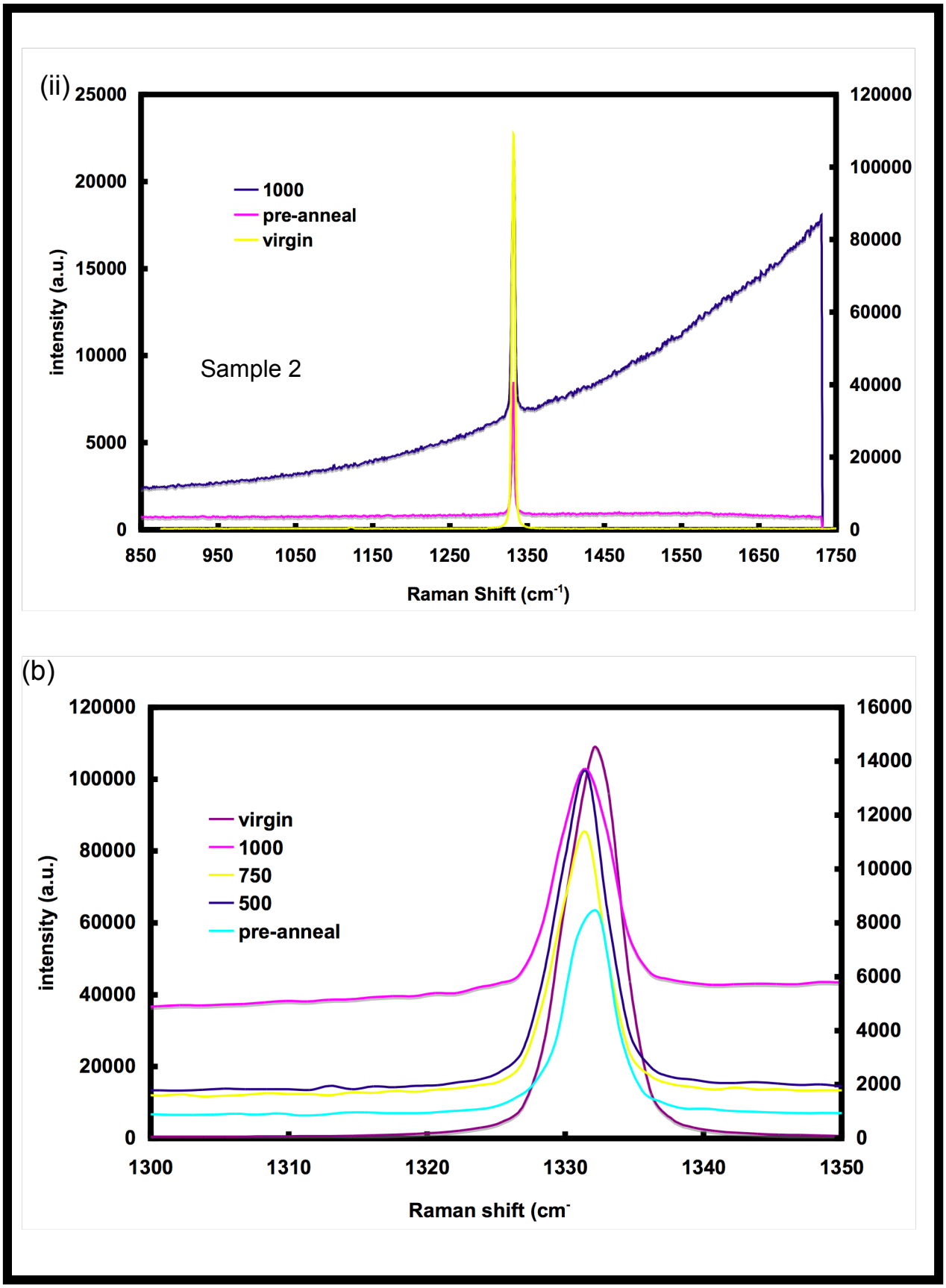
(ii)
intensity (a.u.)
Raman Shift (cm-1)
1000
pre-anneal
virgin
Sample 2
25000
20000
15000
10000
5000
0
120000
100000
80000
60000
40000
20000
0
850
950
1050
1150
1250
1350
1450
1550
1650
1750
(b)
intensity (a.u.)
Raman shift (cm-
virgin
1000
750
500
pre-anneal
120000
100000
80000
60000
40000
20000
0
16000
14000
12000
10000
8000
6000
4000
2000
0
1300
1310
1320
1330
1340
1350

(c)

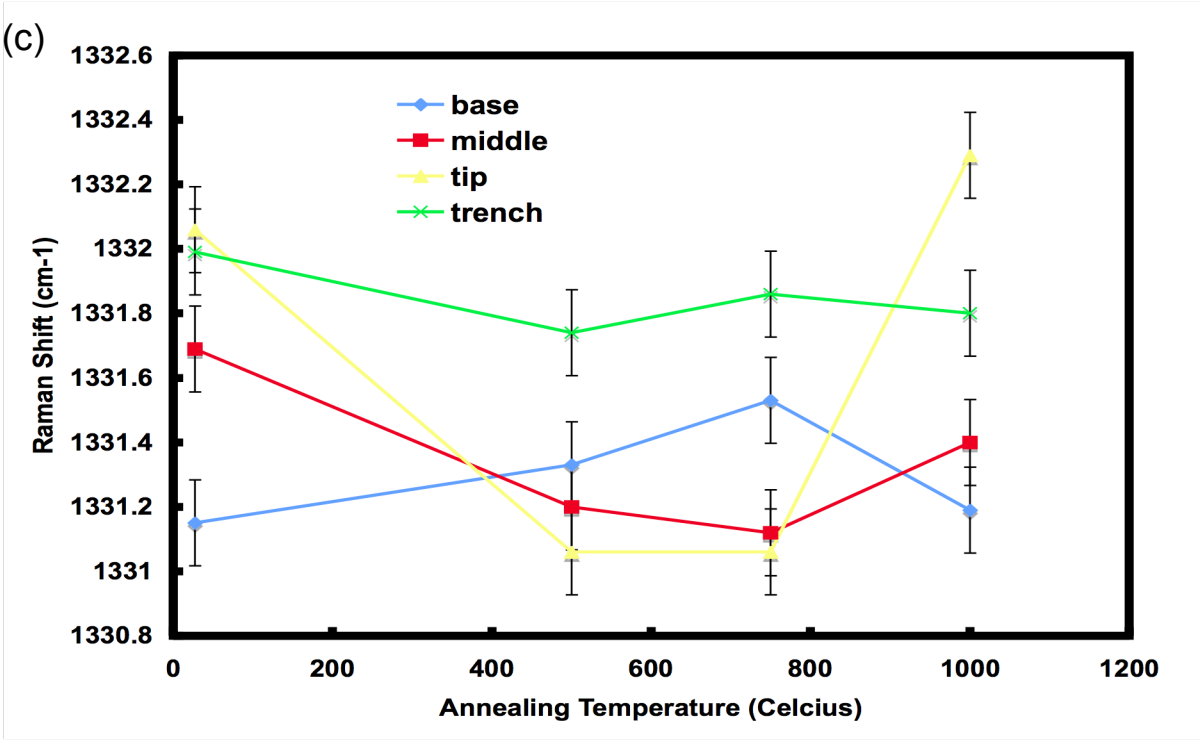
1332.6
1332.4
1332.2
1332
1331.8
1331.6
1331.4
1331.2
1331
1330.8
Raman Shift (cm-1)
base
middle
tip
trench
0
200
400
600
800
1000
1200
Annealing Temperature (Celcius)

(d)

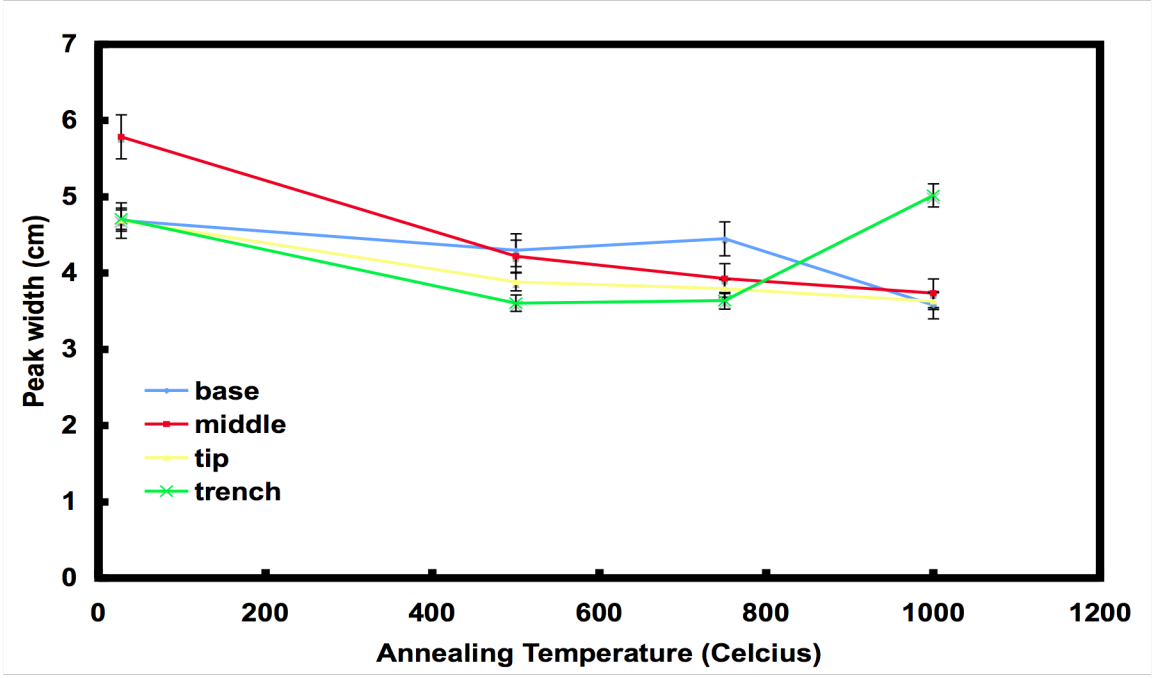
7
6
5
4
3
2
1
0
Peak width (cm)
base
middle
tip
trench
0
200
400
600
800
1000
1200
Annealing Temperature (Celcius)

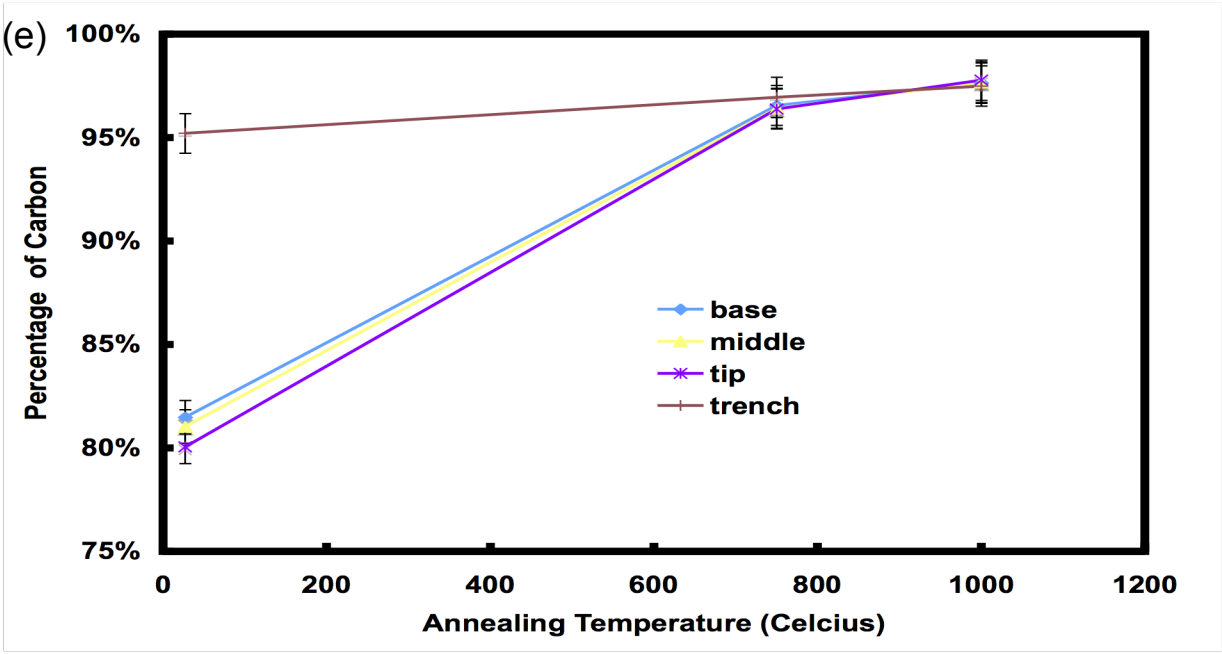

Figure 7.7: Characterisation of cantilever IV, (a) Raman spectra for (i) cantilever 1 and (ii) 2, (b) zoomed-in Raman spectra (c) the distribution and (f) width of the diamond peak at different annealing temperatures for FIB sample and (e) the results of EDS - the percentage of carbon at different areas of the cantilever are plotted against different annealing stages.

7.5 Discussion

Using FIB has been found to be an effective way to finely detail the length and width of an diamond individual cantilever. The SEM images of the cantilever show cantilevers with a varying range of lengths and widths. To get the required depth when milling the FIB had to be used in the form of a focussed 'line' around and several milling lines used to realise the structure. This lead to "scarring" of the remaining diamond as these lines had a small overlap (Figure 7.6). Automation of the FIB process with exact fluence control would overcome this problem. The beam current of the FIB gun could have also been increased to generate deeper penetration with a larger beam, but this lead to an unacceptable level of sputtered material being deposited around the cantilever, presumably because the local pressure increases in this higher

intensity sputtering regime. Very small width cantilevers could be made by gradually encroaching the FIB milling lines towards the cantilever structure. In the present case, widths down to 575 nm have been routinely created with the cross-section of the cantilever body expected to be triangular with a height or thickness of 533nm and a sloping sidewall hypotenuse of 659nm. This beam structure is predicted, based on the calculations shown earlier, to have a significantly better deflection capability compared to conventional rectangular-faced cantilevers of identical length, width and thickness.

It is also noteworthy to mention that the gold-plating and grounding technique applied was adequate to minimise the charging effect to acceptable levels of operation for the fabrication of sub-micron structures such as this. Typically, insulators will experience accumulation of positive charges on the top surface primarily coming from the deposition of Ga^+ ions and the emission of secondary ions through both the former and the imaging SEM electron beam. Highly positively charged surfaces are usually seen as dark features in the SEM image and consequently, deflecting the Ga+ beam observed as drifting making nano-fabrication extremely difficult.

The FIB fabrication of cantilever structures has caused minimal damage in the form of disorder to crystal structure of diamond. This is observed in the Raman spectra shown in Figure 7.7(a-c). In all cases the diamond peak location was around 1331.1 cm^{-1} to 1332.3 cm^{-1} depending on the sample and location on the cantilever structure (Table 1), which are within the range of reported and expected range of Raman peak of 1331-1332 cm^{-1} for diamond prior to any processing [40-41]. The expectation that substantial damage to the crystal lattice will be produced by Gallium ion sputtering using an FIB is found to be not true. However, milling effects do lead to contamination of the near surface region with Ga, with EDS showing around 9% of the sampled region to be Gallium. Annealing processes proved to be effective in removing this contaminant as evidently presented by the significant reduction of Gallium

content and conversely, the increase in the percentage of carbon. Presumably, the cumulative thermal energy supplied to the lattice was sufficient to "soften" the atomic bonds thus facilitating the out-diffusion of the Gallium atoms and concurrently, relieving the presence of internal stress caused by the penetrating Ga+ ions through the removal of crystal defects followed by recrystallization of the diamond lattice.

At the first two annealing temperature stages, a graphite peak (G-peak) at 1575 cm^{-1} could also be seen forming at all locations exampled by the Raman spectra for beam mid-section (Figure 7.7(a)). The first annealing step at 500^{o}C is thought to be the graphite formation stage, as previously observed by Olivero and co-workers when a similar annealing temperature was applied on a single crystal cantilever structure [38]. The higher annealing temperature of 750^{o}C simply exaggerated this feature only to be removed by annealing at 1000^{o}C. This peak represents disordered carbon atoms in the form of graphite resulting from the repairing of the crystal lattice. For the cantilever on sample 2, skipping straight to 1000^{o}C avoided the formation of the graphitic phase but the Raman sloping profile is duplicated. Conversely, the gallium contamination of the diamond was eliminated by the thermal treatment as mentioned in the previous paragraph. Scrutinising the peak width or full width half maximum (FWHM) reveals an effective decreasing trend at all points of the cantilever structure (base, middle and tip) through the annealing stages (Figure 7.7(d)). The FWHM of the Raman line is often taken as a measure of the 'perfection' of the diamond crystallite [43]. This is understood as an indication of the reasonable effectiveness of the diamond crystallinity reordering by the annealing treatment.

The magnitude of damage done from using this FIB only approach for cantilever fabrication appears to be significantly less than previously reported. Olivero and co-workers [38] reported pre-annealing Raman spectroscopy data following showing a broad peak of disordered sp^3 from about 1100cm^{-1} to

1300cm^{-1} and a larger peak width at ~7-8 cm^{-1} compared to ~4-6 cm^{-1} here. The technique used involved a variety of processes that included Helium ion implantation, FIB and acid treatments, which evidently lead to higher damage levels than reported here. In addition, these authors reported that penetrating He^+ ions additionally created new NV centres, which would presumably be avoided using the FIB-only micromachining approach and suggestively demonstrated by the flatness of the pre-anneal Raman spectra. However, the presence of a slope in the Raman spectra after the 1000^{o}C anneal is likely to be the photoluminescence effect coming from the creation of NV centres [43] in the Ib diamond-based cantilever structure. It is very possible that the Ib diamond plate used is littered with lattice vacancies. While these vacancies are immobile at room temperature, annealing at T>700^{o}C allows them to be displaced in the lattice. Single substitutional Nitrogen produces strain in the diamond lattice [44], it is therefore efficient in capturing thermally provoked moving vacancies [45] and N-V centres are in turn produced. Evidencing the inevitable creation of NV centres at 1000^{o}C anneal, the test cantilever on sample 2 reproduced the same sloping Raman profile by discerning the Raman spectra trends through the annealing stages for the test cantilevers on sample 1 and 2 in Figure 7.7(a) (i) and (ii). Therefore such characteristic is deemed to be the by-product of the post-fabrication processes and not directly associated to the FIB-only micromilling technique.

7.6 Conclusion

Fully FIB fabricated single crystal diamond cantilevers with nanometer widths and tens' of micrometer lengths have been demonstrated. These structures may form a useful platform for effective diamond-based chemical and biological sensors following suitable fictionalisation of the cantilever top surface. FIB micromachining provides a simple approach to fabricate MEMS device particularly, cantilevers. The attainable singly supported beam structure differs from conventional design as such that the 'face' or cross-

section is geometrically triangular. The Ga beam can only be angled at a maximum of 54^{o} off normal to the substrate surface. However, calculations showed that the bending capability of triangular-faced cantilevers in general is 3 times to that of the conventional designs. Characterization of the beam structure through Raman spectra revealed minimal lattice damage was inflicted during fabrication. However, Ga contamination level was rather significant. Post-annealing treatment managed to completely evict the contaminants.

7.7 References

[1] G. T. A. Kovacs, *Micromachined Transducers* McGraw-Hill, New York, (1998)

[2] J. Janata, M. Josowicz, and D. M. Devaney, Anal. Chem. 66, R207 (1994)

[3] M. Kim, J. B. Hacker, R. E. Mihailovich, and J. E. DeNatale, IEEE Microw. Wirel. Compon. Lett. 11, 56 (2001)

[4] J. A. Walker, J. Micromech. Microeng. 10, R1 (2000)

[5] R. Wood, R. Mahadevan, V. Dhuler, B. Dudley, A. Cowen, E. Hill, and K. Markus, Mechatronics 8, 535 (1998)

[6] H. Fujita and H. Toshiyoshi, IEICE Trans. Electron. E83C, 1427 (2000)

[7] J. M. Zara and S. W. Smith, Sens. Actuators, A 102, 176 (2002)

[8]P. Vettiger, J. Brugger, M. Despont, U. Drechsler, U. Durig, W. Haberle, M. Lutwyche, H. Rothuizen, R. Stutz, R. Widmer, and G. Binnig, Micro- electron. Eng. 46, 11 (1999)

[9] P. Vettiger, M. Despont, U. Drechsler, U. Durig, W. Haberle, M. I. Lutwyche, H. E. Rothuizen, R. Stutz, R. Widmer, and G. K. Binnig, IBM J. Res. Dev. 44, 323 (2000)

[10] H. Kawakatsu, D. Saya, A. Kato, K. Fukushima, H. Toshiyoshi, and H. Fujita, Rev. Sci. Instrum. 73, 1188 (2002)

[11] M. I. Lutwyche, M. Despont, U. Drechsler, U. Durig, W. Haberle, H. Rothuizen, R. Stutz, R. Widmer, G. K. Binnig, and P. Vettiger, Appl. Phys. Lett. 77, 3299 (2000)

[12] L. R. Carley, J. A. Bain, G. K. Fedder, D. W. Greve, D. F. Guillou, M. S. C. Lu, T. Mukherjee, S. Santhanam, L. Abelmann, and S. Min, J. Appl. Phys. 87, 6680 (2000)

[13] H. Shin, S. Hong, J. Moon, and J. U. Jeon, Ultramicroscopy 91, 103 (2002)

[14] T. Thundat, P. I. Oden, and R. J. Warmack, Microscale Thermophys. Eng. 1, 185 (1997)

[15] T. Thundat, P. I. Oden, P. G. Datskos, G. Y. Chen, and R. J. Warmack, in *The 16th Warner Brandt Workshop on Charged Particle Penetration Phenomena*, Oak Ridge Tennessee, 1996 Oak Ridge National Laboratory, Oak Ridge, TN (1996)

[16] G. Meyer and N. M. Amer, Appl. Phys. Lett. 53, 1045 (1988)

[17] C. S. Smith, "Piezoresistance Effect in Germanium and Silicon," Phys. Rev., vol. 94, no. 1, pp. 42-49 (1954)

[18] V. Ferrari, D. Marioli, A. Taroni, E. Ranucci, and P. Ferruti, IEEE Trans. Ultrason. Ferroelectr. Freq. Control 43, 601 (1996)

[19] Q. M. Wang and L. E. Cross, Ferroelectrics 215, 187 (1998)

[20]S. Zurn, M. Hseih, G. Smith, D. Markus, M. Zang, G. Hughes, Y. Nam, M. Arik, and D. Polla, Smart Mater. Struct. 10, 252 (2001)

[21] D. L. DeVoe and A. P. Pisano, J. Microelectromech. Syst. 6, 266 (1997)

[22] R. Amantea, L. A. Goodman, F. Pantuso, D. J. Sauer, M. Varhese, T. S.

Villianni, and L. K. White, Infrared Technology and Applications XXIV 3436, 647 (1998)

[23] C. L. Britton, R. L. Jones, P. I. Oden, Z. Hu, R. J. Warmack, S. F. Smith, W. L. Bryan, and J. M. Rochelle, Ultramicroscopy 82, 17 (2000)

[24] K. Dahmen, S. Lehwald, and H. Ibach, Surf. Sci. 446, 161 (2000)

[25] G. Binnig, C. F. Quate, and C. Gerber, Phys. Rev. Lett. 56, 930 (1986)

[26] M.N. Gardos, in: B. Bushan Ed. , Tribology Issues and Opportunities in MEMS, Kluwer Scientific Publishers, The Netherlands, p. 341 (1998)

[27] M.N. Gardos, Surf. Coat. Technol. 113,183 (1999)

[28] A.R. Krauss, O. Auciello, D.M. Gruena, A. Jayatissaa, A. Sumant, J. Tucek, D.C. Mancini, N. Moldovan, A. Erdemir, D. Ersoy, M.N. Gardos, H.G. Busmann, E.M. Meyer, M.Q. Ding, Diamond Related Material 10,1952-1961 (2001)

[29] L. Tang, C. Tsai, W.W. Gerberich, L. Kruckeberg, D.R. Kania, Biocompatibility of chemical-vapor-deposited diamond *Biomaterials* 16, 483–8 (1995)

[30] H.J. Mathieu, Bioengineered material surfaces for medical applications *Surf. Interface Anal.* 32 3–9 (2001)

[31] F.Z. Cui F Z, D.J. Li, A review of investigations on biocompatibility of diamond-like carbon and carbon nitride films *Surf. Coat. Technol.* 131, 481–7 (2000)

[32] K. Takahashi, M. Tanga, O. Takai, H. Okamura, DNA bonding to diamond *Bio Indust.* 17 44–51 (2000)

[33] K. Takahashi, M. Tanga, O. Takai, H. Okamura, DNA preservation using diamond chips *Diamond Relat. Mater.* 12 572–6 (2003)

[34] Yang W *et al*, DNA-modified nanocrystalline diamond thin-films as stable, biologically active substrates *Nature Mater.* 1 253–7 (2002)

[35] J. Wang, M.A. Firestone, O. Auciello O and J.A. Carlisle, Functionalization of ultrananocrystalline diamond films by electrochemical reduction of aryldiazonium salts *Langmuir* 20 11450–6 (2004)

[36] G-J. Zhang, K.S. Song, Y. Nakamura, T. Ueno, T. Funatsu, I. Ohdomari, H. Kawarada, DNA micropatterning on polycrystalline diamond via one-step direct amination *Langmuir* 22 3728–34 (2006)

[37] M.Wiora, K.Bruhne, A. Floter, P. Gluche, T.M. Willey, S.O.Kucheyev, A.W. Van Buuren, A.V. Hamza, J. Biener, H.-J. Fecht, DIAMAT 05138 (2008)

[38] P. Olivero, S. Rubanov, P. Reichart, B.C. Gibson, S.T. Huntinggton, J.R. Rabeau. A.D. Greentree, J. Salzman, D. Moore, D.N. Jamieson, S. Prawer, Diamond Relat. Mater. 15 1914-21 (2006)

[39] N.P. Mahalik, MEMS, Tata McGraw-Hill, pg 146, ISBN 0070634459, 9780070634459 (2008)

[40] M.L. Sushko, J.H. Harding, A.L. Schluger, R.A.McKendry, M.Watari, Physics of Nanomechanical Biosensing on Cantilever Arrays, Advanced Materials, Vol. 20 Issue 20, 3848-3853 (2008)

[41] S.M. Huang, Z. Sun, Y.F. Lu, M.H. Hong, Surface and Coatings Technology 151 – 152, 263–267 (2002)

[42] D. Krishnamurti, Proceeding Mathematical Sciences, Vol. 40, No. 5, Nov (1954)

[43] J. Filik, 'Raman Spectroscopy: a simple, non-destructive way to characterise diamond and diamond-like materials', Spectroscopy Europe, Vol. 17 No. 5 (2005)

[44] A.R. Lang, M. Moore, A.P.W. Makepeace, W. Wierzchowski, C.M. Welbourn, "On the Dilatation of Synthetic Type Ib Diamond by Substitutional Nitrogen Impurity". *Philosophical Transactions of the Royal Society: Physical and Engineering Sciences (1990-1995)* 337: 497 (1991)

[45] K. Iakoubovskii, G.J. Adriaenssens, J. Phys.: Condens. Matter 13, 6015–6018 (2001)

Chapter 8

Nanodiamond-coated silicon Cantilever Array for Chemical Sensing

8.1 Introduction

Cantilevers are typically made of single-crystal silicon due to the mature and reliable fabrication technology available with this material. However, Si itself must be modified to offer suitable chemical properties for selective sensing applications. This work reports a simple method for modifying Si cantilevers with a coating of diamond, and shows how highly effective chemical sensing devices may be fabricated using this approach.

To recap, diamond possesses properties favourable for chemical and biological sensing since as a material it can display exceptional chemical inertness and natural biocompatibility [1-3], whilst be readily chemically functionalised for sensing purposes. For example, photochemical chlorination, amination and carboxylic functionalisation processes have been widely demonstrated [4-5]. These functionalized surfaces have also been modified with DNA, enzymes and proteins [6] for biological sensing. Diamond cantilever structures have been successfully fabricated by patterned growth of nanocrystalline diamond (NCD) thin films or reactive ion etching NCD layers to form the required shapes [7-9]. The free-standing beams were released by the use of an undercutting selective silicon wet etch process. However, NCDs' mechanical properties are reported to be dependent on the grain size, and are always inferior to single crystal diamond [9]. A single crystal diamond-based cantilever structure as previously been reported, having been fabricated by a focused ion beam (FIB)-assisted lift-off technique which employed MeV ion implantation, followed by FIB micro-patterning and selective chemical etching [10]. The undercut clearance below the cantilever was reported to be approximately 0.2μm. This makes it inaccessible to micro-capillary tube insertion for diamond surface fictionalization that is expected to be required for subsequent sensing applications. A simpler process has been demonstrated, using a technique solely based on the application of the FIB to mill and pattern a free-standing cantilever in a single crystal diamond plate, which provided a solution to the problem associated with limited clearance under the cantilever previously reported [11]. However, the processing

complexities and time associated with deploying these techniques limits the commercial prospects for such an approach. Here we propose a hybrid-solution, where inexpensive pre-fabricated Si cantilevers can be coated with nanodiamond particles offering the benefits of established Si technology with the properties of a diamond surface for sensing applications.

8.2 Device Fabrication

Nano-diamonds produced by a detonation process [12] (DNDs) from New Metals & Chemicals Corporation, Japan were used throughout. The DNDs had been prepared using techniques described by Williams and co-workers [13]. DNDs in the size range 5-15nm were suspended in de-ionised water and attached to Si cantilevers using sonication. Silicon structures (Micromotive Microteknik, Germany) in the form of an array of 8 cantilevers (length 450μm, width 90μm, thickness 2μm – Figure 8.1(a)) were immersed in the DND containing solution diluted with de-ionized water at a ratio of 0.5ml : 6.5ml respectively, and sonicated for 10 minutes. Sonication allows the DND particles in the solution to be agitatedly dispersed and attached to the silicon cantilevers surface by Van der Waals forces (Figure 8.1(b)-(d)). This is followed by a slow evaporation of the host solution in a drying cabinet at a temperature ~ 50 – 60^{o}C overnight. Direct extraction of the cantilever array chip from the DND solution was found to leave the cantilevers in severely bent conditions.

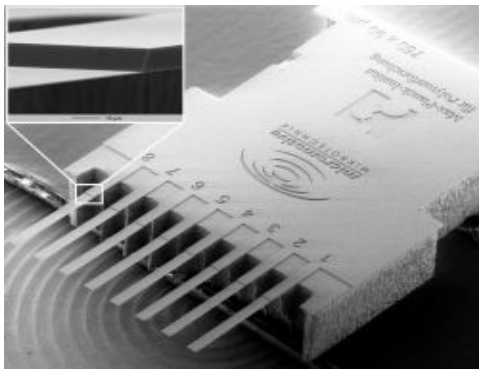

Figure 8.1: SEM image of the cantilever array chip used for this work (courtesy of Micromotive Microteknik, Germany)

For the sensing experiment, a separate chip was used and duly coated with DND particles by means of sonication. The bottom-side of the cantilevers was then passivated with a Cr/Au bi-layer at 3nm and 30nm respectively thus ensuring sensing events to occur exclusively on the topside. For reliable optical detection (using the Atomic Force Microscopy set-up) of the cantilever deflections, the surface optical reflectivity was improved by coating the tip of the cantilevers with a Cr/Au bi-layer also at 3nm : 30nm ratio at a horizontal dimension of ~100μm x 100μm at the cantilever tip-end. This should allow enhanced collection of the reflected light emitted from the laser diode focused onto the Cr/Au coated tip by the AFM position sensitive detector (PSD). Deposition of the metallic bi-layer was done in an Edwards A360 Bell Jar thermal evaporator unit in a vacuum pressure of ~10^{-6} mbar. The tip-end coating was made possible by means of a simple homemade shadow mask.

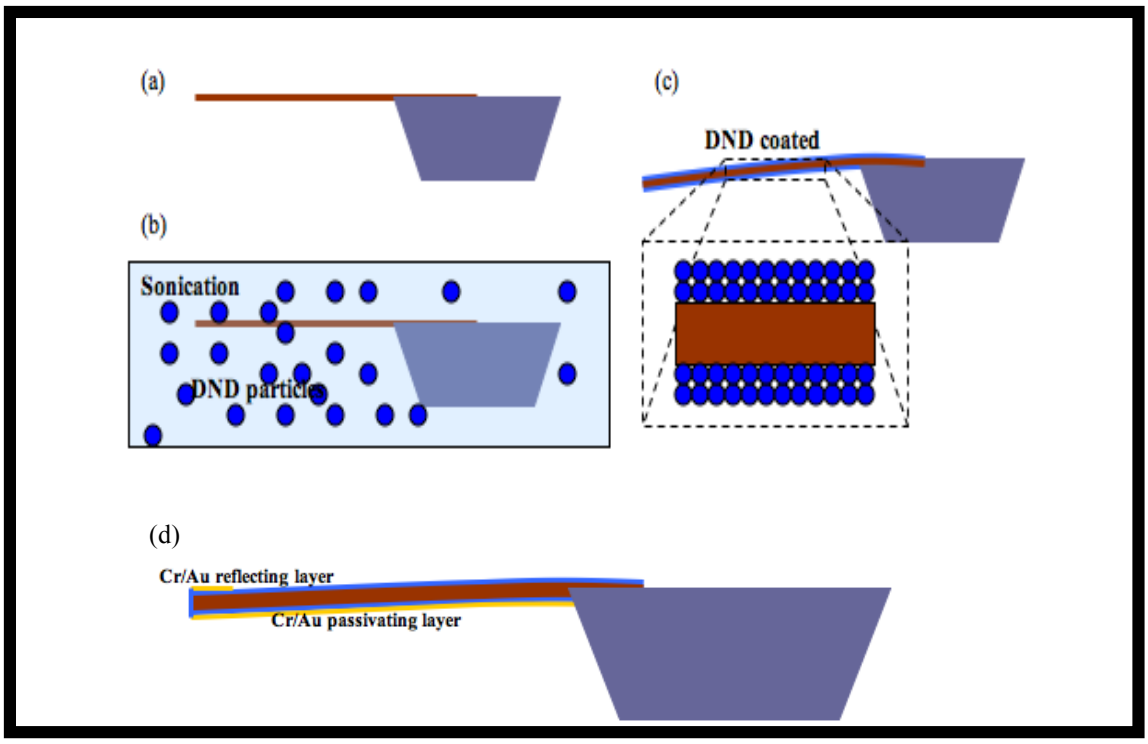

Figure 8.1: DND-Si cantilever fabrication. Side profiles of (a) as-received bare Si cantilever (b) DND attachment onto Si silicon cantilever by sonication (c) DND-Si cantilever (d) Sensor concept: Additional Cr/Au layers for passivation and reflected optical signal enhancement

8.3 Experimental Methods

The static and dynamic modes of the cantilever arrays were first characterized using an atomic force microscope (AFM, Veeco Dimension V). The cantilever of the AFM having a much higher spring constant (k), was used as a micro-indenter to gradually press the cantilever down (Figure 8.2(b)) and consequently generating the force versus deflection curve for each test cantilever The resonance frequency is then determined by having each cantilever calibrated by the AFM.

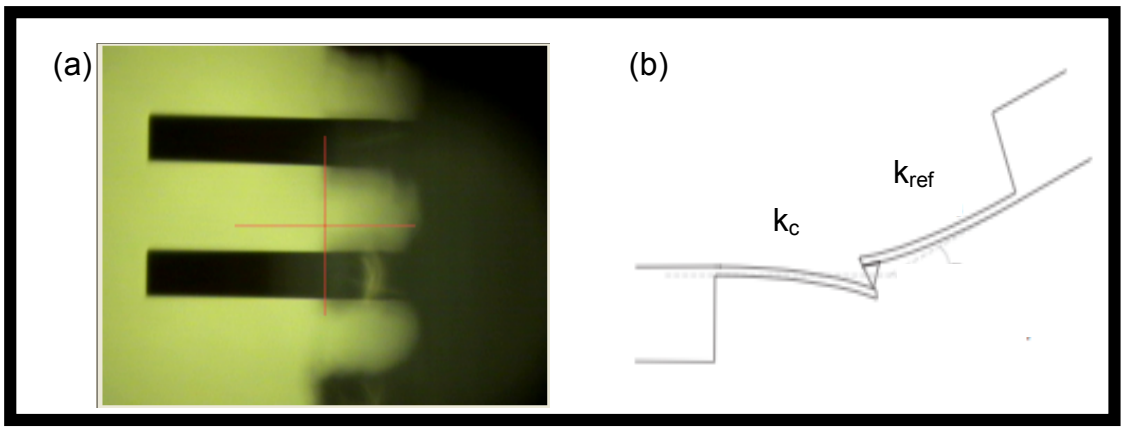

Figure 8.2: (a) A top view of the cantilever array taken by the AFM visual system (b) Static deflection of a cantilever of unknown spring constant against a reference cantilever.

Having the cantilever chip displacing the AFM cantilever and subsequently clamped on the mount, the cantilevers were simultaneously driven by the AFM piezoelectric actuator but sequentially scanned to ascertain the individual resonance frequency. With the light from the laser diode directed onto the tip of the cantilever, and the reflected beam is collected by the position sensitive detector (PSD) on the AFM, the respective force-induced static deflections and piezoelectrically driven dynamic oscillations were measured using the AFM built-in optical sensing capability. In addition to cantilever testing, the AFM was used to image the Si structures before and after DND coating.

As a proof of the sensor concept, the DND coated Si cantilevers were

exposed to 2,4 Dinitrotoluene (Sigma-Aldrich) vapour at 5 concentration levels in a temperature-controlled air-tight glass cell. Thermal energy was applied to the air-tight glass cell to control the vapour pressure of the 2,4 Dinitrotoluene using a hot-plate monitored by an external thermocouple. The vapour pressure curve as a function of temperature (~270–340 K) for 2,4 Dinitrotoluene can be readily expressed using the Clausius–Clapeyron relationship:

$$\log_{10} P\,(\text{Torr}) = a - b/T\,(\text{K}) \qquad (1)$$

where *a* and *b* coefficients equivalent to 13.16 ± 0.40 and 4948 ± 20 respectively [14].

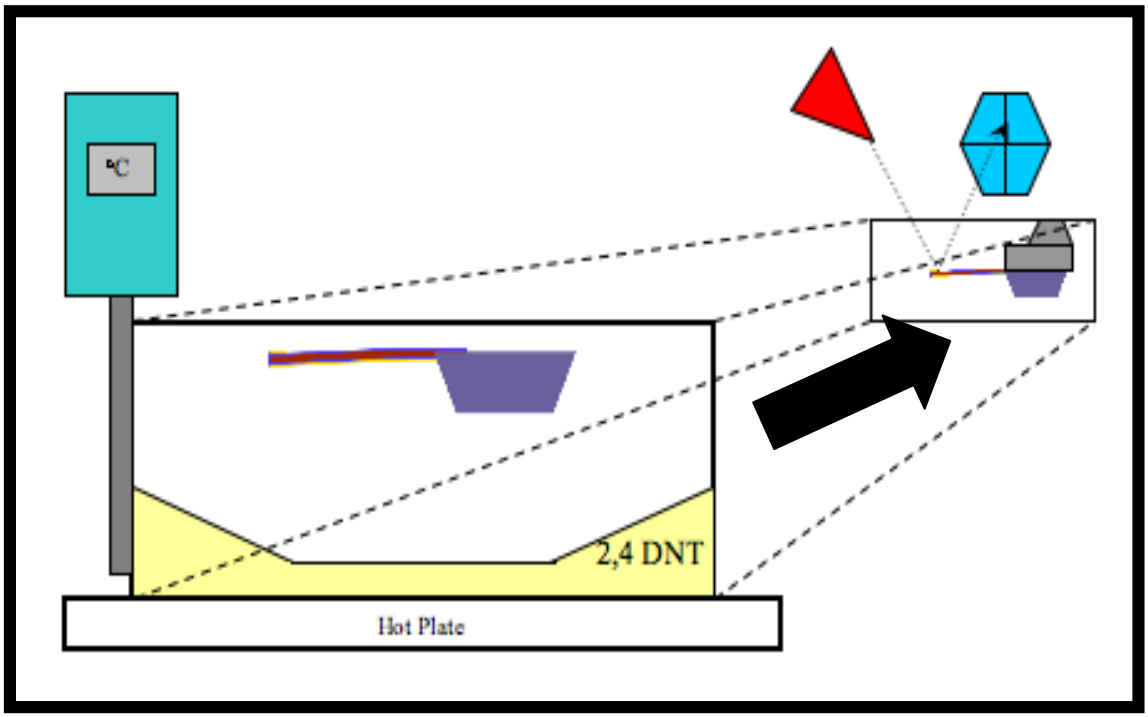

Figure 8.2: Schematic representation of the cantilever measurement system using the AFM built-in optical position sensitive detector (PSD)

Prior to 2,4 Dinitrotoluene vapour exposure, the cantilevers were first dynamically characterized for the determination of the original resonant frequencies. This is followed by placement of the cantilever chip mounted on the AFM cantilever holder in the glass cell partially filled with 2,4

Dinitrotoluene. The temperature of the glass cell was set at 5, 20, 35, 40 and 50^{o}C and using equation (1), these temperatures should generate a vapour concentration of 0.02, 0.17, 1.14, 2.08 and 6.56ppm respectively. For 5^{o}C exposure, the glass cell with both 2,4-DNT and cantilever inside was kept refrigerated with the temperature set at 5^{o}C. At each temperature stage the exposure period was limited to ~10 minutes and changes in the resonance frequency immediately captured by the AFM set-up were taken as a measure of chemisorption on the cantilevers.

Evidencing the existence surface groups and the chemisorption of 2,4 Dinitrololuene on DND coatings, the Fourier Transform Infra-Red (FTIR) spectroscopy technique was employed using a PC-run Perkins-Elmer FTIR scanner. Potassium Bromide (KBr) known for displaying infra-red transparency assumed the role of solid host-material. Through the use of a micropipette, the DND particles were deposited on KBr discs formed by a highly leveraged mechanical-presser. Since KBr readily dissolves in water-based solution, the deposition of DND particles was done with the KBr discs placed on a hot-plate at temperatures ~ 70 – 100^{o}C to allow quick evaporation of water to prevent the KBr discs from dissolving. FTIR measurements were made at 13 scans each on DND-KBr discs, before and after exposure to 2,4-dinotrotoluene vapour with the former at room temperature and the latter at room temperature and 40^{o}C, each over a period of ~10 minutes. The exposure to 2,4-dinitrololuene was done in the same air-tight glass cell, replicating the ambient conditions for the sensing experimental work. FTIR absorption peaks to be observed related to compounds representing 2,4-dinitrotoluene is deemed as justification of the chosen method to control the vapour pressure of 2,4-dinitrotoluene for eventual sensing by the DND-coated cantilevers. Solid-state devices for the detection of threat signatures are an active area for research [15]; in the current case 2,4-DNT was chosen as a safe analogue for the detection of the explosive tri-nitrotoluene (TNT).

8.4 Results

AFM images for uncoated and DND coated Si cantilever surfaces are shown in figure 7.3(a) and (b). Little structure is apparent on the uncoated cantilever, as would be expected. In Figure 8.3 (b) (i-v), it can be observed that uniform coating of the DND particles on the Si cantilever surfaces was achieved. DND particles of sizes 5-15nm can be discerned, but these have aggregated to form clusters of particles in the size range 20-100nm. The particles are strongly adherent, not being removed by routine physical abrasion or cleaning.

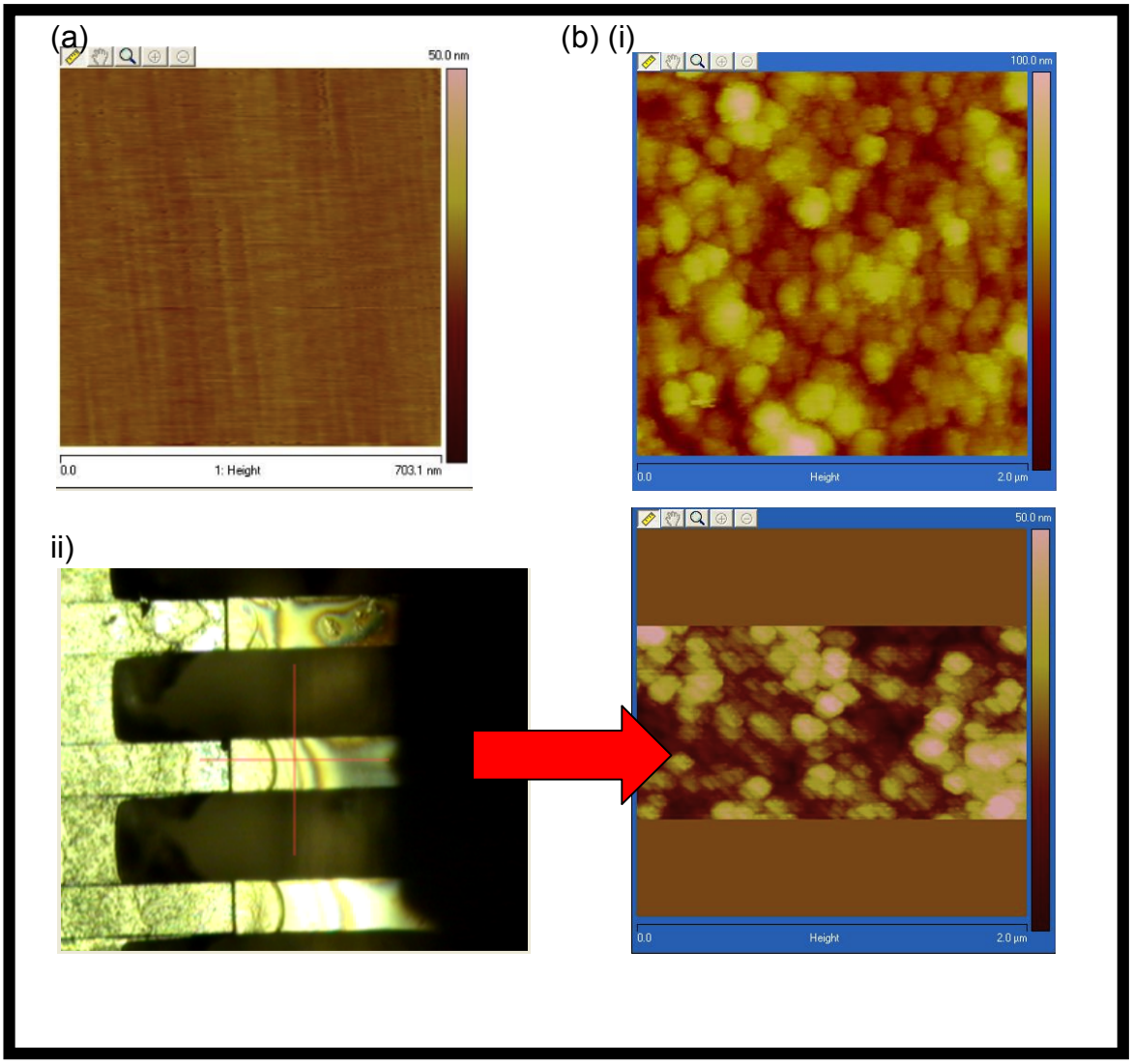

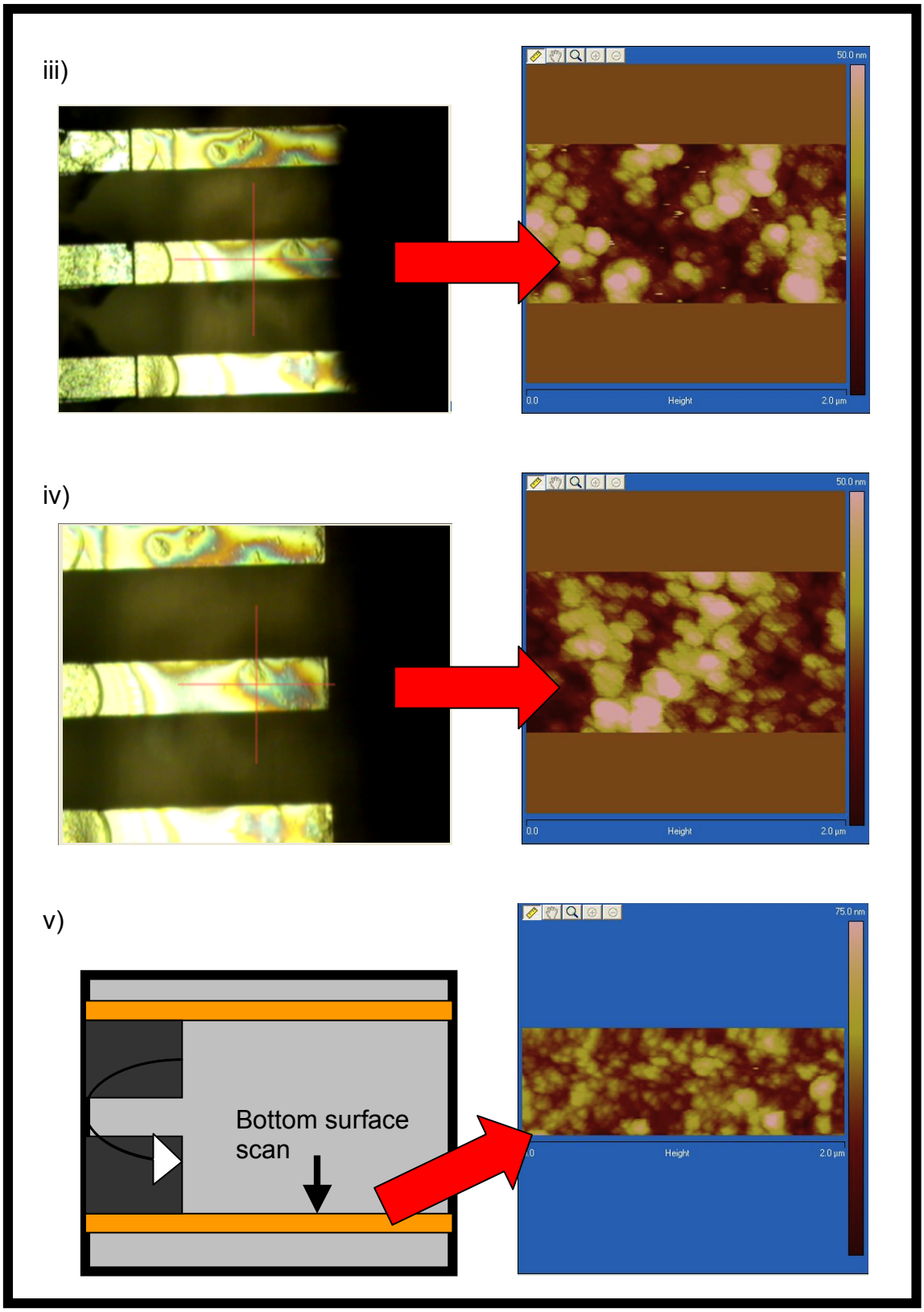

Figure 8.3: AFM images from the Si cantilevers (a) before and (b) at the respective positions as shown by the accompanying optical images after coating with detonation nanodiamonds (DNDs). The length scale is the same for both x and y axis. The height scale is indicated at the top of each colour scale bar.

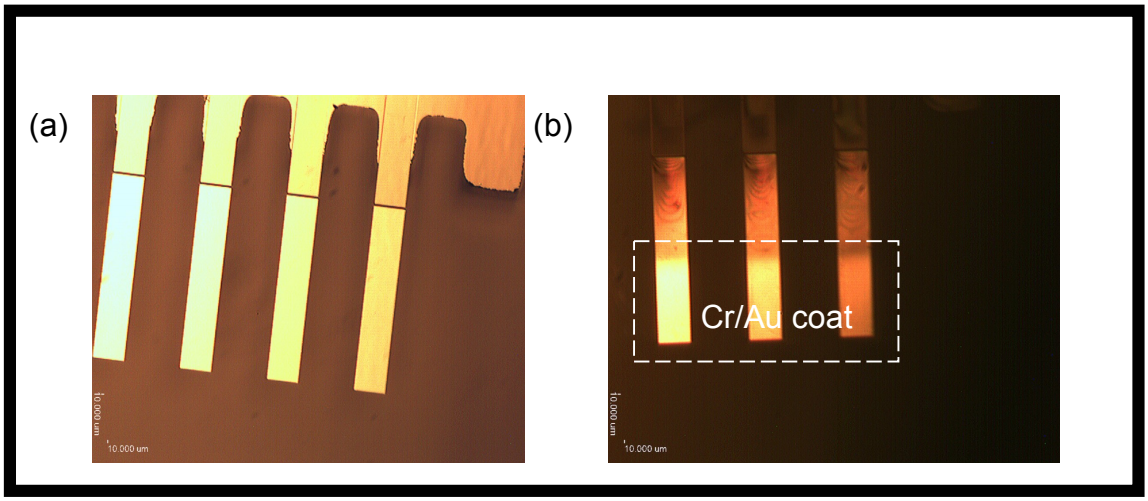

Figure 8.4 Optical top-view of (a) bare silicon cantilever array (b) DND-coated cantilever array with thin Cr/Au coat at the tip area for enhanced optical reflectivity.

Static-mode characterisation of the cantilevers yielded force versus deflection graphs shown in Figure 8.4. Data is presented for two cantilevers (labelled as C1 and C2) with and without DND coatings. In all cases the deflection increases linearly with force, as would be expected. The two Si cantilevers differ slightly in absolute deflection per unit force, but show similar slopes. Once DND-coated, both cantilevers require more force to obtain the deflection levels recorded before coating; the slope of the lines equates to the spring constant (k), mathematically defined as force/deflection (N/m), which has increased. The spring constants determined from this data are given in Table 8.1, where it can be seen that the increase in the value of k upon DND coating is around a factor of 7.

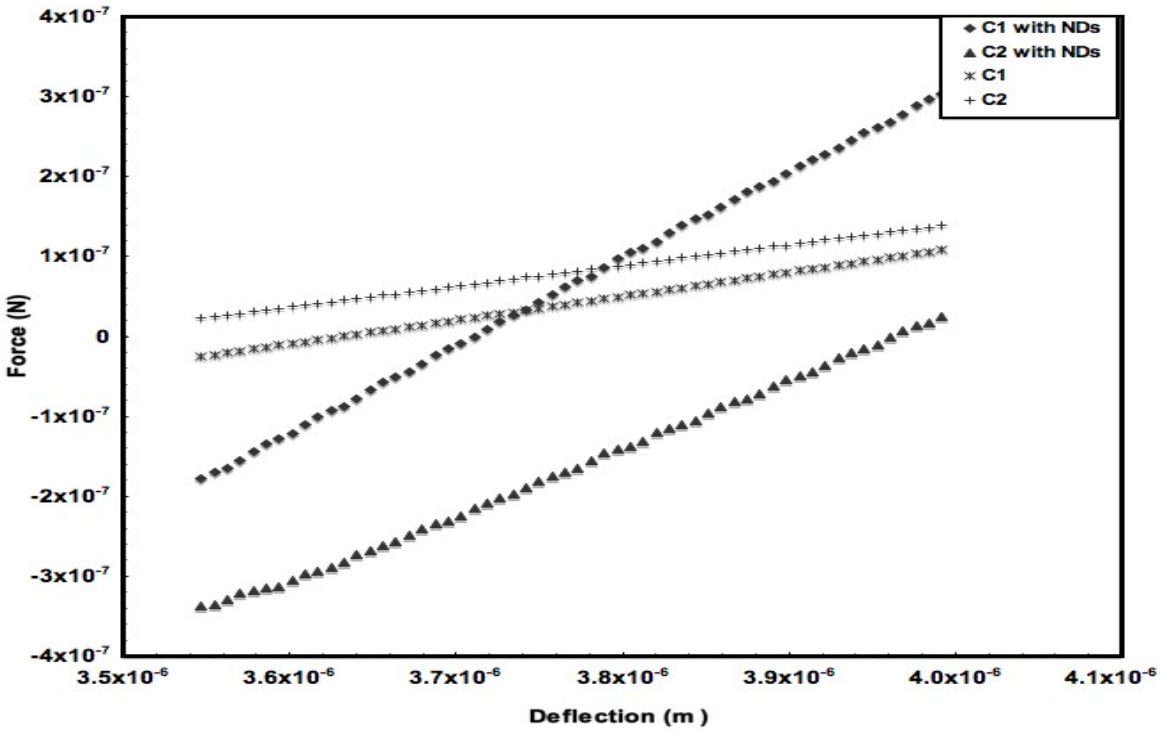

Figure 8.4: Force (x 10^{-7} N) plotted against deflection (μm) for two Si cantilevers, C1 and C2, with and without a detonation nanodiamond (DND) coating.

	Spring constant, k_s (N/m)	
Cantilever	Bare Silicon	With nano-diamonds
1	0.145	1.034
2	0.129	0.835

Table 8.1: Static Mode characterisation – spring constant values determined from figure 2.

The parameters extracted for each cantilever during dynamic mode analysis are shown in table 8.2. The resonant frequency prior to coating is of the order of 25kHz, which decreases by over 2kHz in the presence of the DNDs.

	Resonance Frequency (kHz)				Nano-diamonds	
Cantilever	Bare, f_1	With NDs, f_2	Δf_a	k_d (N/m)	Loading Mass (g)	Particles (cm^{-2})
1	25.44	23.08	-2.36	0.512	$1.79x10^{-9}$	$1.98x10^{11}$
2	25.35	23.06	-2.29	0.508	$1.74x10^{-9}$	$1.92x10^{11}$

Table 8.2**:** Dynamic Mode characterisation for the Si cantilevers with and without DND coatings, giving resonant frequency values and shifts, mass loading and particle density.

Table 8.3 shows the dynamic mode analysis for the DND and Cr/Au coated Si cantilevers following exposure to 2,4 Dinitrotoluene (DNT) vapour. The resonant frequency decreases by around 5 - 148Hz for an exposure concentration of 0.02ppm or 20ppb. The experimental resonant frequency responses to the exposure of 2,4-DNT at 0.02, 0.17, 1.14, 2.08 and 6.56ppm are illustrated in Figure 7.5 (a) – (e). Cantilever 1,2,7 and 8 together have their resonant frequencies dampened only at 20ppb followed by increases up to 6.56ppm of 2,4-DNT. In short, the resonance frequency responses to increasing 2,4-DNT vapour follow a general V-shaped trend, bottoming at 0.02 for cantilever 1,2,7 and 8 before increasing with the vapour concentration up to 6.56ppm.

(a)

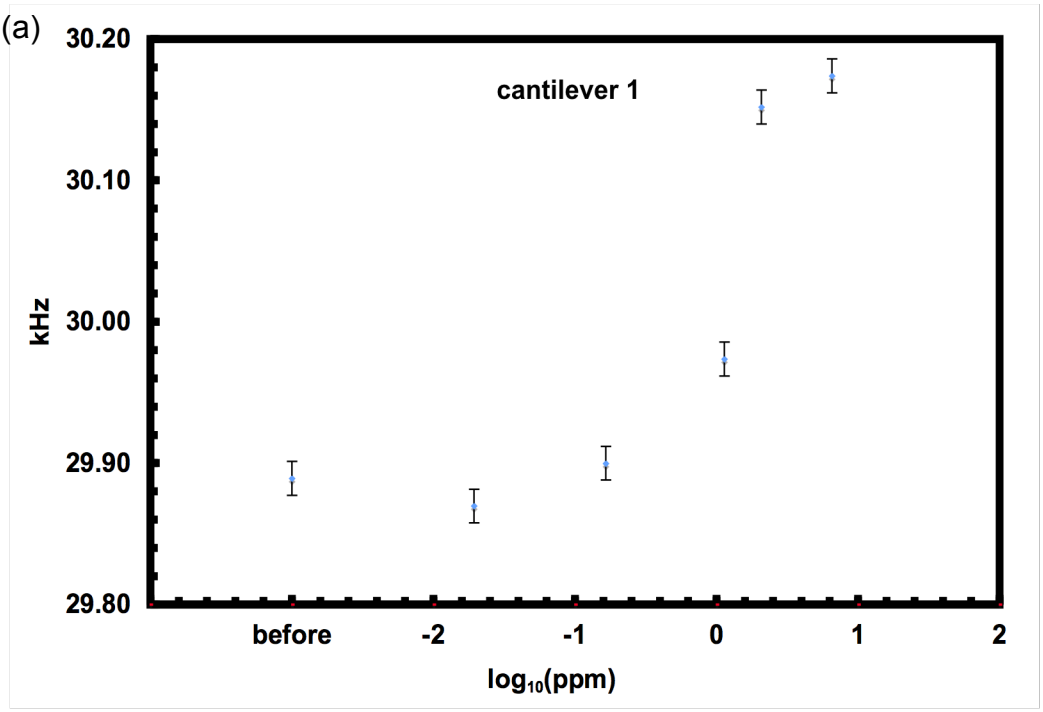
cantilever 1
30.20
30.10
30.00
29.90
29.80
kHz
before
-2
-1
0
1
2
log10(ppm)

(b)

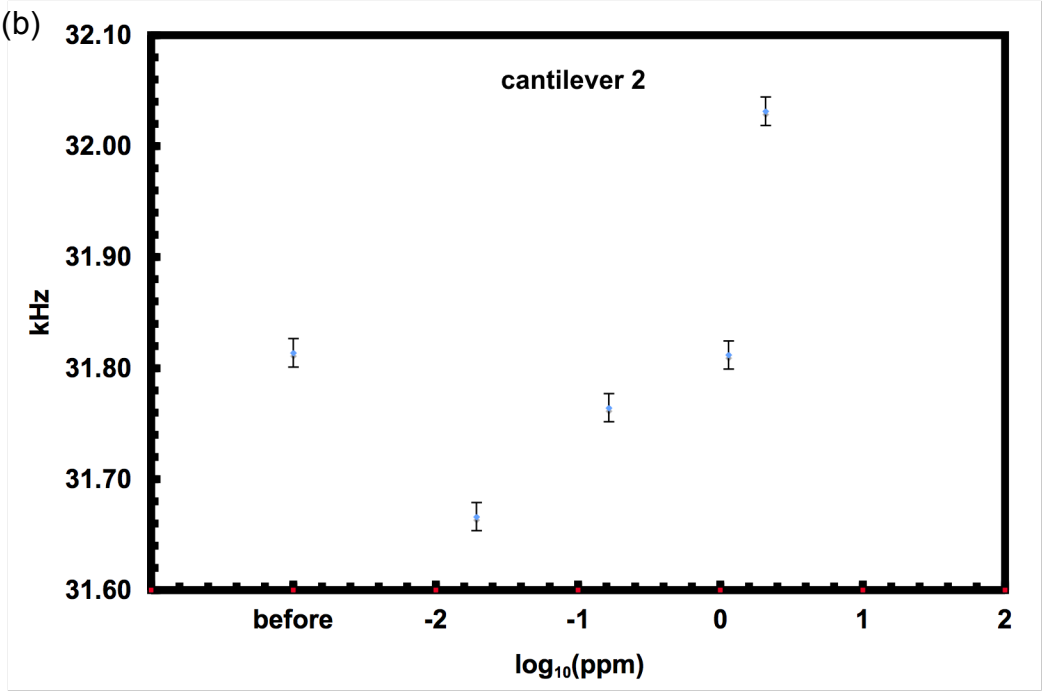
cantilever 2
32.10
32.00
31.90
31.80
31.70
31.60
kHz
before
-2
-1
0
1
2
log10(ppm)

(c)

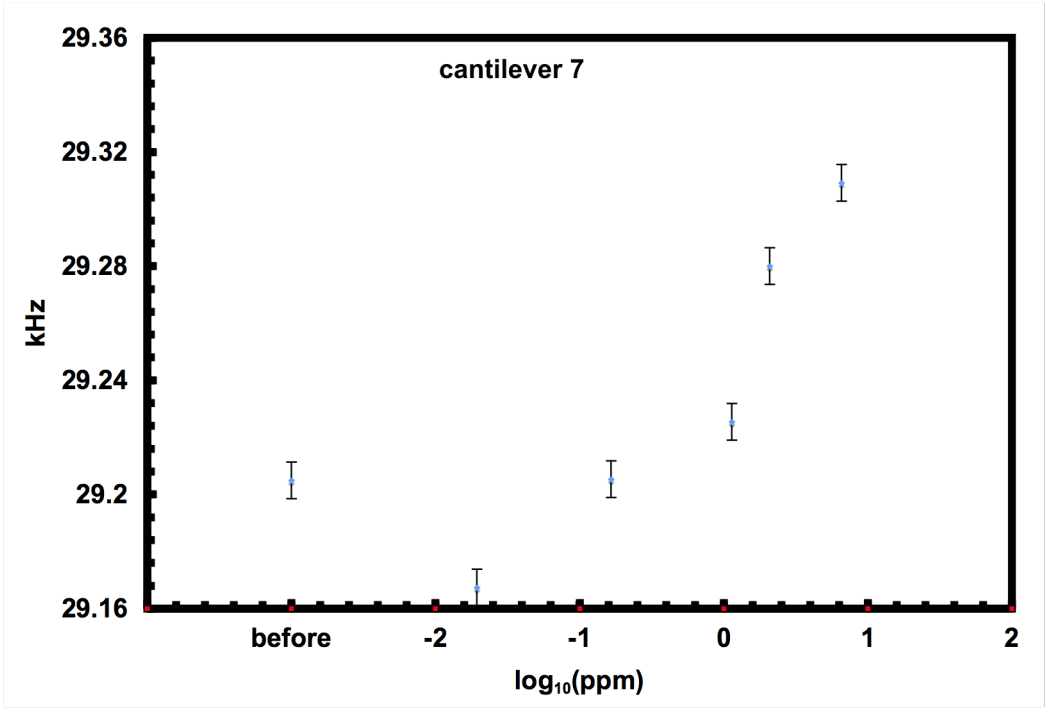

(d)

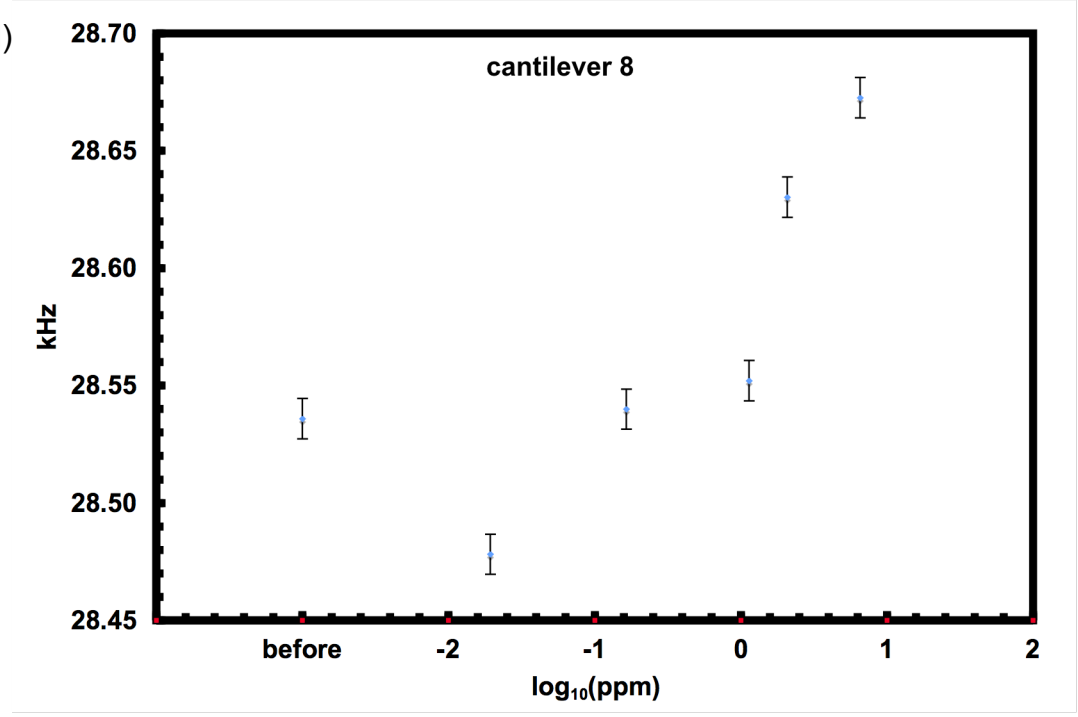

Figure 8.5: Resonant frequency shifts of DND-coated cantilever (a) c1, (b) c2, (c) c5 (d) c7, (e) c8 before exposure to 2,4 Dinitrotoluene (DNT) and following exposure to 0.02, 0.17, 1.14, 2.08 and 6.56ppm 2,4-DNT vapour exposure.

In Figure 8.6 (a-c), the FTIR absorbance spectra for the as-deposited DND are shown. Absorbance peaks associated to the carboxyl (COOH) group on the DND surface are seen at 1718.69 and 1632.30 cm^{-1} locations assigned to the C=O and O-H bonds respectively. After exposure to 2,4-DNT vapour at 0.17 and 2.08ppm concentration levels, FTIR absorbance peaks representing chemisorbed 2,4-DNT in the form of N-O are apparent at 1545.13 and 1545.34 cm^{-1} as evidently shown in Figure 8.6 (b) and (c). Closer inspection on the FTIR spectra reveals subtle red-shifting i.e. decrease in bond vibrating frequency for the C=O and O-H bonds by 0.82 cm^{-1} and 6.06 cm^{-1} respectively (Table 8.4). The magnitude of the absorbance peaks related to N=O commensurate with the concentration levels of 2,4-DNT vapour with the higher concentration at 2.08ppm generating higher absorbance intensity at 2.88A compared to 2.68A for 0.17ppm. A prominent peak at 2925.15 cm^{-1} represents C-H bend. However, the movement of this C-H peak from 2925.15 $\rightarrow$ 2925.41 $\rightarrow$ 2923.76 cm^{-1} is not as correlative as those of C=O and O-H bonds.

Groups	FTIR peaks (cm^{-1})		
	Before 2,4-DNT	2,4-DNT (@0.17ppm)	2,4-DNT (@2.08ppm)
C-H	2925.15	2925.41	2923.76
C=O	1718.69	1718.18	1717.82
O-H	1632.30	1631.24	1626.24
N=O	-	1545.13	1545.34
Intensity of N=O peak		2.68A	2.88A

Table 8.4**:** Absorbance peaks associated to functional group, COOH and chemisorbed 2,4-DNT (A – arbitrary unit for absorbance)

(a)

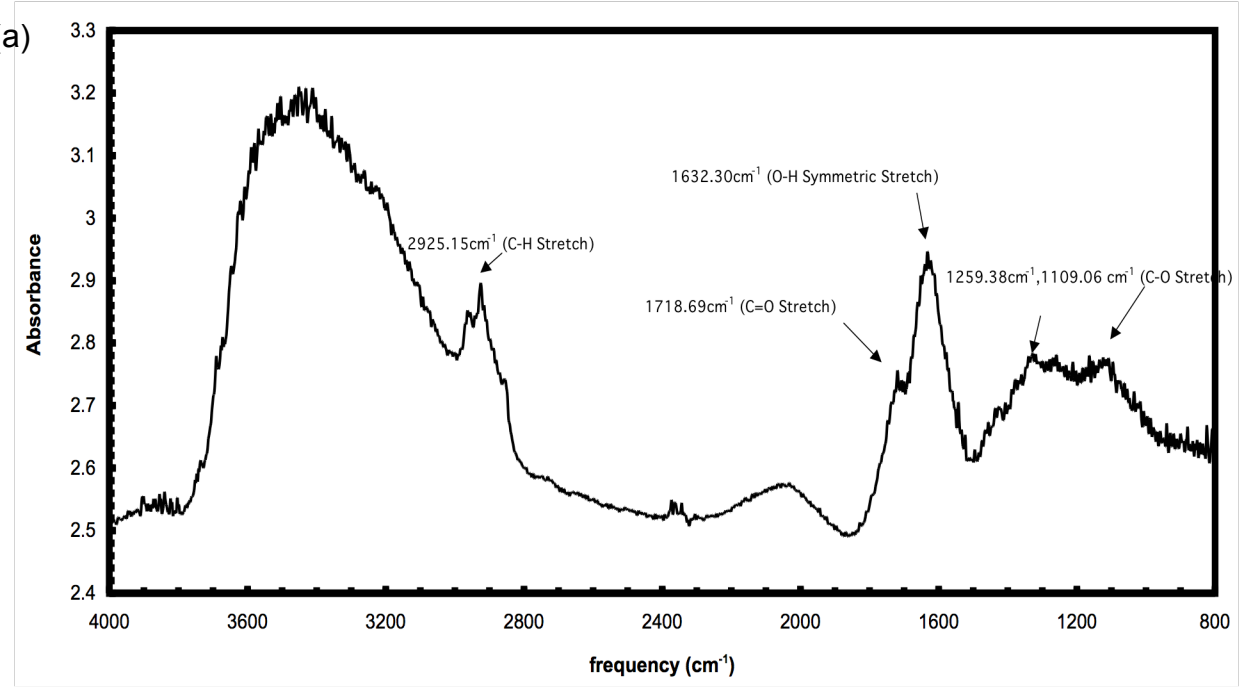
Absorbance
frequency (cm-1)
2925.15cm-1 (C-H Stretch)
1632.30cm-1 (O-H Symmetric Stretch)
1718.69cm-1 (C=O Stretch)
1259.38cm-1,1109.06 cm-1 (C-O Stretch)

(b)

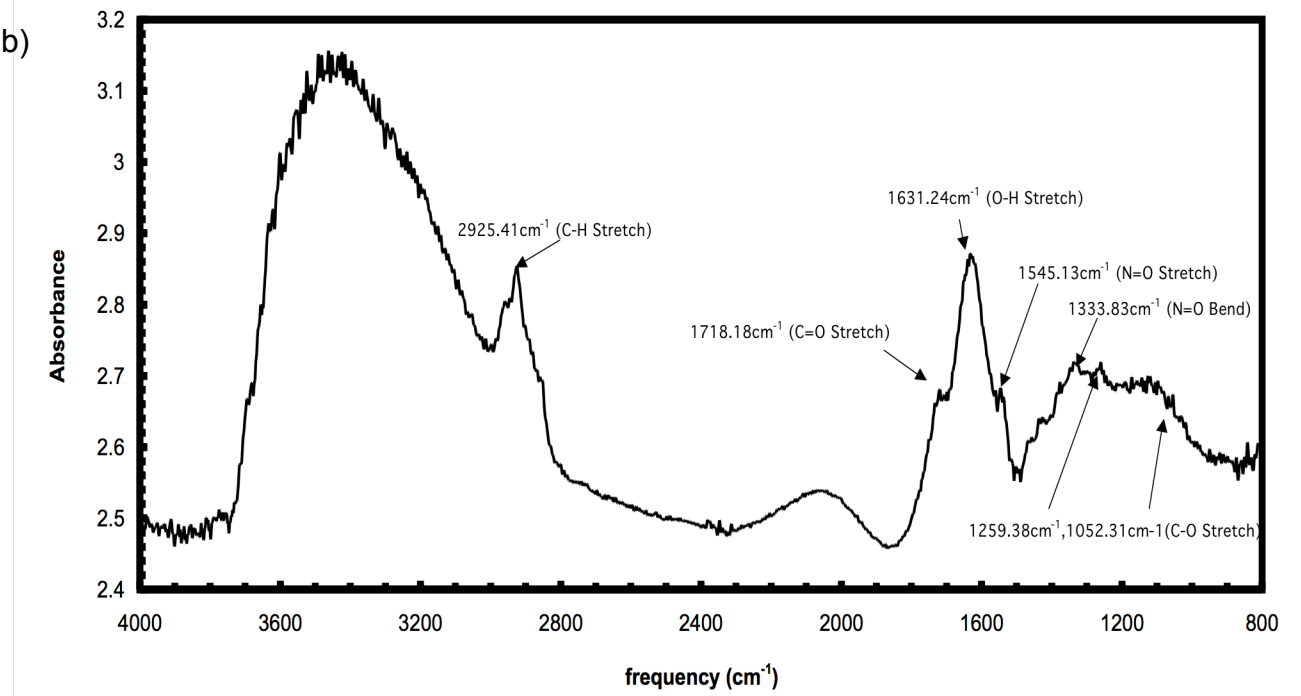
Absorbance
frequency (cm-1)
2925.41cm-1 (C-H Stretch)
1631.24cm-1 (O-H Stretch)
1545.13cm-1 (N=O Stretch)
1333.83cm-1 (N=O Bend)
1718.18cm-1 (C=O Stretch)
1259.38cm-1,1052.31cm-1(C-O Stretch)

(c)

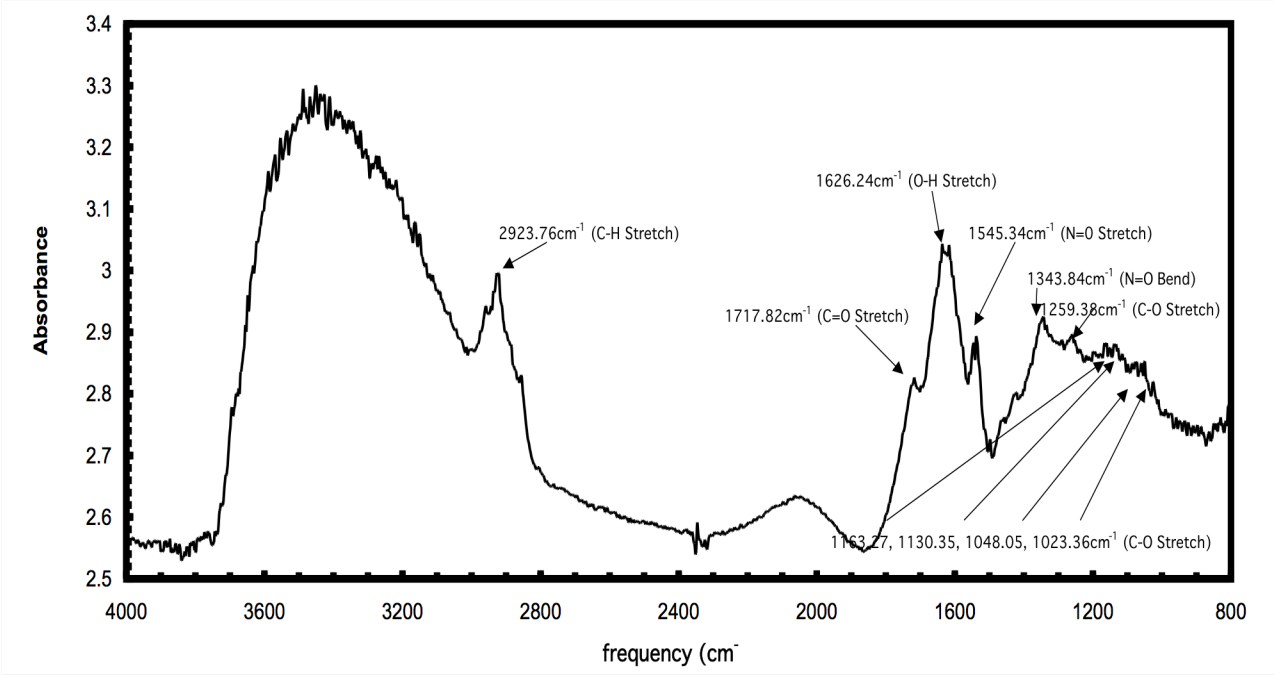

Figure 8.6: FTIR absorbance spectra of DND surface (a) before and after exposure to 2,4 Dinitrotoluene at (b) 20^{o}C and (c) 40^{o}C showing peaks representing adsorption of 2,4 Dinitrotoluene.

8.5 Discussion

The extracted spring constant (k) values from the static mode characterisation of the cantilevers indicate the mechanically pre-bent steady state of the cantilevers as a result of the DNDs mass loading effect. The k values increase by a factor of 7.1 and 6.5 for cantilever 1 and 2 respectively. Physically, the lower halves of the beam structures in such a condition are in a contracted state and the resulting tensile stress generates a stiffening effect, thus lower deflection response per unit applied force and consequently higher k values as shown in Figure 8.4. This indicates a departure from the constant k value or continuous linearity suggested by Stoney's formula [16], which does not take into account the stiffening effect by the tensile stress on the bottom surface of a pre-stressed cantilever [17]. Stoney's formula is still applicable if the cantilever's response to the applied stress is divided into 2 separate regimes i.e. pre-relaxed and pre-stressed. In short, the nano-diamond coated

cantilever must be viewed as a mechanical structure with its own 'intrinsic' set of static characteristics. Qualitatively, the pre-stressed quiescent state of the coated cantilever can be reconciled with the dynamic mode response of the cantilevers whereby the mass loading effect-induced damped oscillation is observed.

In the dynamic mode, the periodic upwards and downwards oscillating deflection passes through both the pre-relaxed and pre-stressed points. With the total additional coating layer at ~140nm and cantilever thickness 2μm, the diamond-silicon thickness ratio $\delta \leq 0.1$ will ensure the dominance of silicon's intrinsic micro-mechanical characteristics [18]. Hence the dynamic spring constant (k) remains a constant value. Driven by the actuating piezoelectric element in the AFM holder, the bare silicon cantilevers are individually tuned to determine the undamped resonance frequencies. The decrease in the resonance frequencies after the DND coating is expected as it arises from the increase in mechanical loading on the cantilever structure, which leaves the cantilever in a pre-damped state. With the spring constant (k) considered to be unchanged, the equation (1) can be applied to determine the extra mass (M) burden on the cantilever beam whilst factoring in the effective mass (m_{eff}) of the cantilever stemming from its dimensions and density of the silicon component. The effective mass of a rectangular cross section singly supported beam is ~0.24 of its real mass [19],

$$k = w_0^2 \times (M_{eff} + m_{eff}) \qquad (1)$$

where $w_0 = 2\pi f_0$ and f_0 is the cantilever resonance frequency. Since the DNDs evidently have a full coverage on the silicon beams, the calculated load is really the effective mass (M_{eff}) of the DND layer and needs to be divided by 0.24 to obtain the actual mass (M). Taking a single nano-diamond particle having an average diameter of ~5nm and having the density of diamond, yields the particle coverage per unit area to be around $2 \times 10^{11} cm^{-2}$ (Table 8.2). Moreover superficially from the formula, the change in the resonance frequency can be deduced to be inversely proportional to the added loading mass. Hence, the result of the experiment is in good agreement with

theoretical expectations. It can be noted that this density is similar to reported values for DND attachment on Si for seeding purposes during the preparation of diamond thin films [13]. Uniformly distributed load (UDL) theory can be applied to calculate the steady-state bending of the pre-stressed DND coated silicon cantilever [20]. Given,

$$I = \frac{tw^3}{12} \tag{2}$$

$$\delta_m = \frac{W.L^3}{8.E.I} \tag{3}$$

and a uniformly distributed load, W = 1.7 x 10^{-10} N, generates a possible pre-stressed maximum deflection, of δ_m = 0.213pm, where I is the 2nd moment of inertia, L, t and w cantilever length, thickness and width respectively and E being the Young's modulus.

The sensing capabilities of the as-fabricated DND and Cr/Au coated Si cantilever were evaluated with consecutive exposures to different concentration levels of 2,4-DNT, at 0.02, 0.17, 1.14, 2.08 and 6.56ppm. The 2nd cantilever chip is placed in an air-tight temperature-controlled vapour cell and dynamically characterised using the AFM set-up upon the expected adsorption event of the 2,4-DNT vapour on the ND-coated Si beam.

Chemisorption on conjugatively receptive surfaces may create tensile or compressive stress [21]. As a result of extensive purification treatment, the DND particles used here are left partially carboxylated and hydroxylated [22,23]. It has been demonstrated that the basic lone pairs of the nitro-groups on 2,4-DNT bind to strongly acidic polymers [24]. Hence, it can be considered that the hydrogen-bond acidic sites of the carboxylated termination part of the DNDs interact with the weakly basic lone pairs found on the oxygen atoms of the nitro-groups of the 2,4-DNT in the present case. Carboxylic groups being Brønsted-Lowry acids are proton donors, and the likely scenario would be proton transfer from COOH termination on the DNDs to the aromatic nitro-

groups of the 2,4-DNT. The adsorbed species will have applied mechanical loading onto the cantilever structure, also producing resonance at a lower frequency. This expectation is confirmed by negative shifts of the resonant frequency at the first concentration level for cantilever 1,2,7 and 8. The peculiar portion of the result is apparent in Figure 8.5 whereby at the final 4 concentration levels respectively, the DND coated cantilevers resonate at correspondingly higher frequencies. This phenomenon is suggested to be a result of the emerging dominance of tensile stress generated on the chemisorbed DND surface. 2,4-DNT vapour may have caused a number of neighbouring -COOH terminations to be bonded to a single 2,4-DNT molecule thus locally compressing the DND surface. The distance between two oxygen atoms, which are respectively from two adjacent $–NO_2$ groups has been calculated to be ~0.52nm [25]. Because the nanodiamond particles are terminated with carboxyl, hydroxyl, forms of ketone and ester groups [22], and hydrogen as evidenced by the FTIR scans (Figure 8.6(a)) it is very likely that the distance between nearest two -COOH terminals being larger than 0.52nm. Tensile stress is therefore generated as suggested in Figure 8.8(b). The proposed resonance frequency response model is schematically illustrated in Figure 8.9.

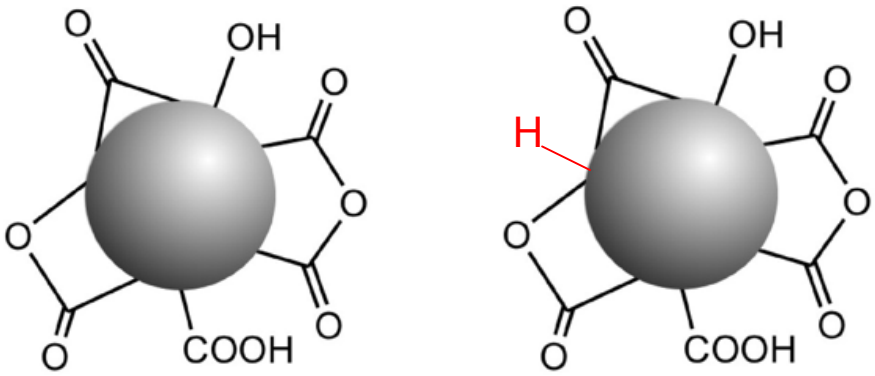

Figure 8.7: (a) Surface termination by Kruger et al [22] (b) A modified model with an additional H-termination as indicated by FTIR scans here and presented by Osawa et al [26]

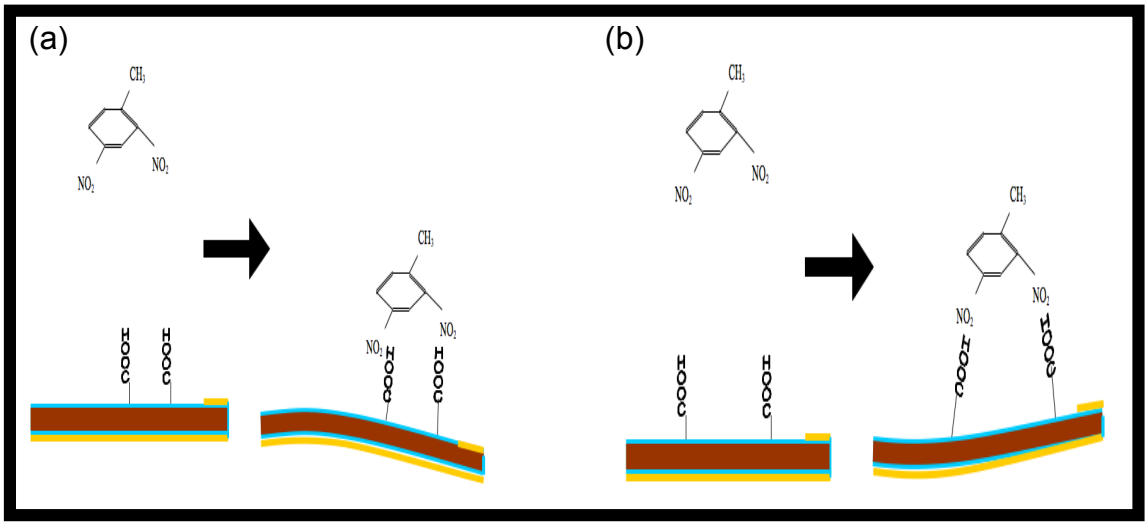

Figure 8.8: Effects of COOH density on dominance of (a) mechanical loading and (b) tensile stress generation

In a previous theoretical modelling study made that both mass mechanical loading and change in the spring constant (k) through generated local tensile or compressive stress upon chemisorption on cantilever structures can occur simultaneously and competing vectorially. It is shown that below a certain critical adsorption density, the resonance frequency will be lowered. And when the adsorption density is above that critical point, the resonance frequency will increase [27]. Furthermore, Thundat *et al* and co-workers and Chen *et al* observed that physical adsorption could cause the resonance frequency to either increase or decrease through interplay between small changes in spring constant (k) and effective beam mass through adsorption [28-30]. As a result the following equation was formulated,

$$\nu_2 = \nu_1\left[1+\frac{1}{2}\left(\frac{\delta K}{K}-\frac{\delta m^*}{m^*}\right)\right] \qquad (4)$$

where v_1 and v_2 are resonance frequency before and after adsorption respectively, K is spring constant and m*, the effective cantilever mass [28]. Based on the observed trends, it is probable at low vapour concentrations that the chemisorption events are scarcely spread and not interconnected

because the DND surface are only partially carboxylated, thus giving rise to the dominance of mechanical loading of the adsorbed molecule, in this case the 2,4-DNT. When the vapour concentration increases beyond a critical point of which the localized tensile stress points bridge up (Figure 8.9), the resulting tensile force on the upper surface and higher spring constant ($k+\delta k$) incrementally cancels out the mass mechanical loading ($m+\delta m$) as per Equation (4). Eventually, a homogenous tensile stress is generated rendering the DND surface to be in a contracted state and make the whole cantilever structure stiffer thus explaining the higher resonant frequencies (Figure 8.9). Generation of tensile stress was also observed on a siloxane-based TNT-sensitive bi-layer self-assembled directly on the SiO_2 surface of a surface-stress-style micro-cantilever, which relies on the interaction between -COOH group and $-NO_2$ of TNT for sensing mechanism [25].

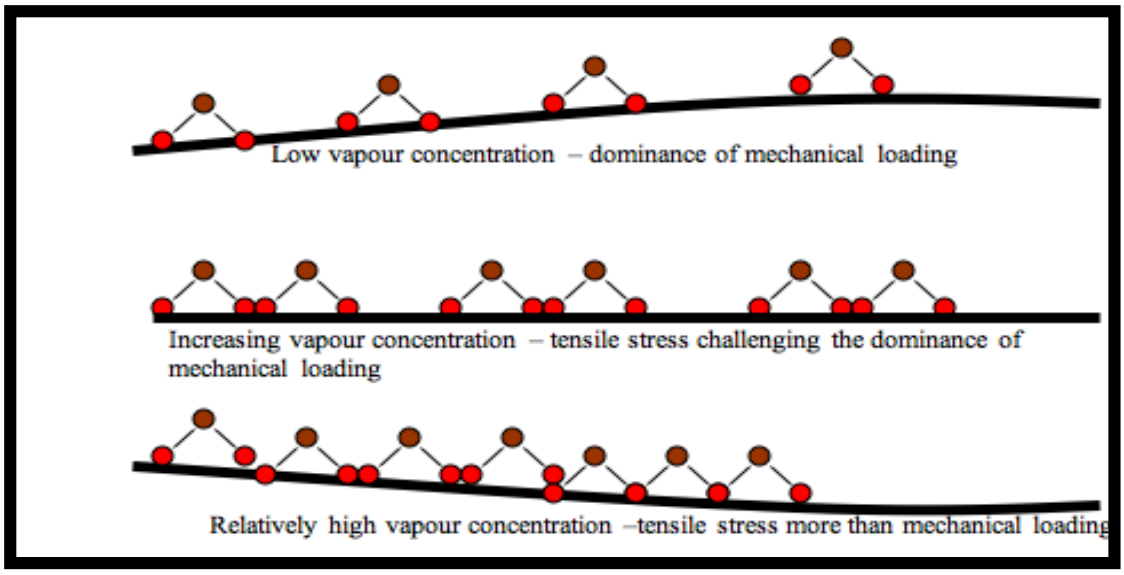

Figure 8.9: Proposed model for the frequency responses to 2,4-DNT concentration in terms of mechanical loading and tensile stress interplay

In the mechanical-loading dominant regime, the drop in resonance frequency variation observed between cantilever 1,2,7 and 8 over 20ppb is likely to stem from dissimilar distribution or density of the COOH group on the DND surface, with cantilevers having the higher density exhibiting the bigger drop (Figure 8.8(a)). Initially, the nitro groups of the 2,4-DNT do not have to 'pull in' pairs of

far-apart COOH site, minimising the generation of tensile stress. Subsequently, as the vapour concentration increases the additional 2,4-DNT admolecules are forced to bond with pairs of COOH sites of greater distance than the adjacent NO_2 group on the 2,4-DNT with the eventuality of generating tensile stress (Figure 8.8(b)). Evidence of vapour saturation can also be observed from the change of resonant frequency as the concentration level jumps from 1.14 to 2.08 and 2.08 to 6.56ppm, the cantilevers apparently show signs of being desensitized. This lends more support to the model elucidating the cantilever V-shape response presented here.

Quantitatively, after exposure to 2,4-DNT at concentrations of 0.02ppm or 20ppb, the resonance frequency of nano-diamond coated cantilever 1,2,7 and 8 dampened by 19, 148, 38 and 58 Hz respectively (Table 8.3). Pinnaduwage et al achieved a sensitivity of ~1.67Hz/ppb using an SFXA-polymer coated 'V'-shaped Si cantilever having a spring constant of 0.4 N/m. The sensing mechanism also relies on the proton transfer from the available -OH group to the $-NO_2$ of the 2,4-DNT [31]. The sensitivity achieved here ranges from a comparably respectable ~0.95 to 7.4Hz/ppb on cantilever structures with higher effective spring constant of ~0.8-1 N/m, possibly even higher judging from the pre-exposure resonance frequencies of the microcantilever sensors on the 2nd chip. Giving this design a normalised minimum performance advantage by a factor of 1.1 and a maximum of 4.4. It is noteworthy to mention again that the DND particles used here are only partially carboxylated thus promising much superior sensitivity is achievable when the surface is fully carboxylated.

The FTIR measurement on the DND on a KBr disc before exposure to 2,4-DNT vapour confirmed the existence of the carboxyl group manifested as absorbance peaks for O-H and C=O bonds at 1632.30 and 1718.69 cm^{-1} respectively. Exposure to the vapour at a temperature of 20^{o}C shows a peak representing nitro groups in the form of N=O at 1545.13 and at 40^{o}C the same peak was slightly blue-shifted to 1545.34 cm^{-1}. Expectedly, the absorbance peak assigned to nitro groups at 1545.34 cm^{-1} carries an intensity of ~2.88 after exposure to 2,4-DNT vapour at 40^{o}C is larger compared to ~2.68 when

the temperature was set at 20^{o}C. The larger the presence of a particular chemisorption generated FTIR-active bond, the greater the amount of incident IR energy absorbed. Hence, the intensity of an FTIR absorbance peak qualitatively reflects the amount of the adsorbed molecules, in this case on the DND surface. The intensities of the peaks at different temperature stage confirm the chemisorption of 2,4-DNT on DND surface in the temperature range used and crucially, justifying the method of controlling the vapour concentration in the glass-cell by applied external thermal energy. Further evidence pointing at chemisorption of 2,4-DNT would be the clear progressive red-shift of absorbance peaks (1632.30 → 1631.24 → 1626.24 cm^{-1}) assigned to O-H of the COOH group over zero, 0.17 and 2.08ppm. The other branch of the COOH group namely C=O, the red-shift are modest at 1718.69 → 1718.18 → 1717.82 cm^{-1}. The decrease in the vibrating frequency of the molecular bonds can be attributed to increasing loading effect of the adsorbed 2,4-DNT molecules with vapour concentration. The accentuation and intensification of C-O absorbance peaks at 1052.31 and 1259.38 cm^{-1} at 0.17ppm 2,4-DNT concentration and emergence of more C-O peaks at 1023.36, 1048.05, 1130.35, 1163.27 and 1259.76 cm^{-1} lend more support to the reduction of the COOH group to COO^- by proton transfer to the NO_2 group of the 2,4-DNT and indirectly the chemisorption event. Observing the movement of the C-H absorbance peak 2925.15 → 2925.41 → 2923.76 cm^{-1}, it can be claimed that chemisorption of 2,4-DNT on H-terminated surface occurs only at relatively higher vapour concentration hence less sensitive. In support to this, C-H surface group on nanodiamond particles has been shown in a previous work to have relatively lower sensitivity towards 2,4-DNT molecules compared to diamond surfaces supporting –OH terminations [32].

8.6 Conclusion

The viability of fabricating effective hybrid cantilever structures by nano-diamond coating pre-fabricated silicon devices with a Cr/Au passivation layer on the bottom surface has been demonstrated. Improved optical detection signal was achieved by sacrificing a small area at the tip to a coating of Cr/Au.

The preferred mode of sensing utilizes the characteristic resonance frequency shift affected by the induced surface stress, be it compressive or tensile in nature as well as mass loading. Expectedly, the negative resonance frequency shift after the chemisorption of 2,4-DNT, and high sensitivity at low vapour concentrations i.e. in the ppb range and a positive shift at relatively higher concentrations suggests excellent sensor function should be achievable using this approach. FTIR scans indicate that both negative and positive shifts are results of the chemisorption event albeit the former is caused by generation of compressive stress and mechanical loading and the latter, tensile stress.

8.7 References

[1] L. Tang, C. Tsai, W.W. Gerberich, L. Kruckeberg, D.R. Kania *Biomaterials* 16 483–8 (1995)

[2] H.J. Mathieu, *Surf. Interface Anal.* 32 3–9 (2001)

[3] F.Z. Cui, D.J. Li, *Surf. Coat. Technol.* 131 481–7 (2000)

[4] K. Takahashi, M. Tanga, O. Takai, H. Okamura, *Bio Indust.* 17 44–51 (2000)

[5] K. Takahashi, M. Tanga, O. Takai, H. Okamura, *Diamond Relat. Mater.* 12 572–6 (2003)

[6] W. Yang W *et al, Nature Mater.* 1 253–7 (2002)

[7] A.R. Krauss, O. Auciello, D.M. Gruena, A. Jayatissaa, A. Sumant, J. Tucek, D.C. Mancini, N. Moldovan, A. Erdemir, D. Ersoy, M.N. Gardos, H.G. Busmann, E.M. Meyer, M.Q. Ding, Diamond Relat. Materi. 10, 1952-1961 (2001)

[8] A. Bongrain, E. Scorsone, L. Rousseau, G. Lissorgues, S.Saada, P. Bergonzo, Procedia Chemistry 1, 754–757 (2009)

[9] M.Wiora, K.Bruhne, A. Floter, P. Gluche, T.M. Willey, S.O.Kucheyev, A.W. Van Buuren, A.V. Hamza, J. Biener, H.-J. Fecht, DIAMAT 05138 (2008)

[10] P. Olivero, S. Rubanov, P. Reichart, B.C. Gibson, S.T. Huntinggton, J.R. Rabeau. A.D. Greentree, J. Salzman, D. Moore, D.N. Jamieson, S. Prawer, Diamond Relat. Mater. 15 1914-21 (2006)

[11] B.Z. Kupfer, R.K. Ahmad, A.Zainal, R.B. Jackman, Diamond and Related Materials, Volume 19, Issues 7-9, Pages 742-747, July-September (2010)

[12] O.A. Shenderova, V.V. Zhirnov and D.W. Brenner, *Crit. Rev. Solid State Mater. Sci.* 27**,** 227–356 (2002)

[13] O.A. Williams, O. Douheret, M. Daenen, K. Haenen, E. Osawa and M. Takahashi, Chemical Physics Letters 445, 255–258 (2007)

[14] A. Freedman, P.L. Kebabian, Z. Li, W.A. Robinson and J.C. Wormhoudt, Meas. Sci. Technol., 19, 125102 (2008)

[15] National Research Council (U.S.). Committee on Defeating Improvised Explosive Devices: Basic research to Interrupt the IED Delivery Chain, Countering the threat of improvised explosive devices: basic research opportunities, abbreviated version, National Academies Press (2007)

[16] G.C.A.M. Janssen, M.M. Abdalla, F. van Keulen, B.R. Pujada and B. van Venrooy, Thin Solid Films, 517, 1858-1867 (2009)

[17] Y. Zhang, Q. Ren, Y. Zhao, J. Phys. D: Appl. Phys. 37, 2140-2145 (2004)

[18] C.A. Klein, J. Appl. Phys. Vol. 8, No. 9 (2000)

[19] G.Y. Chen, T. Thundat, E.A. Wachter, R.J. Warmack, J. App. Phys. 77, 3618-22 (1995)

[20] Reddy, C.S: Basic Structural Analysis, Second Edition, Tata McGraw-Hill Publishing Company Ltd., New Delhi, (1981)

[21] B. Bushan, Springer Handbook of Nanotechnology, chp. 16 p. 447 (2006)

[22] A. Krueger, J. Stegk, Y. Liang, L. Lu, G. Jarre, Langmuir, 24, 4200-4204 (2008)

[23] Ushizawa, K.; Sato, Y.; Mitsumori, T.; Machinami, T.; Ueda, T.; Ando, T. *Chem. Phys. Lett.*, *351*, 105-108 (2002)

[24] E.J Houser, T.E. Mlsna, V.K. Nguyen, R.Chung, R.L. Mowery, R.A. McGill, Rational materials design of sorbent coatings for explosives: application with chemical sensors, Talanta 54, 469-485 (2002)

[25] Y. Chen, P. Xu, X. Li, Nanotechnology 21, 265501 (2010)

[26] E. Osawa, Pure Appl. Chem., Vol. 80, No. 7, pp. 1365–1379 (2008)

[27] J.Q. Zhang, S.W. Yu, X.Q. Feng, J. Phys. D: Appl. Phys. 41 125306 (2008)

[28] T. Thundat, R.J. Warmack, G.Y. Chen, D.P Allison, Appl. Phys. Lett. 64, 2894 (1994)

[29] T. Thundat, E.A. Wachter, S.L Sharp, R.J. Warmack, Appl. Phys. Lett. 66, 1695 (1995)

[30] G.Y. Chen, T. Thundat, E.A. Wachter, R.J. Warmack, J. App. Phys. 77, 3618-22 (1995)

[31] L. A. Pinnaduwage, T. Thundat, J. E. Hawk, D. L. Hedden, P. F. Britt, E. J. Houser, S. Stepnowski, R. A. McGill and D. Bubb, Sensors and Actuators B: Chemical, Vol. 99, 2-3, p. 223-229 (2004)

[32] E. Chevallier, E. Scorsone and P. Bergonzo, Sensors and Actuators B: Chemical, Article in Press (2010)

Figure Captions

Figure 1

Silicon microcantilever array (a) before and (b) after DND attachment and Cr/Au tip-end coating. Shematic diagram representing the Cr/Au-DND cantilever structure

Figure 2

The technique using the AFM cantilever as a microindenter to calibrate the spring constant of the DND coated cantilever

Figure 7

Probable mechanism for the adsorption-specific induced tensile stress on the DND surface of the Si cantilever

2,4-DNT vapour (ppm)	Before			
	f_{c1}	f_{c2}	f_{c7}	f_{c8}
	29.889	31.814	29.205	28.536
	After			
	f_{c1}	f_{c2}	f_{c7}	f_{c8}
0.02	29.870	31.666	29.167	28.478
0.17	29.900	31.764	29.205	28.540
1.14	29.974	31.812	29.226	28.552
2.08	30.152	32.032	29.280	28.630
6.56	30.174	32.066	29.309	28.673

Table 8.3**:** Changes in resonant frequencies for cantilever 1,2,7,8 and 5 after 2,4-DNT exposure

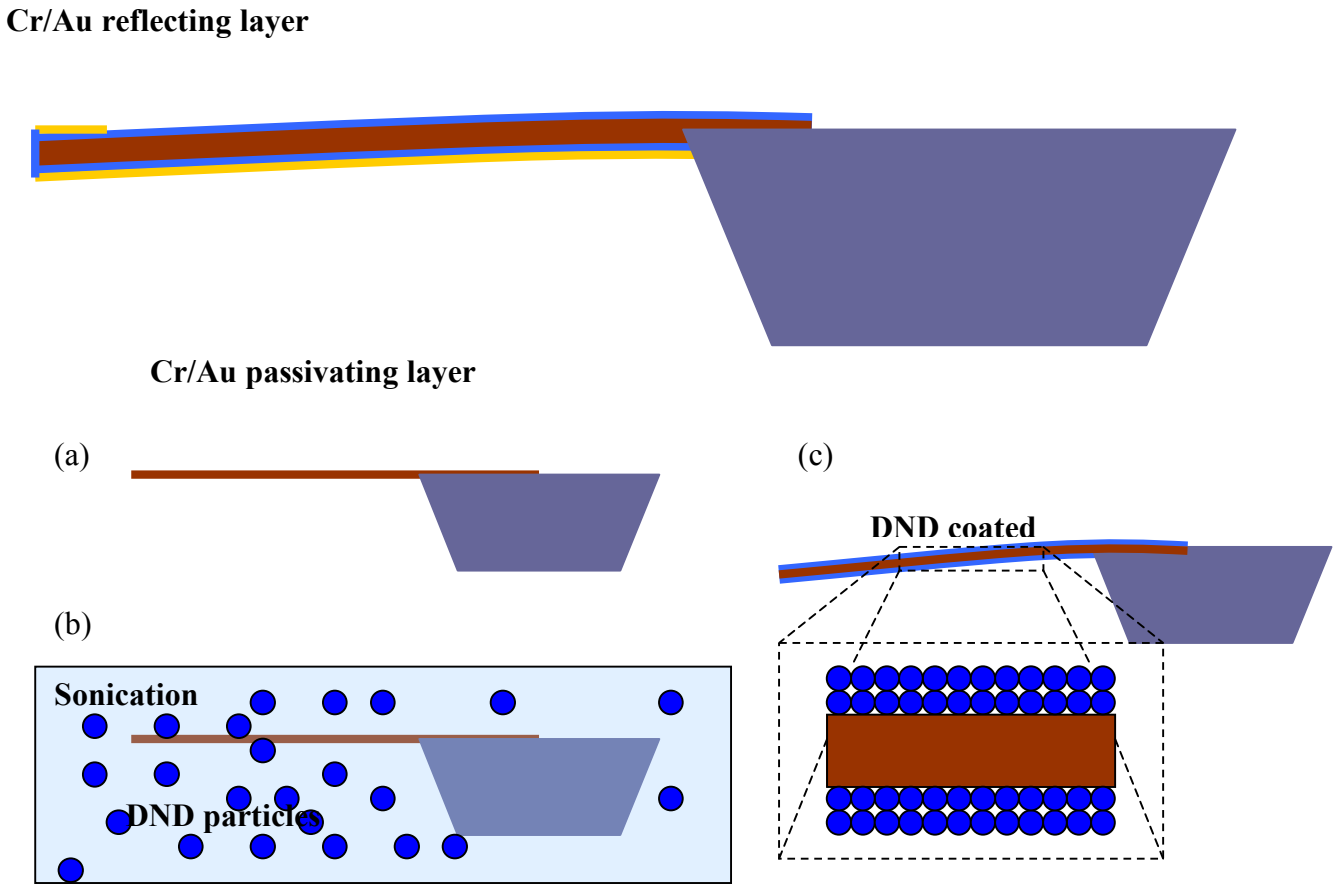
Cr/Au reflecting layer
Cr/Au passivating layer
(a)
(b)
Sonication
DND particles
(c)
DND coated

Chapter 9

Conclusion

Conclusion

Both sophisticated and elegant designs on diamond nanostructured materials for the realisation of chemical sensors have been presented and the relevant device characteristics addressed. ISFET and MEMS cantilever devices fabricated on single crystal diamond show significant relative improvements observed relative to similar device structures and promises of enhanced performance upon further substrate synthesis and device design refinement for technological maturity. Detonation nanodiamond attachment on silicon surface provides a never-seen-before yet also simple, quick and also highly potentially commercial solution in exploiting both the advantageous surface characteristics of diamond and silicon's established ISFET and MEMS cantilever technology.

Chapter 5

The intrinsic-capped delta-doped single crystal diamond ISFET fabricated is an evolutionary design solution addressing the shortcomings of the cap-less design in a previous work. Also worth mentioning, the oxygen-terminated diamond surface employed on this ISFET structure overcomes the instability issues plaguing hydrogen-terminated surface conductivity ISFETs. At doping levels circa 10^{20} cm^{-3}, the relatively high activation energy of boron acceptors at 0.37eV is reduced to ~meV thus allowing room temperature operations. To avoid high impurity scattering, a 'buried' delta (δ) doping profile is employed to accommodate carriers and ionized impurities separation. Summarising the results, two ISFET structures with 5nm and 3.2nm delta thickness exhibit improved near Nernst's limit of pH sensitivity at 52 and 55mV/pH respectively. Current-Voltage measurements yield output characteristics with visibly curved features indication of appreciable channel pinching leading towards drain current saturation, with it being more pronounced on the 3.2nm ISFET. Improved drain current levels is also observed on the 3.2nm ISFET implying better spatial separation of charge carriers and ionized impurities resulting more being released into the capping layer to be modulated by the applied gate voltage. This is corroborated by the measured flatband voltage of 3.2nm

at 3.74V of which is smaller than that of the 5nm ISFET at 4.76V. Current modulation at ~22% as well as apparent onsets of saturation for both devices appears to be of great improvement over uncapped structured ISFETs further suggesting conduction takes place in the semiconducting capping layer rather than the metallic delta-channel. Current stability within 2% is observed over cyclic pH 2 and 10 sequential current-voltage measurements. Electrochemical impedance spectroscopy characterisation producing fitted RC circuits modelling with the 3.2nm device again showing clear and simpler conduction paths. Conclusively, the capped delta structure has been clearly demonstrated to be the correct design solution for diamond ISFETs with the drain current of the thinner delta channel ISFET exhibiting better inclination to pinch-off. It can therefore be deduced that the capping layer is instrumental in providing much improved performance over the previous cap-less delta doped ISFET structure thus moving a step closer to realising full drain current saturation for stable ISFET biasing and operation.

Further work should come in the form of having thinner delta-layers circa 1-2nm and improved quality of the interfacial layers in this structure, which allow more carriers to be released to form better semiconductive channel supported in the capping layer and more importantly, full channel pinch-off within the allowed potential window of the intrinsic diamond gate surface. The anticipated improved ISFET characteristics would be stronger or fuller drain current saturation, increased transconductance and better pH sensitivity.

Chapter 6

A novel hybrid solution to an ISFET design has been proposed, fabricated and tested. By coating the active gate area of silicon ISFET with detonation nanodiamonds, the new device structure allows a matured technology in silicon to exploit the outstanding surface sensing characteristics of diamonds. Such technique importantly sidesteps the long-term instability of hydrogen-terminated surface conductivity ISFET and diamond delta-doping growth issues. Remarkably, the nanodiamond-gated ISFET matched the pH sensitivity of the as received device at 53mV/pH whilst outperforming in the detection of other ions in the liquid phase. The pH sensitivity confirms surface

charge transfer between ions and the carbon-oxygen surface group on nanodiamonds. The hybrid device is able to detect and resolve explosive precursors in the form of NO_2^- and ClO_3^- ions in the liquid medium at various concentration levels, a feat the original device fails to duplicate. In the vapour phase, the output voltage trend responding to 2,4 DNT exposure indicates logical detection through acid-base interaction when referencing against that of the basic NH_3 vapour. It is surmised that the surface group responsible for such detection is the acidic -COOH termination on the nanodiamond surface. With carbon-carbon bond being stronger and stable than carbon-silicon bond, such gating structure on an ISFET is thought to be reliably robust for both sensing pH levels and detecting threat signatures. Such hybrid design solution therefore provides a viable, realistic and commercial opportunity for real-world application of diamond-based sensing devices. However, an in-depth study is needed to probe the solid-state electronic effects of nanodiamond attachment to gate area and this can only be achieved by gating nanodiamonds on a 'bare' oxide-less lab-fabricated silicon FET. A fully carboxylated (sensing sites) nanodiamond gate should also provide better sensitivity. To create selectivity, the nanodiamond may be purposely functionalised for specific target admolecules. Reliable biological detection using grafted probe DNA, antibodies and enzymes is another major potential application. Enhanced sensitivity can be achieved by ensuring full coverage of functional groups accommodating better electrical transduction of chemisorption-induced surface charge variation.

Chapter 7

The difficulty in fabrication of practical single crystal diamond cantilever has been overcome by using only focused-ion beam (FIB) producing a triangle-faced free-standing singly supported beam structure of 16.17 x 3.36 x 2.17 μm dimensions fabricated on type Ib single crystal diamond substrate. Pre-existing technique introduces significant lattice damage and allows very little room for cantilever deflection and manipulation. The triangular face of the cantilever is achieved by FIB milling at an angle. Based on theoretical modelling, the smaller the angle between the base and hypotenuse the larger the deflection per unit force applied. Hence the beam is angled to the

maximum at 54^{o} to achieve the minimum angle at 36^{o} for the triangular face for appreciable beam deflection. Post-fabrication characterisations are applied to ascertain the amount of damage inflicted by this novel milling approach. Raman spectra indicate lattice damage was minimal with very little change in the FWHM of the D-peak juxtaposing that of pre-fabrication, post-fabrication and after the annealing stages at 500, 750 and 1000^{o}C. However, Gallium contamination though rather significant initially at post-fabrication is eliminated by the thermal treatment as revealed by the EDS spectra. This simple technique offers a diamond cantilever structure with better deflectivity, minimal in-fabrication damage and provides adequate surrounding space for cantilever bending and surface functionalisation protocols. Effective diamond-based chemical and biological sensors following suitable surface functionalisation can thus be realised by the advent of FIB-milled triangular face single crystal diamond cantilever structures. However, such cantilever design requires actual mechanical characterisation both in the static and dynamic mode of operation to determine its spring constant (k) and resonance frequency. Actuation of the beam may be achieved through deposited thin layer of piezoelectric material such as zinc oxide, activated by an ac voltage source. Probing the piezoelectric layer could also reveal the corresponding beam deflection and resonance frequency. Eventual sensor function can then be realised through correct surface functionalisation.

Chapter 8

Echoing the design and fabrication simplicity for the work presented in Chapter 6, a diamond-based cantilever is realised in the form of commercially available silicon cantilever array chip covered with a coat of nanodiamond particles. Mechanical characterisation and sensor functionality are easily realised using existing AFM set-up. With the AFM cantilever doubling up as micro-indenter, the static mode spring constant k is revealed to have increased by a factor of 7 after nanodiamond attachement. By supplanting the AFM cantilever, the nanodiamond-coated cantilever is further dynamically characterised and the reduced resonance frequency confirms the mechanical loading by the nanodiamond layer. Applying beam theory, the attached nanodiamond particles coverage is determined to be ~ 10^{11}cm^{-2}. To function

as a sensor, the bottom surface is passivated with a Cr/Au bilayer at 33nm and subsequent exposure to 2,4 DNT vapour at varying concentration levels features a maximum sensitivity of 7Hz/ppb. The same acidic -COOH group on the nanodiamond surface allows the detection of 2,4 DNT through acid-base interaction. FTIR scans show strong absorption peak for the -COOH group and subsequent red-shifts indicating of chemisorption of the 2,4 DNT on the COOH group. Considering the complexities related with diamond growth and structural patterning and release, this cantilever design and subsequent proof of concept sensor work provide a new, simple and economically feasible design solution for diamond-based cantilever fabrication thus fast-tracking the deployment of reliable, robust and crucially, sensitive diamond-based cantilever sensors. Similar to the proposal made for the ND-coated ISFET, a fully carboxylated ND surface should yield increased sensitivity towards 2,4 DNT chemisorption. Another recommended study to be made would be the effect of full surface termination with oxygen and hydrogen respectively on chemisorption selectivity of different chemicals such as 2,4-DNT, RDX, sarin etc in the vapour phase. Further relevant chemical alteration of the functional groups attached on the nanodiamond-coated cantilever allows corresponding biological detection such as DNAs and antigens.

The fabricated devices presented in this thesis are evidencing the potentials of diamond in the field of chemical and biological sensing applications. Novel single crystal diamond-based delta doped ISFET and cantilever designs represent the future of sensing devices and it is apparent that the observations and deductions made from this work have contributed significantly in this research area through the aforementioned new device structures and appropriately providing a new set of bearings to achieve the ultimate goal of reliable single crystal diamond ISFET and cantilever sensors. Conversely, the concept of nanodiamond-silicon hybrid device structures proves to be a unique and innovative approach to exploit the excellent properties of diamond surface without the need to deal with the issues of diamond growth and doping, and capitalising on matured silicon device technology thus facilitating rapid industrialisation, commercialisation and deployment of diamond-based ISFET and MEMS devices.

Relevant Publications

1. Benjamin Z. Kupfer, Rezal K. Ahmad, Aiman Zainal and Richard B. Jackman, Fabrication and characterisation of triangle-faced single crystal diamond micro-cantilevers, Diamond and Related Materials, Volume 19, Issues 7-9, July-September 2010, Pages 742-747, Proceedings of Diamond 2009, The 20th European Conference on Diamond, Diamond-Like Materials, Carbon Nanotubes and Nitrides, Part 2
2. Rezal K. Ahmad, Ana Carolina Parada, Steve Hudziak, Aysha Chaudhary, and Richard B. Jackman, Nanodiamond-coated silicon cantilever array for chemical sensing, Appl. Phys. Lett. 97, 093103 (2010)
3. Rezal K. Ahmad, Ana Carolina Parada, Niall Tumilty, and Richard B. Jackman, Nanodiamond-gated diamond field-effect transistor for chemical sensing using hydrogen-induced transfer doping for channel formation, Appl. Phys. Lett. 97, 203503 (2010)
4. Rezal K. Ahmad, Ana Carolina Parada, Richard B. Jackman, Nanodiamond-gated silicon ion-sensitive field effect transistor, Appl. Phys. Lett , 98, 153507 (2011)